Development of (α,n) Signatures as a Viable Safeguards Measurement for Electrochemical Reprocessing

A Dissertation Presented for the

Doctor of Philosophy

Degree

The University of Tennessee, Knoxville

Stephen N. Gilliam

December 2020

Copyright © by Stephen N. Gilliam, 2020

All Rights Reserved.

Acknowledgments

This work was supported by an Nuclear Energy University Programs (NEUP) grant sponsored by the U.S. Department of Energy, Office of Nuclear Energy, award number DE-NE0008553. The author likewise wishes to gratefully acknowledge the support and assistance of Benjamin Cipiti and Nathan Shoman of Sandia National Laboratory. Part of this work was supported by a one-year fellowship sponsored by the US Nuclear Regulatory Commission under grant NRC-31310019M0039

Furthermore, I would like to extend special gratitude and acknowledge my research advisor, Dr. Jamie B. Coble and also the other members of the defense committee, namely, Dr. Steven E. Skutnik, Dr. Jason P. Hayward, Dr. Angela L. Lousteau and Dr. Braden Goddard.

Abstract

As interest grows in electrochemistry for material separations and reprocessing of nuclear fuel research and development into the safeguard ability of such a system is needed. Plutonium quantification via (α,n) neutrons within the electrorefiner vessel is examined as a potential alternative means given that traditional methods such as multiplicity counting via spontaneous fission tracking may prove ineffective given the material composition of the electrorefiner. An MCNP model of an Epi-Thermal Neutron Multiplicity counter was used in the calculation of curium from a sample of curium, plutonium, and eutectic salt. This and the multiplicity variable α, the ratio between (α,n) neutron and spontaneous fission, were then used to define the plutonium mass as it related to its (α,n) signature. It was shown that theoretically the plutonium mass of such a sample could be estimated within 20%. Due to error associated with falsely counting (α,n) neutrons as spontaneous fission, that produce such a high level of uncertainty this method is not viable with current detector systems. If future detector designs can mitigate the false counting that occurs the method was shown to reproduce plutonium mass estimation to that of comparable uncertainty with multiplicity counting already in practice for non-mixed samples.

Table of Contents

1 Introduction **1**

1.1 Original Contributions 2

1.2 Organization of the Document 3

2 Background **4**

2.1 Electrochemical Reprocessing of Used Fuel 4

2.1.1 Process Description 4

2.1.2 Input Feed 6

2.1.3 Electrolytic Reduction 6

2.1.4 Electrorefining 7

2.1.5 End Product Collection 9

2.2 Neutron Multiplicity Counting 11

2.2.1 Passive Multiplicity Counting 13

2.2.2 Active Multiplicity Counting 15

2.2.3 Neutron Detector Systems 18

2.3 Prior Electrochemical Safeguards Work 23

2.3.1 Application of Neutron Counting for Plutonium Verification 24

2.3.2 Neutron Counting in Electrochemical Systems 26
2.3.3 Additional Methods 29

3 Model and Simulation **32**

3.1 SSPM EChem Model 32
3.1.1 Fuel Generation 33
3.2 Neutron Code Systems 35
3.2.1 SCALE/SOURCES-4C 35
3.2.2 Monte Carlo N-Particle 37

4 Methodology **41**

4.1 Neutron Simulation 41
4.1.1 Spontaneous Fission Simulation 41
4.1.2 (α,n) Simulation 43
4.2 Sample Characterization 50
4.3 MCNP Multiplicity Interpretation 53
4.4 Effective Mass Coefficients 57
4.5 Pu Mass Estimation 58

5 Results and Analysis **61**

5.1 Emission Rate Analysis 61
5.1.1 Epi-thermal Energy Classification 62
5.1.2 Epi-thermal Energy Analysis 66
5.2 Burnup and Enrichment Effects 69

5.3 Geometrical Analysis . . . 72
5.4 Die-Away Time Optimization . . . 76
5.5 ENMC Passive Results . . . 76
5.5.1 Single Elemental Mass Samples . . . 78
5.5.2 Mass of Curium and Eutectic Salt . . . 79
5.5.3 Mass of Plutonium and Eutectic Salt . . . 88
5.5.4 Actual Mass of Plutonium, Curium, and Eutectic Salt . . . 88
5.5.5 Estimation with Varying Enrichment . . . 96
5.5.6 Plutonium Mass Estimation . . . 96

6 Conclusion **108**

6.1 Recommendations and Future Work . . . 109

Bibliography **112**

Appendices **120**

A Appendix A . . . 121
B Appendix B . . . 125
C Appendix C . . . 173

Vita **187**

List of Tables

2.1 Survey of Passive Multiplicity Counters in DOE Facilities [17]. 22

2.2 Neutron Sources in Spent Fuels [34]. 25

2.3 Free Energy of Formation of the Various Metal Chlorides at 500°C [44]. . . . 31

4.1 Nuclear Data Parameters for Isotopes of Curium [24, 9]. 60

5.1 Summary of SSPM EChem (α,n) Results Showing Burnup/Enrichment Mixtures [0-4.5] MeV. 65

5.2 Summary of Geometrical (α,n) Results from Sources and Scale for a Sample Containing Plutonium, Curium, and Eutectic Salt. 77

C.1 Summary of Main Sequence Variables Used for Multiplicity Counting from a Sample Containing Cm and Eutectic Salt. 174

C.2 Summary of 20 GWd Sequence Variables Used for Multiplicity Counting from a Sample Containing Pu, Cm, and Eutectic Salt. 175

C.3 Summary of 25 GWd Sequence Variables Used for Multiplicity Counting from a Sample Containing Pu, Cm, and Eutectic Salt. 176

C.4 Summary of 30 GWd Sequence Variables Used for Multiplicity Counting from a Sample Containing Pu, Cm, and Eutectic Salt. 177
C.5 Summary of 35 GWd Sequence Variables Used for Multiplicity Counting from a Sample Containing Pu, Cm, and Eutectic Salt. 178
C.6 Summary of 40 GWd Sequence Variables Used for Multiplicity Counting from a Sample Containing Pu, Cm, and Eutectic Salt. 179
C.7 Summary of 45 GWd Sequence Variables Used for Multiplicity Counting from a Sample Containing Pu, Cm, and Eutectic Salt. 180
C.8 Summary of 50 GWd Sequence Variables Used for Multiplicity Counting from a Sample Containing Pu, Cm, and Eutectic Salt. 181
C.9 Summary of 55 GWd Sequence Variables Used for Multiplicity Counting from a Sample Containing Pu, Cm, and Eutectic Salt. 182
C.10 Summary of 60 GWd Sequence Variables Used for Multiplicity Counting from a Sample Containing Pu, Cm, and Eutectic Salt. 183
C.11 Summary of 20 GWd Source Strength Variables Used to Calculate Plutonium Mass. 184
C.12 Summary of 25 GWd Source Strength Variables Used to Calculate Plutonium Mass. 184
C.13 Summary of 30 GWd Source Strength Variables Used to Calculate Plutonium Mass. 184
C.14 Summary of 35 GWd Source Strength Variables Used to Calculate Plutonium Mass. 184

C.15 Summary of 40 GWd Source Strength Variables Used to Calculate Plutonium Mass. 185
C.16 Summary of 45 GWd Source Strength Variables Used to Calculate Plutonium Mass. 185
C.17 Summary of 50 GWd Source Strength Variables Used to Calculate Plutonium Mass. 185
C.18 Summary of 55 GWd Source Strength Variables Used to Calculate Plutonium Mass. 185
C.19 Summary of 60 GWd Source Strength Variables Used to Calculate Plutonium Mass. 186

List of Figures

2.1 Flowsheet of a pyrochemical process for Light Water Reactor fuel [45]. 5

2.2 Principle of the electrolytic reduction in electrochemical systems [44]. 8

2.3 Operational diagram for a typical electrorefining unit recreated from [38]. . . 10

2.4 Rossi-alpha distribution showing detected neutron events as a function of time [15]. 21

2.5 Separation action via Gibbs free energy of chloride formation. 28

3.1 Flow diagram outlining the MBA areas throughout the SSPM EChem model [8]. 34

3.2 Fuel discharge burnup and enrichment combinations evaluated. 36

3.3 LASTCALL interface within the Sources-4C software. 38

4.1 Comparison for the spontaneous fission emission rate between MATLAB and Origen. 44

4.2 (α,n) Reaction in the Center-of-Mass System [42]. 49

4.3 (α,n) Reaction in the Laboratory System [42]. 49

4.4 Comparison for the (α,n) emission rate between MATLAB and Origen. . . . 51

4.5 Plutonium and Curium contribution for (α,n) neutrons for 20GWd main sequence burnup and enrichment with a cooling time of 5 years. 54

5.1 Correlation heat map between varying burnup and enrichment values from Origen for the ratio of (α,n) to total neutron emission rate for a cooling time of 5 years. 63

5.2 Correlation heat map between varying burnup and enrichment values from Origen for the ^{238}Pu contribution to (α,n) reactions for a cooling time of 5 years. 64

5.3 Demonstration of the intersection between the spontaneous fission emission rate and the (α,n) emission rate for a cooling time of 5 years. 67

5.4 Ratio of (α,n) to total emission rate for a main sequence burnups across an epi-thermal energy range with cooling time of 5 years. 68

5.5 Ratio of (α,n) to total emission rate for a main sequence burnups and enrichments for each energy bin from 0-300 keV with a cooling time of 5 years. 70

5.6 Plutonium contribution for (α,n) neutrons for main sequence burnup and enrichment from 0-300 keV from Origen for a cooling time of 5 years. 71

5.7 Enrichment effect on the ratio of (α,n) to total emission rate for various burnups from 0-4.5 MeV with a cooling time of 5 years. 73

5.8 Enrichment effect on the ratio of (α,n) to total emission rate for various burnups from 0-300 keV with a cooling time of 5 years. 74

5.9 Die-away time optimization for the ENMC input deck. 77

5.10 Comparison between actual and estimated via ENMC mass of curium. . . . 80
5.11 Comparison between actual and estimated via ENMC mass of plutonium. . . 81
5.12 Percent error for curium mass estimation. 82
5.13 Percent error for plutonium mass estimation. 83
5.14 Comparison between simulated mass and actual mass of Cm-244. 84
5.15 Percent error for Cm-244 and total curium mass estimation. 85
5.16 α variable comparison for a sample containing only curium. 86
5.17 Comparison between Cm-244 mass percent error and total (α,n) contribution to neutron yield. 87
5.18 Comparison between simulated mass and mass of plutonium and salt. 89
5.19 Percent error for plutonium and salt mass estimation. 90
5.20 Comparison between simulated mass and actual mass of Cm-244 for a mixed sample. 92
5.21 Percent error for Cm-244 and total curium mass estimation for a mixed sample. 93
5.22 α variable comparison for SCALE emissions and estimates from the ENMC model for a mixed sample. 94
5.23 Comparison between Cm-244 mass percent error and total (α,n) contribution to neutron yield. 95
5.24 Comparison between simulated mass and actual mass of Cm-244 for a mixed sample. 97
5.25 Percent error for Cm-244 mass estimation for a mixed sample. 98
5.26 α variable comparison for SCALE emissions and estimates from the ENMC model for a mixed sample. 99

5.27 Comparison between Cm-244 mass percent error and total (α,n) contribution to neutron yield. 100

5.28 Comparison between simulated mass and actual mass of plutonium for a mixed sample. 102

5.29 Percent error for plutonium mass estimation for a mixed sample. 103

5.30 α variable correction factor. 105

5.31 Comparison between simulated mass and actual mass of plutonium for a mixed sample under ideal circumstances. 106

5.32 Percent error for the corrected and ideal plutonium mass estimation for a mixed sample. 107

A.1 Empirical relationship of the ratio of (α,n) to total emission rate as a function of burnup from 0-4.5 MeV with a cooling time of 5 years. 121

A.2 Empirical relationship of the ratio of (α,n) to total emission rate as a function of enrichment from 0-4.5 MeV with a cooling time of 5 years. 122

A.3 Emprical relationship of the ratio of (α,n) to total emission rate as a function of burnup from 0-300 keV with a cooling time of 5 years. 123

A.4 Empirical relationship of the ratio of (α,n) to total emission rate as a function of enrichment from 0-300 keV with a cooling time of 5 years. 124

B.1 Comparison between simulated mass and actual mass of Cm-244 for a 25 GWd mixed sample. 125

B.2 Percent error for Cm-244 mass estimation for a 25 GWd mixed sample. . . . 126

B.3 Alpha variable comparison for a 25 GWd mixed sample. 127

B.4 Comparison for 25 GWd between Cm-244 mass percent error and total (α,n) contribution to neutron yield. 128
B.5 Comparison between simulated mass and actual mass of plutonium for a 25 GWd mixed sample. 129
B.6 Percent error for plutonium mass estimation for a 25 GWd mixed sample. . . 130
B.7 Comparison between simulated mass and actual mass of Cm-244 for a 30 GWd mixed sample. 131
B.8 Percent error for Cm-244 mass estimation for a 30 GWd mixed sample. . . . 132
B.9 Alpha variable comparison for a 30 GWd mixed sample. 133
B.10 Comparison for 30 GWd between Cm-244 mass percent error and total (α,n) contribution to neutron yield. 134
B.11 Comparison between simulated mass and actual mass of plutonium for a 30 GWd mixed sample. 135
B.12 Percent error for plutonium mass estimation for a 30 GWd mixed sample. . . 136
B.13 Comparison between simulated mass and actual mass of Cm-244 for a 35 GWd mixed sample. 137
B.14 Percent error for Cm-244 mass estimation for a 35 GWd mixed sample. . . . 138
B.15 Alpha variable comparison for a 35 GWd mixed sample. 139
B.16 Comparison for 35 GWd between Cm-244 mass percent error and total (α,n) contribution to neutron yield. 140
B.17 Comparison between simulated mass and actual mass of plutonium for a 35 GWd mixed sample. 141
B.18 Percent error for plutonium mass estimation for a 35 GWd mixed sample. . . 142

B.19 Comparison between simulated mass and actual mass of Cm-244 for a 40 GWd mixed sample. 143
B.20 Percent error for Cm-244 mass estimation for a 40 GWd mixed sample. . . . 144
B.21 Alpha variable comparison for a 40 GWd mixed sample. 145
B.22 Comparison for 40 GWd Cm-244 mass percent error and total (α,n) contribution to neutron yield. 146
B.23 Comparison between simulated mass and actual mass of plutonium for a 40 GWd mixed sample. 147
B.24 Percent error for plutonium mass estimation for a 40 GWd mixed sample. . . 148
B.25 Comparison between simulated mass and actual mass of Cm-244 for a 45 GWd mixed sample. 149
B.26 Percent error for Cm-244 mass estimation for a 45 GWd mixed sample. . . . 150
B.27 Alpha variable comparison for a 45 GWd mixed sample. 151
B.28 Comparison for 45 GWd between Cm-244 mass percent error and total (α,n) contribution to neutron yield. 152
B.29 Comparison between simulated mass and actual mass of plutonium for a 45 GWd mixed sample. 153
B.30 Percent error for plutonium mass estimation for a 45 GWd mixed sample. . . 154
B.31 Comparison between simulated mass and actual mass of Cm-244 for a 50 GWd mixed sample. 155
B.32 Percent error for Cm-244 mass estimation for a 50 GWd mixed sample. . . . 156
B.33 Alpha variable comparison for a 50 GWd mixed sample. 157

B.34 Comparison for 50 GWd between Cm-244 mass percent error and total (α,n) contribution to neutron yield. 158
B.35 Comparison between simulated mass and actual mass of plutonium for a 50 GWd mixed sample. 159
B.36 Percent error for plutonium mass estimation for a 50 GWd mixed sample. . . 160
B.37 Comparison between simulated mass and actual mass of Cm-244 for a 55 GWd mixed sample. 161
B.38 Percent error for Cm-244 mass estimation for a 55 GWd mixed sample. . . . 162
B.39 Alpha variable comparison for a 55 GWd mixed sample. 163
B.40 Comparison for 55 GWd between Cm-244 mass percent error and total (α,n) contribution to neutron yield. 164
B.41 Comparison between simulated mass and actual mass of plutonium for a 55 GWd mixed sample. 165
B.42 Percent error for plutonium mass estimation for a 55 GWd mixed sample. . . 166
B.43 Comparison between simulated mass and actual mass of Cm-244 for a 60 GWd mixed sample. 167
B.44 Percent error for Cm-244 mass estimation for a 60 GWd mixed sample. . . . 168
B.45 Alpha variable comparison for a 60 GWd mixed sample. 169
B.46 Comparison for 60 GWd between Cm-244 mass percent error and total (α,n) contribution to neutron yield. 170
B.47 Comparison between simulated mass and actual mass of plutonium for a 60 GWd mixed sample. 171
B.48 Percent error for plutonium mass estimation for a 60 GWd mixed sample. . . 172

Chapter 1

Introduction

In recent years, new technology that exemplifies stronger proliferation resistance for nuclear fuel reprocessing facilities has led to the interest in electrochemical reprocessing as a substitute for current methods such as the aqueous PUREX (Plutonium and URanium EXtraction) separation. When designing such facilities with the purpose of fuel fabrication or fuel reprocessing a number of design principles must be taken into consideration to ensure quality control. Among these lies efficient actinide recovery, strong nonproliferation features, waste minimization, and commercial viability [41].

Investment into electrochemical reprocessing facilities will only become acceptable if safeguards applications are properly established to meet current standards set forth by the International Atomic Energy Agency (IAEA) [2]. One such area is proliferation resistant material accountancy measurements applied in operations that focus on quantifying the mass of and track the used nuclear fuel (UNF) as it flows through the process. This begins as soon as material enters the head end and continues as material moves from one material balance area (MBA) to another. It is important during reprocessing to determine where

and when samples will be taken for such measurements. Thus, an understanding of the system in question is necessary. Environmental characteristics for electrochemical systems complicate sampling for assay from the electrorefiner due to the higher temperatures when compared to aqueous systems and the requirement of an inert atmosphere. Furthermore, the complex nature of the sample matrix that could be taken from the electrorefiner complicates the separation and identification of signatures from each constituent component. This is because curium and plutonium remain together throughout the entire processes making quantification of plutonium via the spontaneous neutron signature near impossible. However, recent research has shown that the interactions of α-particles within the eutectic salt allow neutrons produced via (α,n) reactions to dominate the total neutron yield at lower emission energies. Tracing these signatures isotopically shows that ^{238}Pu is a major contributor [19]. The following dissertation presents research that outlines the development of a safeguards technique that utilitzes this (α,n) signature through the multiplicity variable α to quantify the plutonium mass at the electrorefiner.

1.1 Original Contributions

To date, no studies in literature have shown analysis of UNF by utilizing the (α,n) signature as a means to verify plutonium content. This is due to the insignificant contribution of (α,n) neutrons to the total neutron count when compared to that of spontaneous fission in current commercial aqueous reprocessing systems where the main viable target is ^{18}O. However, given that the environment of electrochemical systems contains an impure matrix with a high magnitude of α-particle targets, the intensity of the (α,n) emissions may be

comparable to that of spontaneous fission and offer a means to track plutonium. This research contributes to the field in the following ways:

1. Examination of neutron safeguard applicability and detector selection for electrochemical reprocessing facilities.
2. Investigation of the (α,n) contribution to total neutron yield for electrorefining units.
3. Determination if the (α,n) signature can be detected and isolated from spontaneous fission neutrons.
4. Development of an empirical relationship between (α,n) production and ^{238}Pu content in UNF for electrochemical systems.

1.2 Organization of the Document

The next chapter reviews the relevant information in electrochemical reprocessing development as well as give a fundamental understanding of neutron detection physics and methods for multiplicity counting. Subsequent chapters then address simulation and model design as well as neutron detection for material quantification in reprocessing facilities. Results are then broken down first into an emission rate analysis to show the prevalence of (α,n) neutrons in electrochemical systems. The second half of the results delves into the detector response of an Epi-Thermal Neutron Multiplicity counter. Finally, the work is summarized and future work addressed.

Chapter 2

Background

2.1 Electrochemical Reprocessing of Used Fuel

2.1.1 Process Description

Electrochemical reprocessing, also known as pyroprocessing, is a proposed alternative to conventionally used aqueous methods where the difference lies by relying on Gibbs free energy of metallic fuel and fission products to separate UNF into reusable products. The process is outlined in a conceptual flowchart in Figure 2.1 for the multiple components of the cycle [45]. Multiple electrochemical aspects are used to convert actinides and fission products to a metallic state, if originally in oxide form, and then separate the metallic actinides from the fission products. A voltage potential is run across an electrolytic solution, LiCl-KCl, which results in the desirable products, uranium and transuranics (TRU), deposited onto two cathodes [41]. From here further processing is necessary to transform the cathode deposits into ingot form.

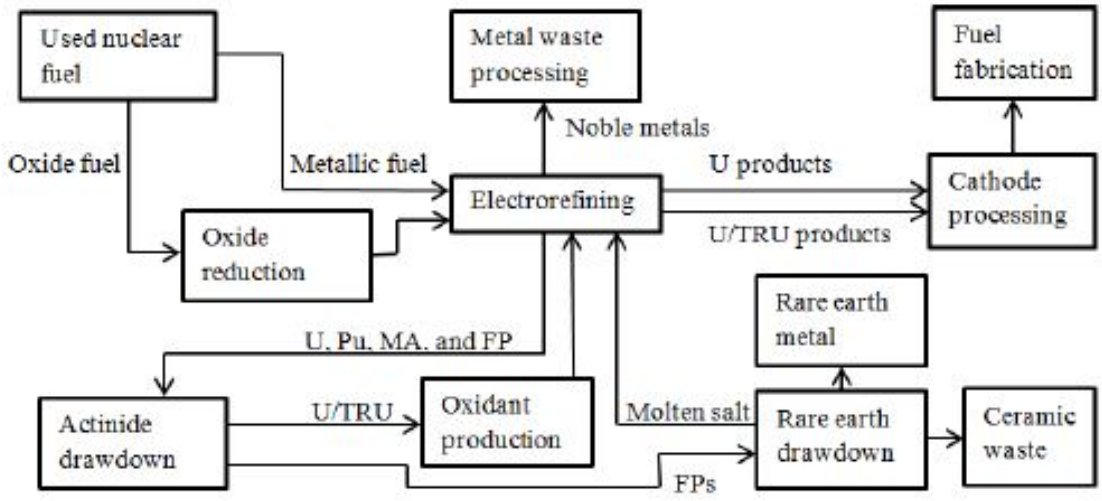


Figure 2.1: Flowsheet of a pyrochemical process for Light Water Reactor fuel [45].

2.1.2 Input Feed

The beginning phase sees the fuel assemblies disassembled by the removal of fuel rods that are then chopped to produce fuel segments approximately one to two inches in length [41]. Once the cladding has been removed, fuel pellets of uranium oxide (UO_2) are then collected from the cladding and transported to the subsequent voloxidation (volumetric oxidation) process, wherein UO_2 is oxidized to produce U_3O_8 powder (Eq. 2.1) [44, 7]. This creates a much larger surface area and thus increases the rate of electroreduction.

$$3UO_2 + O_2 \longrightarrow U_3O_8 \tag{2.1}$$

These materials are then collected and transferred to fuel baskets to begin the electrolytic reduction process. The fuel assembly hardware is transported to the metal waste treatment cell while most of the gaseous fission products, such as tritium, krypton, and xenon are sent to an off-gas treatment system [41].

2.1.3 Electrolytic Reduction

In the case that the input fuel is of oxide form, it must first be reduced into a metallic state before entering the electrorefiner. The reduction process is comprised of three key components: the cathode, anode, and electrolyte shown in Figure 2.2 [44]. The cathode is defined as the fuel basket where the previously chopped fuel is held. An inert material, such as a platinum rod, serves as the oxygen evolving anode, and a molten salt, LiCl-Li_2O, serves as the electrolyte held at 650°C [41, 44]. As a current is run between the cathode and anode, electrons will reduce the metal ion of the metal oxide to yield the base metal at the cathode

(Eq. 2.2). Simultaneously, oxide ions are released into the molten salt and transported to the anode where they are oxidized to produce oxygen gas that is released from the cell (Eq. 2.3) [41]. Here M is the metal ion to be reduced such as the actinide oxides and the bulk of the lanthanide oxides [41].

$$M_xO_y(s) + 2ye^- \longrightarrow xM(s) + yO^{2-} \tag{2.2}$$

$$O^{2-} \longrightarrow \frac{1}{2}O_2(g) + 2e^- \tag{2.3}$$

2.1.4 Electrorefining

In the core of the electrochemical process, metal chlorides are used as feed into the electrorefiner where recovery of uranium and TRU occurs. Here, the metallic product contained in the fuel basket is defined as the anode. The basket is dispensed in a pool of LiCl-KCl salt maintained at 500 °C [41]. Uranium and TRU are then chlorinated at the anode and gradually deposit into the salt over time as shown in Figure 2.3 [38]. A current is then run across the anode basket to a solid cathode deposited in the electrolyte. From there, deposition of uranium onto the solid cathode is controlled by adjusting the cell voltage. The alkaline and alkaline earth constituents form stable chlorides and thus stay within the salt throughout the refining process. The noble metal chlorides tend to stay in a metallic form and reside at the anode due to having a lower free energy for formation. After recovery of uranium at the solid cathode, in which the uranium is reduced back to metallic form, the cell voltage is adjusted to collect uranium and TRU (UTRU) onto a separate liquid cadmium

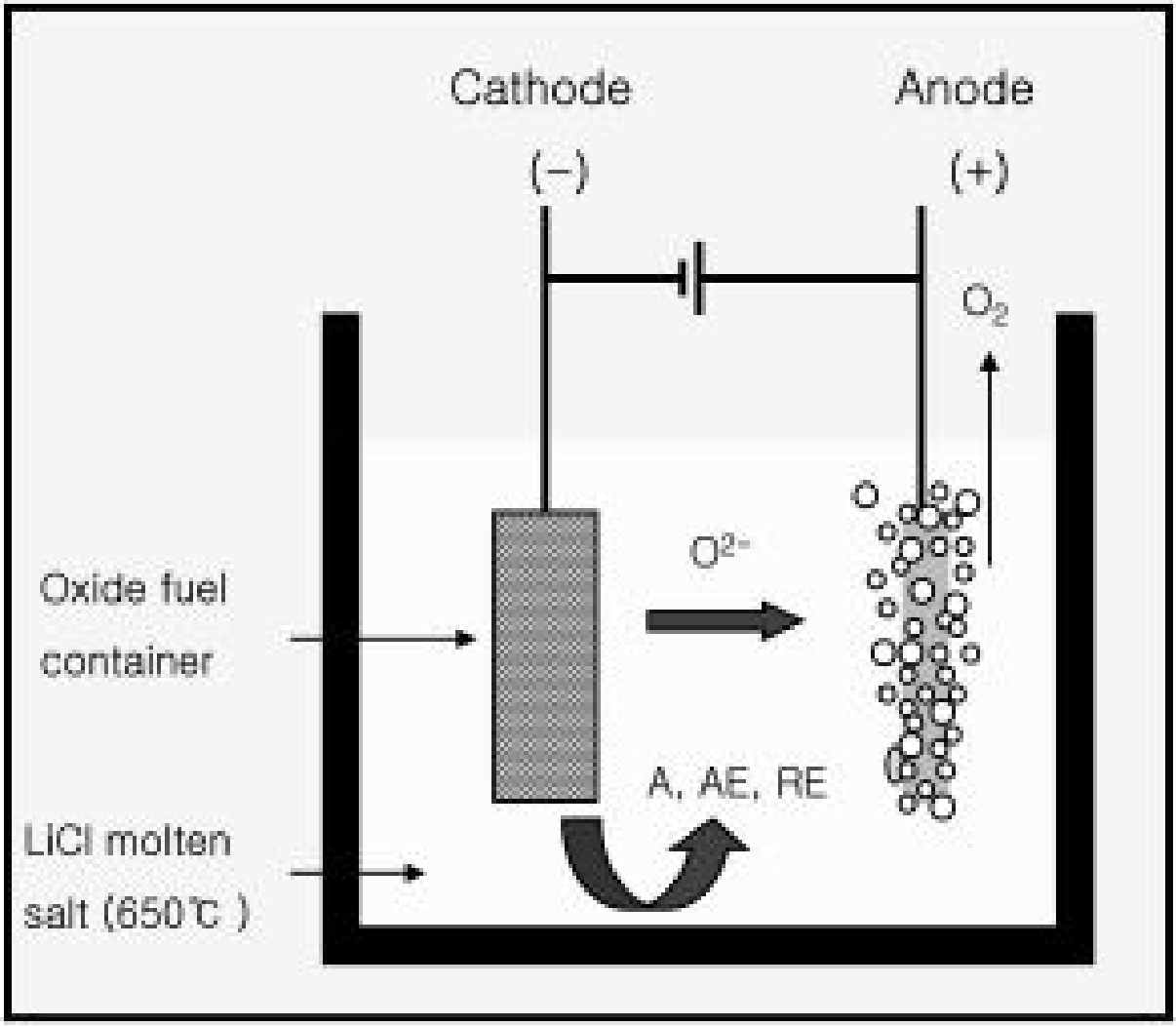


Figure 2.2: Principle of the electrolytic reduction in electrochemical systems [44].

cathode (LCC) [3]. This is done to preserve the uranium content on the solid cathode and prevent contamination from TRU material. Remaining fission products segregate between the anode basket and the molten salt while noble metals with lower potentials, such as rhodium and ruthenium, remain in the anode basket [45].

Due to the light isotopes that make up the eutectic salt acting as targets for α-particles, most notably ^{7}Li and ^{37}Cl, (α,n) neutrons contribute more in magnitude to the total neutron count within the electrorefining unit. This is further supported by the mass difference between the batch size of the deposited fuel and the size of the salt pool. This allows for more (α,n) reactions to occur not only given the cross section of the targets but also by the vast abundance of targets compared to fuel allowing no α-particle to escape the medium. Subsequent units wherein the salt accompanies the recovered material, such as the cathode processing systems, may also be of interest when looking at (α,n) neutrons.

2.1.5 End Product Collection

The backend of the electrochemical cycles sees the processing of both cathodes as well as metal processing from waste left within the anode basket. In the processing of both cathodes, trace amounts of eutectic salt (up to 20-40%) and lanthanide chlorides are present and must first be removed [44]. This is done by two drawdown phases, one for actinides and the other lanthanides. In the actinide drawdown phase, the salt recovered by the cathodes is treated with electrolysis to separate it from the uranium and transuranics. After actinide drawdown is complete, the bulk of the now uranium and TRU free salt is treated in a subsequent electrolysis process to remove the lanthanide fission products [41].

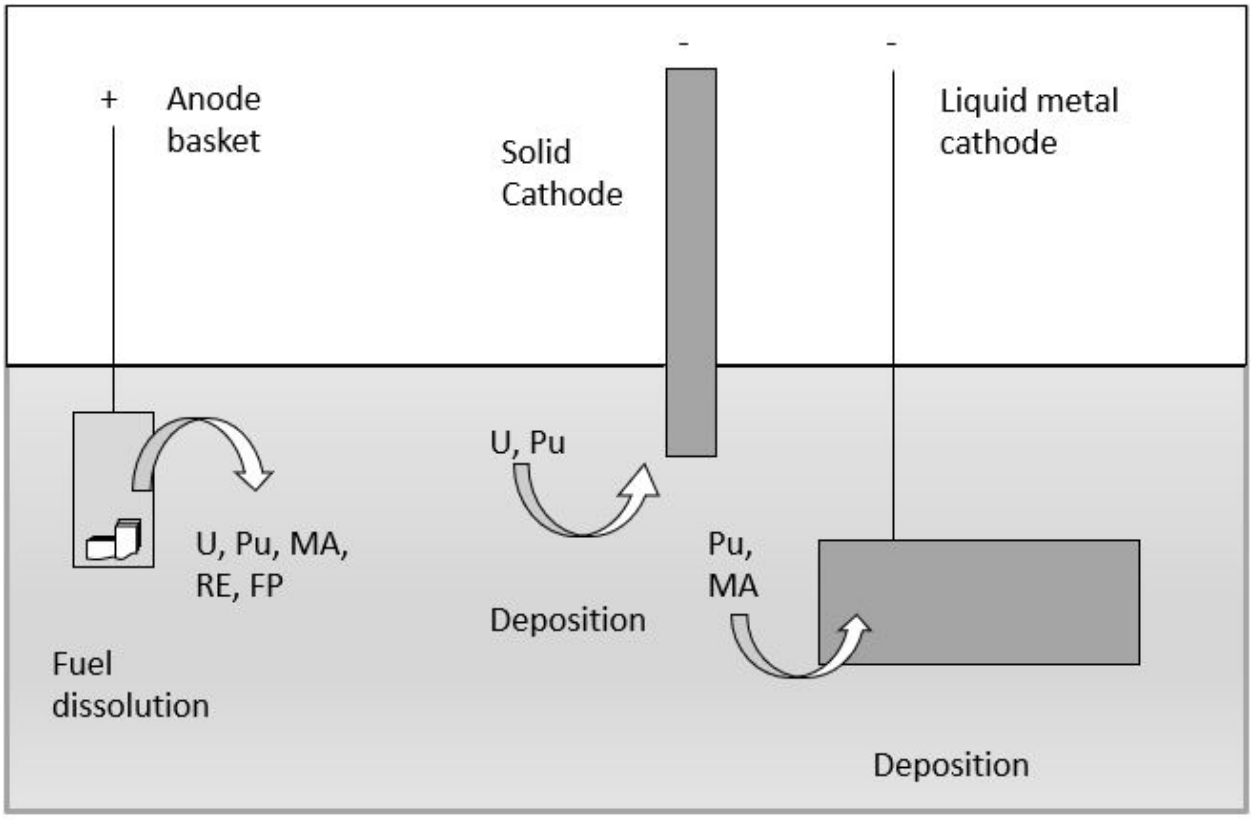


Figure 2.3: Operational diagram for a typical electrorefining unit recreated from [38].

After the removal of the accompanying salt, both cathode products are consolidated into an ingot form. In the case of the uranium cathode, a temperature of 1200 °C is needed [14]. Once in ingot form, the uranium and TRU products can be used for fast reactor fuel fabrication or stored for future use. Noble metals, fission products, and cladding recovered from the anode basket used in the electrorefiner are treated by a distillation process to recover residual salt. The salt then goes through the actinide drawdown process for actinide recovery. Noble metals are combined with the cladding and assembly hardware and melted, at approximately 1700 °C, to form an ingot, which is discharged as a high level waste [41].

2.2 Neutron Multiplicity Counting

In order to quantify the amount of uranium or plutonium present in a sample of UNF, a nondestructive means, neutron multplicity counting, has been used. This technique is an advancement on the previously used coincidence counting method that only measured singles (S) and doubles (D) count rates by also measuring the triples (T) count rate. Each of these variables refer to the estimated number of spontaneous neutrons detected from a single fission event. By taking this third parameter into account, multiplicity counting is able to obtain more accurate assays of impure samples than conventional coincidence counting [17]. This is done by eliminating the need to know either the sample's self-multiplication (M) or the ratio of (α,n) neutron production to spontaneous fission neutron production (α), and also is less sensitive to single neutrons from (α,n) reactions.

Measuring correlated neutrons is currently done by placing nuclear material inside a detector system comprised of multiple detector tubes. By having multiple tubes and looking

for counts within a finite gate width (G), one is able to discriminate between real counts (R) related to an initial event and random counts, often referred to as accidentals (A), that are uncorrelated with the initial event [15]. This is seen in the Rossi-alpha distribution shown in Figure 2.4 given by (Eq. 2.4) across time (t) given a detectors die-away time (τ) [15].

$$S(t) = A + Re^{\frac{-t}{\tau}} \tag{2.4}$$

Immediately after neutrons are detected by the system, there is a small time interval known as the predelay (P) due to the limitations in the detector electronics. After the predelay period, the system will record any electrical pulses made by the initial event, or trigger, for a time (G). This allows for every event captured in the time period (G) to be compared to every other event captured in the same time period. This eliminates some effects produced by deadtime and additionally allows for systems to operate at higher count rates [15]. The storage of the incoming pulses is accomplished via a device known as a shift register. Figure 2.4 demonstrates this process by showing a prompt gate (G) that will collect both real and accidentals ($R+A$) and another that collects only accidentals (A). The separation of these gates is accomplished by a long delay (D). The delay is usually long compared to (τ) so that no neutrons from the initial fission event are still present. Thus, the net difference between the two measurements ($R + A$) and (A) will yield the net real count rate, which is proportional to the spontaneous fission rate of the sample [15].

2.2.1 Passive Multiplicity Counting

Passive multiplicity counters are used to quantify the plutonium content of various samples such as plutonium metal, oxide, scrap, and residues. To do this, spontaneous fission neutrons are measured and correlated back to the ^{240}Pu-effective mass (Eq. 2.5), defined as the mass of ^{240}Pu that would give the same double coincidence response as that obtained from all the even isotopes of plutonium [17]. This value can yield information of the total plutonium content of a sample if the isotopics are known, which can be obtained through gamma spectroscopy. To solve for the (^{240}Pu$_{eff}$), analytical expressions for the singles, doubles, and triples count rates must be determined.

$$^{240}Pu_{eff} = 2.52^{238}Pu + ^{240}Pu + 1.68^{242}Pu \tag{2.5}$$

The analytical form of each count rate equation is shown in (Eqs. 2.6,2.7,2.8) as derived by Bohnel and Cifarelli and Hage based on the point model and four assumptions [17]. These include: that all induced fission neutrons are emitted simultaneously, the detector efficiency is uniform over the sample's volume, the (α,n) neutrons and spontaneous fission neutrons have the same energy spectrum, and the die-away time is approximated by a single exponential time constant [17]. Here, (F) represents the spontaneous fission rate, (ϵ) the neutron detection efficiency, (f_d) the doubles gate fraction, (f_t) the triples gate fraction, (ν_{s_1},ν_{s_2},ν_{s_3}) the factorial moments of the spontaneous fission neutron distribution, and (ν_{i_1},ν_{i_2},ν_{i_3}) the factorial moments of the induced fission neutron distribution.

$$S = F\epsilon M\nu_{s_1}(1+\alpha) \tag{2.6}$$

$$D = \frac{F\epsilon^2 f_d M^2}{2}\left[\nu_{s_1} + (\frac{M-1}{\nu_{i_1}})\nu_{s_1}(1+\alpha)\nu_{i_2}\right] \tag{2.7}$$

$$T = \frac{F\epsilon^3 f_i M^3}{6}\left[\nu_{s_3} + (\frac{M-1}{\nu_{i_1}-1})\left[3\nu_{s_2}\nu_{i_2} + \nu_{s_1}(1+\alpha)\nu_{i_3}\right] + 3(\frac{M-1}{\nu_{i_1}-1})^2\nu_{s_1}(1+\alpha)\nu_{i_2}^2\right] \tag{2.8}$$

Using these equations along with the doubles and triples rates provided by the shift register equipment, one can solve for ($^{240}\mathrm{Pu}_{eff}$), (M), and (α). The first step is to determine the multiplication factor by solving (Eq. 2.9) given the coefficients (Eqs. 2.10,2.11,2.12) as functions of (S), (D), and (T).

$$a + bM + cM^2 + M^3 = 0 \tag{2.9}$$

$$a = \frac{-6T\nu_{s_2}(\nu_{i_1}-1)}{\epsilon^2 f_t S(\nu_{s_2}\nu_{i_3} - \nu_{s_3}\nu_{i_2})} \tag{2.10}$$

$$b = \frac{2D[\nu_{s_3}(\nu_{i_1}-1) - 3\nu_{s_2}\nu_{i_2}]}{\epsilon f_d S(\nu_{s_2}\nu_{i_3} - \nu_{s_3}\nu_{i_2})} \tag{2.11}$$

$$c = \frac{6D\nu_{s_2}\nu_{i_2}}{\epsilon f_d S(\nu_{s_2}\nu_{i_3} - \nu_{s_3}\nu_{i_2})} - 1 \tag{2.12}$$

After solving for (M), the fission rate of the sample can be determined from (Eq. 2.13). The second term in the numerator represents the effect of self-interrogation of the sample due to induced fissions [17]. Once (F) is obtained, it can be related back to the effective

mass of ^{240}Pu via (Eq. 2.14). Finally, the ratio between the (α,n) and spontaneous fission rate is obtained by (Eq. 2.15) which is dependent upon (S), (F), and (M).

$$F = \frac{\left[\frac{2D}{\epsilon f_d} - \frac{M(M-1)\nu_{i_2} S}{\nu_{i_1} - 1}\right]}{\epsilon M^2 \nu_{s_2}} \tag{2.13}$$

$$^{240}Pu_{eff} = \frac{F}{473.5 fissions/s - g} \tag{2.14}$$

$$\alpha = \frac{S}{F \epsilon \nu_{s_1} M} - 1 \tag{2.15}$$

2.2.2 Active Multiplicity Counting

When the sample in question consists primarily of uranium, especially highly enriched uranium (HEU) material, passive methods will not suffice due to uranium's small spontaneous yield. Thus, fissions must be induced upon the sample by an external source. For detectors with fixed end plugs the source used is typically AmLi while detectors that shuffle the source often use ^{252}Cf [Rinard]. This section will discuss the equations associated with active multiplicity counting and highlight differences between them and those of passive counting. Similar to the passive equations, the active equations are based on the measurement of the doubles and triples count rate with the singles rate usually not being useful as it is dominated by the source neutrons [Ensslin et al.]. Thus, an additional parameter, the coupling between the AmLi source neutrons and the sample, is needed. For now, the expressions for the singles, doubles, and triples count rates are given by (Eqs. 2.16,2.17,2.18)

$$S = S_o + B + S_s + FM\epsilon_f\nu_{s_1} \tag{2.16}$$

$$D = \frac{F{\epsilon_f}^2 f_d \nu_{s_2}}{2} C_d \tag{2.17}$$

$$T = \frac{F{\epsilon_f}^3 f_t \nu_{s_3}}{6} C_t \tag{2.18}$$

where:

S_o = background count rate from the AmLi sources without a sample present,

B = background singles rate,

S_s = change to S_o due to scattering and absorption of AmLi neutrons by the sample,

F = induced fission rate,

ϵ_f = efficiency for detecting induced fission neutrons,

ν_{s_1},ν_{s_2},ν_{s_3} = factorial moments for AmLi-induced fission in ^{235}U. (Note that these symbols have a different definition for activie versus passive multiplicity counting.)

C_d = a correction factor for self-multiplication of doubles, and

C_t = a correction factor for self-multiplication of triples,

Next, the empirical equations for the doubles and triples correction factors are given by (Eqs. 2.19,2.20), derived from passive equations. Here, ν_{i_1},ν_{i_2}, and ν_{i_3} are the factorial moments for subsequent generations of fission neutron-induced fission in ^{235}U. Then, using (Eqs. 2.19,2.20) and (Eqs. 2.17,2.18) it is possible to solve for the self-multiplication factor of

the sample without knowing the induced fission rate by solving the cubic function (Eq. 2.21) [Ensslin et al.]. The induced fission rate (F) can be obtained from the doubles count rate equation (Eq. 2.17). To solve for the mass of uranium (^{235}U), coupling must be defined. This can be done by relating it back to the multiplication factor and calibration constants (a, b, c). The empirical relationship for the coupling term is given in (Eq. 2.22). Finally, the mass of uranium (Eq. 2.23) is a function of the multiplication factor, the induced fission rate, coupling of the sample, and the total output of the AmLi soures (Y).

$$C_d = M^2[1 + \frac{(M-1)\nu_{s_1}\nu_{i_2}}{\nu_{s_2}(\nu_{i_l}-1)}] \tag{2.19}$$

$$C_t = M^3[1 + \frac{(M-1)(3\nu_{s_2}\nu_{i_1} + \nu_{s_1}\nu_{i_3}}{\nu_{s_3}(\nu_{i_l}-1)} + \frac{(M-1)^2 3\nu_{s_1}\nu_{i_2}^2}{\nu_{s_3}(\nu_{i_l}-1)^2}] \tag{2.20}$$

$$\begin{aligned} &M^3 + M^2[\frac{3\nu_{s2}(\nu_{i1}-1)\nu_{i2} + \nu_{s1}(\nu_{i1}-1)\nu_{i3} - 6\nu_{s1}\nu_{i2}^2}{3\nu_{s1}\nu_{12}^2}]+ \\ &\quad M^3[\frac{\nu_{s3}(\nu_{i1}-1)^2 + 3\nu_{s1}\nu_{i2}^2 - 3\nu_{s2}(\nu_{i1}-1)\nu_{i2} - \nu_{s1}(\nu_{i1}-1)\nu_{i3} - (\frac{3T}{D\epsilon_f})(\frac{f_d}{f_t})\nu_{s1}(\nu_{i1}-1)\nu_{i2}}{3\nu_{s1}\nu_{12}^2}]+ \\ &\quad \frac{3T}{D\epsilon_f}\frac{f_d}{f_t}[\frac{\nu_{s1}(\nu_{i1}-1)\nu_{i2} - \nu_{s2}(\nu_{i1}-1)^2}{3\nu_{s1}\nu_{12}^2}] = 0 \end{aligned} \tag{2.21}$$

$$C = a - \frac{b(M-1)}{1 + c(M-1)} \tag{2.22}$$

$$^{235}U = \frac{F}{CY} \tag{2.23}$$

2.2.3 Neutron Detector Systems

Neutron multiplicity systems generally have a cylindrical body and consist of multiple detector tubes embedded in high-density polyethylene (HDPE). The tubes are arranged within the moderator in ring formation to optimize the counting response profile [33]. Most of the detector tubes are comprised of ^{3}He gas, but due to the low supply in recent years, BF_3 gas has been proposed as an alternative, especially for high gamma-ray environments. A sample cavity of various dimensions depending on the specific system is centered along the vertical axis of the body. As for electronics, the system generally consists of the previously mentioned shift register followed by typical detector system components such as charge-sensitive preamplifiers, amplifiers, and discriminators.

When determining the appropriate multiplicity counter design given the parameters of a specific problem, four key aspects must be considered. These include: the total neutron efficiency for spontaneous fission neutrons, the sensitivity to the sample matrix materials, the neutron die-away time in the detector moderator material, and the weight and cost of the system [33]. Due to the proposed research revolving around plutonium quantification in electrochemical reprocessing, a survey has been done comparing various types of passive multiplicity counters. What follows is a brief discussion of the multiplicity systems deemed favorable to electrochemical reprocessing. The systems to be addressed tackle the same issue for such sampling, that is the high accidentals rate associated with high (α,n) yields [36]. Results for all systems surveyed in regards to their structure, deadtime, die-away time, and detection efficiency are summarized in Table 2.1.

In-Plant (Pyrochemical) Multiplicity Counter

The pyrochemical counter is a thermal detector system for in-plant use to optimize parameters for sample assaying. The design was developed in 1991 at Loas Alamos Plutonium Processing Facility and consists of two divided halves, allowing it to fit around a glovebox to assay plutonium metal, oxide, and samples from high (α,n) electrorefining salts [17, 26]. As for testing, assays agreed with reference values within 5.1% for metal samples and within 1% for oxide samples given a 3,000 second counting time. When measuring samples from molten salts, measurements of plutonium have agreed with reference values within 4.8% [26]. These salt residues were not expected to assay as well using multiplicity techniques because of the high (α,n) neutron component. To improve the accuracy when measuring such samples, a longer count time than 3000 seconds may be needed for the pyrochemical counter. Overall, the efficiency of pyrochemical detectors is 57% with an associated dead-time of 90ns and die-away time of 47μs [17].

Fiber-Based Line Neutron Counters

The fiber-based line neutron multiplicity counter (FBLNMC) was designed at Savannah River to measure impure samples of plutonium ranging from a few tens of grams to several kilograms [27]. Using Monte Carlo calculations the detector design was able to achieve an efficiency of 58% using 113 ^{3}He tubes allocated among four rings. With the use of a derandomizer, the deadtime obtained by the circuit is 50ns, while still having the same energy response profile as that of the pyrochemical multiplicity counter [27]. Comparing the count rates of the inner and outer rings can also provide a sensitive indication of the mean

energy of the neutrons from a sample. This is strongly influenced by the composition of the sample and relatively the (α,n) neutrons making the assay of molten salt samples more feasible [17].

Epithermal Neutron Multiplicity Counter (ENMC)

A design concept based off previously existing counters, the ENMC is a well counter that uses 10-atm tubes instead of the traditional pressure of 4-atm. This higher pressure allows the ENMC to detect both thermal and epithermal neutrons, resulting in an efficiency of 65% and a die-away time of only 22μs. The 121 ^{3}He tubes are allocated in four major rings surrounding the sample cavity while immersed in less polyethylene moderator than traditional counters. This design feature also contributes to the high efficiency and low die-away time by not fully thermalizing existing neutrons. This optimizes the amount of neutrons lost by ^{3}He capture when compared to competing loss processing such as hydrogen absorption (i.e. reducing time between thermalization and capture) [36]. Due to these optimized parameters, the ENMC is able to handle samples with a higher value of accidentals and thus a higher (α). The practical limit of (α) is 10 to 12 before the counting time yielding a precision of 1% begins to exceed one hour [36]. This allows for bulk samples of plutonium assay times to be 5 to 40 times shorter than the prior thermal neutron multiplicity counters mentioned. The largest relative gains are for the most impure items with high (α,n) rates, where such gains reduce counting times from hours to 20 or 30 minutes [17].

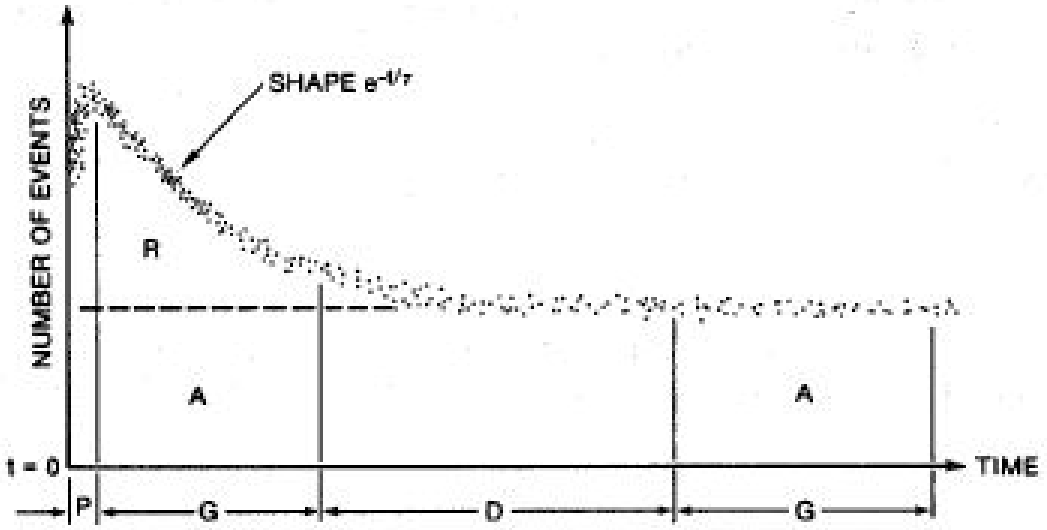


Figure 2.4: Rossi-alpha distribution showing detected neutron events as a function of time [15].

Table 2.1: Survey of Passive Multiplicity Counters in DOE Facilities [17].

Multiplicity Counter Name	Location	Application	No. of tube rings	No. of ^{3}He tubes	No. of Amptek preamps	Derand-omizer	Dead-time (ns)	Det. Eff (%)	Die-Away Time (μs)
Five-Ring Multiplicity Counter	Los Alamos	Technology Development	5	130	34	Yes	36	53	49
Three-Ring Multi-plicty Counter	Los Alamos	Technology Development	3	60	12	Yes	83	45	63
Pyrochemical Mul-tiplicty Counter	Los Alamos	In-plant metals,oxides	4	126	36	No	90	57	47
Plutonium Scrap Multiplicty Counter	Hanford, Japan	Pu Inventory Verification	$3\frac{1}{2}$	80	19	No	121	55	47
ARIES Neutron Counter	Los Alamos	Pu metals and residues	$3\frac{1}{2}$	80	20	Yes	60	55	47
FB-Line Multiplicty Counter	Savannah River	Metal,oxide inventory	4	113	24	Yes	50	58	50
30-Gallon Multiplicty Counter	Rocky Flats, Livermore	Inventory Verification	3	126	54	Yes	25	42	55
High-Efficiency Neutron Counter	Los Alamos	Waste Assay	2	113	16	No	171	32	50
Epithermal Neutron Multiplicty Ctr.	Los Alamos	Pu inventory Verification	4	121 10atm	27	Yes	37	65	22
KAMS Neutron Multiplicty Counter	Savannah River	Receiptss Verification	3	198 10atm	54	Yes	19	52	37.3
Super HENC Multi-plicty Counter	Rocky Flats	Standard Waste Box As-say	[]	260 10atm	32	Yes	[]	40.3	[]

2.3 Prior Electrochemical Safeguards Work

As the development of electrochemical reprocessing systems advances, attention must be given to the necessary safeguards challenges that arise from inherent differences from current aqueous methods. This encompasses the implementation of more extensive data collection and evaluation methods to accurately measure nuclear content [13]. Traditional neutron verification of UNF in aqueous systems currently uses information obtained from the spontaneous fission of curium to quantify the amount of plutonium present. This has been done by either separating out the information of each element via the neutron multiplicity methods mentioned previously or by the evaluation of the plutonium to curium (Pu/Cm) ratio from traditional coincidence counting [34]. Although variable across different fuel, investigation has shown that spontaneous fission neutrons on average account for 95% of neutron emissions from UNF while ^{244}Cm is the dominant source of said emissions for fuel within aqueous systems. Thus, current research into the quantification of plutonium in electrochemical systems is being conducted by investigating the spontaneous fission yield produced by curium [4]. This indirect method can at times be unreliable depending on multiple factors such as the consistency of the (α,n) to spontaneous fission ratio (α), low detector efficiency forcing the use of singles measurement as opposed to doubles for coincidence counting, and the consistency of the Pu/Cm ratio across different waste streams and the resulting applicability of detection measurements given the ratio magnitude [34]. This section gives a look at the current state of safeguard applications for nuclear fuel reprocessing using neutron detection for material accountancy of plutonium.

2.3.1 Application of Neutron Counting for Plutonium Verification

The verification of plutonium within UNF is important for reasons such as: confirming content declared by a regulated facility, making shipper/receiver mass declarations, and quantifying the input mass at a reprocessing facility [39]. Diversion of a significant quantity, 8 kg of plutonium, or substitution is also of concern. Currently a direct method to quantify the mass of plutonium within UNF does not exist. This is often made difficult due to interference from accompanying fission products with strong gamma yields as well a complex spontaneous neutron matrix, especially when TRU material isn't chemically separated [4]. Table 2.2 shows an isotopic breakdown of light water fuel for spontaneous fission and (α,n) yields calculated by [34]. The nuclear composition calculation code ORIGEN2 was used to generate the listed fuel after a cooling period of five years and uranium enrichments ranging of 3%, 4.1%, and 6% [6]. Most neutrons originate from the spontaneous fission of ^{244}Cm. Furthermore, the contribution of (α,n) reactions constitutes less than 10% of total neutron production, with the highest value being 6.6% for the UOX fuel at 20 GWd/tu. This makes multiplicity methods difficult when quantifying plutonium in UNF since a majority of the neutrons will come from the accompanying ^{244}Cm. To attempt such an analysis will result in large errors [34]. Feasibility studies have been performed at the Korean Atomic Energy Research Institute (KAERI) where single isotope samples and mixed samples were tested. In the case of mixed samples consisting of ^{239}Pu and ^{244}Cm the neutron multiplicity of the plutonium was only distinguishable from curium when ^{239}Pu had a mass fraction of 10^8 or more when compared to ^{244}Cm [23].

Table 2.2: Neutron Sources in Spent Fuels [34].

Neutron Sources		Light Water Reactor (LWR)		
		UOX 20 GWd/tu	UOX 45 GWd/tu	MOX 50 GWd/tu
(α,n)	Total	6.6%	1.9%	1.3%
	^{238}Pu	2.3	0.8	0.4
	^{239}Pu	0.7	0.0	0.0
	^{240}Pu	0.8	0.1	0.0
	^{241}Am	2.1	0.2	0.1
	^{242}Cm	0.0	0.0	0.0
	^{244}Cm	0.7	0.8	0.8
Spontaneous Fission	Total	93.3%	98.1%	98.7%
	^{238}U	0.0	0.0	0.0
	^{238}Pu	0.4	0.0	0.1
	^{240}Pu	4.1	0.5	0.2
	^{242}Pu	0.9	0.2	0.1
	^{242}Cm	0.2	0.0	0.0
	^{244}Cm	87.6	96.8	97.6
	^{246}Cm	0.1	0.6	0.6

Thus, an indirect method where the Pu/Cm ratio is measured could be used to verify plutonium content. This can occur either by destructive or nondestructive analysis before and after MBAs and then allows one to relate plutonium contribution (Eq. 2.24) to the total neutron count [43]. Here, $^{2}44Cm_{KMP}$ is the concentration of ^{244}Cm at key measurement points which can be obtained by calculating either adjusted (D) or (S) equations given the location being measured. In most cases, it is often better to use (D) as to avoid the effect introduced by (α,n) neutrons [34]. The technique has been applied for aqueous methods to verify the content of UNF and likewise can be applied in electrochemical systems given that curium and plutonium are not separated throughout the process [20]. However, obtaining the Pu/Cm ratio within acceptable precision and accuracy is a very challenging task [28].

$$Pu = (\frac{Pu}{^{244}Cm})^{244}Cm_{KMP} \tag{2.24}$$

2.3.2 Neutron Counting in Electrochemical Systems

One concern, specifically within electrochemical systems, is the assumption that the aformentioned ratio is constant, which may be false due to the different energy potential between plutonium and curium [43]. This stems from plutonium and curium having different thermodynamic properties within the molten salt of the electrochemical system. When converted to molten chlorides, as happens within the electrorefiner, the elements will have varying enthalpies and entropies that can be correlated to the ionic radii of the metal ions [40]. Studies have examined the separation efficiency of TRUs during the multistage extraction onto the LCC and found that actinides and lanthanides within the mixture have unique

distribution coefficients which is related to the Gibbs free energy of formation and the extraction rate [25]. Table 2.3 breaks down the free energy of formation of the various metal chlorides present at the electrorefiner [44]. Here, the center column identifies the chlorides that will be transported throughout the salt with those of lower free energy of formation value having a higher affinity for extraction. The other two columns represent high stability compounds that will remain in the salt and low stability compounds that will not be chlorinated and will remain within the anode basket. This is shown further in Figure 2.5 and can be seen that curium has a slightly lower value for Gibbs free energy of formation and thus will be extracted at a slower rate than plutonium resulting in a non-constant ratio value [35, 40].

A 1-D transient electrorefiner model, titled ERAD (Enhanced REFIN Anodic Dissolution), has been developed by Cumberland to simulate the dissolution of materials from the anode, mass transport through the salt, and deposition onto a cathode for uranium and plutonium mixtures [12]. This new model was based on a previous 1-D code, REFIN, developed to relax assumptions on the steady state nature of the environment as well as include electromigration physics [12]. Updates from REFIN to ERAD include an anodic passivation layer as well as an enforced solubility limit near the anode to limit current density. This is done by assuming the rate of each reaction is related to electrode potential by a detailed version of the Butler-Volmer equation given by (Eq. 2.25) [12].

$$i = i_o\left(\frac{X_{0x}(0,t)}{X^*_{0x}} exp\left(\frac{\alpha n F}{RT}(E - E_{eq})\right) - \frac{X_{Red}(0,t)}{X^*_{Red}} exp\left(-\frac{(1-\alpha)nF}{RT}(E - E_{eq})\right)\right) \quad (2.25)$$

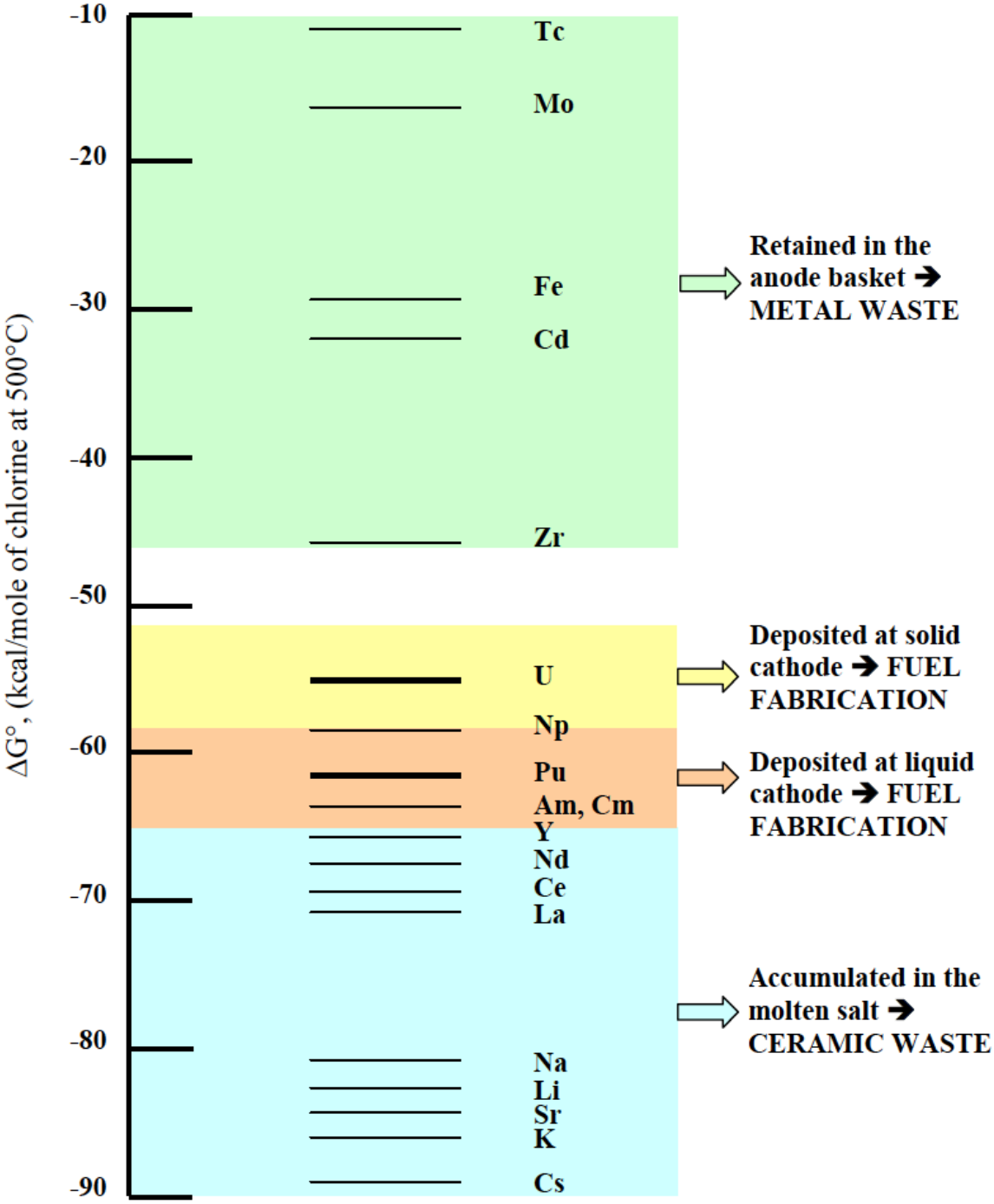


Figure 2.5: Separation action via Gibbs free energy of chloride formation.

Here, (E) is the electrode potential, (α) is the transfer coefficient, the superscript (*) indicates evaluation in bulk electrolyte, and Red and Ox subscripts indicate reduced and oxidized species. The exchange current density (i_o) is taken to (Eq. 2.26) where (k_o) is the rate constant.

$$i_o = Fk_o X_{0x}^{*(1-\alpha)} X_{Red}^{*\alpha} \tag{2.26}$$

Studies by Gonzalez using an adjusted version of ERAD where curium is also accounted for show that curium would need to be raised to above 1 wt% to support deposition onto a solid cathode [22]. It was also found that the Pu/Cm ratio was three orders of magnitude higher on the cathode surface than within the salt. This further suggests that accountancy through the Pu/Cm ratio for electrochemical systems is not a valid approach. The study concluded that a neutron balance approach would be ineffective at safeguarding a nuclear fuel pyroprocessing facility. Additional research where deposition is simulated onto a LCC would give a more representative analysis but for the initial investigation there were too many unknown properties for such a system [22].

2.3.3 Additional Methods

Techniques complimentary to multiplicity counting have been examined for the ingot product at the end of the electrochemical cycle. Namely, passive neutron albedo reactivity (PNAR) and differential die-away time (DDAT). Although these methods look specifically at the spontaneous fission signature, it is important to examine them for a diversity and defense-in-depth approach. Firstly, PNAR is a passive technique that has been investigated to find

a relationship between the detector signal and the plutonium mass in a U/TRU ingot. The detector relies on a cadmium liner that surrounds He-3 tubes dispersed in polyethylene. Measurements are taken with and and after the removal of the liner. The ratio of the two count rates can then be established for the sample. Studies have investigated this ratio with respect to burnup, enrichment, and cooling time and found a relationship between the cadmium ratio and plutonium content [29]. Results have shown an error in plutonium estimation as high as 18% depending on the fuel parameters but additional efforts utilizing borated water as a medium for the detectors might improve this error. Investigation in ongoing using various apparatus parameters and sample compositions controlled through the thermodynamic properties during extraction.

The second alternative neutron technique, DDAT, is an active method primarily used to determine fissile material in waste containers. A neutron generator is used to induce fission within the sample which creates a difference in die-away time. This difference comes from the inducing neutrons versus the fission neutrons and can be correlated to the fissile content present in the sample [32]. This technique has been combined with that of passive coincidence counting when examining mixed samples for better discrimination between the curium and plutonium content.

Table 2.3: Free Energy of Formation of the Various Metal Chlorides at 500°C [44].

High Stability		Electrotransportable		Low Stability	
	$-\Delta, G_r^\circ$		$-\Delta, G_r^\circ$		$-\Delta, G_r^\circ$
$BaCl_2$	87.9	$CeCl_3$	68.6	$CdCl_2$	32.3
CsCl	87.8	$NdCl_3$	67.9	$FeCl_2$	29.2
KCl	86.7	YCl_3	65.1	$NbCl_5$	26.7
$SrCl_2$	84.7	$AmCl_3$	64.0	$MoCl_2$	16.8
LiCl	82.5	$CmCl_3$	64.0	$TcCl_4$	11.0
NaCl	81.2	$PuCl_3$	62.4	$RhCl_3$	10.0
$CaCl_2$	80.7	$NpCl_3$	58.1	$PdCl_2$	9.0
$LaCl_3$	70.2	UCl_3	55.2	$RuCl_4$	6.0
$PrCl_3$	69.0	$ZrCl_4$	46.6		

Chapter 3

Model and Simulation

3.1 SSPM EChem Model

The basis for evaluating material flow for an electrochemical system was originally the separations and safeguards performance electrochemical (SSPM EChem) model (developed by Sandia National Laboratory) shown in Figure 3.1. SSPM EChem is a Matlab/Simulink based continuous event model, that tracks nuclear material (on the elemental and isotopic levels) by modeling the major components of the electrochemical processes [8]. This is done by dividing the process into two MBAs. The first MBA deals with the storage, shredding, and voloxidation processes to prepare the fuel into a batch format. The second MBA tracks the material as it is partitioned into its desirable constituents and processed to obtain a final product and waste form. The software uses measurement blocks to represent the conditions for which the processes involved go through during facility operation. The system tracks the mass flow rate in kg/sec of elements with atomic numbers ranging from 1 to 99 as well the eutectic salt [8]. The elements comprising the fuel are then broken down

into isotopes, totaling 266, via predetermined ratios for each of the specified units in the diagram. Highlighted in green and blue are certain streams that are of interest in terms of process monitoring and material accountability. This research presents proof of concept on the capability of neutron detection for various fuel parameters at the salt inventory of the electrorefiner. What follows is a discussion of expanding the fuel database currently in the model and using that with previously developed neutron simulation to characterize emissions at the electrorefiner [1].

3.1.1 Fuel Generation

Due to the SSPM EChem model originally having a total of 45 different fuel sources via various burnup, enrichment, and cooling time combinations, which was expanded using ORIGEN to total 935 unique combinations for a 17x17 Westinghouse assembly [1]. This was done by using a semi-empirical relationship (Eq. 3.1) relating fuel discharge burnup to initial enrichment for commercial pressurized water reactor fuel, a range of burnup values from 20 to 60 GWd/MTHM in increments of 5 GWd/MTHM were selected and corresponding enrichment values calculated [18]. Seventeen different cooling times were used for each of the burnup/enrichment combinations with a cooling time of five years being used for the analysis discussed in this work.

$$(EN) = 0.31BU^{0.65} \tag{3.1}$$

This analysis uses the line directly correlated with (Eq. 3.1) as the main sequence line, representing a range of plausible burnup/enrichment combinations for commercial fuel under

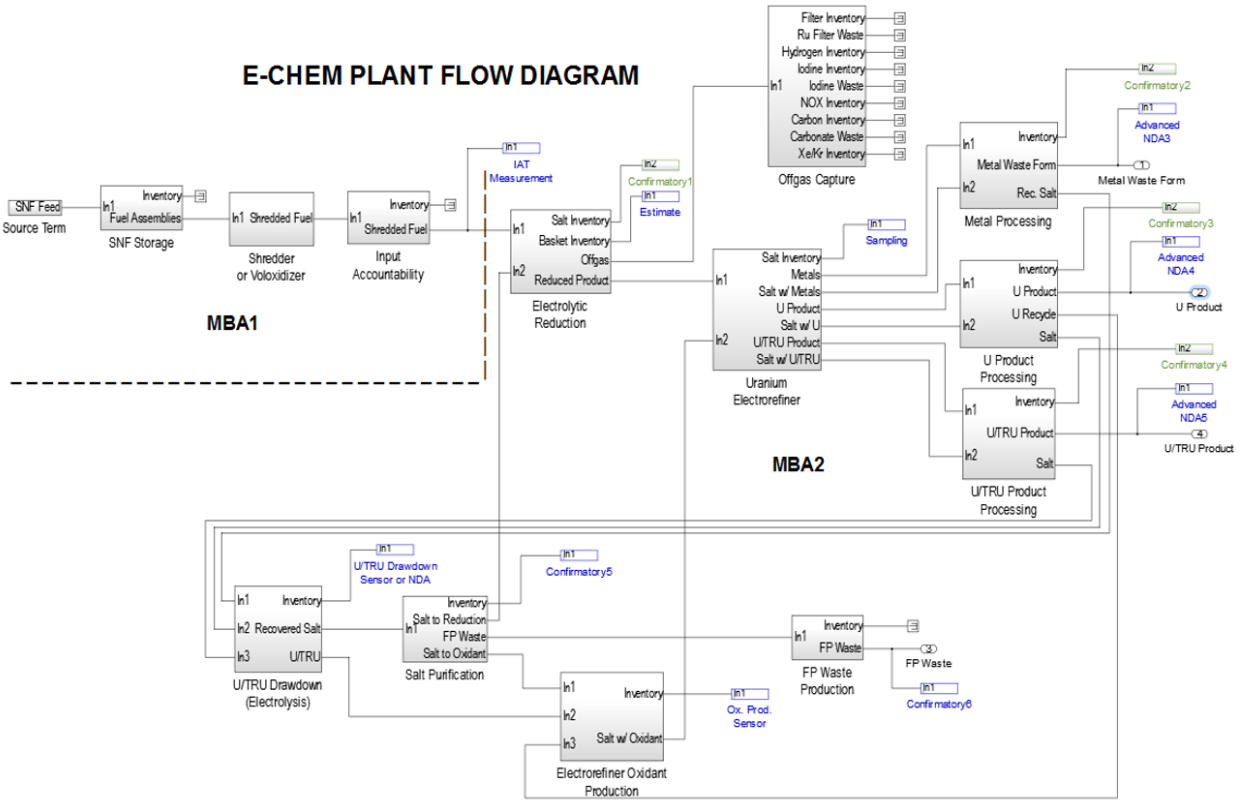


Figure 3.1: Flow diagram outlining the MBA areas throughout the SSPM EChem model [8].

normal conditions. Using these optimized enrichment values, a bandwidth of 5 and 10% was also examined to explore slight deviations from normal fuel parameters. These 45 cases comprise the main sequence band and demonstrate a range of realistic burnup/enrichment fuel characteristics seen in Figure 3.2.

3.2 Neutron Code Systems

This work used three main coding systems to further examine neutron production and tracking. The first two are Scale and Sources-4C which were used to obtain neutron emission rates in substitute for the EChem module when it came to sample compositions to be placed into an ENMC. The last is known as Monte Carlo N-Particle (MCNP) code and was used in the neutron transport and detection of a sample placed in an input deck representation of an ENMC. All three systems are briefly discussed in the following sections.

3.2.1 SCALE/SOURCES-4C

The Scale code system is a widely-used modeling and simulation suite for nuclear safety analysis and design that is developed, maintained, tested, and managed by the Reactor and Nuclear Systems Division (RNSD) of Oak Ridge National Laboratory (ORNL) [6]. This language was used to obtain the emission rates of various sample mixtures as well as take the ratio between the different origins of neutrons. This allowed for a comparison between ideal and detected alpha values as well as determine the magnitude of the (α,n) source.

Sources-4C is a computer coding language that determines neutron production rates and spectra from (α,n) reactions, spontaneous fission, and delayed neutron emission due

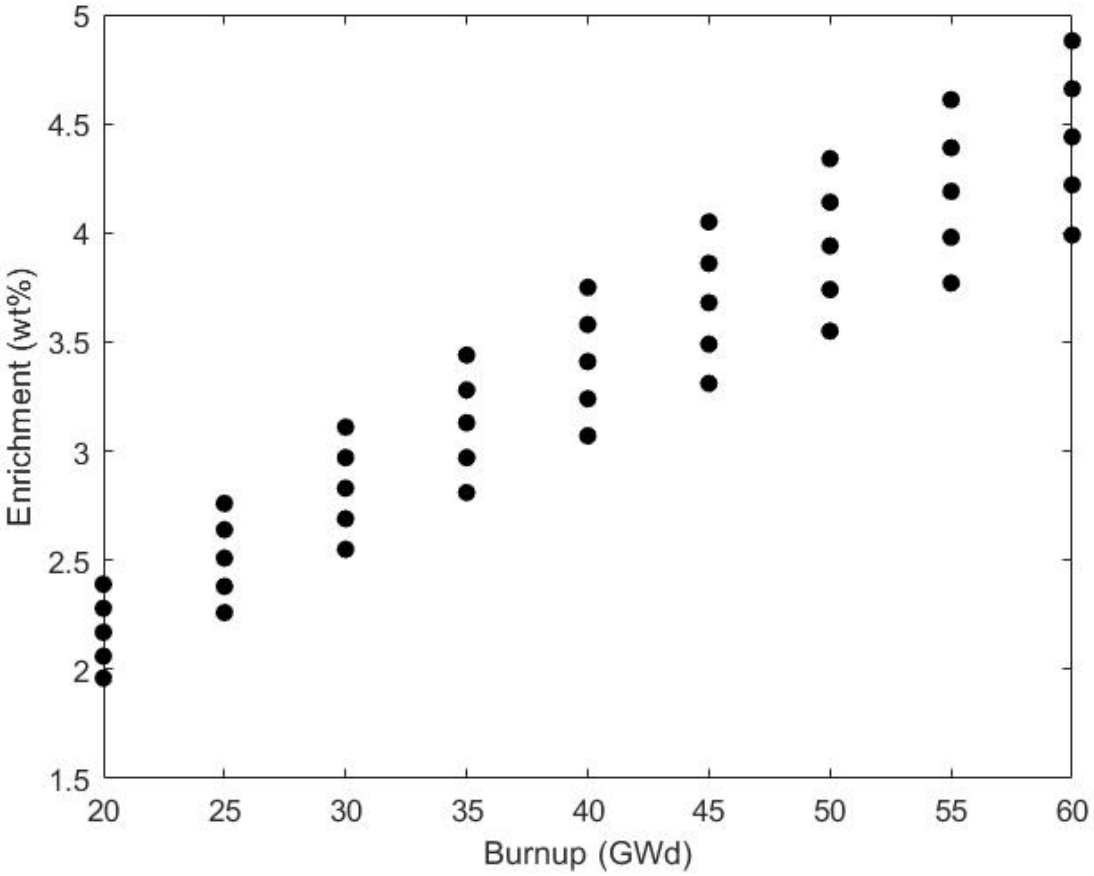


Figure 3.2: Fuel discharge burnup and enrichment combinations evaluated.

to radionuclide decay. The code is capable of calculating (α,n) source rates and spectra in four types of problems: homogeneous media (i.e., an intimate mixture of α-emitting source material and low-Z target material), two-region interface problems (i.e., a slab of α-emitting source material in contact with a slab of low-Z target material), three-region interface problems (i.e., a thin slab of low-Z target material sandwiched between α-emitting source material and low-Z target material), and (α,n) reactions induced by a monoenergetic beam of α-particles incident on a slab of target material. The Sources-4C code system is composed of an F77 source code, an executable, one input file, up to six output files, and four library files [42]. The Sources-4C code was used to obtain the equations for calculating the (α,n) and spontaneous fission emission rate and validate the analysis done in Scale.

In an effort to streamline the process of creating the input file, the Los Alamos Sources-4C Tape1 Creator and Library Link (LASTCALL) program was developed.This was done in an attempt to simplify the calculation process and reduce the number of errors introduced by novice users during the input file creation. The software is written in Fortran using Compaq Visual Fortran and is an optional tool that utilizes a user interface launched from an executable. The default view is shown in Figure 3.3. The executable will generate an input file (tape1) allowing Sources-4C to run, within LASTCALL, and produce typical output files.

3.2.2 Monte Carlo N-Particle

One of the most common and powerful simulation software packages for radiation transport MCNP. This is nondeterministic code that uses Monte Carlo methods to determine radiation



Figure 3.3: LASTCALL interface within the Sources-4C software.

transport for such particles as neutrons, gamma rays, electrons, and coupled transport through a 3-dimensional geometry or material composition [5]. In addition to transporting radiation, MCNP has a variety of tallies that can determine many properties of interest, such as particle flux and interaction rates. One variant of MCNP is the software program called Monte Carlo N-Particle eXtended (MCNPX), which uses the same transport methods as MCNP, but includes extra features, such as particle coincidence tallying [5]. Through use of MCNPX v2.6, various nuclear and detector properties can be directly determined, in addition to singles, doubles, and triples count rate of any gate length and pre-delay.

Like all computer simulations, MCNPX has aspects that may be different from a physical measurement. These aspects include slight variations in room temperature and pressure, inexact placement of the measurement sample, and cosmic-ray interaction rates. It should be noted that many of these aspects can be minimized or accounted for by careful control of a measurement system. One major difference between MCNPX simulations and physical measurements is the accidentals gate [21]. Because MCNPX simulates one particle at a time, there is no such thing as an accidental neutron. Because of this, MCNPX does not have an accidental gate to account for other neutron events, which may be occurring simultaneously with the neutron event of interest. This feature of simulating one particle at a time in some ways can be considered a benefit since it significantly reduces the uncertainty in the doubles and triples count rates. Many simulations of physical neutron multiplicity measurements using MCNPX have been performed to benchmark the code, including measurements made as part of this dissertation. It has been determined that there is no significant bias in the MCNPX results compared to those of the physical measurements, other than those of user error and uncertainties in nuclear data [5].

ENMC Input Deck

The ENMC input deck uses MCNPX to simulate each measurement made by the ENMC. The MCNPX input deck which was used in all the simulations was originally developed at LANL and provided to the author by Dr. Braden Goddard [20]. The internal MCNPX spontaneous fission spectra was used for all spontaneous fission simulations. (α,n) spectra were acquired from an internal ORNL developed program which uses Scale libraries to generate the spectra[6]. Each actinide standard consisted of two MCNPX simulations, (α,n) and spontaneous fission. Each simulation ran for 60 minutes of simulated counting time. The tallies used in the simulations consisted of gated and non-gated F8 coincidence tallies to determine relevant neutron multiplicity values, as well as F4 tallies to determine the neutron flux and fission rate within the measured standard.

Chapter 4

Methodology

4.1 Neutron Simulation

This section discusses the development of neutron emission simulation used in the analysis based on two sources: prompt neutrons produced from spontaneous fission events and (α,n) reactions which occur primarily in low-Z material. The simulation of the neutron emission rates were done within the MATLAB software and accomplished by using equations provided in the SOURCES-4C manual and parsing the necessary variables from Origen [42]. This was done for spontaneous fission and (α,n) neutrons; the summation of the two resuls in the total neutron emission rate. This allows the emitted neutrons to be traced back to a specific reaction or isotope.

4.1.1 Spontaneous Fission Simulation

Spontaneous fission is distributed in energy by a Watt fission spectrum (Eq. 4.2) using characteristic constants, (A) and (B), of fissioning isotopes. The variable ($R_k(SF)$) gives

the average number of spontaneous fission neutrons emitted per decay of nuclide k (Eq. 4.1). Here, (F_k^{SF}) is the spontaneous fission branching fraction and ($\nu(SF)$) is the average number of prompt neutrons.

$$R_k(SF) = F_k^{SF}\nu(SF) \tag{4.1}$$

$$\chi_k^{SF} = R_k(SF)e^{\frac{-E}{A}}\sinh\sqrt{BE} \tag{4.2}$$

Thus, the driving source of these neutrons is the decay of the emitting isotope via a probability distribution function. To calculate the total neutrons produced, the integral must be evaluated over all energies (Eq. 4.3) and normalized in the form of (Eq. 4.4) with the yielding normalization factor given by (Eq. 4.5). To verify the equations provided within the SOURCES-4C manual were implmented correctly, validation runs were completed by comparing the results of the MATLAB code to that of ORIGEN generated outputs. The spontaneous fission comparison is seen in Figure 4.1 and reproduced the ORIGEN results within 0.5%.

$$\begin{aligned}\int \chi_k^{SF} = \frac{1}{4}A[&-\sqrt{\pi AB}exp(\frac{AB}{4})erf(\frac{A\sqrt{B}-2\sqrt{E}}{2\sqrt{A}}) \\ &+\sqrt{\pi AB}exp(\frac{AB}{4})erf(\frac{A\sqrt{B}+2\sqrt{E}}{2\sqrt{A}}) \\ &-2[exp(2\sqrt{4BE})-1]exp(\frac{-A\sqrt{BE}+E}{A})]\end{aligned} \tag{4.3}$$

$$\int_0^\infty C * \chi_k^{SF}(E)dE = 1 \tag{4.4}$$

$$C = \frac{2}{\sqrt{\pi b A^3}} e^{\frac{AB}{4}} \tag{4.5}$$

4.1.2 (α,n) Simulation

The production of spontaneous fission neutrons is kinematically different from the origin of (α, n) neutrons which depend not on one but two isotopes in the medium. The first is an α emitter such as ^{238}Pu. As the α-particle is released and travels through the medium it has a probability of interacting with a target, such as ^{7}Li. The probability of an (α,n) interaction with a nuclide i by an α-particle at energy E traveling from x to $x+dx$ is shown in (Eq. 4.6). Here (N_i) is the atom density of nuclide i, $(\sigma_i(\mathrm{E}))$ is the energy dependent cross section, and $(\frac{dE}{dx})$ is the stopping power. Thus, the probability of an interaction when taking into account the changing energy from the slowing down of the α-particle is calculated by taking the integral from one energy (E_α) to a lesser energy (E'_α) (Eq. 4.7).

$$N_i \sigma_i dx = \frac{N_i \sigma_i(E)}{\frac{dE}{dx}} \tag{4.6}$$

$$p_i(E_\alpha \longrightarrow E'_\alpha) = \int_{E_\alpha}^{E'_\alpha} \frac{N_i \sigma_i(E)}{\frac{dE}{dx}} dE \tag{4.7}$$

To calculate the probability of an interaction occuring before the α-particle has stopped within the medium, given by (Eq. 4.8), the energy is integrated from zero to the original α energy. This function is often referred to as the thick-target neutron production function.

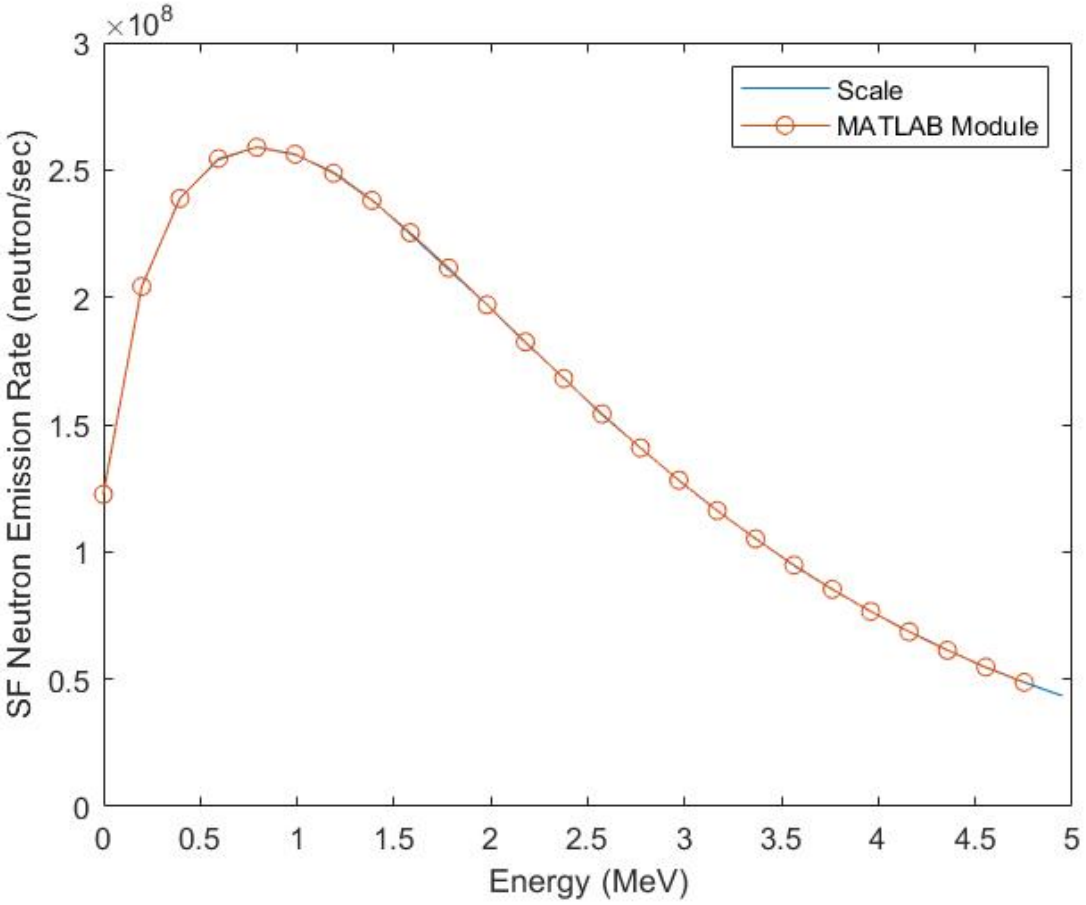


Figure 4.1: Comparison for the spontaneous fission emission rate between MATLAB and Origen.

$$P_i(E_\alpha) = \int_0^{E_\alpha} \frac{N_i \sigma_i(E)}{-\frac{dE}{dx}} dE \tag{4.8}$$

Introducing the stopping cross section (Eq. 4.9) can further simply the previous function. The stopping cross section is defined by the stopping power and the total atom density (N) of the medium consisting of j constituents, shown in equation (Eq. 4.10). Now the thick-target neutron production function is expressed in terms of the stopping cross section, in (Eq. 4.11).

$$\epsilon(E) = -\frac{1}{N}\frac{dE}{dx} \tag{4.9}$$

$$\begin{aligned} \epsilon(E) &= \frac{1}{N}\sum_{j=1}^{J} N_j \epsilon_j(E) \\ where : N &= \sum_{j=1}^{J} N_j \end{aligned} \tag{4.10}$$

$$P_i(E_\alpha) = \frac{N_i}{N}\int_0^{E_\alpha} \frac{\sigma_i(E)}{\epsilon(E)} dE \tag{4.11}$$

Next, one must consider the rate at which nuclides within the material will decay via alpha emission. This fraction given in (Eq. 4.12) may occur with the emission of one of L possible alpha energies. The intensity, (f_{kl}^{α}), is the fraction of all decays of nuclide k resulting in an α-particle of energy (E_l). Thus, the fraction of nuclide k decays resulting in a reaction in a medium containing i nuclides is given in (Eq. 4.13).

$$F_k^{\alpha} = \sum_{l=1}^{L} f_{kl}^{\alpha} \tag{4.12}$$

$$R_k(\alpha, n) = \sum_{l=1}^{L} f_{kl}^{\alpha} \sum_{i=1}^{I} P_i(E_l) \tag{4.13}$$

The fraction of target i product level m reactions of source k α-particles occurring in the energy group g is given by (Eq. 4.14). The variable $(P_i(\mathrm{E}_l))$, defined by (Eq. 4.15), is the discrete form of (Eq. 4.11) where g represents the discretization of the energy binning.

$$H_{i,k}^{l}(m) = \frac{P_i(E_{l+1}) - P_i(E_l)}{P_i(E_\alpha)} \tag{4.14}$$

$$P_i(E_l) = \frac{N_i}{N} \sum_{g=1}^{G-1} \frac{1}{2} [\frac{\sigma_i^{g+1}}{\epsilon^{g+1}} + \frac{\sigma_i^{g}}{\epsilon^{g}}](E^{g+1} - E^{g}) \tag{4.15}$$

The second half of the process comes when an α-particle makes contact with a target. The resultant neutron energy is dependent upon the incident energy of the α-particle and the resulting product level of the target nuclide. This aspect is represented by (Eq. 4.16) where $(S_{i,k})$ is the branching fraction of α-particles at energy (E_α) reacting with target nuclide i and producing product level m and $(H_{i,k}^{l})$ is the fraction of target i product level m reactions of source nuclide k α-particles occurring in the energy group g.

$$F_{i,k}^{l}(m) = S_{i,k}(m) H_{i,k}^{l}(m) \tag{4.16}$$

Similarly, the minimum and maximum neutron energy that can be produced is a result of the mass and velocity of the α-particle and target nuclide, as well as the excitation of the recoil nuclide. These calculations are conducted in a center-of-mass (COM) system assuming an isotropic neutron angular distribution. Taking into account the conservation of

momentum, the velocity of the COM is dependent on the α-particle velocity in a laboratory setting along with the α-particle and target nuclide mass. Subtracting this velocity from the particle velocities yields (Eq. 4.17) and (Eq. 4.18), which are the α-particle and target nuclide velocities in the COM system. Each are dependent on a variation of the α and target masses, (m_α) and (m_t) along with the α-particle velocity in a laboratory setting, (v_α^{lab}).

$$v_\alpha^{CM} = v_\alpha^{lab}(\frac{m_t}{m_\alpha + m_t}) \tag{4.17}$$

$$v_t^{CM} = v_\alpha^{lab}(\frac{m_\alpha}{m_\alpha + m_t}) \tag{4.18}$$

Observing the conservation of energy in the COM system seen in Figure 4.2, the neutron kinetic energy given in (Eq. 4.19) is dependent on five variables: the Q-value of the reaction; the excitation level of the recoil nucleus (E_{ex}); and the kinetic energies of the alpha particle (KE_α), the target nucleus (KE_t), and the recoil nucleus (KE_r). The kinetic energy of the recoil nucleus, along with the relationship between the kinetic energy of the α and target nucleus, are shown in (Eq. 4.20) and (Eq. 4.21).

$$KE_n = (Q - E_{ex}) + KE_\alpha + KE_t + KE_r \tag{4.19}$$

$$KE_r = \frac{1}{2}m_r v_r^2 = \frac{1}{2}\frac{m_n^2}{m_r}v_r^2 = KE_n(\frac{m_n}{m_r}) \tag{4.20}$$

$$KE_\alpha + KE_t = E_\alpha^{lab}(\frac{m_t}{m_\alpha + m_t}) \tag{4.21}$$

Substituting (Eq. 4.20) and (Eq. 4.21) into (Eq. 4.19) and solving for the kinetic energy of the neutron yields (Eq. 4.22). The variable (Q_m) is a simplification made and is equal to the (Q) minus the (E_{ex}). Using the definition of kinetic energy, the neutron velocity in the COM system is represented by (Eq. 4.23). This can be converted to the neutron velocity in the laboratory system, seen in Figure 4.3, according to (Eq. 4.24) by adding the velocity of the COM.

$$KE_n = Q_m(\frac{m_r}{m_t + m_n}) + E_\alpha(\frac{m_t}{m_\alpha + m_t})(\frac{m_r}{m_r + m_t}) \tag{4.22}$$

$$v_n = \frac{+}{-}\sqrt{\frac{Q_m}{m_n}(\frac{m_r}{m_r + m_n}) + \frac{E_\alpha}{m_n}(\frac{m_t}{m_\alpha + m_t})(\frac{m_r}{m_r + m_t})} \tag{4.23}$$

$$v^{lab} = (\frac{m_\alpha}{m_\alpha + m_t})\sqrt{\frac{2E_\alpha}{m_\alpha}}\frac{+}{-}\sqrt{\frac{Q_m}{m_n}(\frac{m_r}{m_r + m_n}) + \frac{E_\alpha}{m_n}(\frac{m_t}{m_\alpha + m_t})(\frac{m_r}{m_r + m_t})} \tag{4.24}$$

Using the neutron velocity in the laboratory frame and definition of kinetic energy the resultant neutron energy permitted is represented by (Eq. 4.25). The variables a_1, a_2, and a_3 are defined in (Eq. 4.26) where the masses are those of the neutron, α-particle, target, and recoil nucleus respectively. The resulting neutron emission rate from (α,n) reactions is given by (Eq. 4.27).

$$E_{n,m}^{\pm} = (\sqrt{E_\alpha a_1}(\frac{1}{1 + a_1})\frac{+}{-}\sqrt{\frac{Q_m}{m_n}(\frac{1}{1 + a_3}) + E_\alpha(\frac{a_2}{1 + a_2})(\frac{1}{1 + a_3})})^2 \tag{4.25}$$

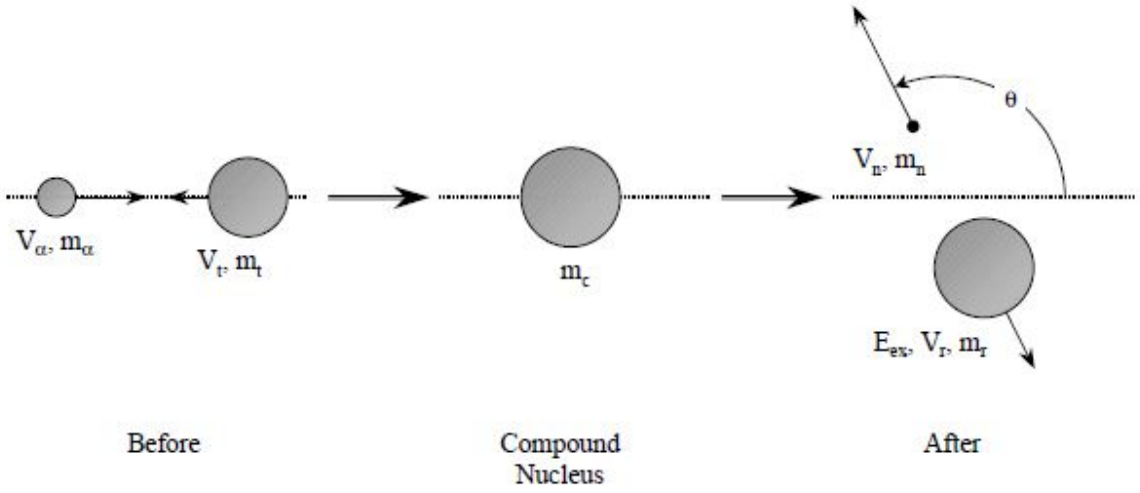


Figure 4.2: (α,n) Reaction in the Center-of-Mass System [42].

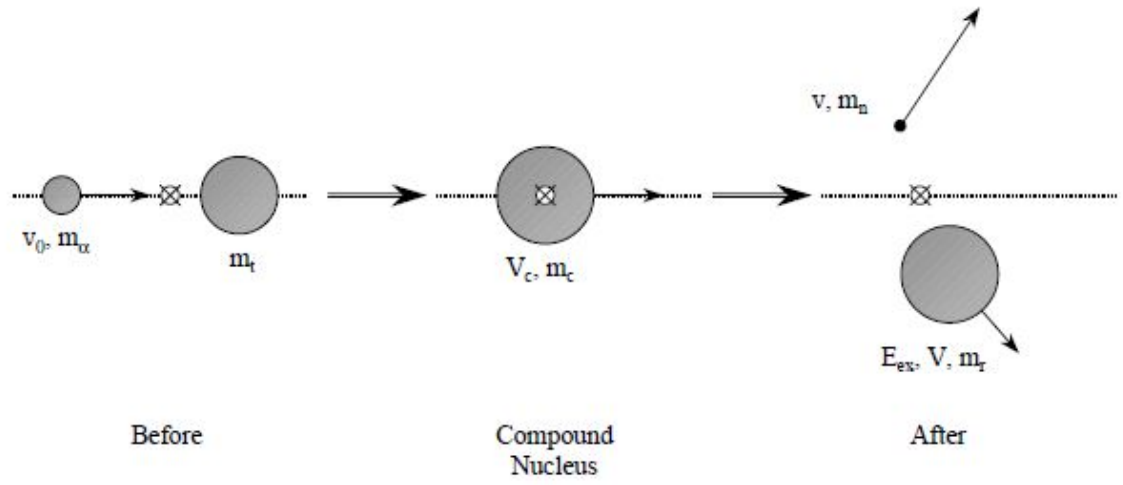


Figure 4.3: (α,n) Reaction in the Laboratory System [42].

$$a_1 = \frac{m_n}{m_\alpha}, a_2 = \frac{m_t}{m_\alpha}, a_3 = \frac{m_n}{m_r} \tag{4.26}$$

$$\chi_k^{(\alpha,n)} = R_k(\alpha, n) F_{i,k}(m) \frac{E_{g+1} - E_g}{E_{n,m}^+ - E_{n,m}^-} \tag{4.27}$$

The results of validation testing for the (α,n) reaction can be seen in Figure 4.4. The MATLAB simulations reproduced the ORIGEN results to sufficient fidelity 3.5%.

4.2 Sample Characterization

When taking a sample from the electrorefiner, multiple factors come into play with regard to its composition. These factors include: the location the sample was taken from (i.e. the depth as well as the proximity to either cathode or anode), the point in extraction process at which the sample is taken (i.e. mass migration, single extraction, and coextraction), and what number batch it is since the vessel was last cleaned. When determining the characteristics of the samples to be placed within the ENMC input deck, it was important to simplify the problem in order to focus on discriminating spontaneous fission from (α,n). Specifically, since the traditional means of using the Pu/Cm ratio will not be effective for an electrochemical system a method must be created for material quantification when mixed samples include both nuclides. It is for this reason a simplified matrix was used that consisted of plutonium, curium, and LiCl-KCl to represent a sample taken from the electrorefiner. This takes into account four out of the five highest grossing (α,n) sources, excluding ^{241}Am, that produce at minimum 98% of (α,n) neutrons. Next, it was decided to use a homogeneous mixture

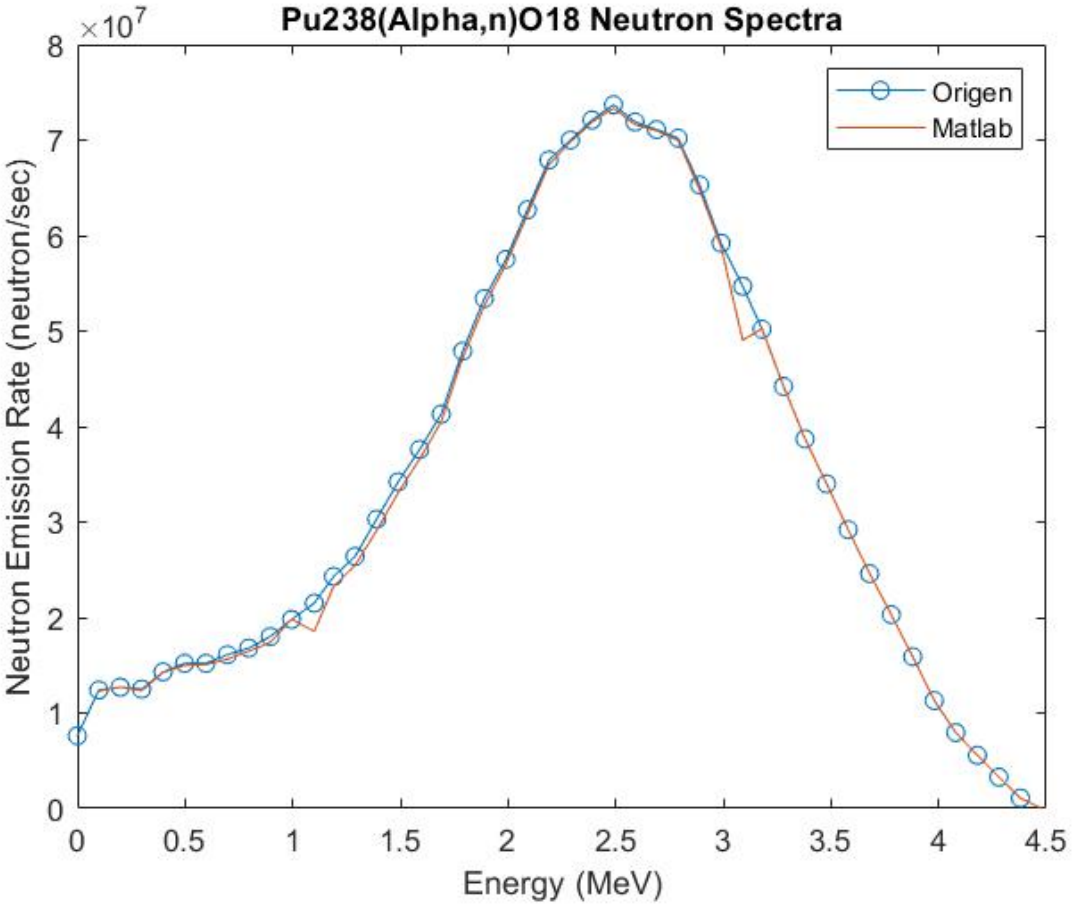


Figure 4.4: Comparison for the (α,n) emission rate between MATLAB and Origen.

as opposed to a more realistic heterogeneous one. This was decided due to the difficulty in appropriately constructing a heterogeneous mixture as it was not feasible to experimentally determine what that composition might consist of. This is because theoretically a sample may yield any percent combination of plutonium and curium. Differences in spontaneous fission yield between a homogeneous and heterogeneous mixture are subject to the amount of source nuclides present in the sample. This is of minor concern given that traditional neutron multiplicity methods, discussed in Chapter 2, are able to accurately quantify the curium content via spontaneous fission emissions even in mixed samples. The (α,n) signature is of more concern when looking at the changes arising when simulating a less realistic homogeneous mixture. Using the EChem model, isotopic contributions to the (α,n) signature were examined at the electrorefiner for ^{238}Pu and ^{244}Cm across a time where coextraction was occurring. This is seen in Figure 4.5 where the percent contribution of both isotopes is constant across time. It must be noted that here the Pu/Cm ratio is held constant but the individual isotopic masses as well as the salt mass is changing. This is due to the EChem model not performing the thermodynamic reactions between the fuel and salt. It just gives an approximation to mass flow without the differential electrochemistry. Thus, given the masses presented by the EChem model the electrorefiner is saturated with a substantial amount of salt that slight variations have no effect on the (α,n) yield if all else is held constant. This allowed for a simple scaling down of the masses within the electrorefiner to fit the sample cavity size of the ENMC without losing the significant contribution percentages. To summarize, sample characterization was based off matrix simplification in order to determine if the (α,n) signature of plutonium be isolated and detected using the method discusses later

in this work. This manifested in the homogeneous scaling down of the composition at the eletrorefiner within the EChem model.

4.3 MCNP Multiplicity Interpretation

In order to make use of the information MCNP provides, it is necessary to transform the data via the multiplicity equations. This section goes through the calculations necessary for the analysis discussed. The effective mass is calculated by (Eq. 4.28) which is similar to (Eq. 2.14) shown in Chapter 2 but is now defined in terms of source strength (F_o) so it is not specific to solely ^{240}Pu. Similarly, the variable (α) equation has changed to (Eq. 4.29) with source strength now in the denominator of the fraction.

$$m = \frac{\frac{2D}{\epsilon f_d} - \frac{M(M-1)\nu_{i2}S}{\nu_{i1}-1}}{\epsilon F_o M^2 \nu_{s2}} \tag{4.28}$$

$$\alpha = \frac{S}{mF_o\epsilon\nu_{s1}M} - 1 \tag{4.29}$$

The die-away time may be approximated as a single exponential. This is done by performing two measurements with two different gate widths, ($G1$) and ($G2$). If the second gate width is twice the size of the first then the resulting die-away time equation is given by (Eq. 4.30). To obtain the optimal gate width one must multiply the die-away time by 1.257 [17]. The gate fractions are defined as the counts detected within the finite gate divided by the counts of an infinitely long gate. When assuming the single exponential die-away

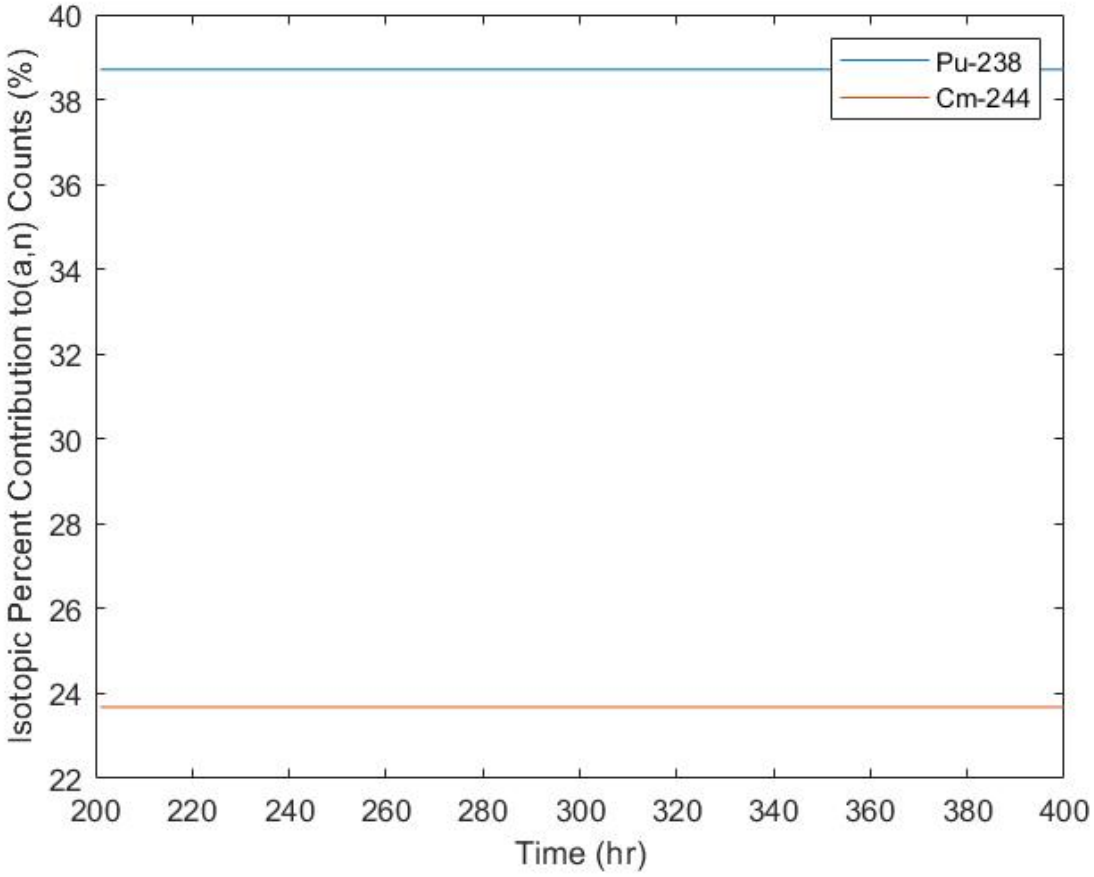


Figure 4.5: Plutonium and Curium contribution for (α,n) neutrons for 20GWd main sequence burnup and enrichment with a cooling time of 5 years.

time this becomes (Eq. 4.31) for the doubles gate fraction and (Eq. 4.32) for the triples gate fraction respectively.

$$\tau = \frac{-G1}{Ln(\frac{D_{G2}}{D_{G1}}) - 1} \tag{4.30}$$

$$f_d = e^{(-P/\tau)}\left(1 - e^{(-G/\tau)}\right) \tag{4.31}$$

$$f_t = f_d^2 \tag{4.32}$$

Because the statistical uncertainty is significantly smaller than the systematic uncertainty, several semi-empirical equations have been created to estimate multiplicity count rate systematic uncertainties based off, count rates, gate width, pre-delay width (T_p), measurement time (T_G), and die-away time [11]. The equations for the singles, doubles, and triples systematic uncertainty can be seen below in (Eq. 4.33-4.35). Here (σ_S), (σ_D), and (σ_T) are the singles, doubles, and triples count rate standard deviations.

$$\sigma_S = \zeta_S\sqrt{S/t} \tag{4.33}$$

$$\sigma_D = \zeta_D\sqrt{(D + 2A)/t} \tag{4.34}$$

$$\sigma_T = \zeta_T\sqrt{(T + 2A_t)/t} \tag{4.35}$$

The variables (A) and (A_T) are the doubles and triples accidentals rate respectively. They can be computed as follows in (Eq. 4.36) and (Eq. 4.37). Within these expressions, the signal triggered gate utilization fraction (GUF) is represented by (f_2) and the random triggered GUF is represented by (g_2). If the die-away profile is represented by a pure exponential (f_2) and (g_2) may be solved for by (Eq. 4.38) and (Eq. 4.39).

$$A = S^2 T_G \tag{4.36}$$

$$A_T = (1 + \frac{g_2}{f_2}) S(DT_G) + \frac{1}{2} S(ST_G)^2 \tag{4.37}$$

$$f_2 = e^{-T_p/\tau}(1 - e^{-T_G/\tau}) \tag{4.38}$$

$$g_2 = 1 - \frac{(1 - e^{-T_G/\tau})}{T_G/\tau} \tag{4.39}$$

The last part to the standard deviation of the counts is found by calculating the expression for (ζ). These are seen in equations (Eqs. 4.40-4.42) where they are functions of the doubles count rate, signal triggered GUF, and random triggered GUF.

$$\zeta_S = \sqrt{1 + 2\frac{D/f_2}{S}} \tag{4.40}$$

$$\zeta_D = \sqrt{1 + 8g_2\frac{D/f_2}{S}} \tag{4.41}$$

$$\zeta_T = \sqrt{1 + 10 g_2 \frac{D/f_2}{S}} \tag{4.42}$$

4.4 Effective Mass Coefficients

The multiplicity equation for $^{240}\mathrm{Pu}_{eff}$ is well documented and given as (Eq. 2.5) in Chapter 2. For the method developed for this work, however, the ^{244}Cm effective mass must be calculated. What follows is a derivation of such an equation [10]. For doubles counting with a neutron detector with a flat neutron energy response, we define the $^{244}\mathrm{Cm}_{eff}$ coefficient of nuclide xxx relative to ^{244}Cm, γ_{xxx}, on a per-unit-mass basis, in terms of basic nuclear data by the following relation (Eq. 4.43) where (g) is the specific spontaneous fission rate, in terms of fissions per unit time per unit mass, and again (ν_2) is the second factorial moment of the normalized spontaneous fission prompt neutron multiplicity distribution. The specific spontaneous fission rate is calculated from the spontaneous fission half-live via (Eq. 4.44). Here the molar mass is represented by (A), $(t_{\frac{1}{2}})$ is the spontaneous fission half-life, and (N_A) is Avogadro's number. Combining (Eq. 4.43) and (Eq. 4.44) yields the final nuclide coefficient formula (Eq. 4.45).

$$\gamma_{xxx} = \frac{(g * \nu_2)_{xxx}}{(g * \nu_2)_{244}} \tag{4.43}$$

$$g = \frac{1}{A} N_A \frac{ln(2)}{t_{\frac{1}{2}}} \tag{4.44}$$

$$\gamma_{xxx} = \frac{(\frac{\nu_2}{A*t_{\frac{1}{2}}})_{xxx}}{(\frac{\nu_2}{A*t_{\frac{1}{2}}})_{244}} \tag{4.45}$$

The molar masses are known to high accuracy, and so the uncertainty in the γ_{xxx} factors is determined, for all practical purposes, solely by the uncertainties in the second factorial moments and the spontaneous fission half-lives. Table 4.1 summarizes the nuclear data parameters used in the present study [30]. Propagation of variance by first-order Taylor series expansion to the mathematical expression for γ_{xxx} gives (Eq. 4.46) where (σ) is the standard deviation. The final equation for the $^{244}\mathrm{Cm}_{eff}$ mass is given by (Eq. 4.47).

$$Uncertainty_{xxx} = (\frac{\sigma_{\nu_{2,xxx}}}{\nu_{2,xxx}})^2 + (\frac{\sigma_{t_{\frac{1}{2},xxx}}}{t_{\frac{1}{2},xxx}})^2 \tag{4.46}$$

$$^{244}Cm_{eff} = (1.64 \pm 0.056 f_{242} + f_{244} + 0.84 \pm 0.01 f_{246}) m_{Cm} \tag{4.47}$$

4.5 Pu Mass Estimation

Here, a first principles method was developed to determine the elemental masses of a sample containing curium and plutonium while mixed with eutectic salt. The method sees the traditional definition of the (α) variable disassembled into two components that represent the curium contribution and the plutonium contribution. This is shown in (Eq. 4.48) where the spontaneous fission originates from curium with a source strength of ($F_{Cm}(SF)$) and plutonium with a source strength of ($F_{Pu}(SF)$). The numerator gives the (α,n) breakdown with ($F_{Cm}(\alpha, n)$) representing the (α,n) source strength of curium and ($F_{Pu}(\alpha, n)$)

representing the (α,n) source strength of plutonium. Rearranging the equation to solve for the mass of plutonium (m_{Pu}) yields (Eq. 4.49). It is seen that this method relies on information from a mixed sample simulation.

$$\alpha = \frac{F_{Cm}(\alpha, n)m_{Cm} + F_{Pu}(\alpha, n)m_{Pu}}{F_{Cm}(SF)m_{Cm}\nu_{s1} + F_{Pu}(SF)m_{Pu}} \tag{4.48}$$

$$m_{Pu} = \frac{F_{Cm}(SF)m_{Cm}\nu_{s1}\alpha - F_{Cm}(\alpha, n)m_{Cm}}{F_{Pu}(\alpha, n) - F_{Pu}(SF)\alpha} \tag{4.49}$$

Table 4.1: Nuclear Data Parameters for Isotopes of Curium [24, 9].

	^{242}Cm		^{244}Cm		^{246}Cm	
	Average	Error (%)	Average	Error (%)	Average	Error (%)
$t_{\frac{1}{2}}$ (yrs)	$(7.00\pm0.2)10^6$	2.85	$(1.32\pm0.02)10^7$	1.51	$(1.81\pm0.02)10^7$	1.10
v_2	5.13±0.1	1.94	5.94±0.07	1.17	6.94±0.03	0.43

Chapter 5

Results and Analysis

5.1 Emission Rate Analysis

The initial runs for all 45 cases were completed using an energy range of [0-4.48] MeV with a bin width of 0.1 MeV based on the default output from ORIGEN. The first step was to review specific quantities such as the ratio between (α,n) emissions and total neutron emissions as well as the plutonium contribution to (α,n) emissions, of which a numerical overview can be seen in Table 5.1. Each will identify if any trend is visible across the fuel domain as well as give indication if plutonium quantification could be accomplished for (α,n) emission in electrochemical reprocessing. The former captured at hour 444 of simulation can be seen in Figure 5.1 where the black dots represent the main sequence band of realistic fuel parameters defined earlier. A breakdown demonstrates how maintaining a constant burnup while fluctuating the enrichment increases the contribution from (α,n) neutrons. Moving along the x-axis, an increase in the burnup decreases the the (α,n) contribution. The change

in the (α,n) contribution is not constant across either axis however it only varies by a range of 20% from the lowest to highest value being 19-38%.

Next, the ^{238}Pu contribution to (α,n) emissions was broken down in Figure 5.2 across the same energy range. The trends seen when holding each axis constant and changing the other is the same as seen in Figure 5.1. Here the range of ^{238}Pu contribution varies between 24-37% within the domain space and only 27-38% within along the main sequence line. Again, the trend is not constant across either axis and further investigation better extracts the (α,n) signature and then the plutonium contribution from said signature. Thus, examination within a finer energy range may allow for more direct tracking of ^{238}Pu and other plutonium isotopes. The determination and classification of a epi-thermal energy range and analysis within that range is discussed in the next section.

5.1.1 Epi-thermal Energy Classification

Once these correlations had been demonstrated across the energy range from [0-4.48] MeV, the intersection between spontaneous fission and (α,n) emissions was inspected to determine at what energy, for each burnup/enrichment combination, the (α,n) emissions start to dip below that of spontaneous fission. An example showcasing the highest intersection point, in terms of energy, is seen in Figure 5.3. This will allow construction of a region to be examined for better discrimination between the two neutron producing reactions. After observing the intersection for each burnup/enrichment case, a value of 0.3 MeV was chosen as the cutoff point to differentiate between epi-thermal and fast energies. This energy was chosen as it was the lowest intersection before the spontaneous fission emission rate was never below that of

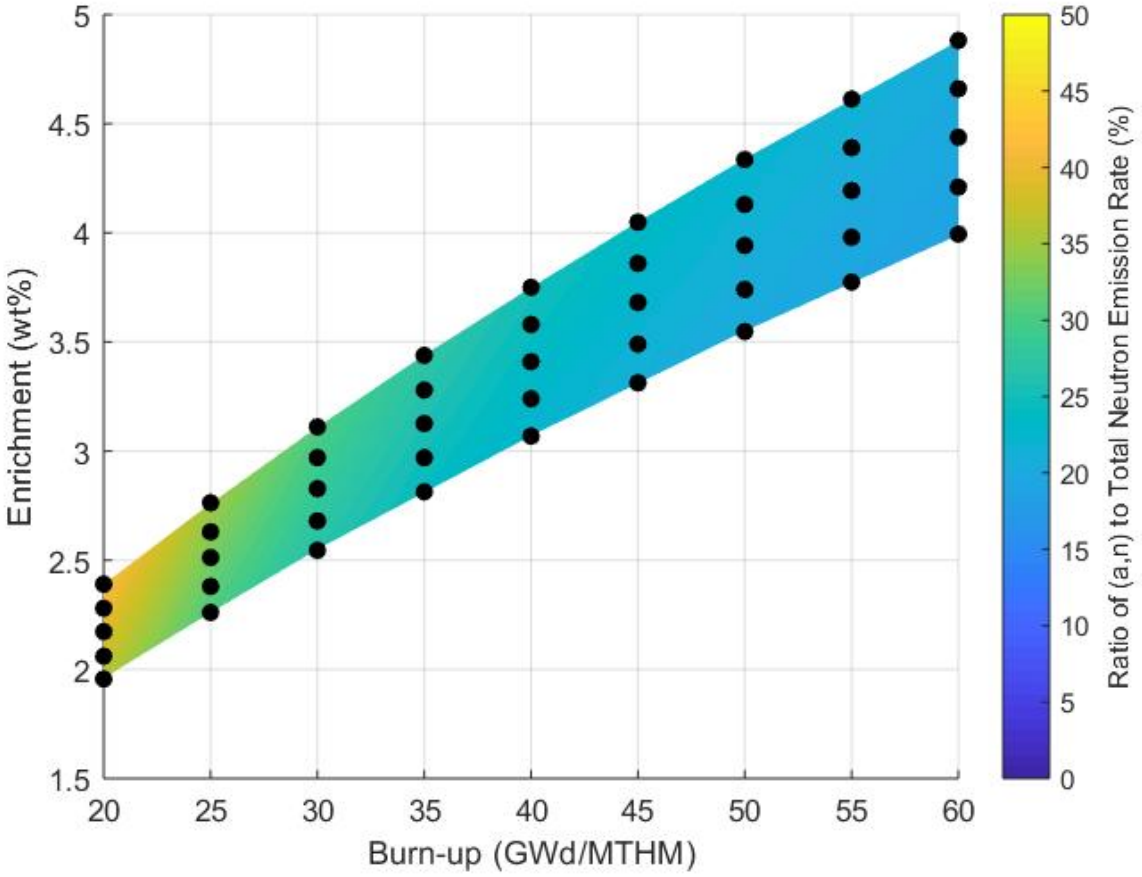


Figure 5.1: Correlation heat map between varying burnup and enrichment values from Origen for the ratio of (α,n) to total neutron emission rate for a cooling time of 5 years.

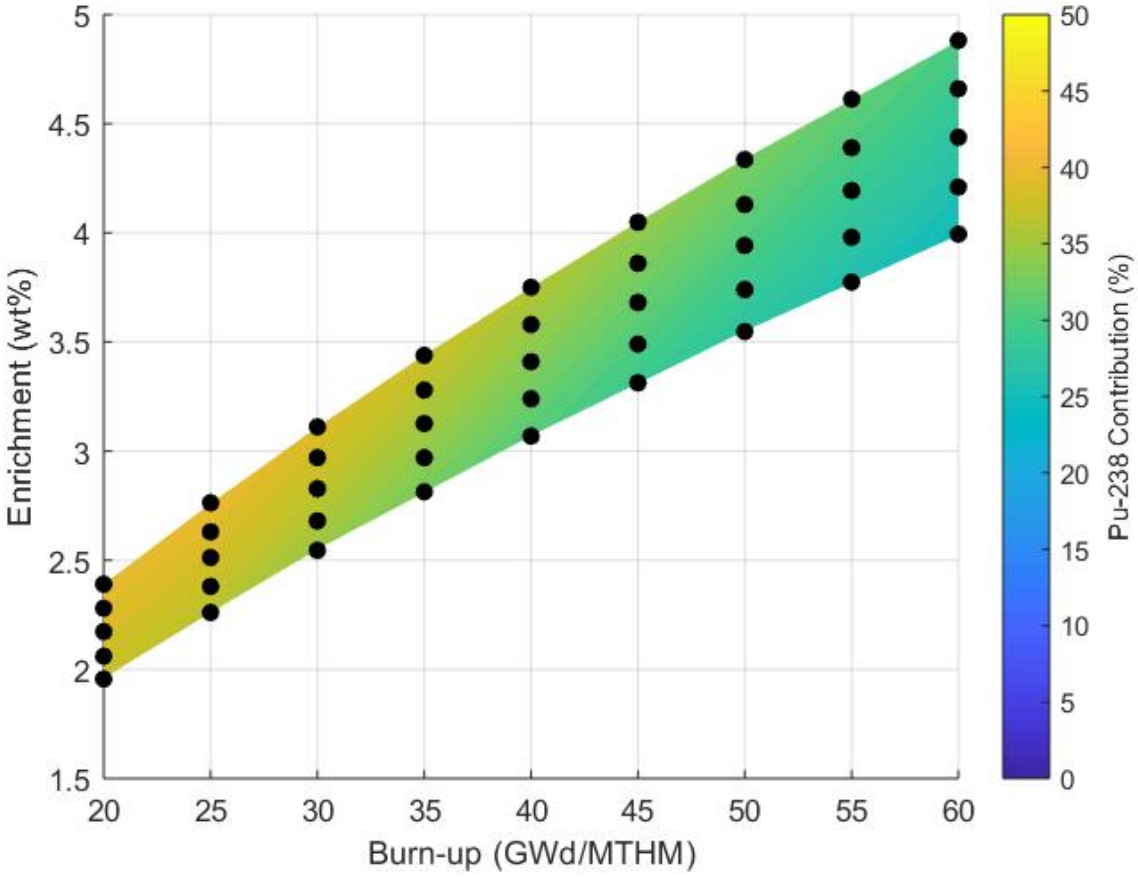


Figure 5.2: Correlation heat map between varying burnup and enrichment values from Origen for the ^{238}Pu contribution to (α,n) reactions for a cooling time of 5 years.

Table 5.1: Summary of SSPM EChem (α,n) Results Showing Burnup/Enrichment Mixtures [0-4.5] MeV.

Burnup (GWd/MTHM)	Enrichment (%)	Percent (a,n) Contribution to Total Counts (%)	Percent Isotopic Contribution to (a,n) (%)				
			Pu-238	Pu-239	Pu-240	Am-241	Cm-244
20	2.17	38.96	38.48	4.27	5.84	24.17	24.58
25	2.51	32.55	38.16	2.99	4.4	19.06	33
30	2.83	28.43	36.88	2.16	3.38	15.08	40.37
35	3.13	25.68	35.23	1.62	2.65	12.07	46.54
40	3.41	23.73	33.48	1.24	2.12	9.77	51.71
45	3.68	22.31	31.78	0.97	1.73	8.01	56.01
50	3.94	21.24	30.21	0.78	1.43	6.67	59.56
55	4.19	20.39	28.77	0.64	1.21	5.61	62.57
60	4.44	19.70	27.46	0.53	1.03	4.77	65.11

the (α,n) rate. This intersection was last observed for the cases consisting of a burnup of 40 GWd, with the highest appearing at a burnup of 20 GWd at 1.1 MeV as shown in Figure 5.3. Thus, by setting this value as the threshold, the thermal region for each burnup/enrichment combination below 40 GWd will always present a higher magnitude (α,n) emission than that of spontaneous fission. It should again be noted that this is the case only when an intersection is present.

5.1.2 Epi-thermal Energy Analysis

Using 0.3 MeV as the cutoff between the epi-thermal and fast regions, the epi-thermal section was cut into three bins ranging from [0-0.3] MeV, each with a width of 0.1 MeV again captured at hour 444 of simulation. After an epi-thermal region had been defined that corresponds to a higher (α,n) emission magnitude, the same quantities were captured to observe how they changed and if they could detangle the (α,n) neutrons from that of spontaneous fission neutrons. This time, since trends across the domain space had been previously examined, only the main sequence line following the empirical relationship (Eq. 3.1) was used to capture realistic scenarios. Figure 5.4 demonstrates the ratio between (α,n) emissions and total neutron emissions for cases following the main sequence line across each of the three thermal energy bins. The horizontal black line indicates where (α,n) neutrons constitute 50% of the total emission rate. Each of the nine cases for all three energy bins cluster around the 50% threshold. This, however, does not give us a good indication of the how the ratio varies, only that it decreases with increasing burnup.

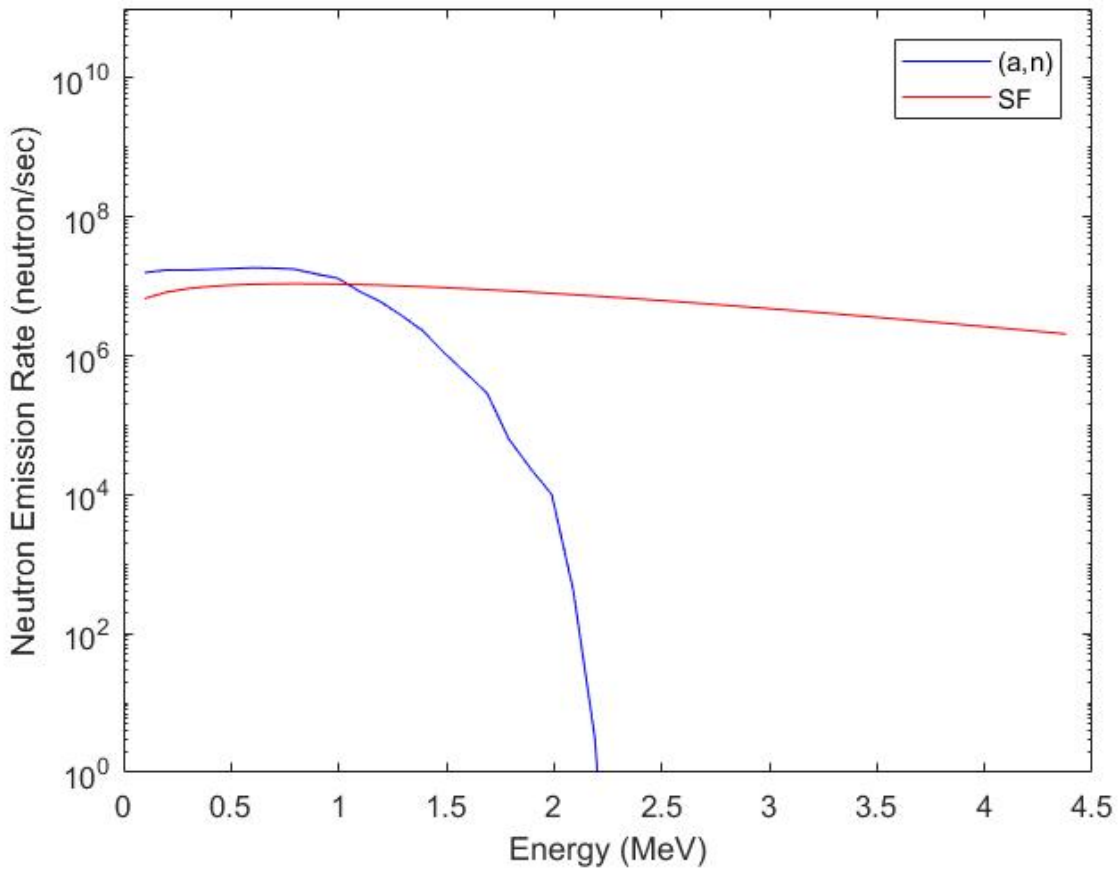


Figure 5.3: Demonstration of the intersection between the spontaneous fission emission rate and the (α,n) emission rate for a cooling time of 5 years.

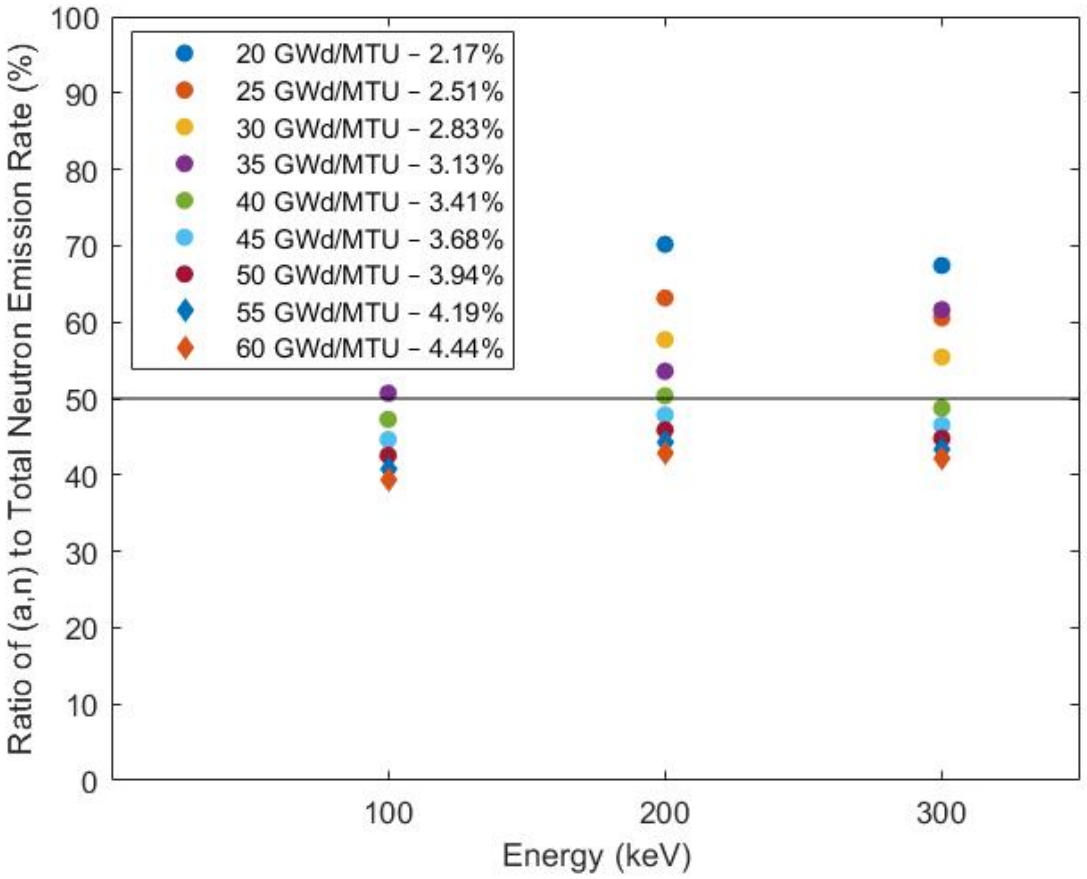


Figure 5.4: Ratio of (α,n) to total emission rate for a main sequence burnups across an epi-thermal energy range with cooling time of 5 years.

To expand upon this, a breakdown for the main sequence line can be seen in Figure 5.5 as a function of burnup to better visualize the decrease in the amount that (α,n) neutrons contribute. This better demonstrates which energy bins within the classified thermal region contribute most to the (α,n) emissions. It appears that neutrons whose energies falls within the 100-200 keV bin are the ones most likely to come from an (α,n) reaction. The ratio for all three bins ranges between 39-67%. Examining values across the main sequence line in Figure 5.1, narrowing the energy range to a classified thermal region increases the lower percentage value for (α,n) contributions from roughly 18% to 39%.

Next, the plutonium contribution was calculated for ^{238}Pu, ^{239}Pu, and ^{240}Pu with the summation of all three being total plutonium content. The isotopes of ^{241}Am and ^{244}Cm were also examined thus including the five isotopes that constituted 98% of the (α,n) neutrons. Figure 5.6 shows all six trends as a function of burnup for the main sequence line. ^{239}Pu and ^{240}Pu each constitute the least out of the plutonium isotopes and less than 10% individually to the overall (α,n) emission rate. For ^{238}Pu, the range of contribution is between 33-41% with that of total plutonium contribution ranging between 36-54%. This shows an increase within the main sequence line for ^{238}Pu when compared to values across the wider energy range shown in Figure 5.2. As burnup increases, so does the ^{244}Cm contribution ranging from 18-56%.

5.2 Burnup and Enrichment Effects

Isolating the main sequence line, the (α,n) contribution was plotted against burnup and enrichment to see each individual trend more clearly. Figure 5.7 demonstrates a leveling in

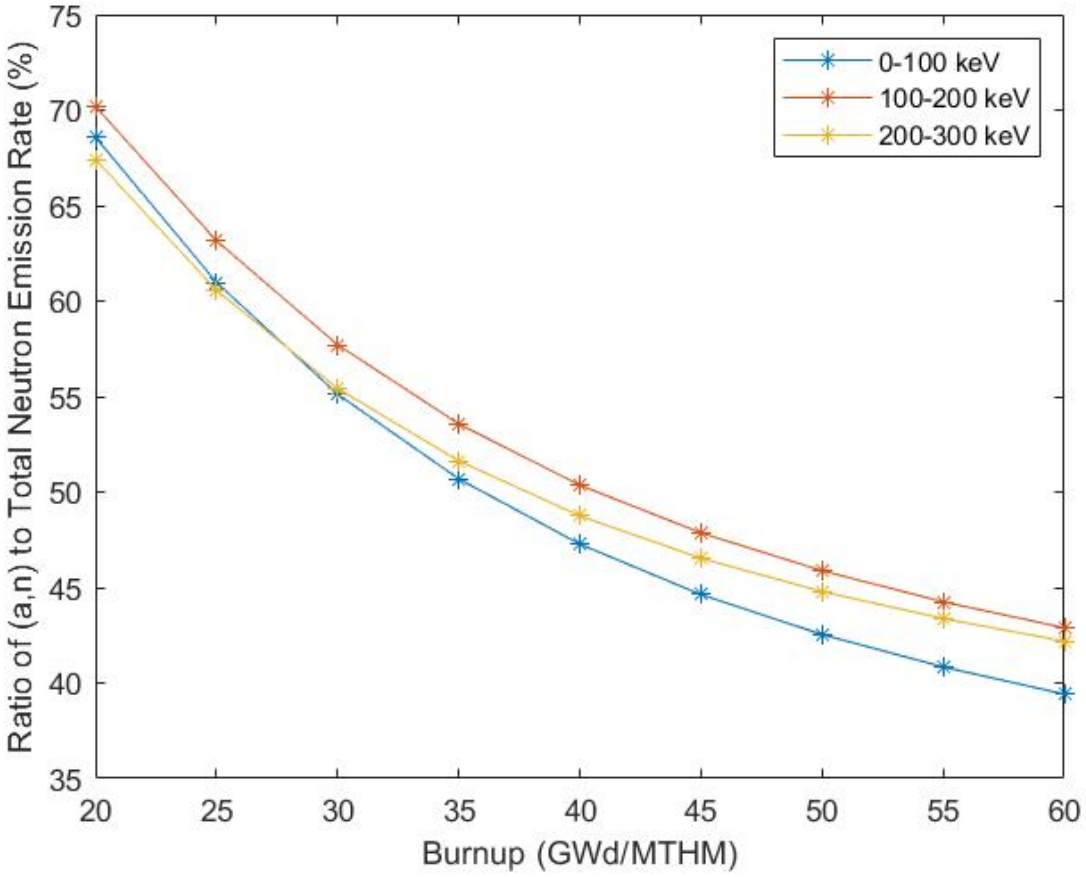


Figure 5.5: Ratio of (α,n) to total emission rate for a main sequence burnups and enrichments for each energy bin from 0-300 keV with a cooling time of 5 years.

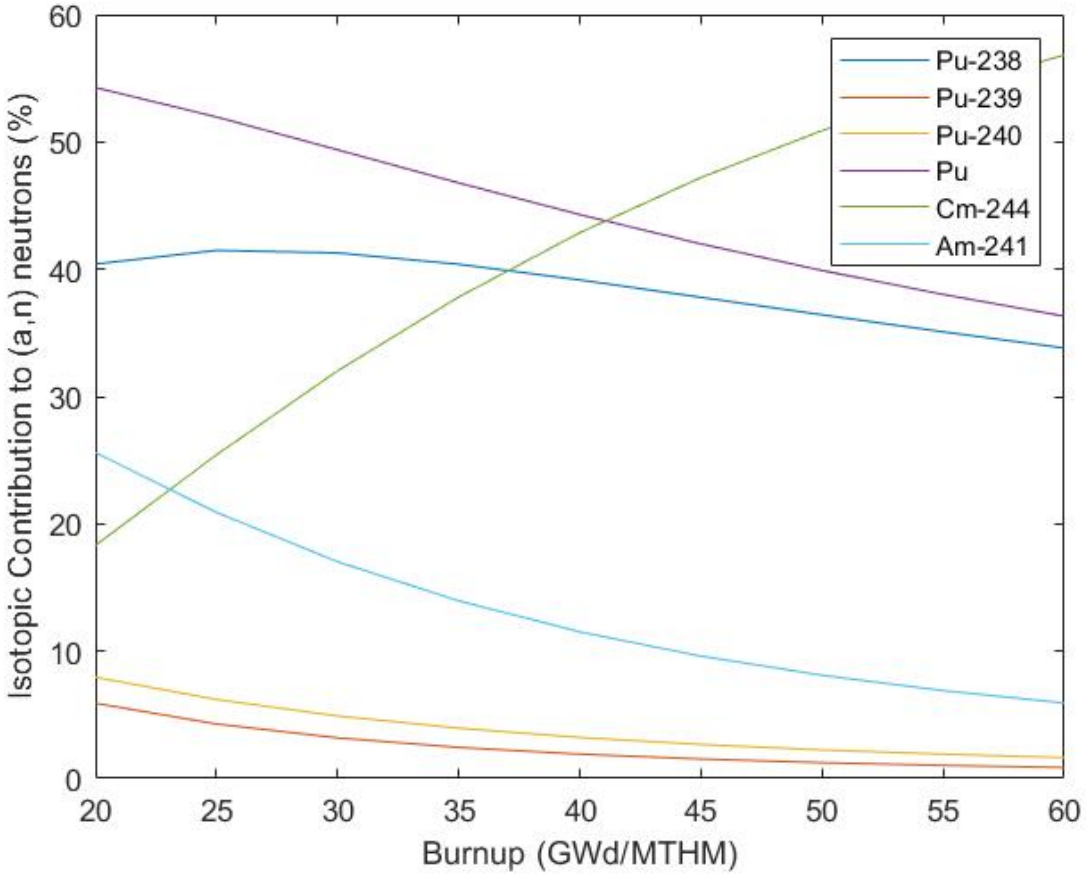


Figure 5.6: Plutonium contribution for (α,n) neutrons for main sequence burnup and enrichment from 0-300 keV from Origen for a cooling time of 5 years.

the (α,n) contribution as burnup increases. This is seen as the gaps between the burnup lines become smaller with increasing burnup values. Thus, moving from a burnup of 20 GWd to 25 GWd has more of an impact than going from 55 GWd to 60 GWd when using (Eq. 3.1) for enrichment. In addition, plotted as a function of enrichment Figure 5.7 also demonstrates that holding burnup constant and increasing enrichment shows an increase in (α,n) contribution. This effect becomes less predominant as the burnup increases (i.e. the slope of the line flattens).

Next, the (α,n) contribution was plotted against burnup and enrichment to again see each individual trend more clearly, this time across the epithermal energy range. Figure 5.8 shows as the gaps between the burnup lines becoming smaller with increasing burnup values although not to the extent as with the larger energy range. In addition, it also demonstrates that the slope of each burnup decreases with increasing enrichment but not as much as was seen in Figure 5.7.

5.3 Geometrical Analysis

In preparation for an MCNP analysis, a geometrical study was conducted using Sources-4C software to better establish a more accurate physical representation of the neutron yield and to characterize the neutron yield for a sample given design parameters from the ENMC input deck. It is important to note that this analysis as well as that to come within MCNP is being done on a homogeneuous sample that consists of Pu, Cm, and LiCl-KCl. The analysis started by characterization of two cases in terms of size, one representing a full scale electrorefiner vessel while the other represents the cavity size of an ENMC [31, 20].

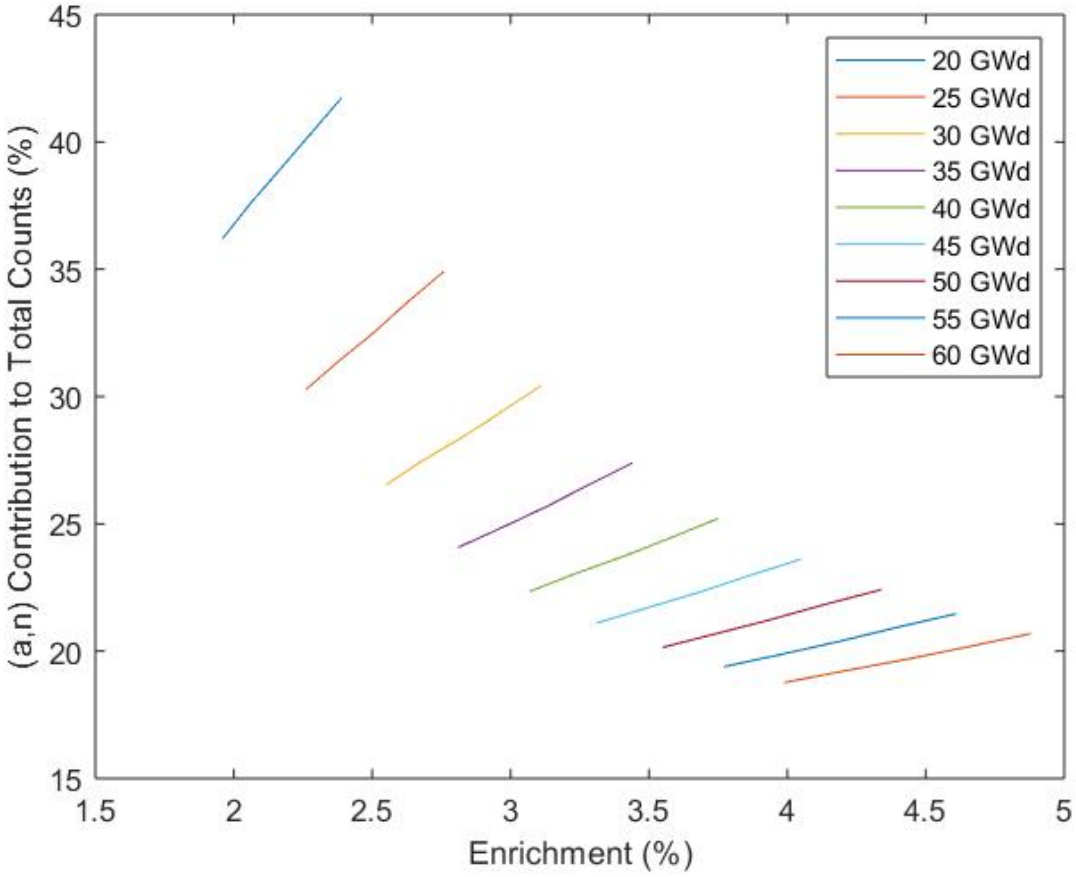


Figure 5.7: Enrichment effect on the ratio of (α,n) to total emission rate for various burnups from 0-4.5 MeV with a cooling time of 5 years.

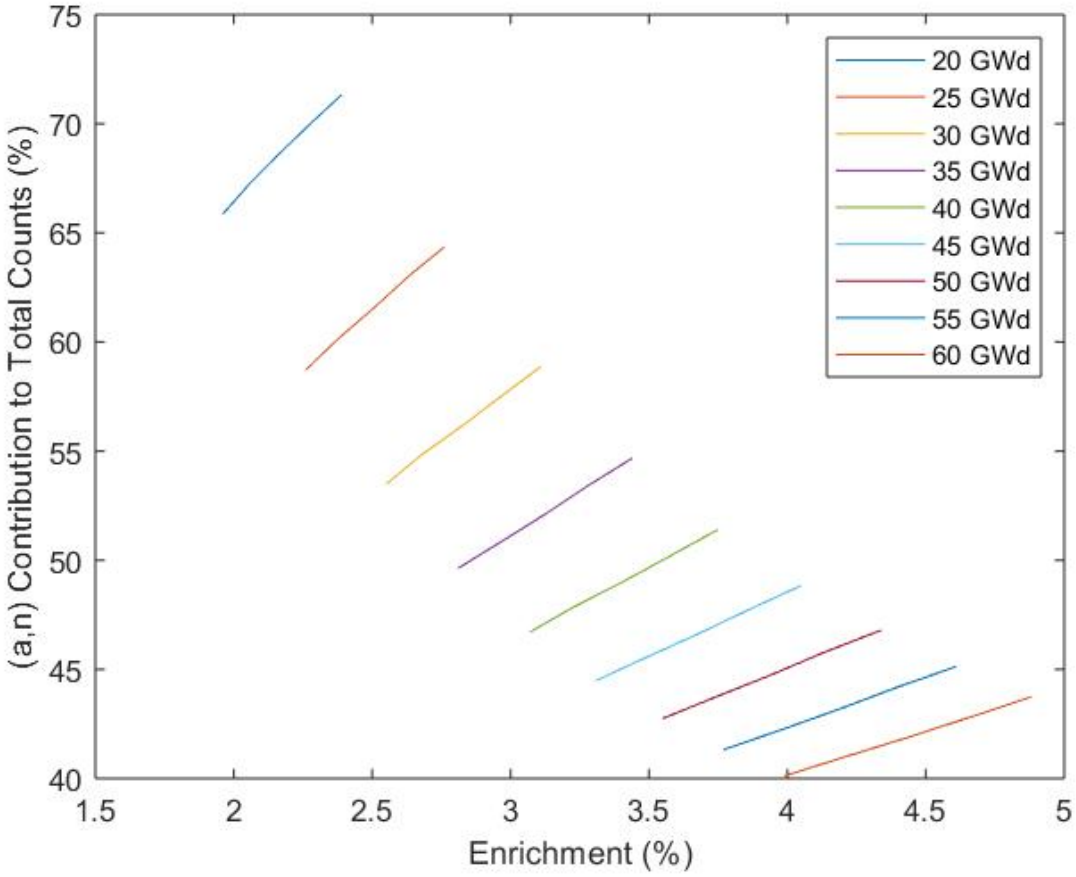


Figure 5.8: Enrichment effect on the ratio of (α,n) to total emission rate for various burnups from 0-300 keV with a cooling time of 5 years.

The isotopic ratios were taken from the SSPM EChem model and the density of the salt from literature regarding operational electrorefiner vessels [31]. Given that the ratio values will remain constant across the two geometric cases, with appropriate scaling down for the smaller cavity size, the outcome of each will be the same in terms of (α,n) and isotopic percentage breakdown. The results of the geometrical analysis are shown in Table 5.2. Even though Sources-4C takes into account factors other than mass such as atom density and atom fraction, the physical representation of the α-particle movement and thus probability of interaction effects the overall (α,n) yield the same magnitude as produced via Scale. The trend seen previously regarding burnup effect and leveling out of percentages as it increases still holds true. Also, lowering the sample composition to consist of only two neutron source nuclides, plutonium and curium, changes the isotopic contribution to the (α,n) yield. Here, ^{238}Pu now consists as much as 50% of the total (α,n) yield at lower burnups but only contributes roughly 29% at higher burnups as seen previously. The reason for the increase in percentage at lower burnups, yet similar percentages at higher burnups as seen when including more nuclides for a more complex matrix is the absence of ^{241}Am. At the lower burnups, when ^{241}Am is included, it accounts for a fairly large percentage of the (α,n) yield but its contribution drops off as the burnup increases. When removing it from the mixture, this results in a larger impact at lower burnups where it had a higher contribution. Thus, the inclusion of ^{241}Am in a future analysis will effect the error seen in plutonium mass estimation, predominantly at lower burnups.

Since SCALE is used to obtain the fission rates used in conjunction with MCNP outputs, the same analysis was done using this software. These comparative results produced the same values as seen in Table 5.2.

5.4 Die-Away Time Optimization

Prior to calculating the effective mass of curium, the proper die-away time must be determined to ensure accuracy of the resulting count rates. This is done by running the ENMC model with a fixed predelay and varying gate widths. Here, a beginning gate width of 10μs was chosen and increased by 2μs up to 100μs. Then the increments increased by 50μs until the final value of 250μs was reached. The doubles value was then plotted as a function of the gate widths and a single exponential was fitted to the data. Figure 5.9 demonstrates this and shows both a single exponential and a two-term fit. The optimal gate width for the ENMC input deck was 22μs based on the single exponential fit parameter τ. This is a more complete version of the exponential equation shown in (Eq. 4.30) and is done to ensure the proper die-away time is calculated. Using (Eq. 4.30), the same result will be reached but only if the two gate widths used cover a large enough range. For example, using gate widths of 32μs and 64μs will yield a die-away time of 22μs but when gate widths of 12μs and 24μs are used then the die-away time comes to roughly 18μs. A change in die-away time this large can yield an incorrect doubles gate fraction when using (Eq. 4.31) as the incorrect die-away time isn't representative of a single exponential trend. Thus, the fitting approach is often preferred to ensure correct results.

5.5 ENMC Passive Results

The results presented for the ENMC input deck consist of four scenarios. The first scenario examines a pure sample of curium and a pure one of plutonium in the absence of salt. This will highlight the capability of the ENMC under normal conditions where the spontaneous

Table 5.2: Summary of Geometrical (α,n) Results from Sources and Scale for a Sample Containing Plutonium, Curium, and Eutectic Salt.

Burnup (GWd/MTHM)	(α,n) (%)	Isotopic Contribution (%)	
		Pu-238	Cm-244
20	32	51	32
25	27	47	40
30	24	44	47
35	22	40	52
40	21	37	57
45	20	35	60
50	19	32	63
55	19	30	65
60	18	29	68

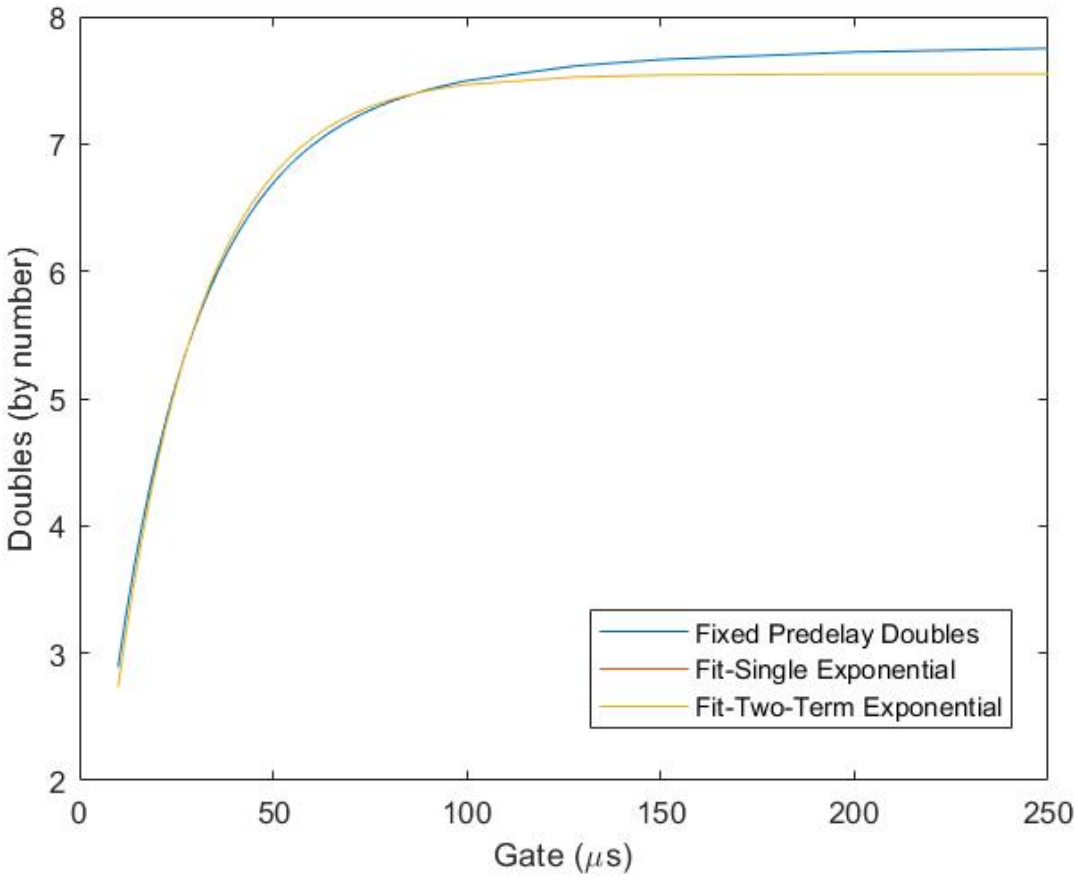


Figure 5.9: Die-away time optimization for the ENMC input deck.

fission signature is used to quantify material. The second and third scenarios use the curium mass with eutectic salt and plutonium mass with eutectic salt to highlight the contribution from each element with salt present. The final scenario uses the the mass of plutonium, curium, and eutectic salt obtained from the SSPM EChem model with a breakdown of the (α,n) contribution shown in the previous section. Following the results from each scenario the method for calculating the plutonium mass via the multiplicity variable α are demonstrated. Also, the 20 GWd sample is broken down into its five enrichment values from the emission rate analysis to see how enrichment effects the calculation of the plutonium mass. The other eight burnup values and their enrichment figures are given in Appendix B.

5.5.1 Single Elemental Mass Samples

Two single elemental samples were examined to test the capabilities of the ENMC and demonstrate its accuracy when measuring the spontaneous fission yield with no interference from an (α,n) signature. Figures 5.12 and 5.11 show a comparison between the actual mass of each sample and the simulated mass. It is seen that each simulated mass trend follows that of the actual mass and is visually close to the actual mass. To get a better understanding of how the ENMC input deck performed the error for both samples can be seen in Figures 5.12 and 5.13. The curium sample has an error range of -0.9% to -1.6% while the plutonium sample's error ranges from -0.4% to -1.6%. The cause of the error comes from the efficiency of neutron counting of the ENMC. Both ranges are in accordance with what has been documented in literature for a standard ENMC configuration. Furthermore, the exact ENMC input used in

this study was used prior by Dr. Braden Goddard and similar results were obtained for an array of plutonium standards [21].

5.5.2 Mass of Curium and Eutectic Salt

Figure 5.14 gives the simulated ^{244}Cm mass compared to the actual as a function of burnup. Similar to the previous sample, the simulated mass follows the same trend as the actual mass but visually looks closer to the actual mass. The percent error, Figure 5.15, is much smaller ranging from -10.8% to -9.9%. The improvement in accuracy of mass estimation is due to the removal of plutonium and the (α,n) signature. Thus, the newer sample is not as diluted and there are not as many accidental coincidence counts.

The α variable simulated in MCNP, using (Eq. 2.15), is still lower than that of the actual α variable obtained from Scale as seen in Figure 5.16. This is because there is still a relatively large error in the ^{244}Cm mass calculation which means that accidental coincidence counting is still occurring from the (α,n) signature produced from curium. This gives rise to a larger spontaneous fission value thus increasing the denominator in (Eq. 2.15). Again, the (α,n) percent contribution was compared to that of the ^{244}Cm mass percent error to demonstrate that the (α,n) signature is the source of error. Figure 5.17 shows the percent comparisons and that each trend follows a general trend in regard to a change in burnup. Each holds relatively steady which is to be expected since the spontaneous fission signature from curium vastly outweighs its (α,n) signature.

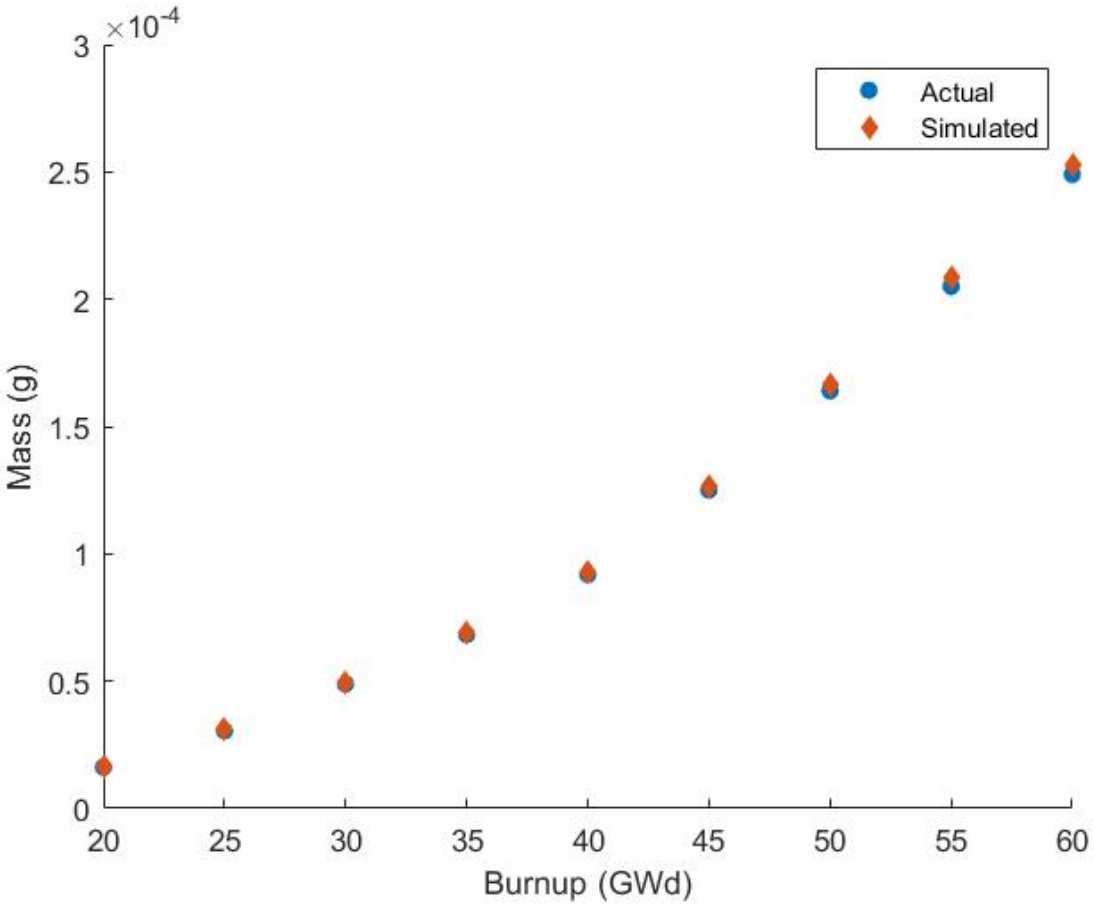


Figure 5.10: Comparison between actual and estimated via ENMC mass of curium.

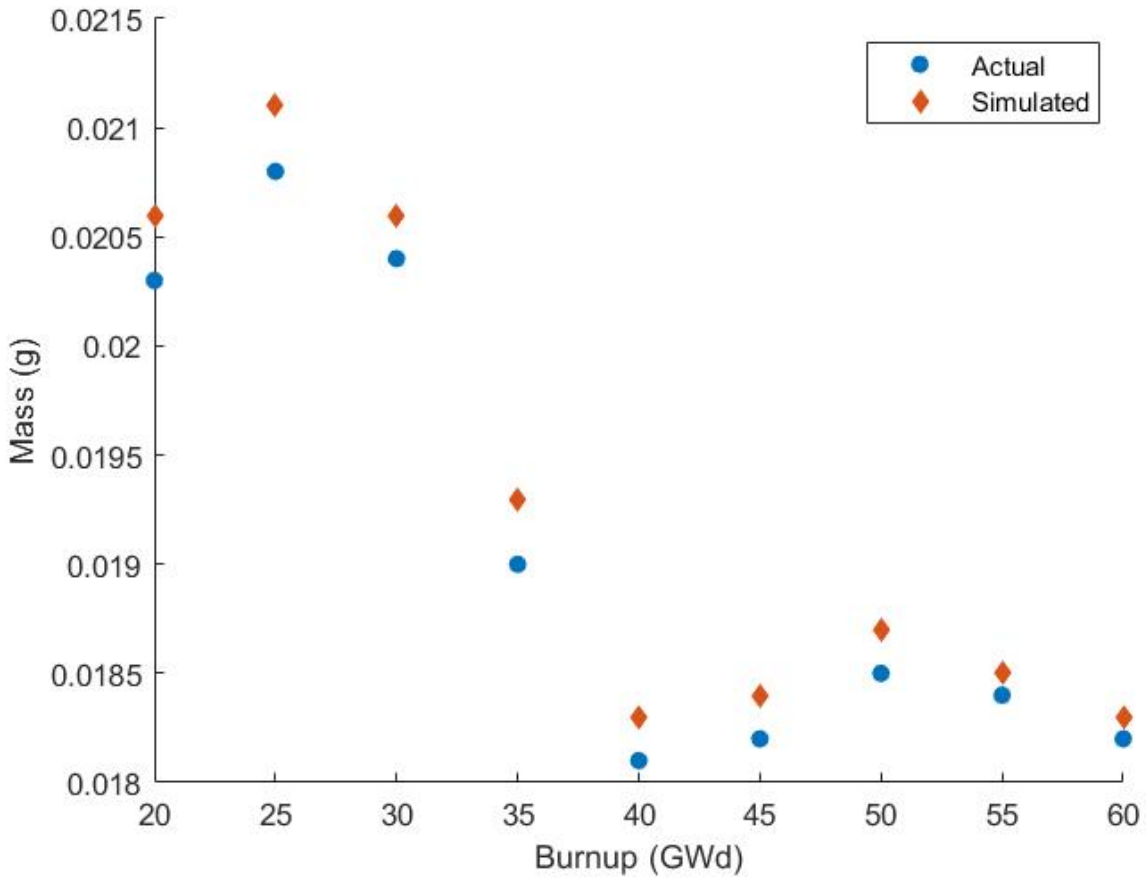


Figure 5.11: Comparison between actual and estimated via ENMC mass of plutonium.

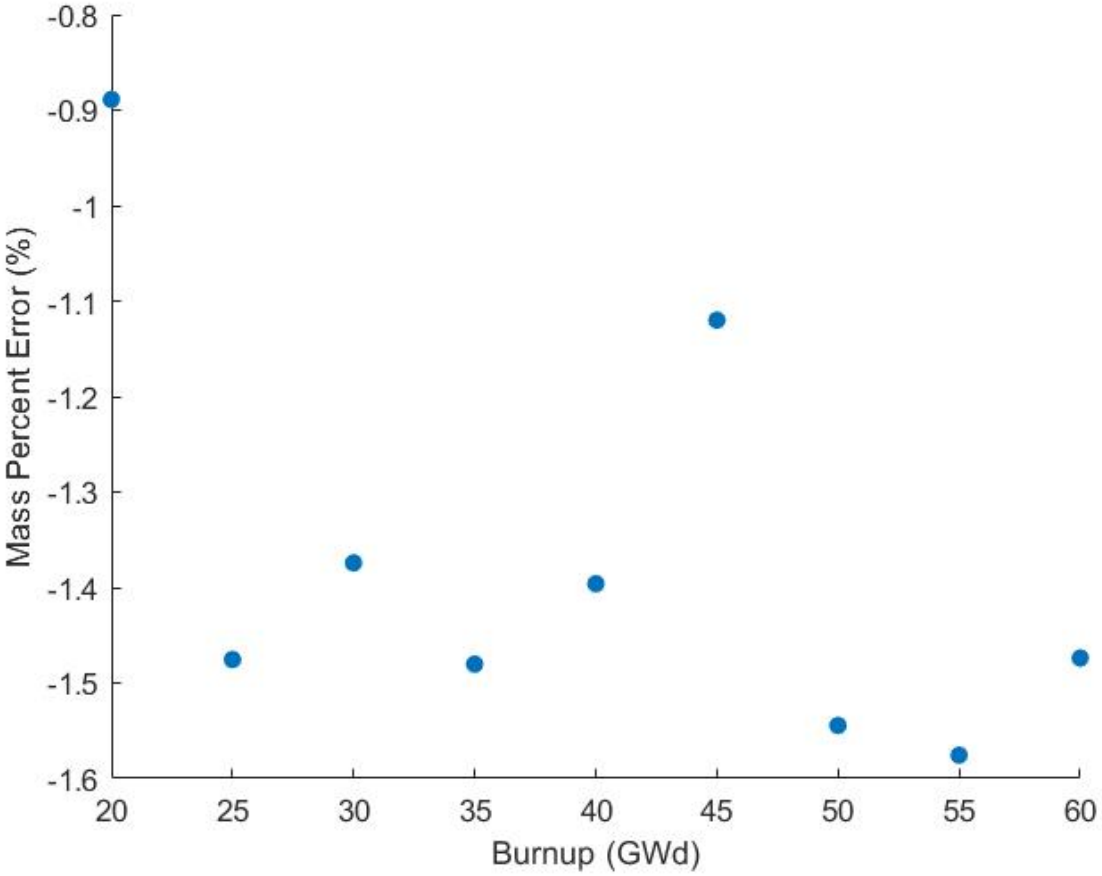


Figure 5.12: Percent error for curium mass estimation.

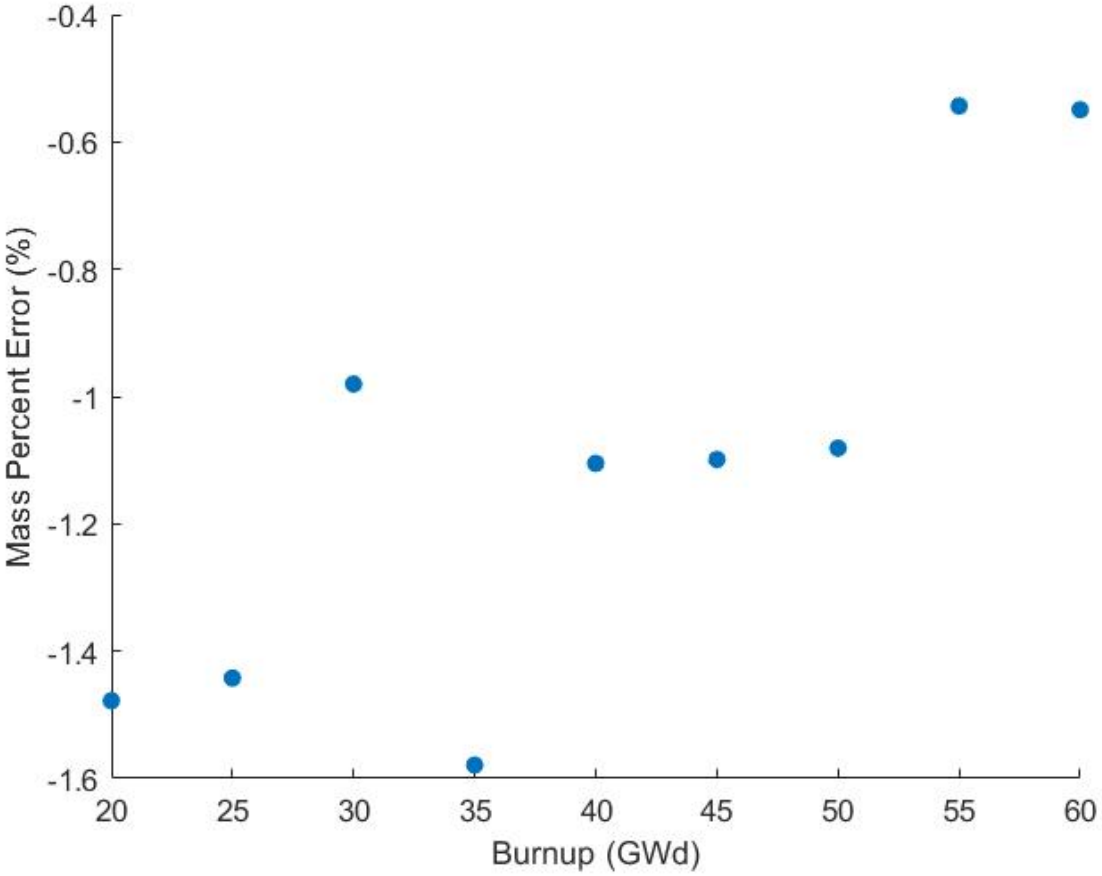


Figure 5.13: Percent error for plutonium mass estimation.

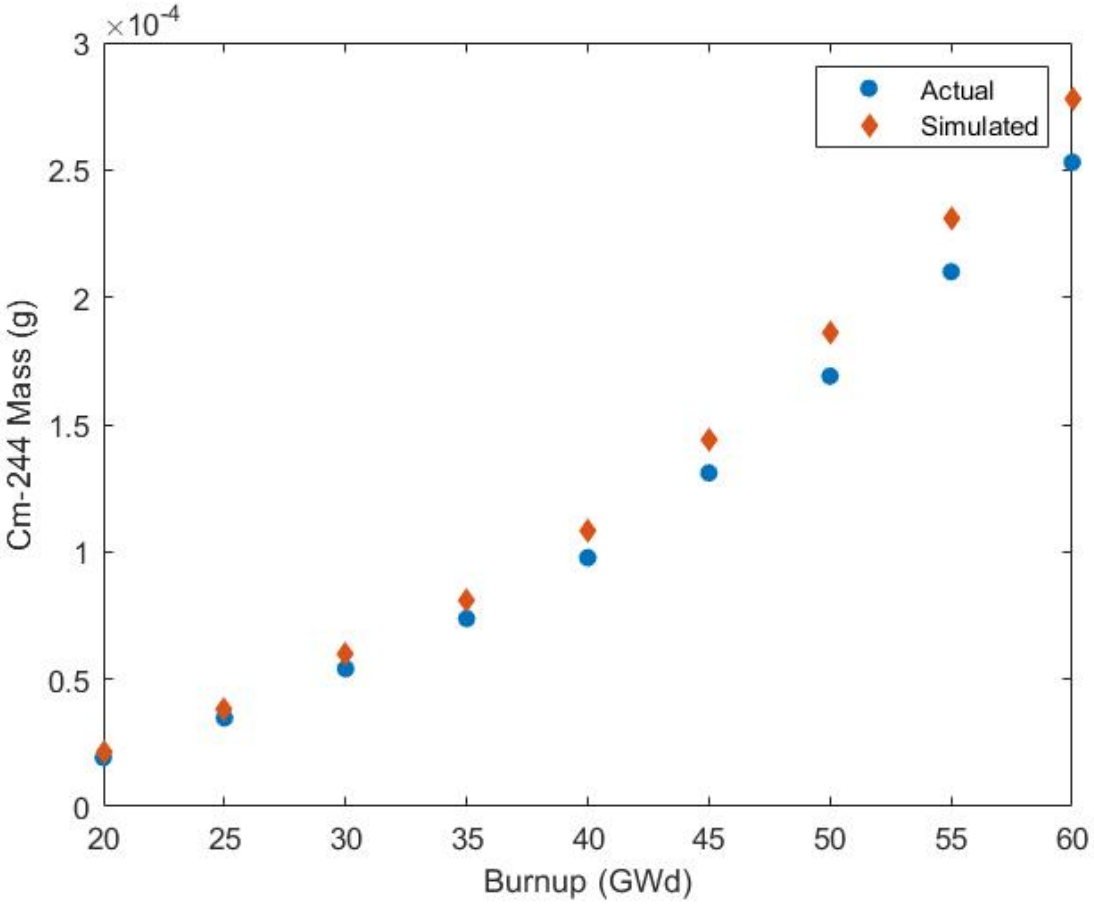


Figure 5.14: Comparison between simulated mass and actual mass of Cm-244.

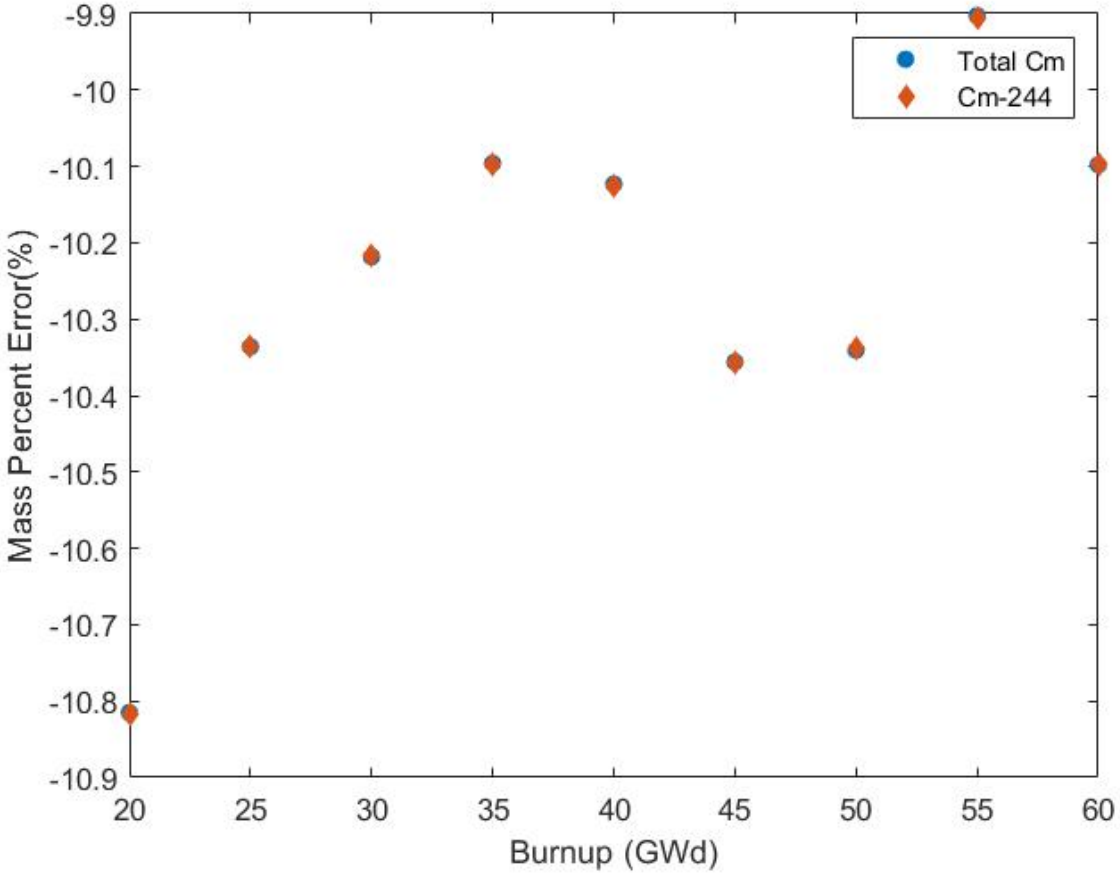


Figure 5.15: Percent error for Cm-244 and total curium mass estimation.

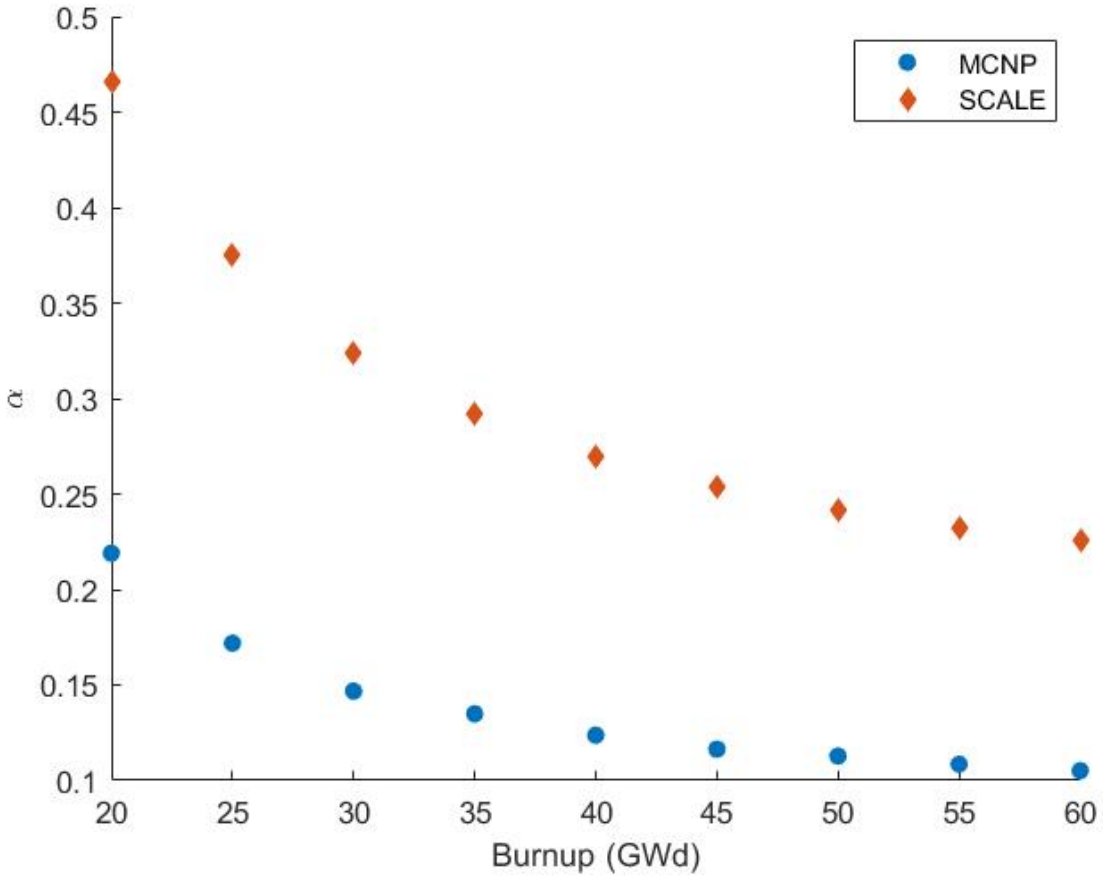


Figure 5.16: α variable comparison for a sample containing only curium.

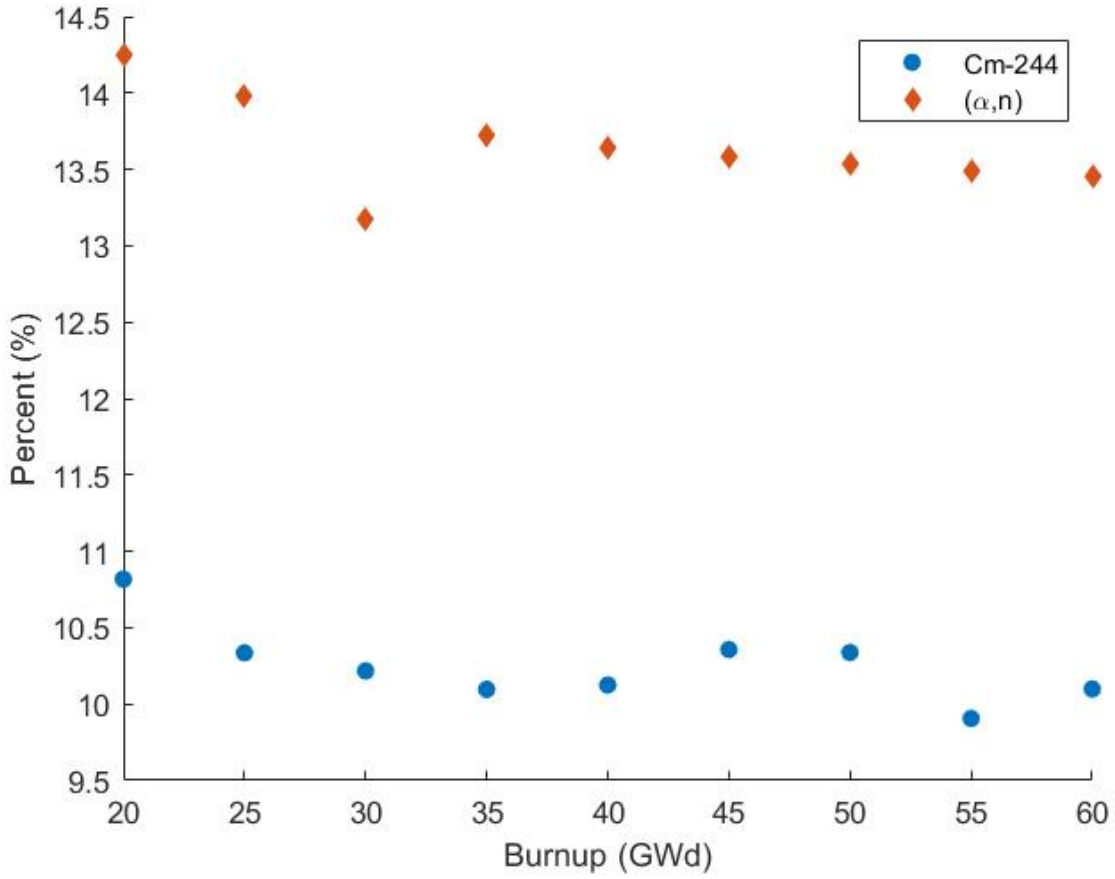


Figure 5.17: Comparison between Cm-244 mass percent error and total (α,n) contribution to neutron yield.

5.5.3 Mass of Plutonium and Eutectic Salt

Figure 5.18 gives the simulated plutonium mass accompanied with salt compared to the actual mass as a function of burnup. The simulated mass is much greater than the actual mass so they had to be plotted using different y-axes. The percent error, Figure 5.19, shows a trend that begins to plateau as burnup increases but the magnitude of the error is significantly high on the order of 10^5. The reasoning behind this is that plutonium has a relatively small spontaneous fission yield. Thus, when a sample is simulated accompanied with salt the dominant source of the neutrons are from the (α,n) source. The breakdown of neutron origin gives (α,n) a contribution range of 88-92% across the nine burnups. This overwhelming influence from (α,n) neutrons gives rise to a very high singles rate with little contribution from the doubles and triples which come more from spontaneous fission. Furthermore, the factorial moments are an indication of the spontaneous fission signature. With little influence from spontaneous fission the factorial moments will give rise to large error in the multiplicity calculation for the plutonium mass.

5.5.4 Actual Mass of Plutonium, Curium, and Eutectic Salt

The mass of the plutonium, curium, and eutectic salt from the EChem model was scaled down to the sample cavity size within the ENMC input deck. Then multiplicity equations were used to calculate the curium mass of the sample. Figure 5.20 shows the results as a function of burnup for the calculation of the ^{244}Cm mass. The simulated mass follows the same trend as the actual mass but has a slightly higher value which is more predominant in the higher burnup region. As burnup increases the percent error becomes smaller and

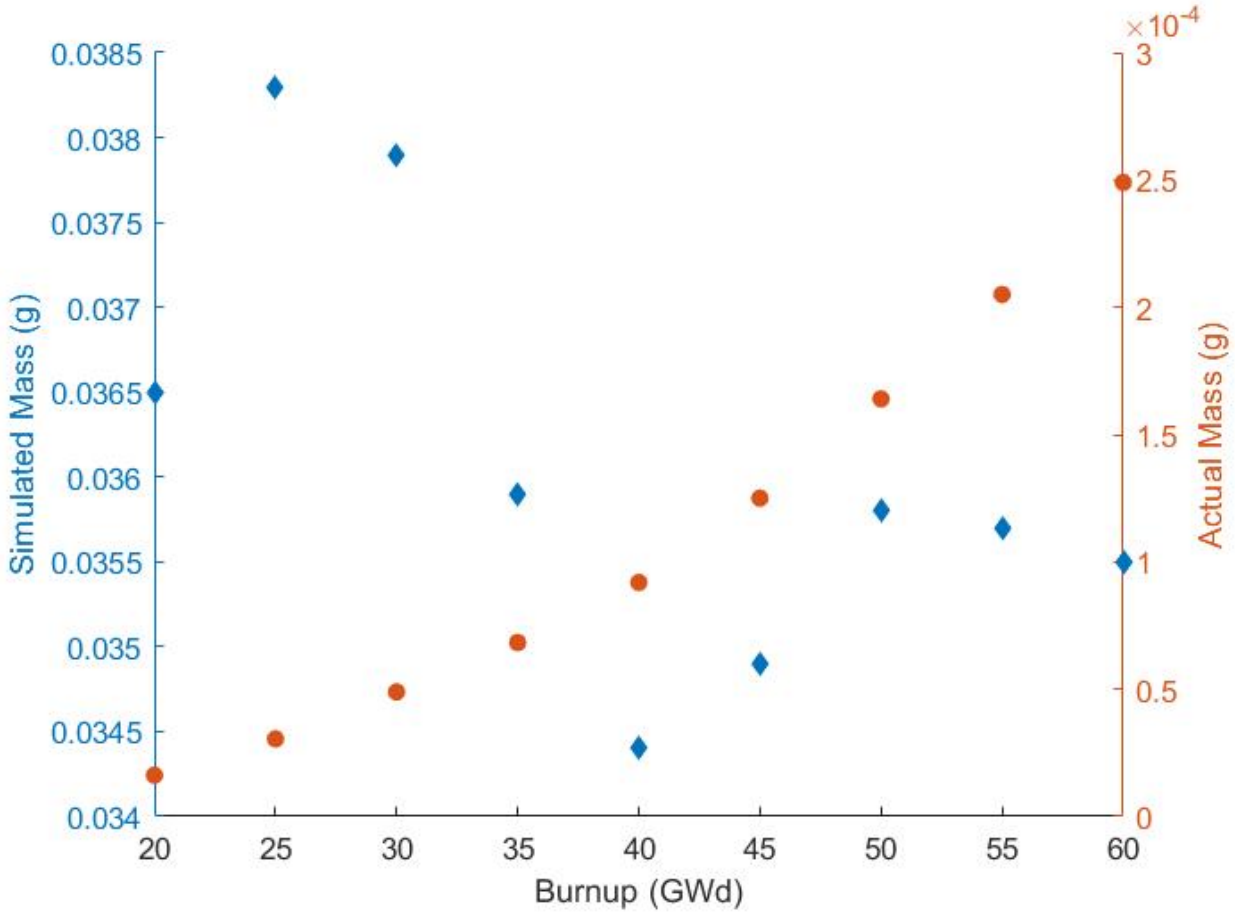


Figure 5.18: Comparison between simulated mass and mass of plutonium and salt.

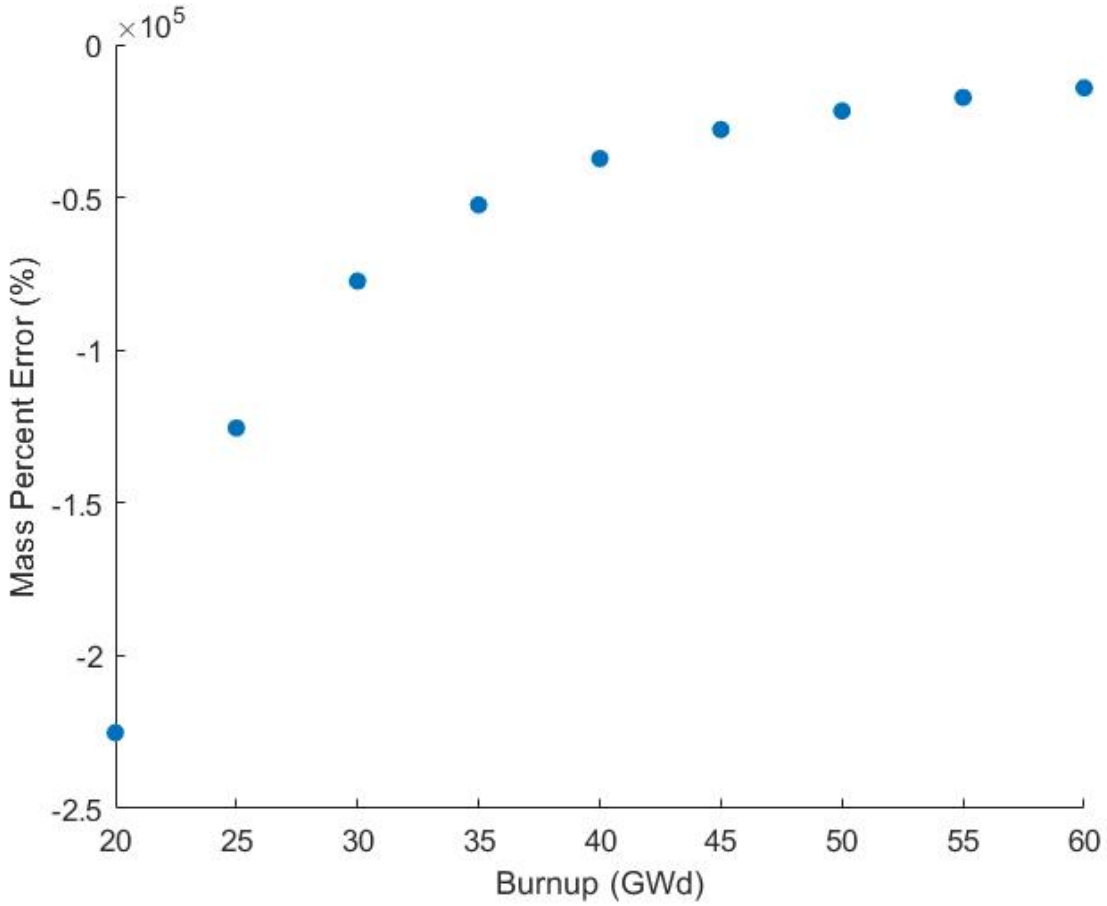


Figure 5.19: Percent error for plutonium and salt mass estimation.

starts to steady out. The entire range seen in the percent error is -28% to -14%. The error is shown in Figure 5.21 where the largest percent error is at the lowest burnup value of 20 GWd. These values and general trend can be attributed to the large accidental counting of (α,n) neutrons as spontaneous fission neutrons. Aside from the influence of the efficiency of the ENMC design, this phenomenon is a result of the coincidence rate of (α,n) neutrons based on their intensity for the given sample. This would cause an overestimation of ^{244}Cm mass, as seen, and explain why the error steadies out as burnup increases. As burnup increases the curium content also increases which causes the spontaneous fission signature to overtake that of (α,n). This is demonstrated in Table 5.1. With less (α,n) contribution, the rate that the ENMC associates accidentals, (α,n) neutrons, as spontaneous fission also decreases resulting in less error.

Looking at the α variable, the explanation for overestimation of ^{244}Cm is correct. Figure 5.22 shows the results from MCNP and compares them with the output produced from Scale. Those produced in MCNP are lower by a relative factor of 0.47 which will be examined in the Plutonium Mass Estimation section. Reexamining the definition of α, which is the ratio between (α,n) and spontaneous fission neutrons, the reasoning for the lower values again is due to the accidental coincidence. To better associate how the (α,n) neutrons effect the estimation of curium the (α,n) percent contribution was plotted alongside the absolute value of ^{244}Cm mass percent error in Figure 5.23. The two percentages follow the same trend and each steady out as burnup increases for the same reasons already explained. This gives even more indication that the accuracy of estimating curium in mixed samples containing eutectic salt rely heavily on the (α,n) signature present.

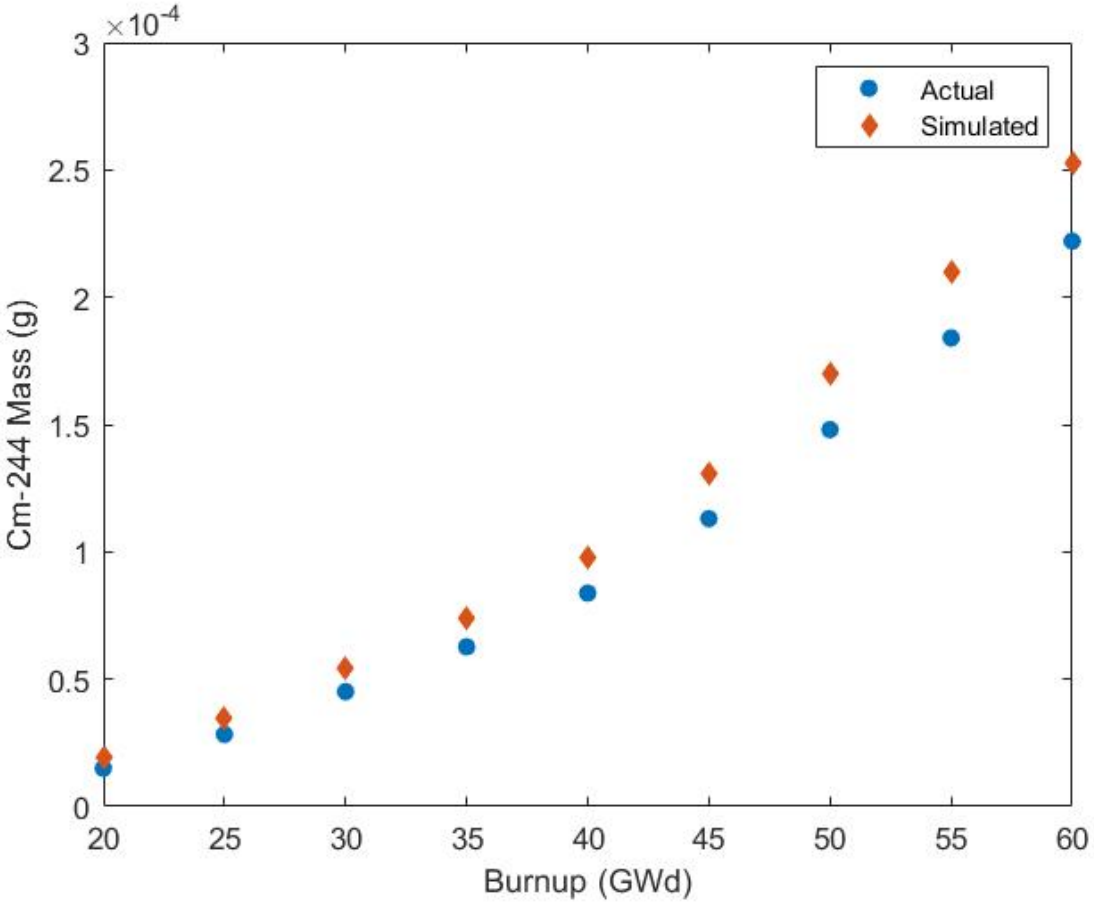


Figure 5.20: Comparison between simulated mass and actual mass of Cm-244 for a mixed sample.

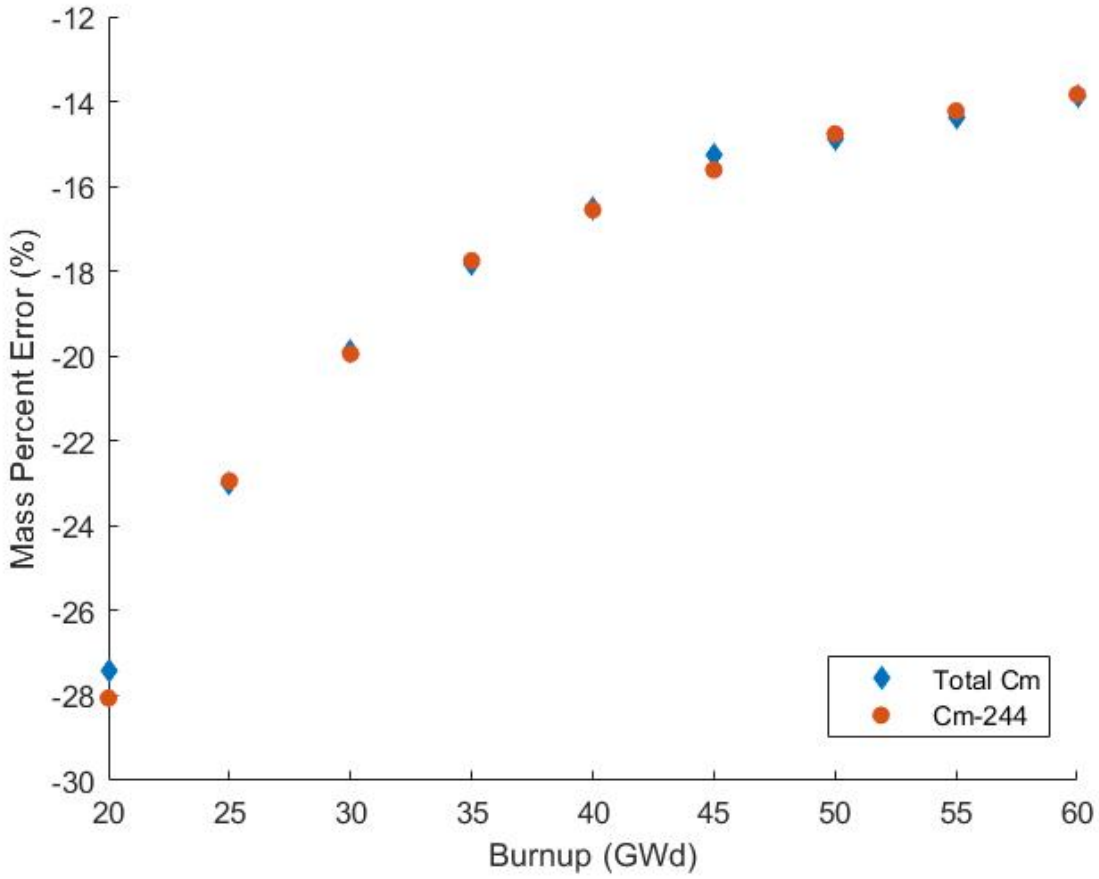


Figure 5.21: Percent error for Cm-244 and total curium mass estimation for a mixed sample.

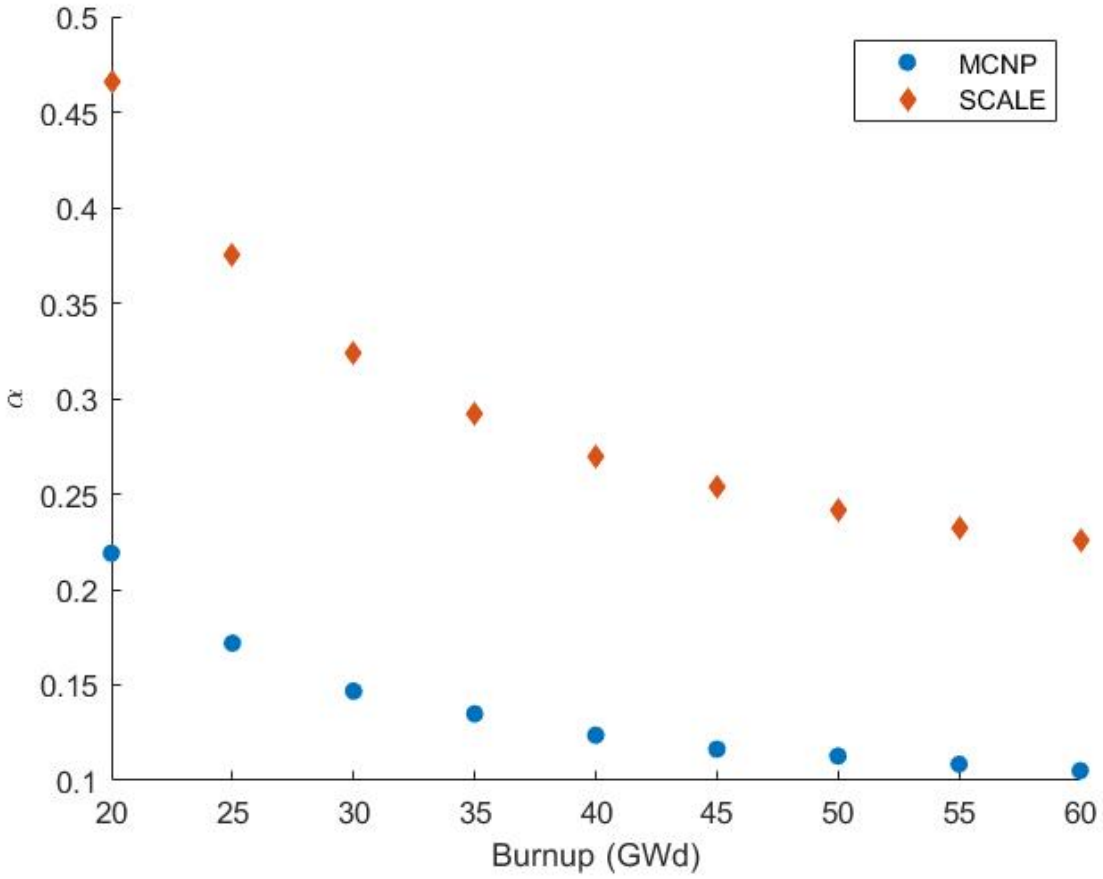


Figure 5.22: α variable comparison for SCALE emissions and estimates from the ENMC model for a mixed sample.

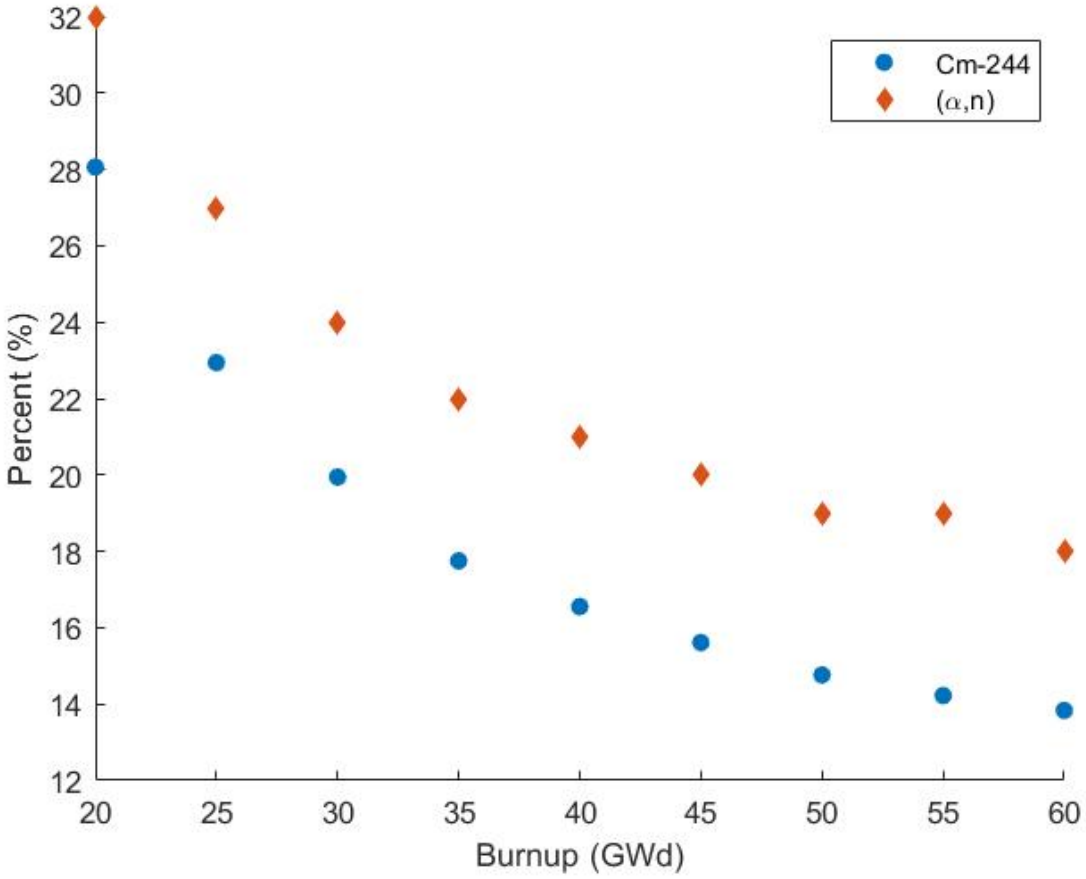


Figure 5.23: Comparison between Cm-244 mass percent error and total (α,n) contribution to neutron yield.

5.5.5 Estimation with Varying Enrichment

The trends shown thus far were also examined for the single 20 GWd case with its five enrichment values to provide more insight on how enrichment may effect the (α,n) yield and mass calculation. For all enrichments, the sample contained plutonium, curium, and eutecic salt. Figure 5.24 shows the comparison between the simulated and actual ^{244}Cm mass. Here the mass decreases as a function of enrichment and the simulated value is greater than the actual mass. This is to be expected as from the previous analysis there is a large accidental coincidence regarding the spontaneous fission signature. The associated error, seen in Figure 5.25, shows that as as enrichment increases the mass percent error becomes larger. This is explained by the trend that as enrichment increases overall curium mass decreases. Thus, the spontaneous fission contribution decreases as a whole and the accidental coincidence of (α,n) neutrons holds more weight yielding a larger error.

The α variable increases with increasing enrichment as seen in Figure 5.27. This increase can be explained by the lower spontaneous fission yield associated with a lower curium mass. Again, the simulated α variable is lower than the actual one obtained from Scale. Finally, the plot comparing the (α,n) contribution to that of the ^{244}Cm mass percent error shows a similar trend as explored from the previous analysis. Figure 5.27 demonstrated that each percentage increases with increasing enrichment.

5.5.6 Plutonium Mass Estimation

Once the curium mass was calculated and the α variable examined (Eq. 4.49) was used to calculate the plutonium mass for each of the nine main sequence samples. Figure 5.28 shows

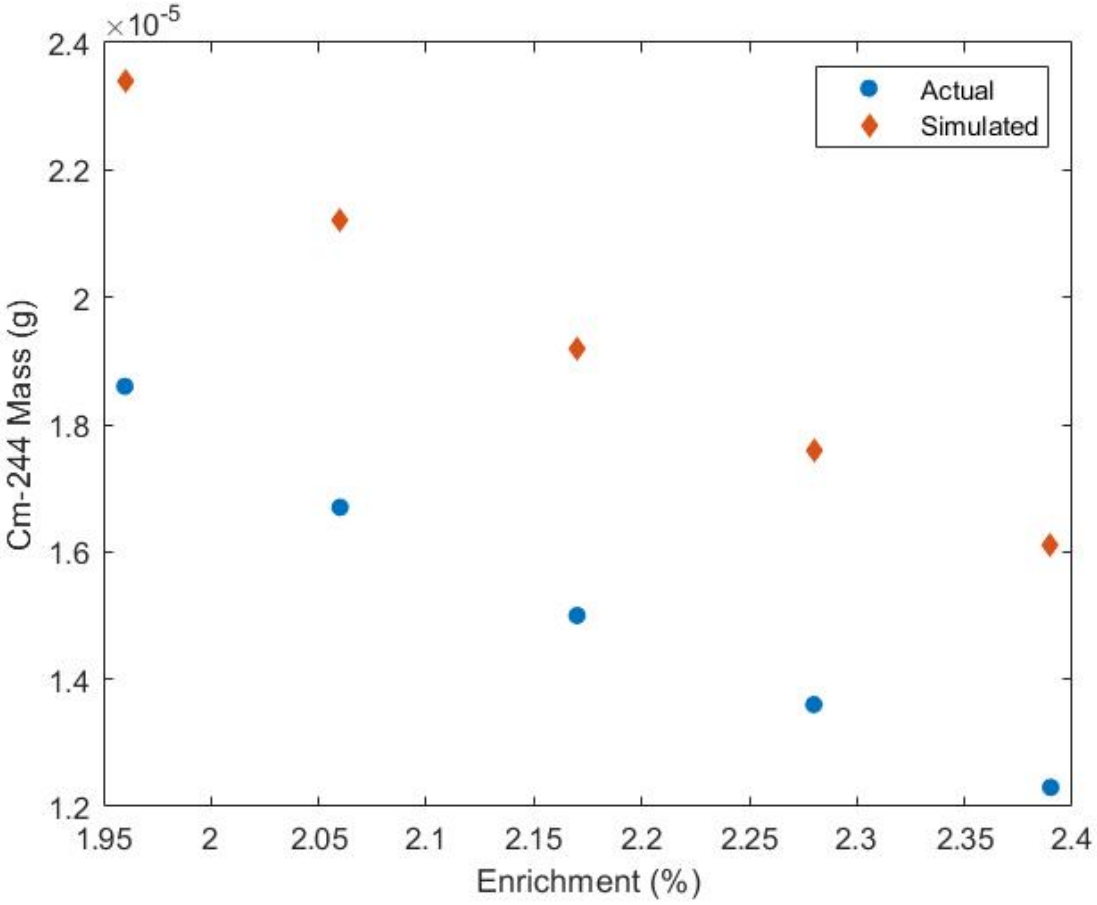


Figure 5.24: Comparison between simulated mass and actual mass of Cm-244 for a mixed sample.

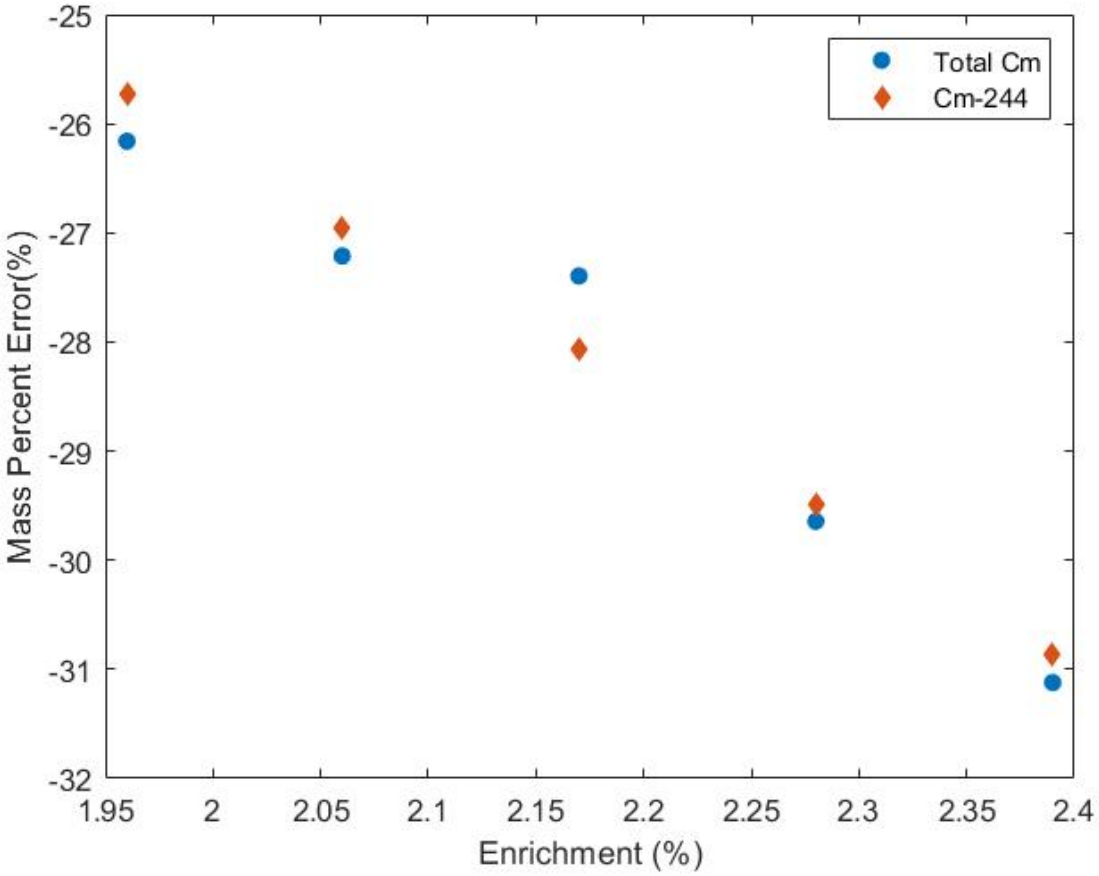


Figure 5.25: Percent error for Cm-244 mass estimation for a mixed sample.

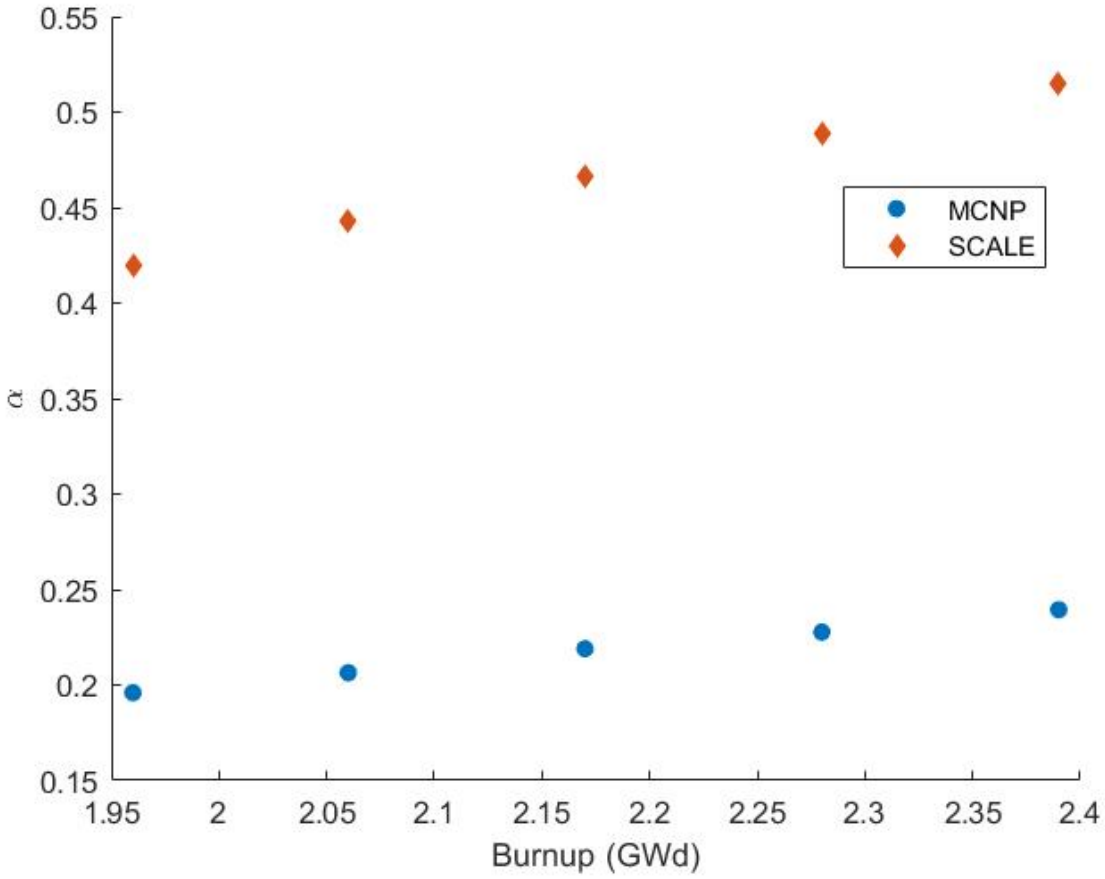


Figure 5.26: α variable comparison for SCALE emissions and estimates from the ENMC model for a mixed sample.

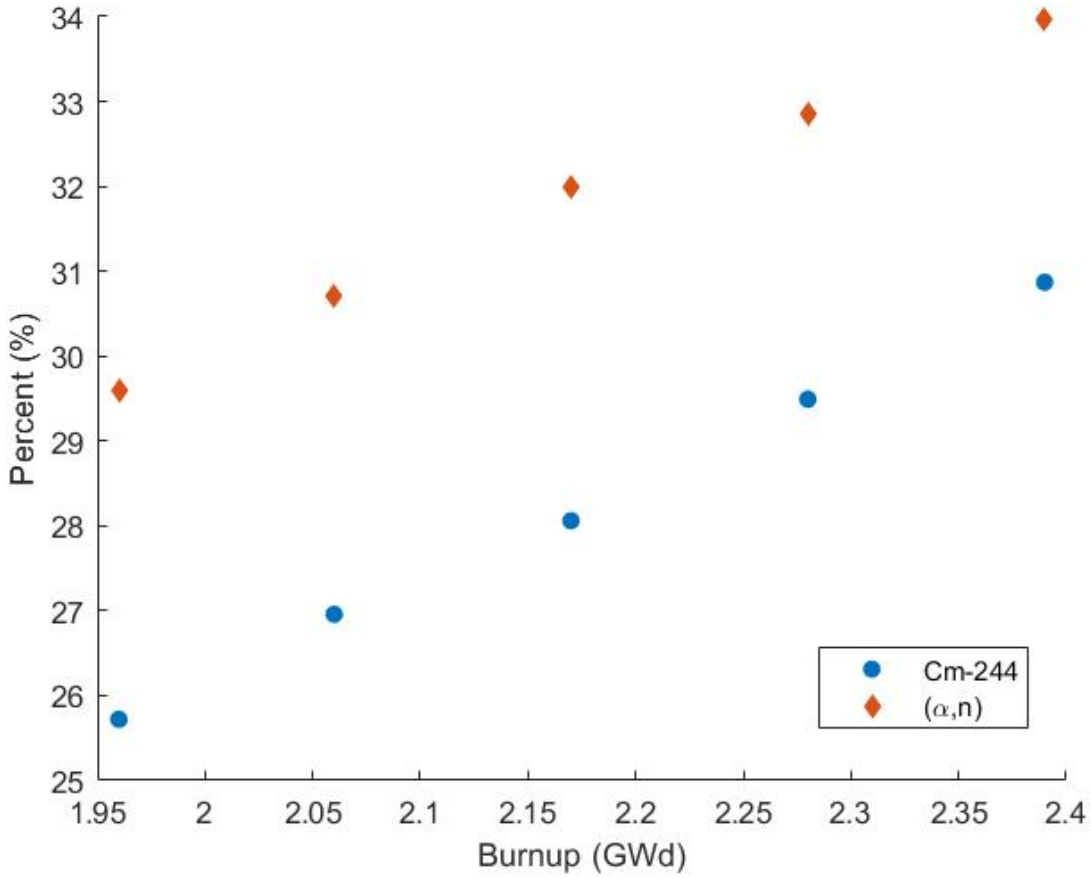


Figure 5.27: Comparison between Cm-244 mass percent error and total (α,n) contribution to neutron yield.

the simulated result compared to the actual plutonium mass of each sample. Starting at the 35 GWd sample and beyond the calculated mass is negative. Those samples that do possess positive mass estimates are well under the actual plutonium mass. The mass difference is so great the range exhibited in Figure 5.29 ranges from 60-170%. This large error can be attributed to the error associated in calculating the ^{244}Cm mass and the α variable. This also explains the negative calculated plutonium mass cases. For these instances the error from ^{244}Cm and α carry through the calculations and end with a negative mass calculated.

To attempt to correct for some of the error a correction factor was calculated using the MCNP and SCALE α variables. Here, the MCNP α variable used for this correction comes from (Eq. 2.15). This factor examines the ratio between the MCNP α variable to that obtained from SCALE. This will allow a correction in the α variable resulting in only the error associated with the curium mass calculation to effect the plutonium mass. Figure 5.30 shows the correction factor ratio as a function of burnup for each of the nine main sequence cases. Each case has a correction factor given for each of its five enrichment values. The range across all cases is a ratio of 0.453 to 0.469 with the solid blue line representing the average over the entire range at a value of 0.464. It is recommended that when implementing the correction factor to calculate the plutonium, the average ratio per burnup is used. To show the optimal results possible the factor associated with the specific burnup/enrichment case was used which yielded an instance of using the exact α variable obtained from SCALE. The correction factor results as well as results for a proof of concept case labeled are seen in Figure 5.31. The exact α and curium mass were used for the ideal case. Thus, the ideal case demonstrates the efficacy of (Eq. 4.49) using the actual α and curium mass in the sample. Here, a drastic change is seen as the calculated masses are no longer negative and both follow

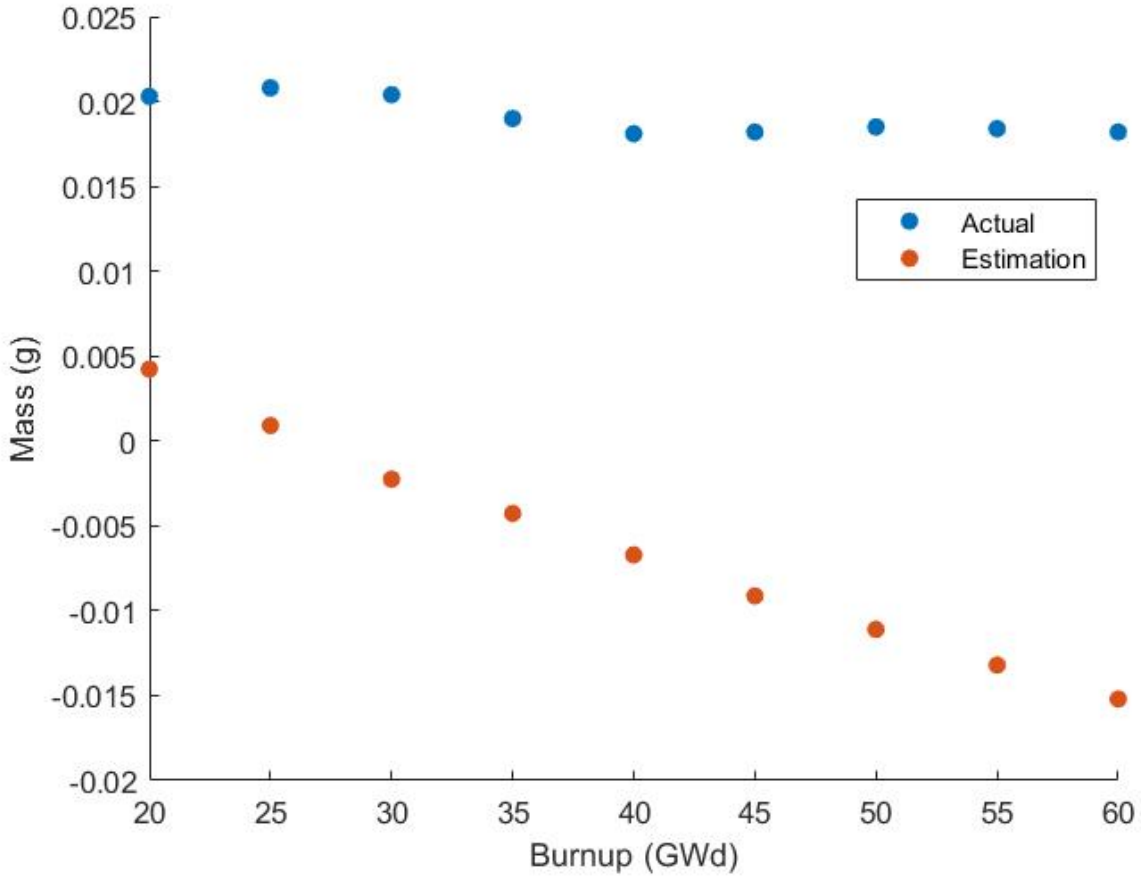


Figure 5.28: Comparison between simulated mass and actual mass of plutonium for a mixed sample.

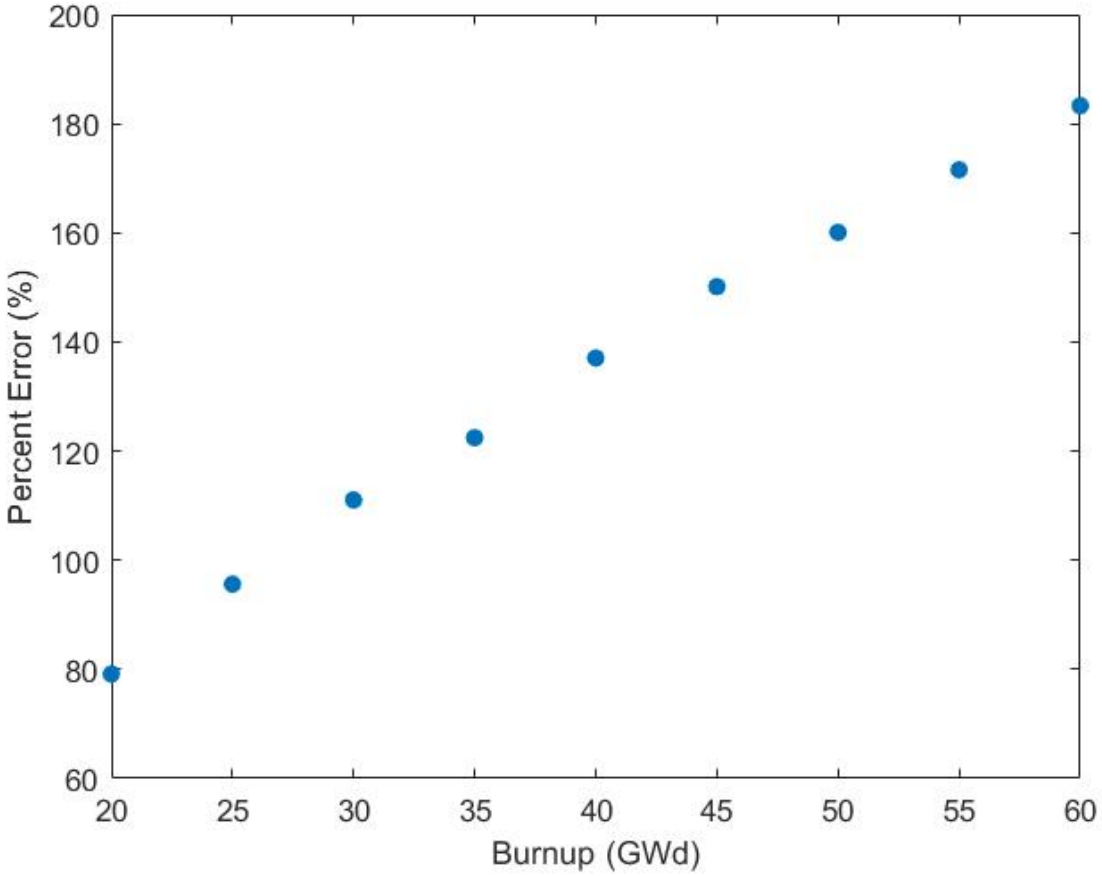


Figure 5.29: Percent error for plutonium mass estimation for a mixed sample.

the general trend of the actual mass. The correction factor mass is greater than the actual mass due to it still having error associated with the curium calculation. The ideal mass matches the actual mass to demonstrate the efficacy of this method.

The percent error for the correction factor and ideal cases is shown in Figure 5.32. Here it is seen that the error for the correction factor cases matches that of the percent error for the curium mass. This stands to reason as the only error present in the calculation is that of the curium mass calculation.

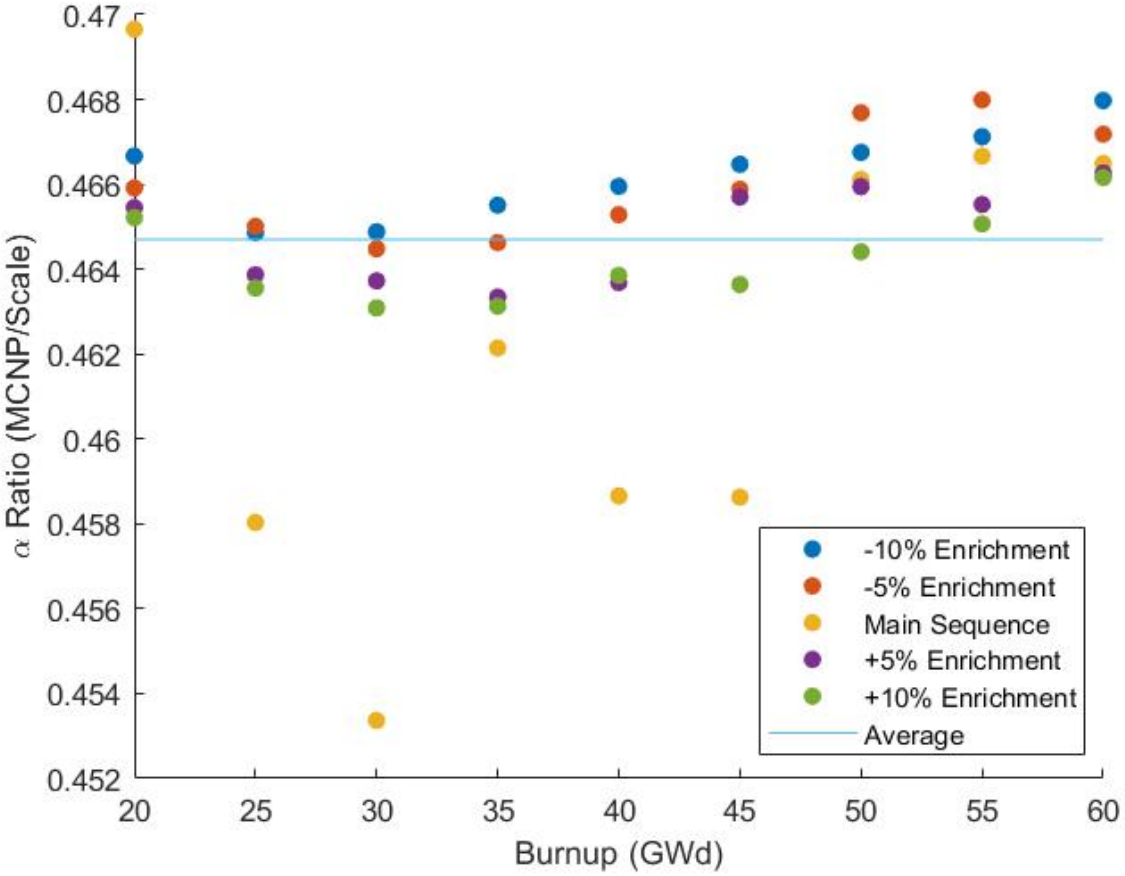


Figure 5.30: α variable correction factor.

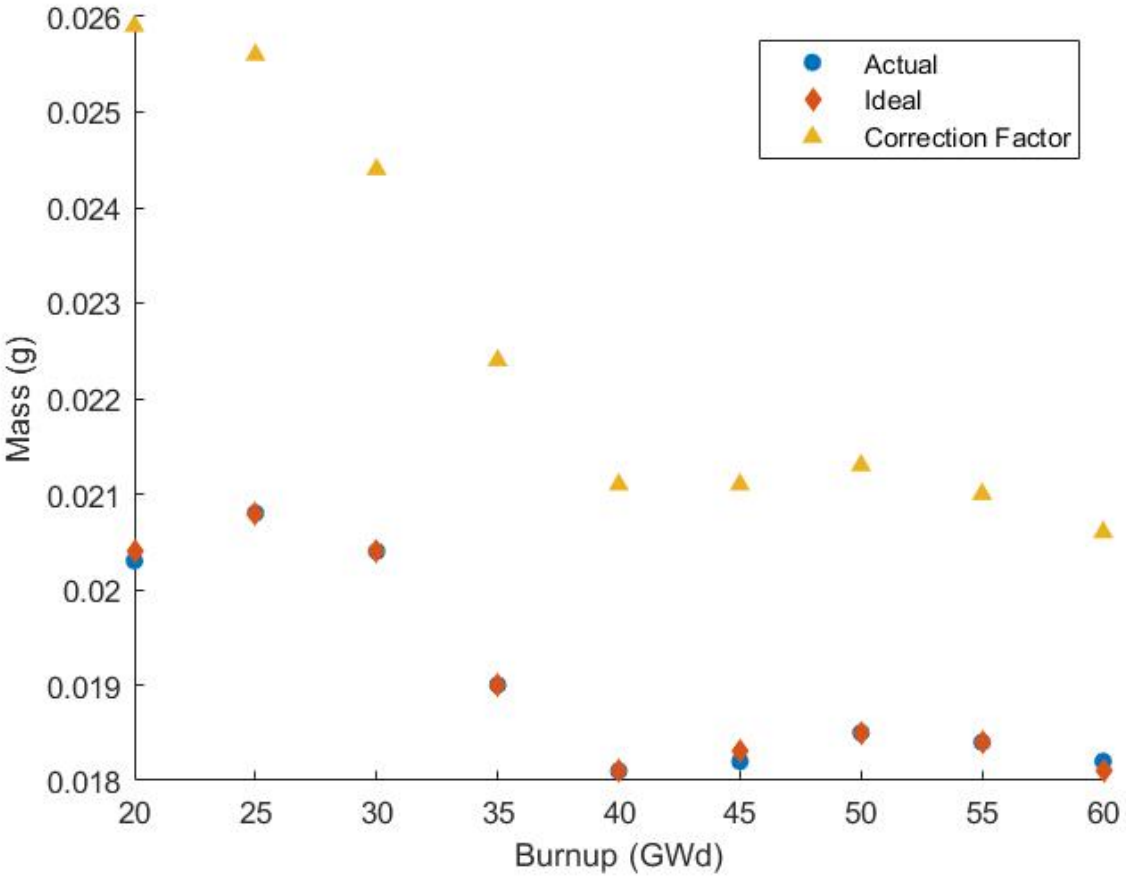


Figure 5.31: Comparison between simulated mass and actual mass of plutonium for a mixed sample under ideal circumstances.

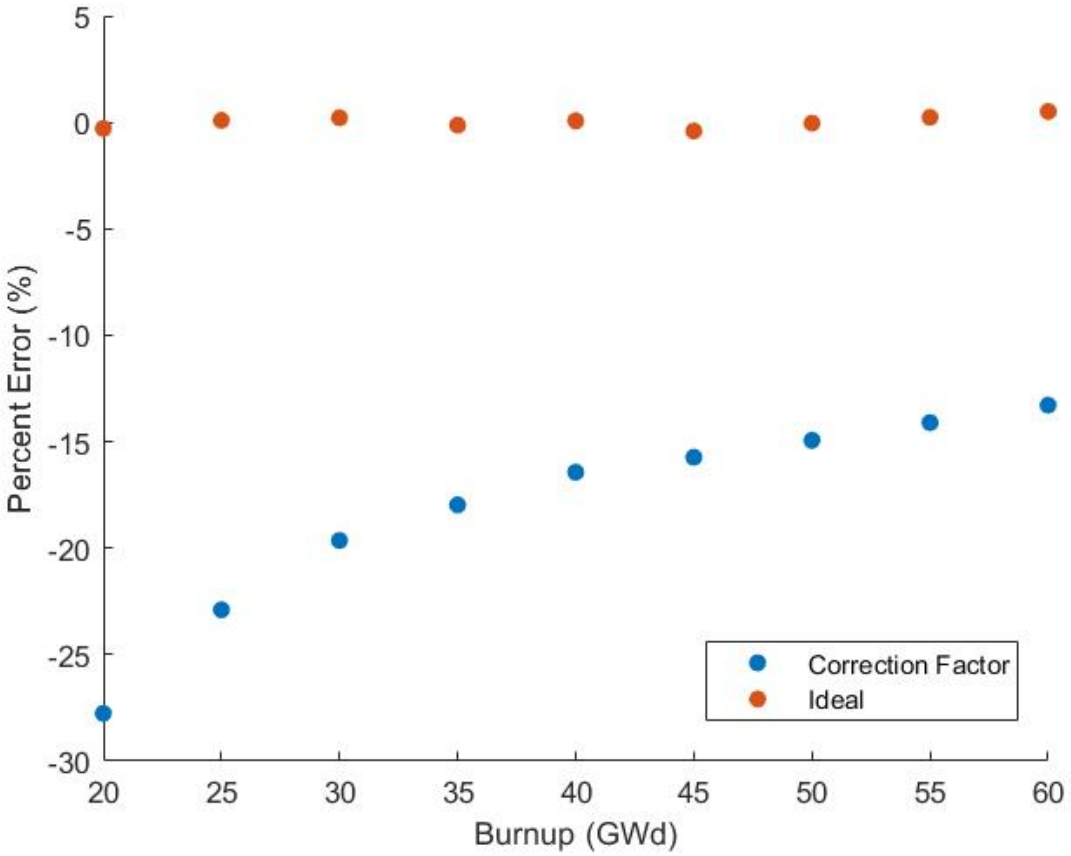


Figure 5.32: Percent error for the corrected and ideal plutonium mass estimation for a mixed sample.

Chapter 6

Conclusion

Safeguards applications are of vital importance when it comes to reprocessing facilities where material is a target for hostile adversaries. Especially in relatively new systems, such as electrochemical reprocessing, adequate measures must be in place to prevent the diversion of material. When it comes to neutron counting, research has been and continues to be done at the end ingot product by means of spontaneous fission tracking. However, no previous research had examined sampling from the electrorefiner unit and the efficacy of the (α,n) signature produced within. Thus, the (α,n) signature was examined through MCNP simulation across multiple burnup and enrichment combinations and it was determined that the emission yield was of much greater magnitude than seen in aqueous reprocessing. Next, the isolation of the (α,n) signature was attempted using an ENMC to calculate the plutonium mass at the electrorefiner. A preexisting Simulink model was used to obtain and scale down fuel mass for sample compositions for the detector and then the curium mass was calculated using multiplicity counting equations. From there, the α variable describing the ratio between (α,n) to spontaneous fission neutrons was deconstructed into its source

components to isolate the plutonium mass. It was seen that great error occurred during the calculation of curium due to the coincidence of (α,n) neutrons. This then carried over into the plutonium mass calculations and resulted in extreme error. Therefore, resulting methods described in the literature above are not recommended for current practical use to estimate the plutonium content when it comes to mixed samples containing eutectic salt. A correction factor was applied to reduce associated error arising from the α variable and gave an error range of 28-13%. Although this is not ideal it demonstrates that if the error associated with the accidental coincidence can be addressed, this method may be viable for calculating plutonium.

6.1 Recommendations and Future Work

The first issue to address is the accidental counts associated with calculating the ^{244}Cm mass. This would involve either altering an existing neutron counting instrument or the development of a new design to better discriminate between (α,n) and spontaneous fission neutrons. One avenue is to take advantage of the natural energy distribution difference between spontaneous fission and (α,n) neutrons. Performing measurements to isolate these signatures and correlate each back to the respective sources might provide better accuracy. This is challenging when using multiplicity techniques as one of the major assumptions is both neutron reactions have the same energy spectrum due to the polyethelyne moderator thermalizing the neutrons. If this is able to be done then the error using the described method for calculating plutonium will mirror that of current implemented safeguards methods shown for the single elemental samples. Once error is reduced, the next step is to simulate the

process by adding ^{241}Am into the sample. This isotope is the third largest (α,n) contributor and is present within the electrorefiner. Thus, it is important to know how the higher (α,n) count contributed from this isotope will effect the steps taken in the analysis explained in this document. It is important to reduce the accidental coincidence first as it is theorized adding ^{241}Am to the mixture will only increase the error associated with such. Afterwards other constituents of the fuel can be added to give a more holistic view of the composition likely to be seen within the electrorefiner. With little to no more major (α,n) or spontaneous fission sources, however, adding the remaining fuel constituents likely won't effect the overall outcome. This is still important to aid in developing the procedure when sampling from the electrorefiner. Performing physical experiments and simulation focusing on the thermodynamic properties of the fuel will allow for a better understanding on the influence of where and when sampling should occur within the electrorefiner. Thus, combining this method with others such as cyclic voltammetry might provide more insight on the plutonium mass.

In adjacent to improving the developed technique, using it in conjunction with other preexisting neutron methods will allow for better proliferation diversity. PNAR is the recommended technique as it has been used on electrochemical mixed samples where curium and plutonium are both present at the ingot. It must be noted that due to the sources of error discussed, the results won't align exactly but could aid as a verification indicator for what is calculated at the electrorefiner. It is theorized that due to the high (α,n) yield produced at the electrorefiner PNAR wouldn't fair better for sampling at this location but has shown to produce better results on mixed samples when no salt is present. Examining the die-away time by means of DDA may prove useful to aid in discriminating the two neutron

reaction sources much like separating them out by energy could accomplish. Thus, DDA is another method that could compliment multiplicity sampling at the electrorefiner. However, it is not a technique that could currently be deployed there itself due to the high (α,n) yield interference.

Bibliography

[1] Bachmann, A., Coble, J., and Skutnik, S. (2018). Elemental and isotopic concentration tracking for electrochemical reprocessing safeguards. In *Advances in Nonproliferation Technology and Policy Conference 2018 (ANTPC 2018)*. 33

[2] Bean, R. (2010). Project report on development of a safeguards approach for pyroprocessing. *Idaho National Laboratory, INL/EXT-10-20057, Idaho Falls, ID, USA*. 1

[3] Benedict, R., Solbrig, C., Westphal, B., Johnson, T., Li, S., Marsden, K., and Goff, K. (2007). Pyroprocessing progress at idaho national laboratory. *Advanced Nuclear Fuel Cycles and Systems (GLOBAL 2007)*. 9

[4] Borrelli, R. (2013). Use of curium spontaneous fission neutrons for safeguardability of remotely-handled nuclear facilities: Fuel fabrication in pyroprocessing. *Nuclear Engineering and Design*, 260:64–77. 23, 24

[5] Briesmeister, J. F. (1986). Mcnp: a general monte carlo code for neutron and photon transport. version 3a. revision 2. Technical report, Los Alamos National Lab. 39

[6] Bucholz, J. (1982). Scale: a modular code system for performing standardized computer analyses for licensing evaluation. Technical report, Oak Ridge National Lab. 24, 35, 40

[7] Choi, E.-Y. and Jeong, S. M. (2015). Electrochemical processing of spent nuclear fuels: an overview of oxide reduction in pyroprocessing technology. *Progress in Natural Science: Materials International*, 25(6):572–582. 6

[8] Cipiti, B. B. (2010). Optimizing near real time accountability for reprocessing. Technical report, Sandia National Laboratories. xi, 32, 34

[9] Croft, S., Bourva, L.-A., Weaver, D., and Ottmar, H. (2001). ˆ 2ˆ 4ˆ 0pu effective mass ofˆ 2ˆ 3ˆ 8pu andˆ 2ˆ 4ˆ 2pu in relation to passive neutron coincidence and multiplicity counting. *Journal of Nuclear Materials Management*, pages 10–19. viii, 60

[10] Croft, S., Cleveland, S. L., and Nicholson, A. D. (2015). Calculation of the 240pu-effective coefficients for neutron correlation counting-inmm. Technical report, Oak Ridge National Lab.(ORNL), Oak Ridge, TN (United States). 57

[11] Croft, S., Swinhoe, M. T., and Henzl, V. (2011). A priori precision estimation for neutron triples counting. In *2011 2nd International Conference on Advancements in Nuclear Instrumentation, Measurement Methods and their Applications*, pages 1–7. IEEE. 55

[12] Cumberland, R. M. and Yim, M.-S. (2014). Development of a 1d transient electrorefiner model for pyroprocess simulation. *Annals of Nuclear Energy*, 71:52–59. 27

[13] Durst, P. C., Therios, I., Bean, R., Dougan, A., Boyer, B., Wallace, R., Ehinger, M., Kovacic, D., and Tolk, K. (2007). Advanced safeguards approaches for new reprocessing facilities. *Pacific Northwest National Laboratory. PNNL-16674. www. pnl. gov/main/publications/external/technical_reports/pnnl-16674. pdf.* 23

[14] Dytlewski, N., Krick, M., and Ensslin, N. (1993). Measurement variances in thermal neutron coincidence counting. *Nuclear Instruments and Methods in Physics Research Section A: Accelerators, Spectrometers, Detectors and Associated Equipment*, 327(2-3):469–479. 11

[15] Ensslin, N. et al. (1991). Principles of neutron coincidence counting. *Passive Nondestructive Assay of Nuclear Materials*, 550. xi, 12, 21

[Ensslin et al.] Ensslin, N., Krick, M., Geist, W., and Pickrell. Active neutron multiplicity counting. *Passive Nondestructive Assay of Nuclear Materials*. 15, 17

[17] Ensslin, N., Krick, M., Langner, D., Pickrell, M. M., Reilly, T., and Stewart, J. (2007). Passive neutron multiplicity counting. *Passive Nondestructive Assay of Nuclear Materials*, pages 6–20. viii, 11, 13, 14, 19, 20, 22, 53

[18] Favalli, A., Vo, D., Grogan, B., Jansson, P., Liljenfeldt, H., Mozin, V., Schwalbach, P., Sjöland, A., Tobin, S. J., Trellue, H., et al. (2016). Determining initial enrichment, burnup, and cooling time of pressurized-water-reactor spent fuel assemblies by analyzing passive gamma spectra measured at the clab interim-fuel storage facility in sweden. *Nuclear Instruments and Methods in Physics Research Section A: Accelerators, Spectrometers, Detectors and Associated Equipment*, 820:102–111. 33

[19] Gilliam, N., Coble, J., and Skutnik, S. (2018). (α, n) source terms as a novel signature for pyroprocessing safeguards. In *Advances in Nuclear Nonproliferation Technology and Policy Conference (ANTPC 2018)*. 2

[20] Goddard, B. (2013). *Quantitative NDA measurements of advanced reprocessing product materials containing uranium, neptunium, plutonium, and americium.* Texas A&M University. 26, 40, 72

[21] Goddard, B., Charlton, W., Gariazzo, C., and Peerani, P. (2011). A concept for quantitative nda measurements of advanced reprocessing product materials. In *Proceedings of GLOBAL*, pages 11–16. 39, 79

[22] Gonzalez, M., Hansen, L., Rappleye, D., Cumberland, R., and Simpson, M. (2015). Application of a one-dimensional transient electrorefiner model to predict partitioning of plutonium from curium in a pyrochemical spent fuel treatment process. *Nuclear Technology*, 192(2):165–171. 29

[23] Han, B.-Y., Shin, H., Ahn, S.-K., Eom, S.-H., and Kim, H.-D. (2011). A feasibility study on the measurement of mixed nuclear material composition by using fission neutron multiplicity distribution. *Journal of Korean Physical Society*, 59:1430–1433. 24

[24] Holden, N. E. and Hoffman, D. C. (1993). Spontaneous fission half-lives for ground state nuclides. Technical report, Brookhaven National Lab., Upton, NY (United States). viii, 60

[25] Kinoshita, K., Inoue, T., Fusselman, S., Grimmett, D., Roy, J., Gay, R., Krueger, C., Nabelek, C., and Storvick, T. (1999). Separation of uranium and transuranic elements from rare earth elements by means of multistage extraction in licl-kcl/bi system. *Journal of Nuclear Science and Technology*, 36(2):189–197. 27

[26] Langner, D., Krick, M., Parks, D., and Hooper, K. (1993). Thermal neutron multiplicity measurements using the pyrochemical multiplicity counter at lawrence livermore national laboratory. Technical report, Los Alamos National Lab. 19

[27] Langner, D. G., Sweet, M. R., Salazar, S. D., and Kroncke, K. E. (1998). Fb-line neutron multiplicity counter operation manual. Technical report, Los Alamos National Lab. 19

[28] Lee, K. (2008). Spent fuel management with pyroprocessing _the advantages of the pyroprocessing optioin from the perspective of waste management. *KAERI Nuclearancy*, 1(8). 26

[29] Lee, T.-H., Menlove, S., Menlove, H. O., Shin, H.-S., and Kim, H.-D. (2020). A direct nondestructive assay for the pu of u/tru ingot in pyroprocessing using 244cm neutron albedo reactivity technique and its error. *Nuclear Technology*, pages 1–9. 30

[30] Lestone, J. (2014). A comparison between two evaluations of neutron multiplicity distributions. *arXiv preprint arXiv:1410.2148*. 58

[31] Li, S. X., Johnson, T. A., Westphal, B. R., Goff, K. M., and Benedict, R. W. (2005). Electrorefining experience for pyrochemical reprocessing of spent ebr-ii driver fuel. Technical report, Idaho National Laboratory (INL). 72, 75

[32] Martinik, T. (2016). *Development of Differential Die-Away Instrument for Characterization of Swedish Spent Nuclear Fuel*. PhD thesis, Uppsala University. 30

[33] Menlove, H. (1991). Neutron coincidence instruments and applications. 18

[34] Miura, N. and Menlove, H. (1994). The use of curium neutrons to verify plutonium in spent fuel and reprocessing wastes. Technical report, Los Alamos National Lab. viii, 23, 24, 25, 26

[35] Osipenko, A., Mayershin, A., Smolenski, V., Novoselova, A., and Kormilitsyn, M. (2012). Electrochemistry of curium in molten chlorides. In *Recent Trend in Electrochemical Science and Technology*. InTech. 27

[36] Pickrell, M., Veal, K., and Ensslin, N. (2007). Fast and epithermal neutron multiplicity counters. In *Passive Nondestructive Assay of Nuclear Materials 2007 Addendum*. Los Alamos National Laboratory Los Alamos, NM. 18, 20

[Rinard] Rinard, P. M. 9. shufflers phillip m. rinard. 15

[38] Salanne, M., Simon, C., Turq, P., and Madden, P. A. (2008). Calculation of activities of ions in molten salts with potential application to the pyroprocessing of nuclear waste. *The Journal of Physical Chemistry B*, 112(4):1177–1183. xi, 7, 10

[39] Tobin, S. J., Sandoval, N. P., Fensin, M. L., Lee, S. Y., Ludewigt, B. A., Menlovea, H., Quiter, B., Rajasingume, A., Schearf, M., Smith, L., et al. (2010). Determination of plutonium content in spent fuel with nondestructive assay. 24

[40] Toda, T., Maruyama, T., Moritani, K., Moriyama, H., and Hayashi, H. (2009). Thermodynamic properties of lanthanides and actinides for reductive extraction of minor actinides. *Journal of nuclear science and technology*, 46(1):18–25. 26, 27

[41] Williamson, M. and Willit, J. (2011). Pyroprocessing flowsheets for recycling used nuclear fuel. *Nuclear Engineering and Technology*, 43(4):329–334. 1, 4, 6, 7, 9, 11

[42] Wilson, W. B., Perry, R. T., Charlton, W., Parish, T., and Shores, E. (2005). Sources: a code for calculating (α, n), spontaneous fission, and delayed neutron sources and spectra. *Radiation protection dosimetry*, 115(1-4):117–121. xi, 37, 41, 49

[43] Woo, S. M., Chirayath, S. S., and Fratoni, M. (2018). Nuclide composition non-uniformity in used nuclear fuel for considerations in pyroprocessing safeguards. *Nuclear Engineering and Technology*. 26

[44] Yoo, J.-H., Seo, C.-S., Kim, E.-H., and Lee, H.-S. (2008). A conceptual study of pyroprocessing for recovering actinides from spent oxide fuels. *Nuclear Engineering and Technology*, 40(7):581–592. viii, xi, 6, 8, 9, 27, 31

[45] Zhou, W. (2017). *Integrated Model Development for Safeguarding Pyroprocessing Facility*. PhD thesis, The Ohio State University. xi, 4, 5, 9

Appendices

A Appendix A

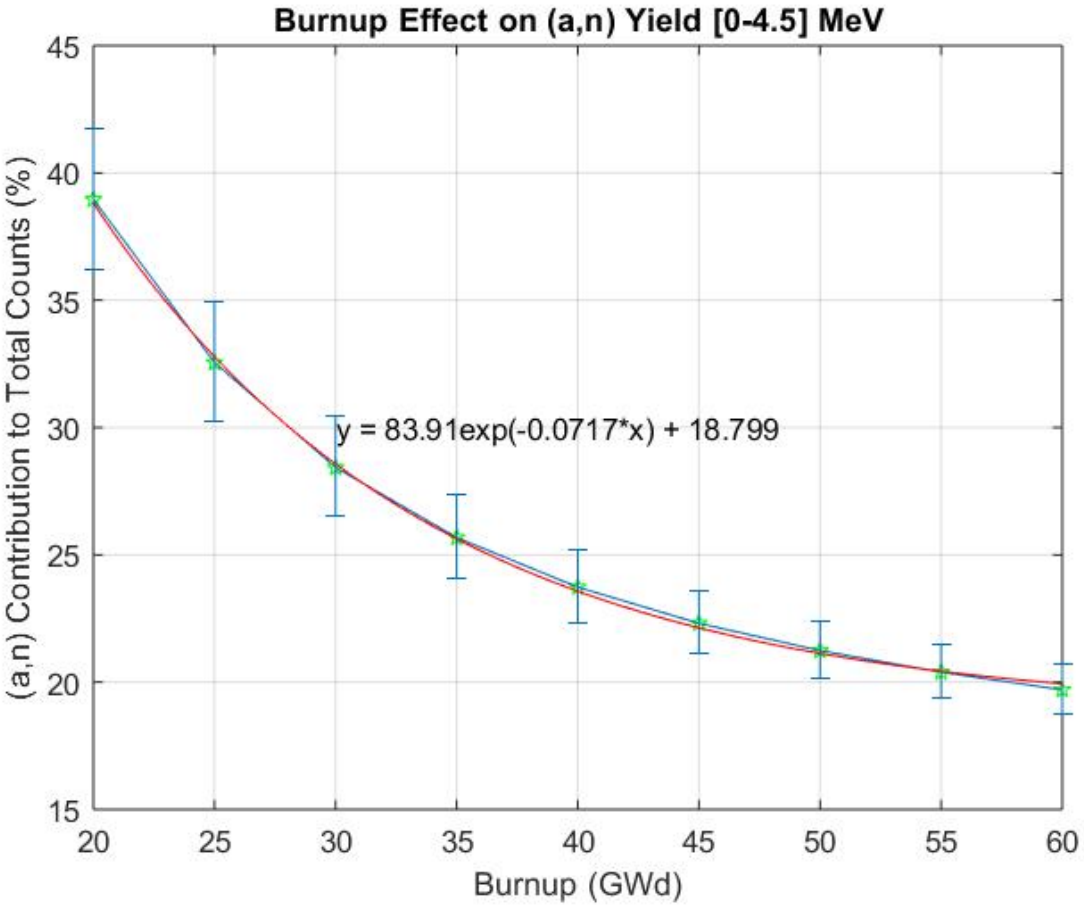


Figure A.1: Empirical relationship of the ratio of (α,n) to total emission rate as a function of burnup from 0-4.5 MeV with a cooling time of 5 years.

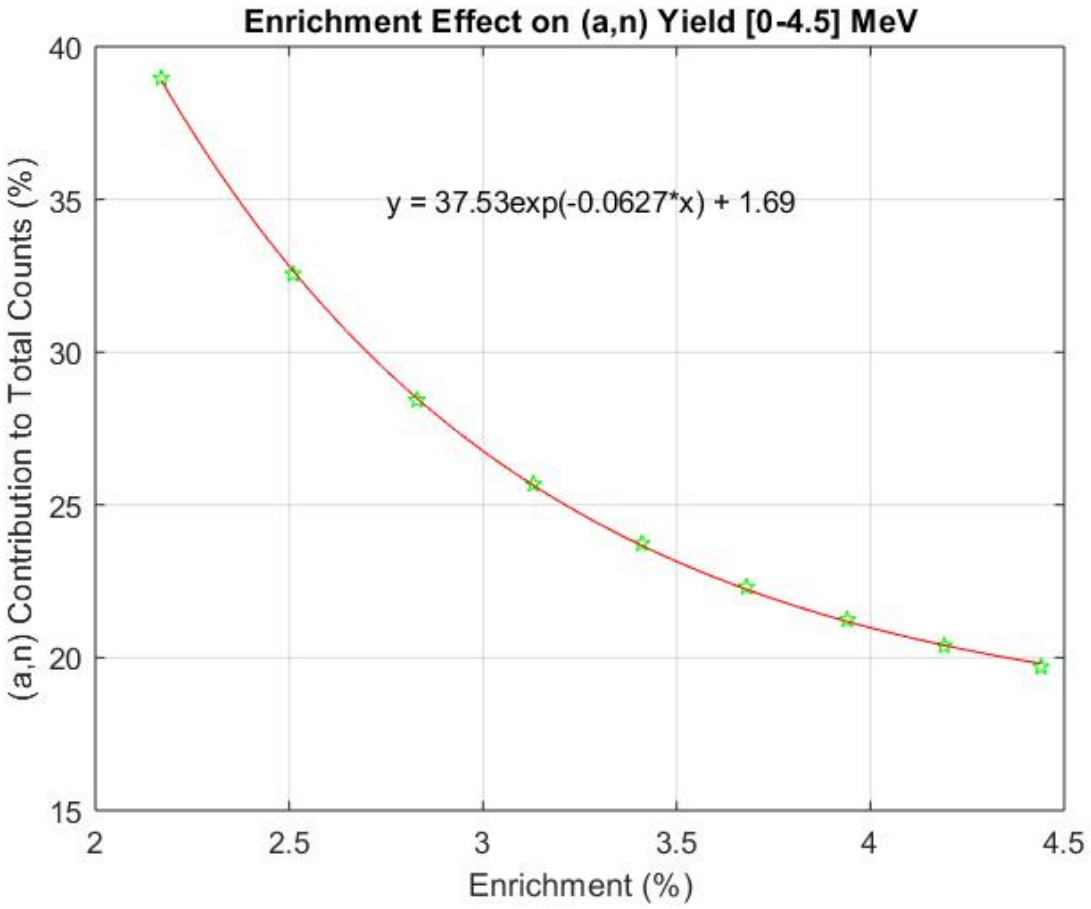


Figure A.2: Empirical relationship of the ratio of (α,n) to total emission rate as a function of enrichment from 0-4.5 MeV with a cooling time of 5 years.

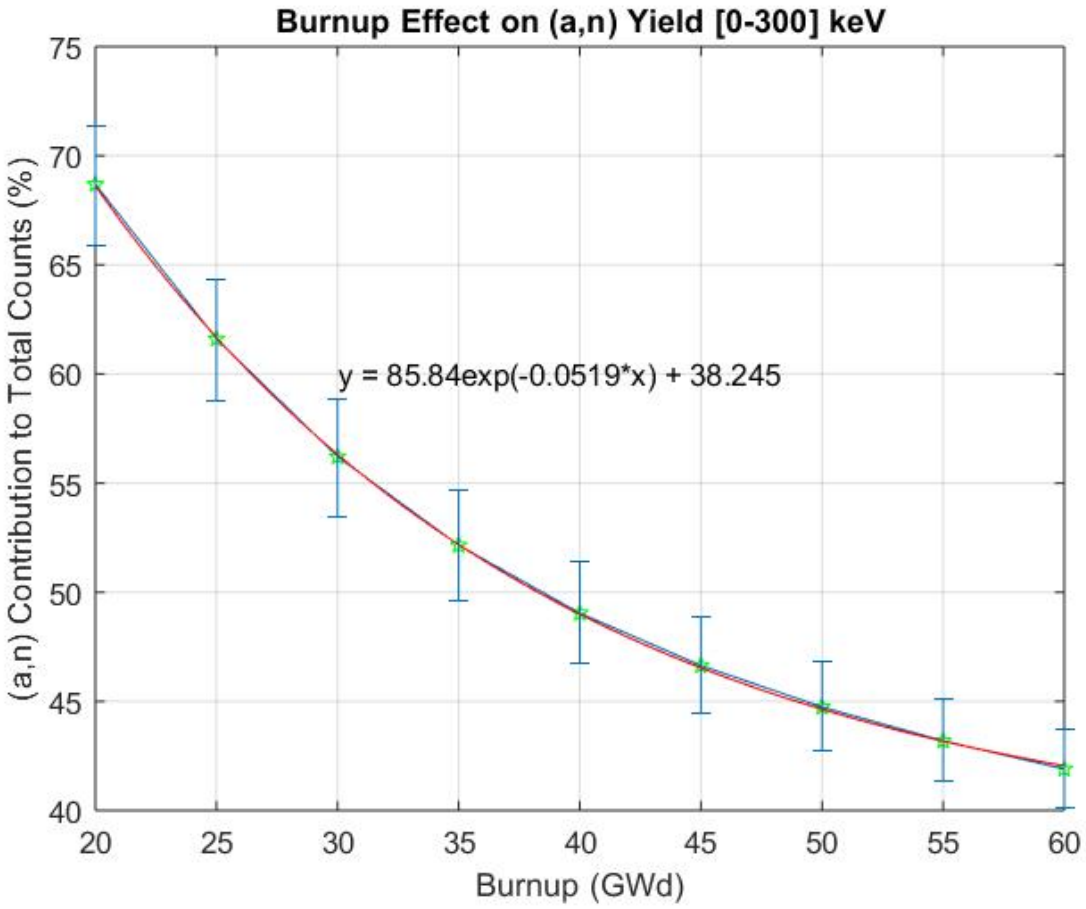


Figure A.3: Emprical relationship of the ratio of (α,n) to total emission rate as a function of burnup from 0-300 keV with a cooling time of 5 years.

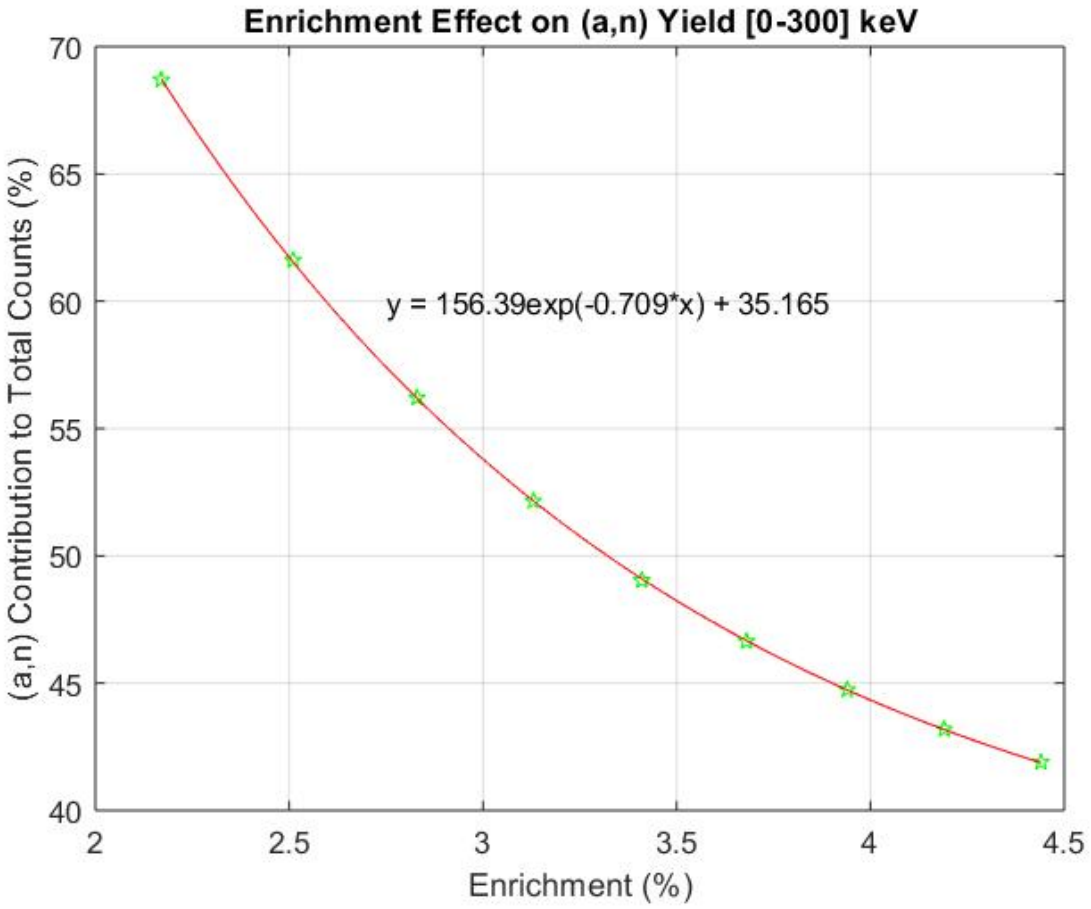


Figure A.4: Empirical relationship of the ratio of (α,n) to total emission rate as a function of enrichment from 0-300 keV with a cooling time of 5 years.

B Appendix B

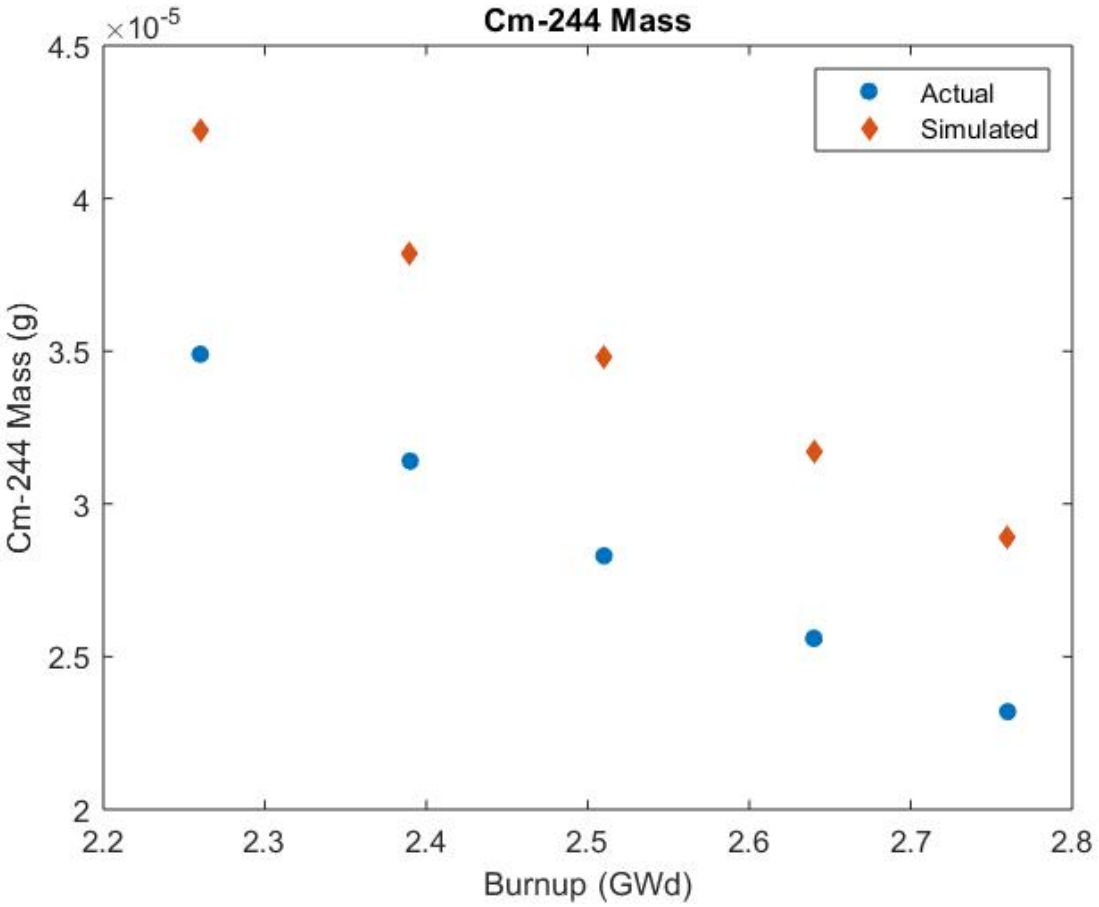


Figure B.1: Comparison between simulated mass and actual mass of Cm-244 for a 25 GWd mixed sample.

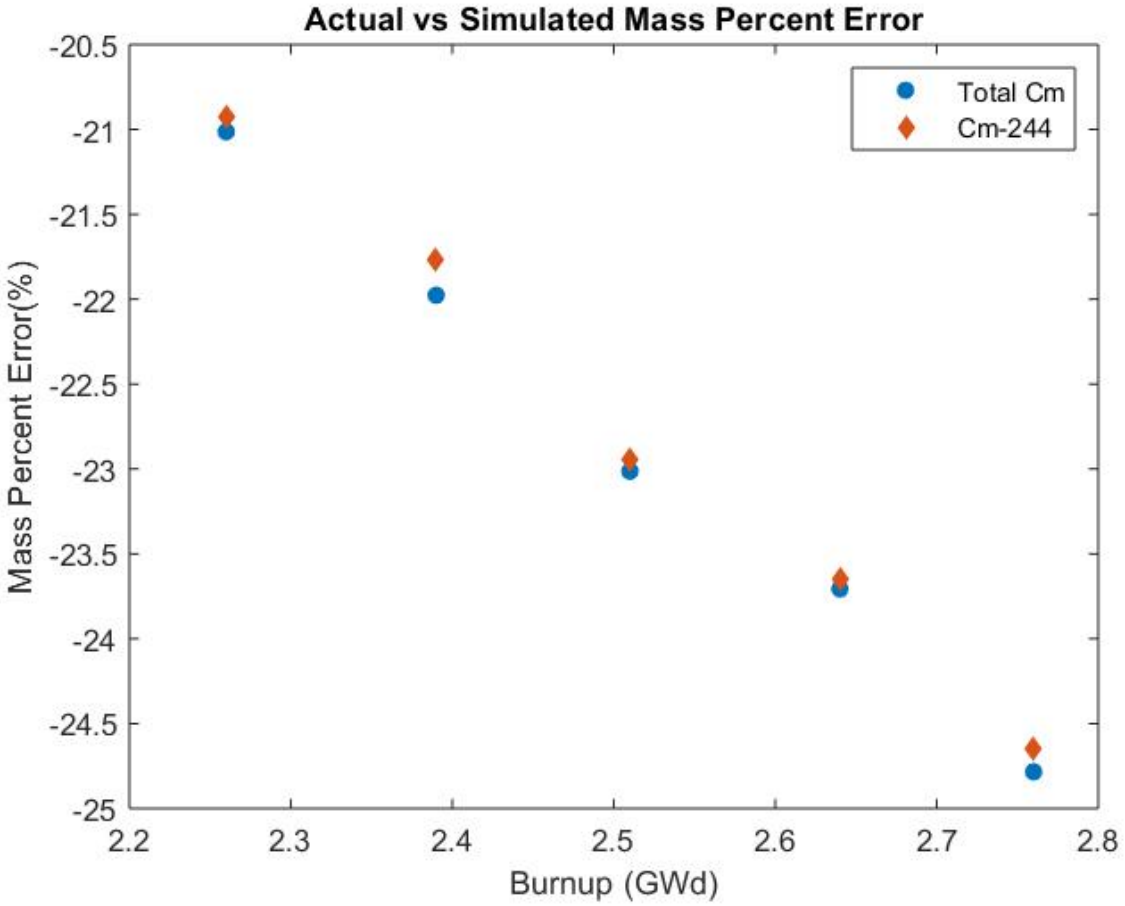


Figure B.2: Percent error for Cm-244 mass estimation for a 25 GWd mixed sample.

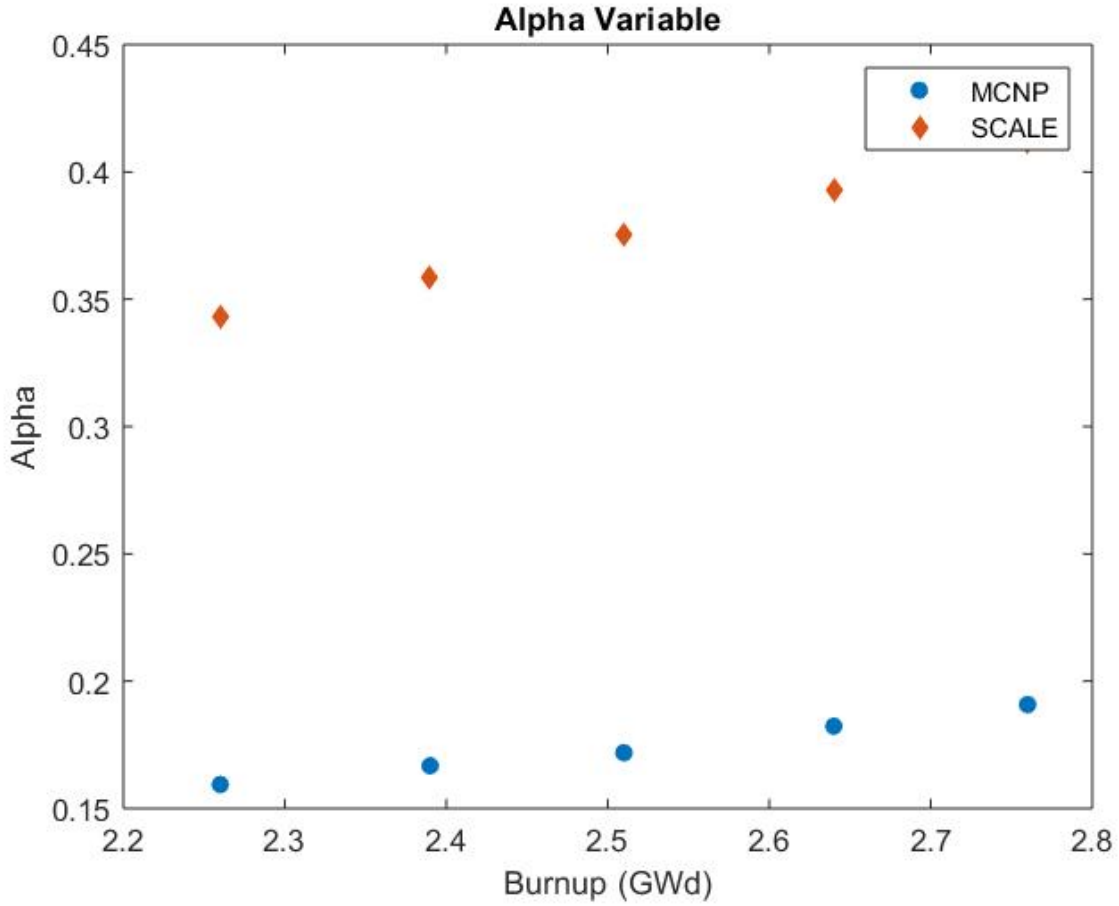


Figure B.3: Alpha variable comparison for a 25 GWd mixed sample.

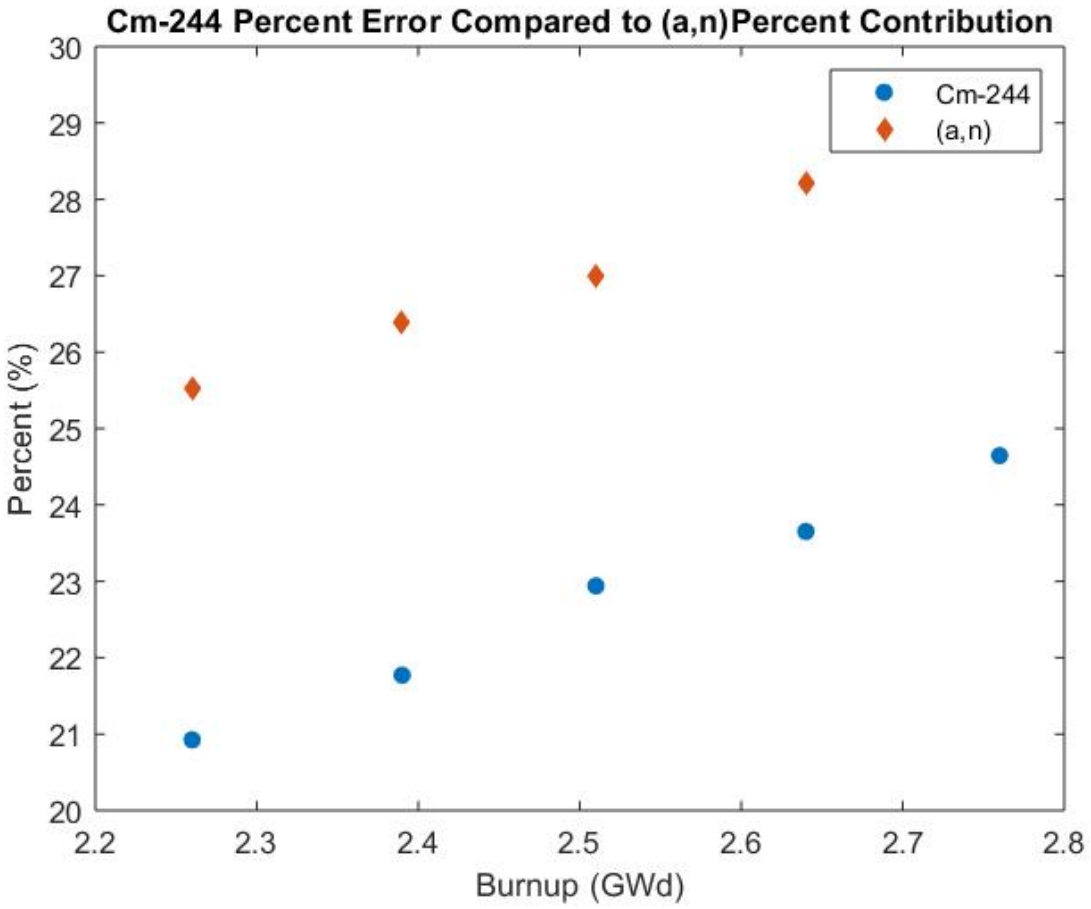


Figure B.4: Comparison for 25 GWd between Cm-244 mass percent error and total (α,n) contribution to neutron yield.

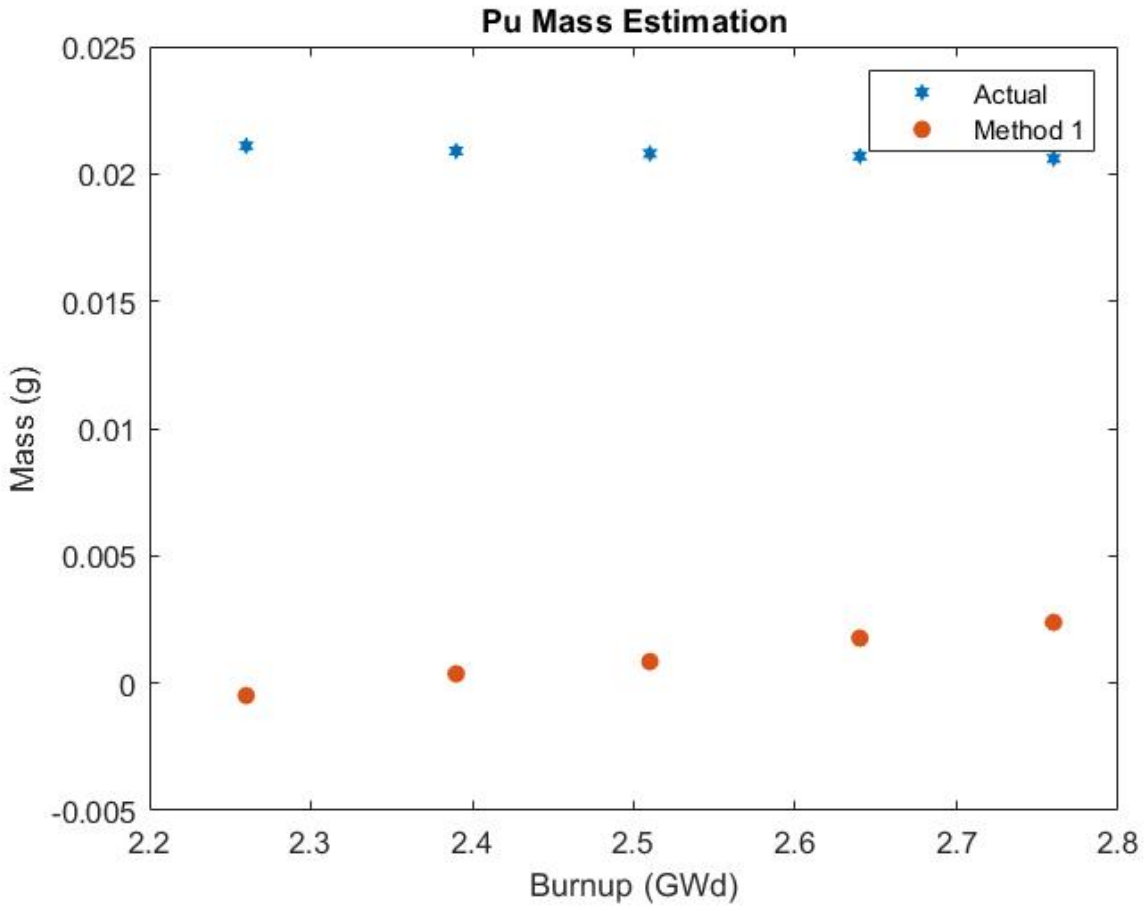


Figure B.5: Comparison between simulated mass and actual mass of plutonium for a 25 GWd mixed sample.

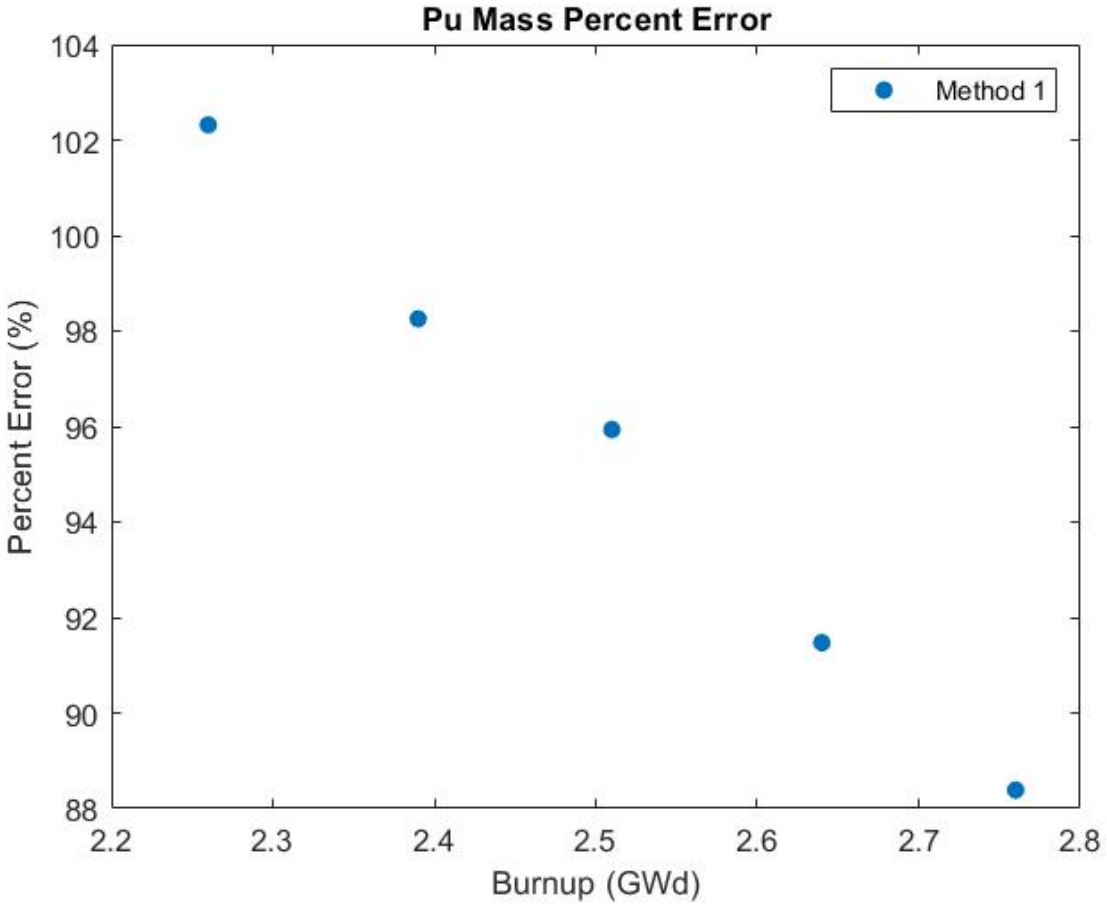


Figure B.6: Percent error for plutonium mass estimation for a 25 GWd mixed sample.

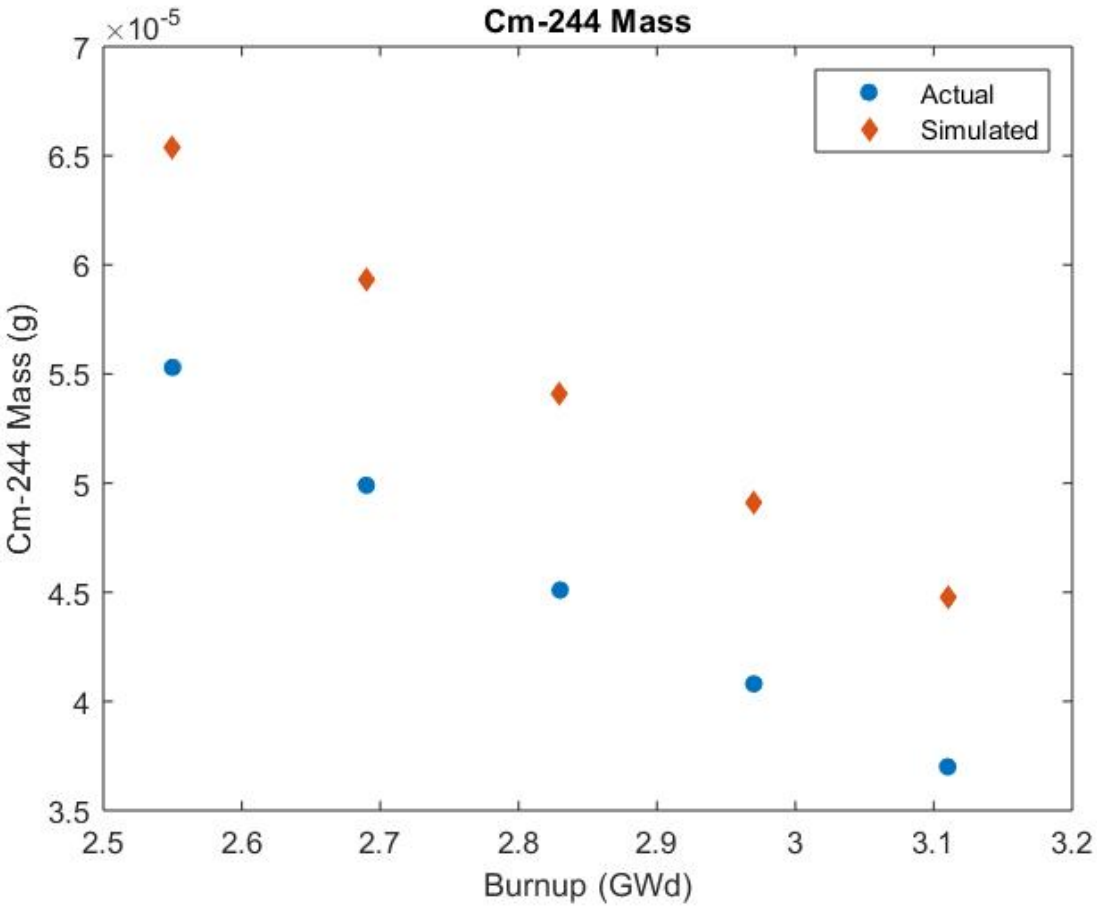


Figure B.7: Comparison between simulated mass and actual mass of Cm-244 for a 30 GWd mixed sample.

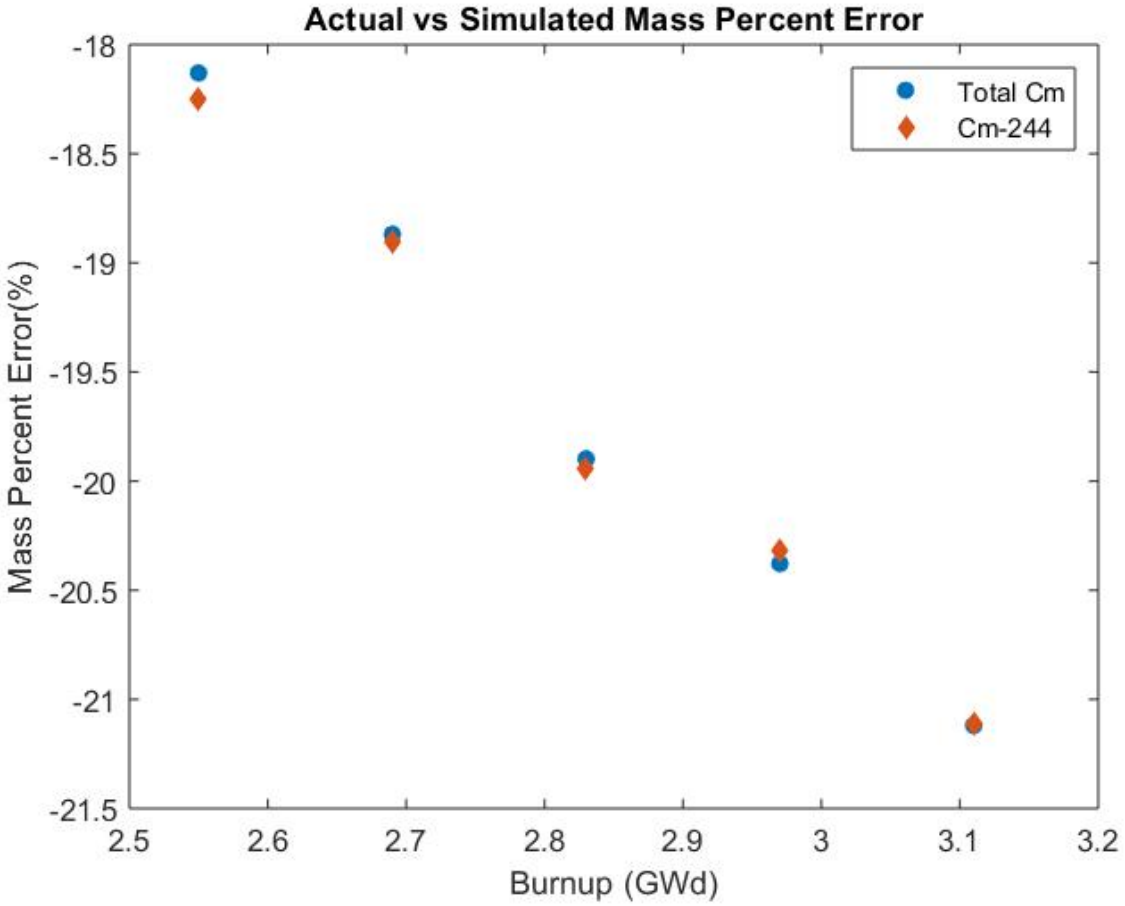


Figure B.8: Percent error for Cm-244 mass estimation for a 30 GWd mixed sample.

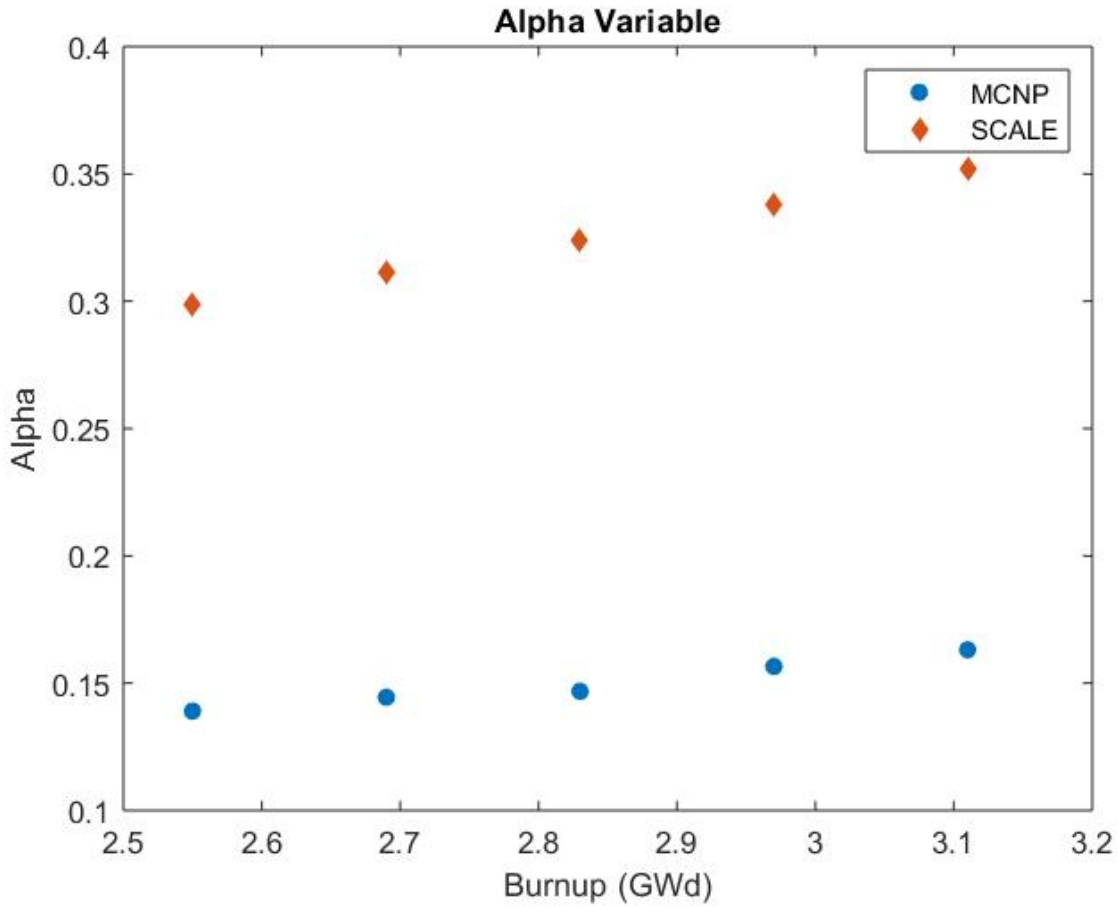


Figure B.9: Alpha variable comparison for a 30 GWd mixed sample.

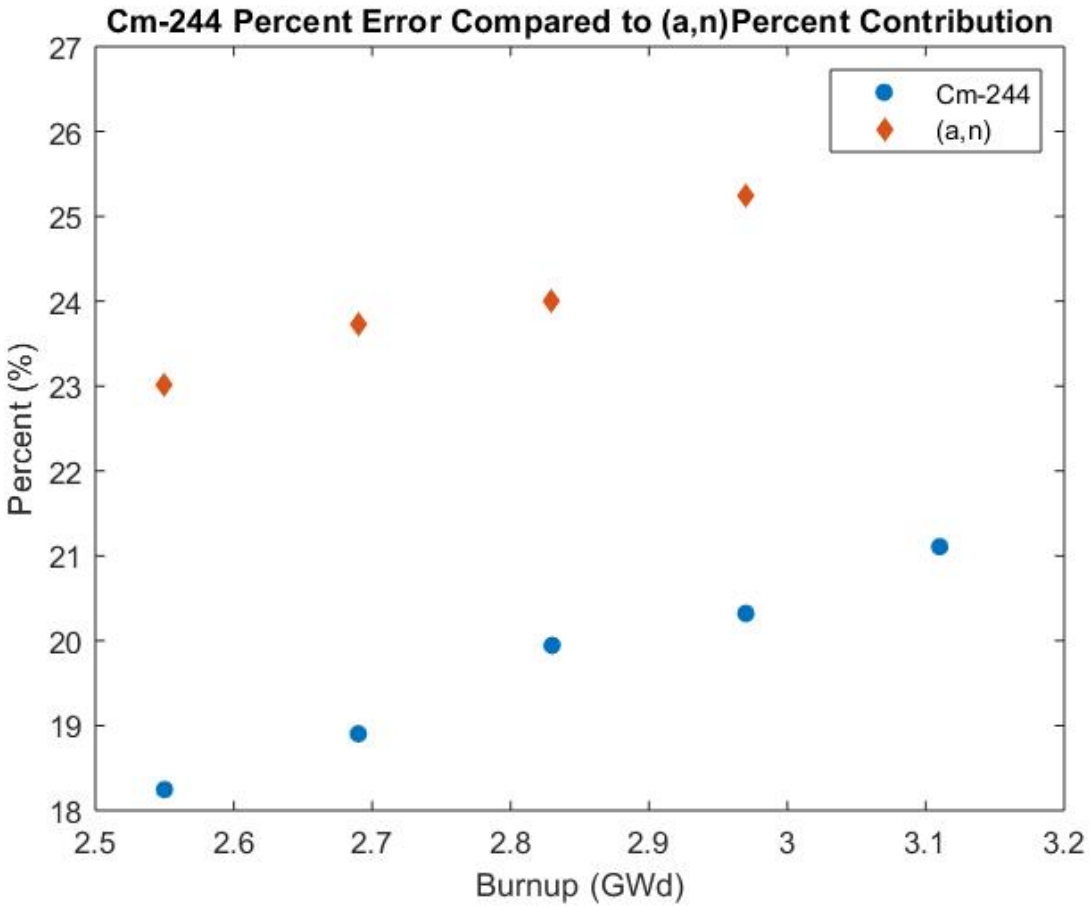


Figure B.10: Comparison for 30 GWd between Cm-244 mass percent error and total (α,n) contribution to neutron yield.

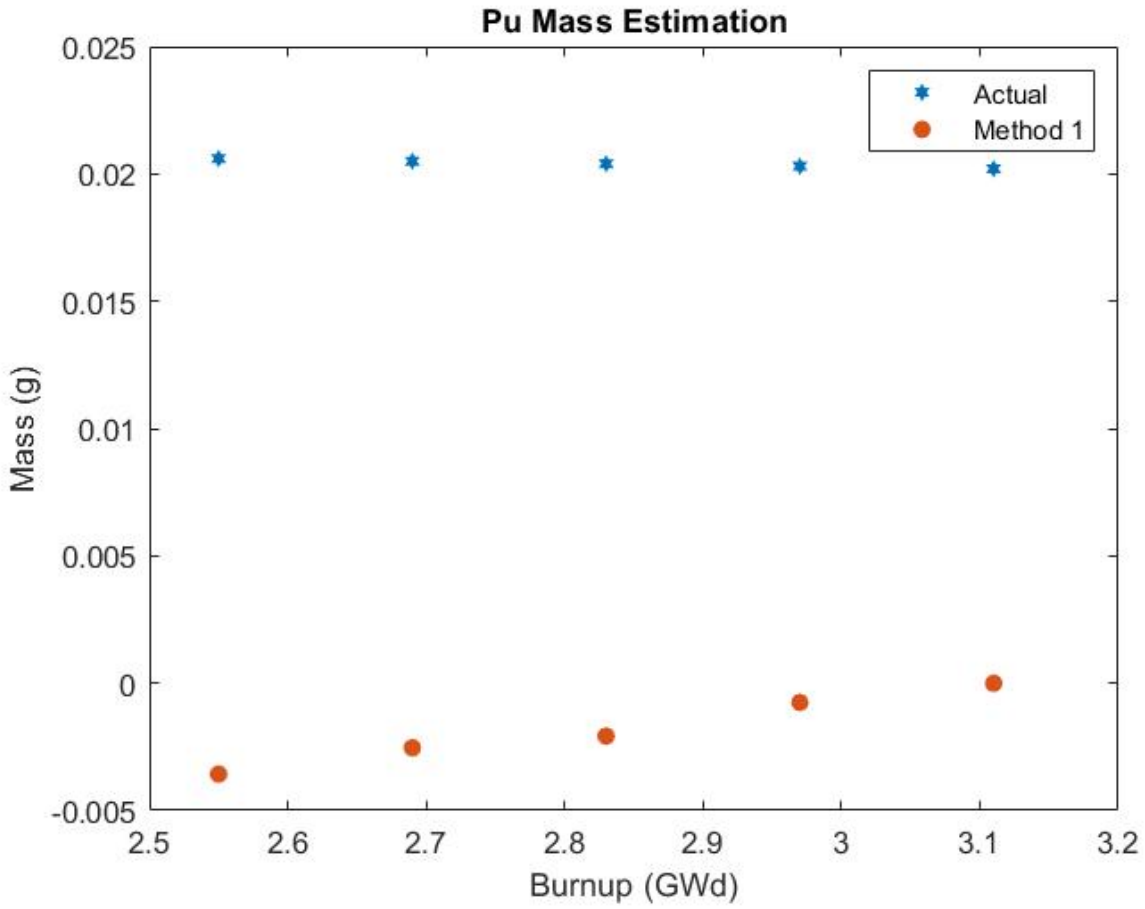


Figure B.11: Comparison between simulated mass and actual mass of plutonium for a 30 GWd mixed sample.

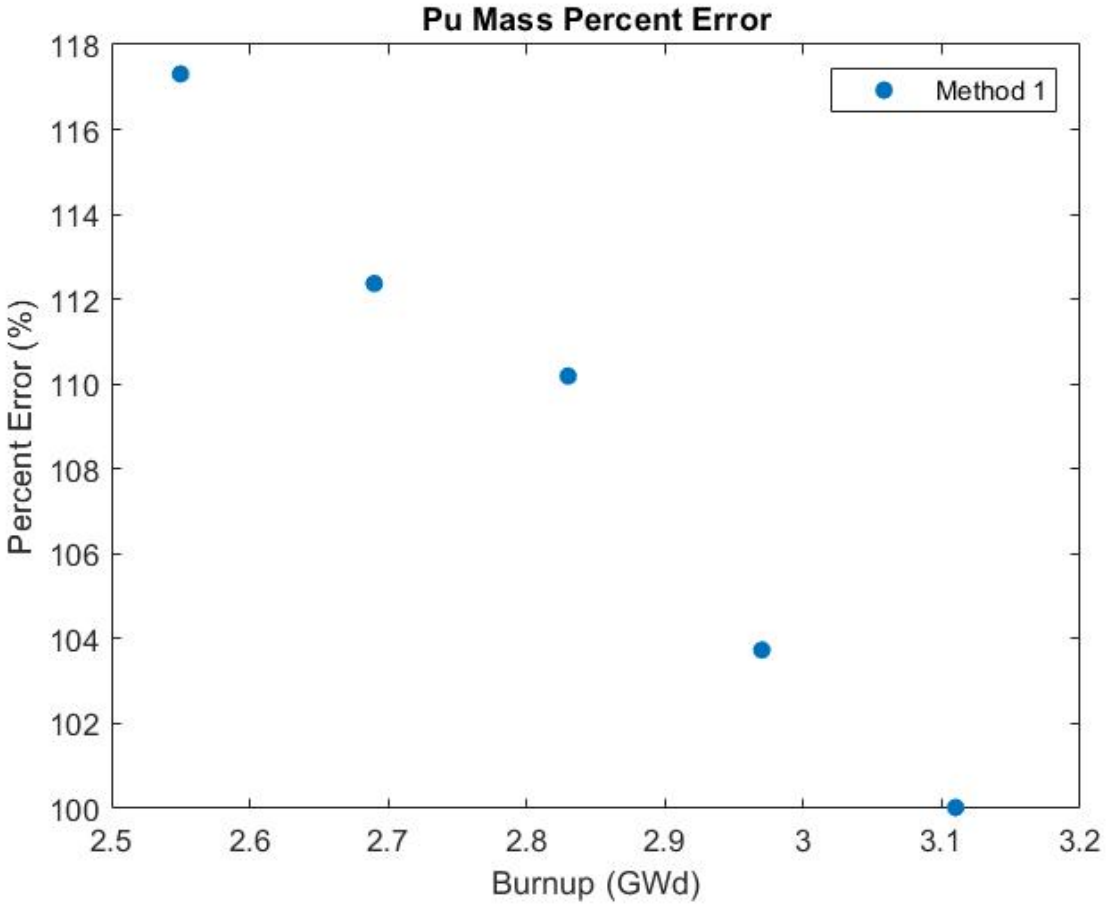


Figure B.12: Percent error for plutonium mass estimation for a 30 GWd mixed sample.

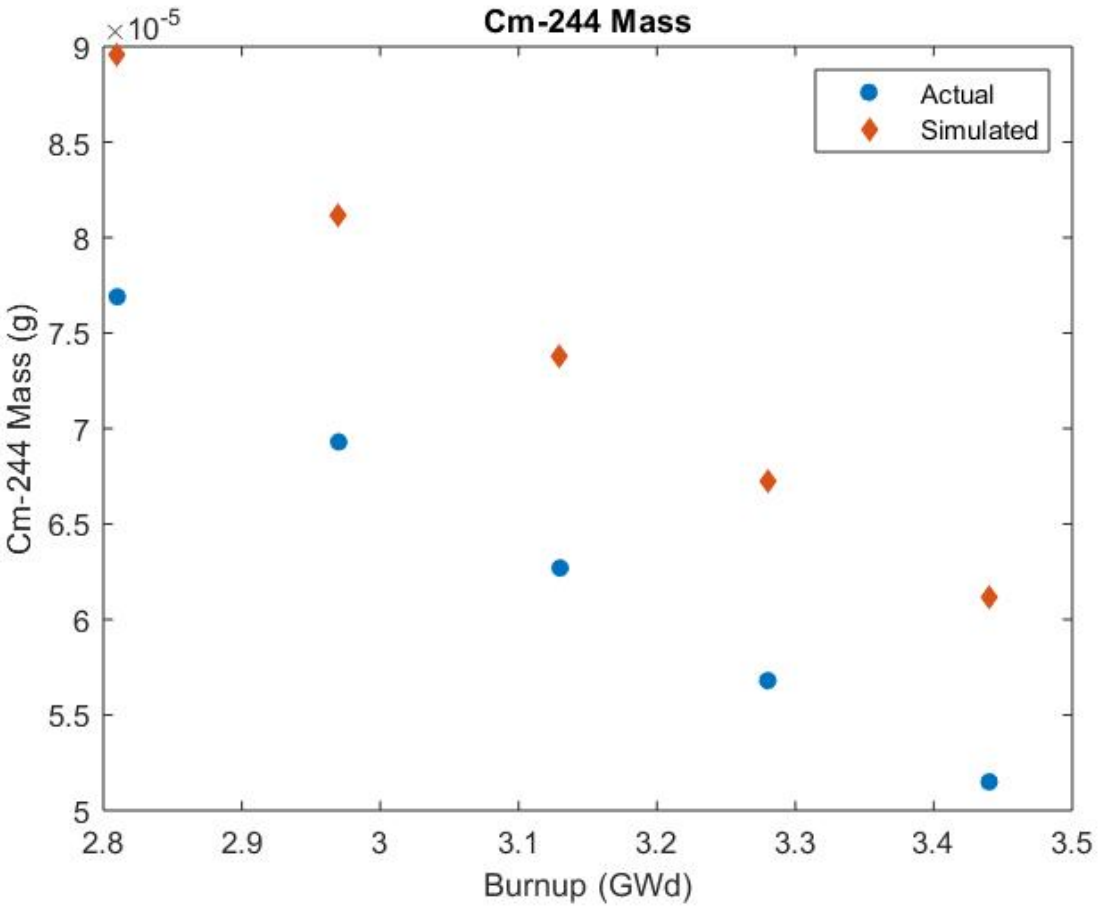


Figure B.13: Comparison between simulated mass and actual mass of Cm-244 for a 35 GWd mixed sample.

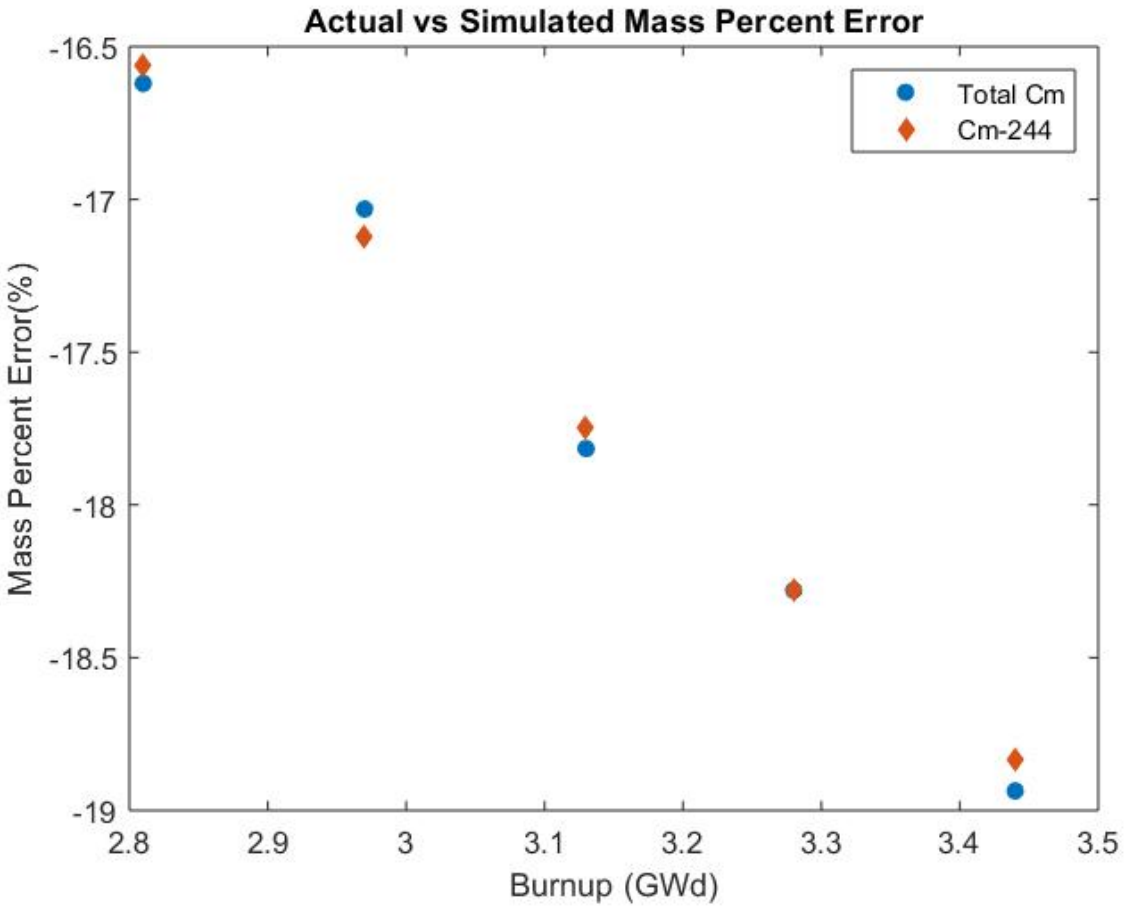


Figure B.14: Percent error for Cm-244 mass estimation for a 35 GWd mixed sample.

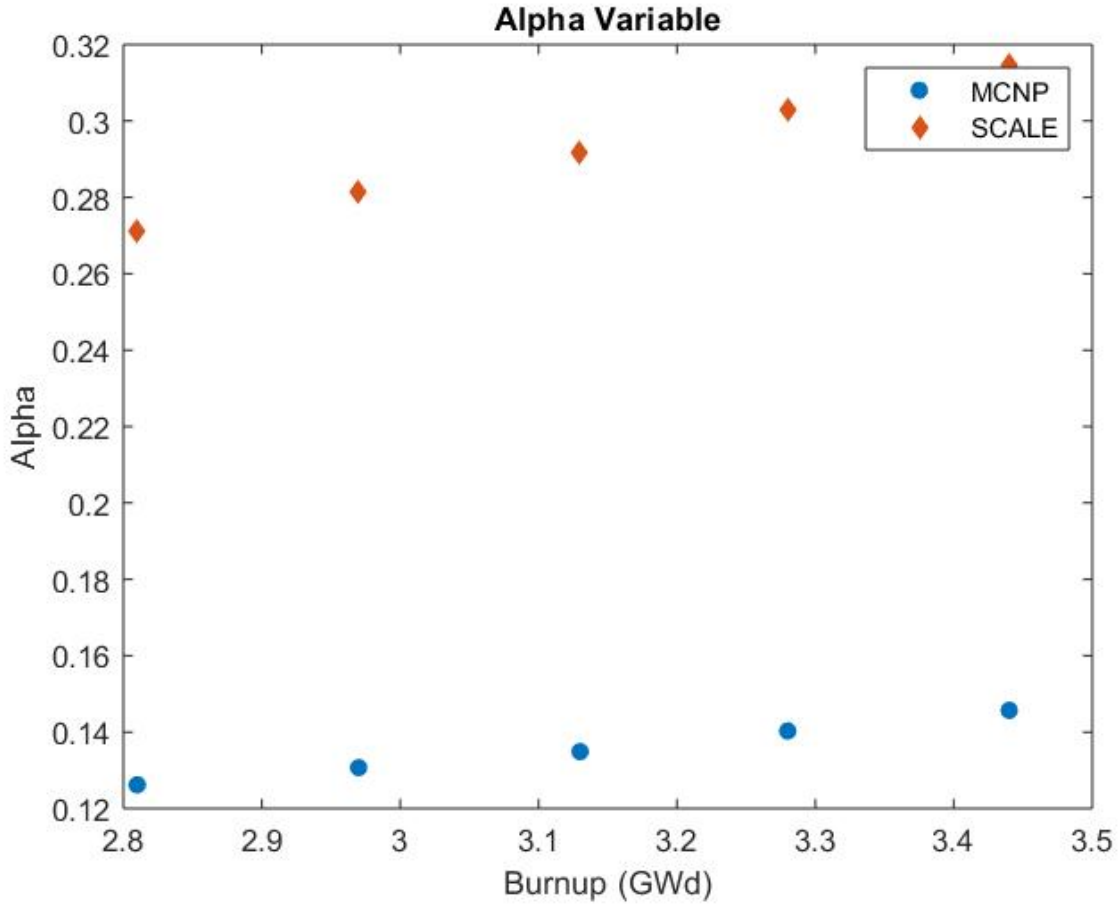


Figure B.15: Alpha variable comparison for a 35 GWd mixed sample.

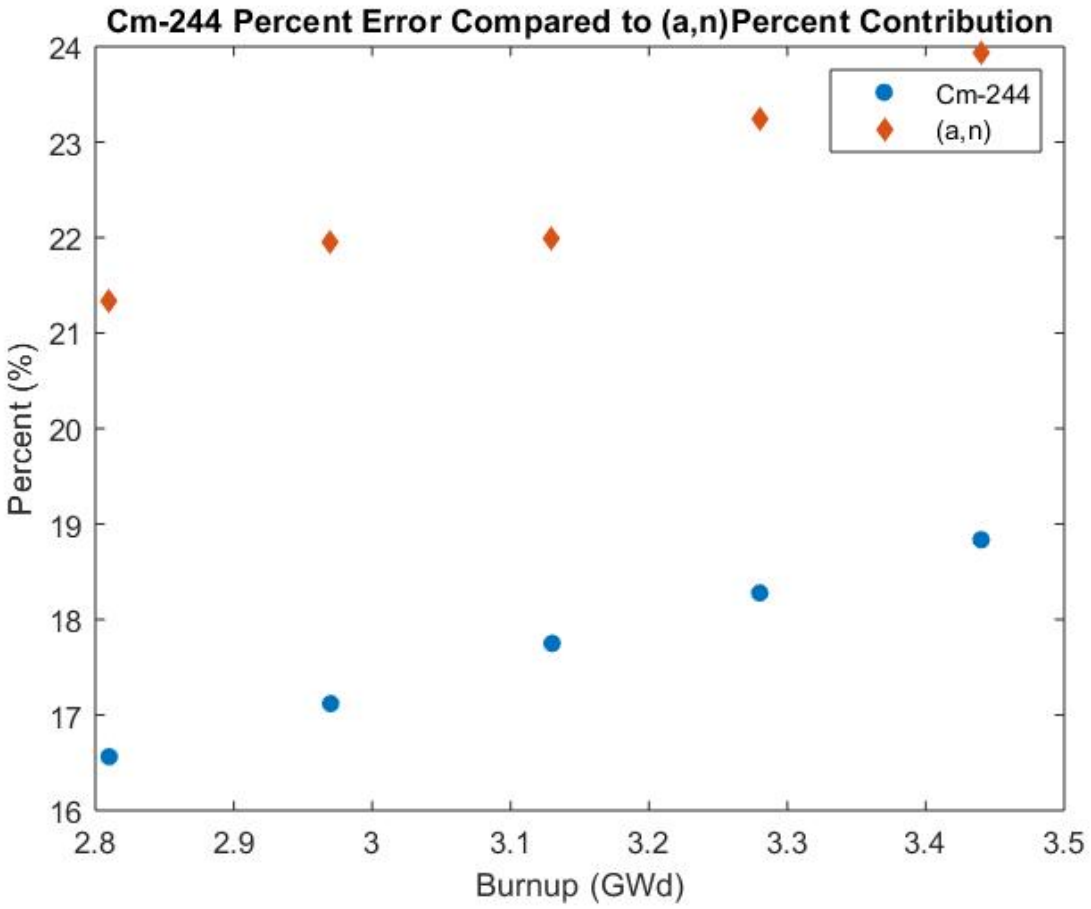


Figure B.16: Comparison for 35 GWd between Cm-244 mass percent error and total (α,n) contribution to neutron yield.

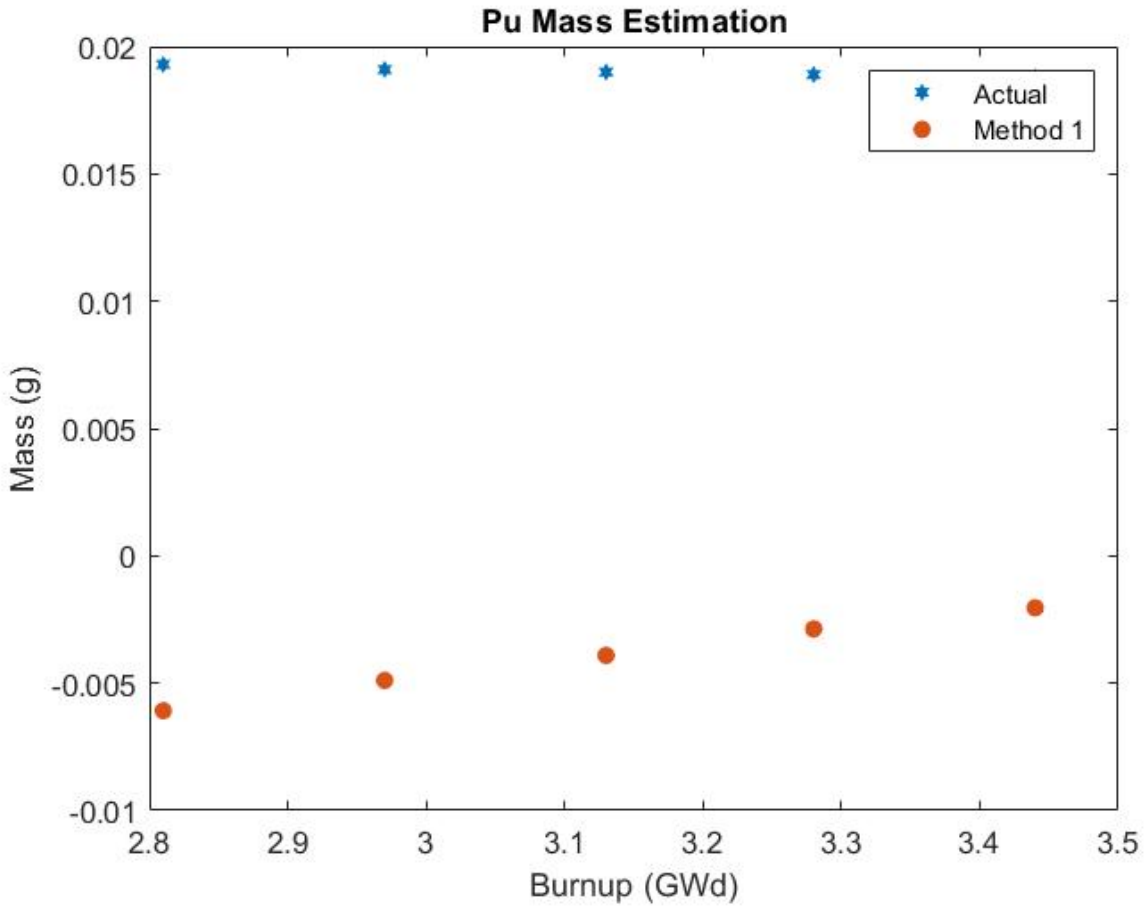


Figure B.17: Comparison between simulated mass and actual mass of plutonium for a 35 GWd mixed sample.

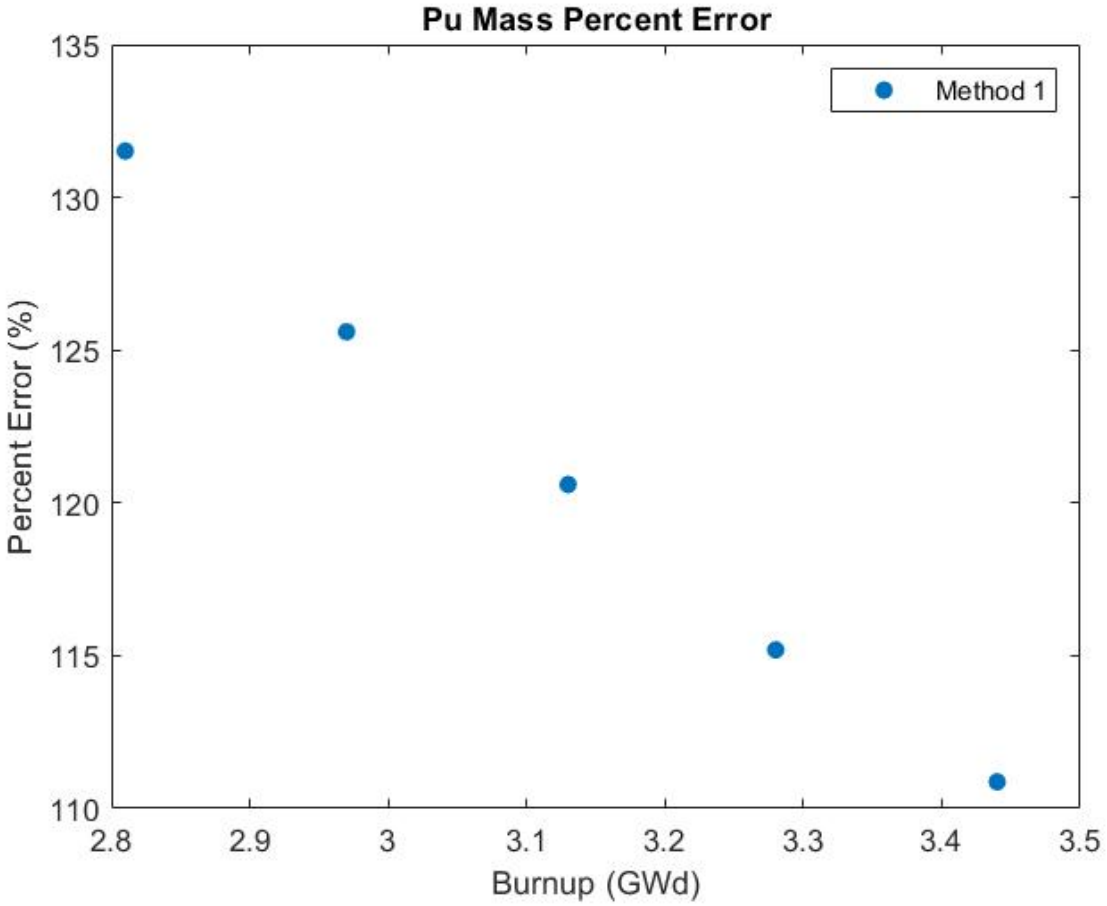


Figure B.18: Percent error for plutonium mass estimation for a 35 GWd mixed sample.

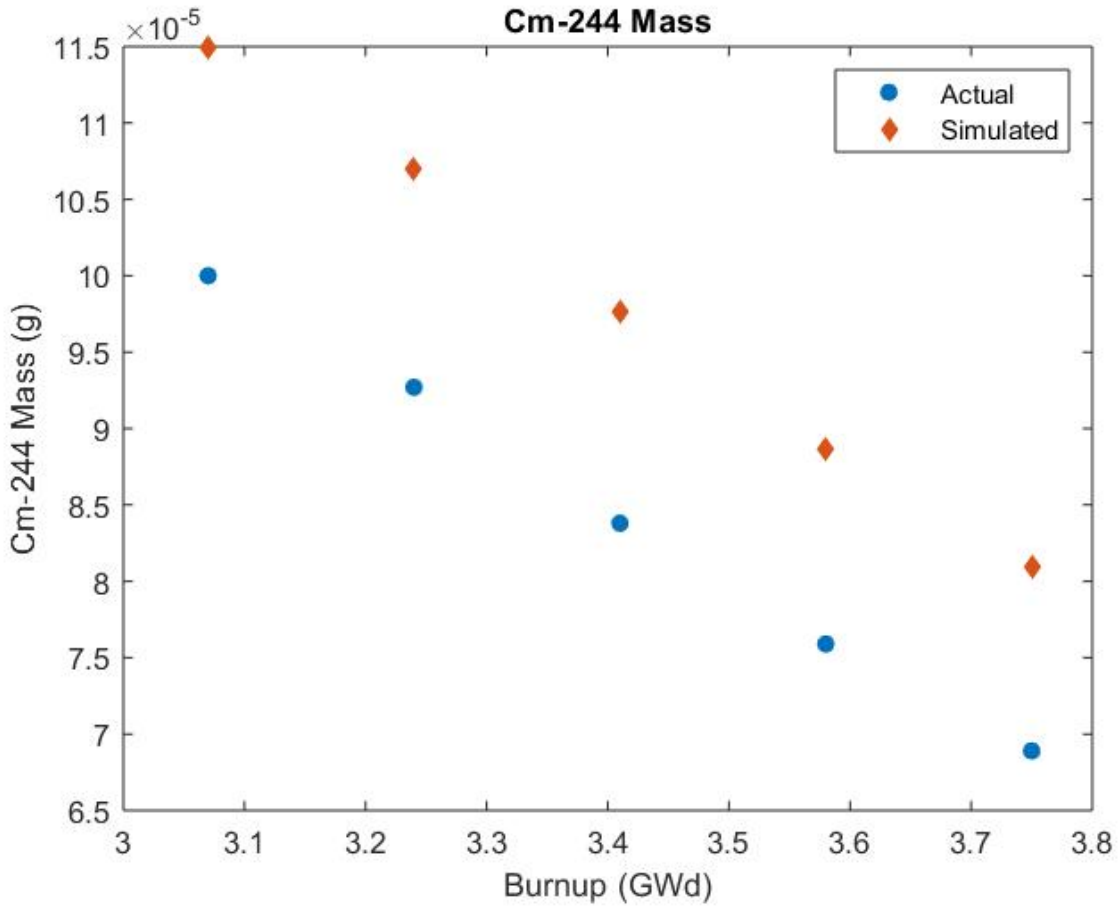


Figure B.19: Comparison between simulated mass and actual mass of Cm-244 for a 40 GWd mixed sample.

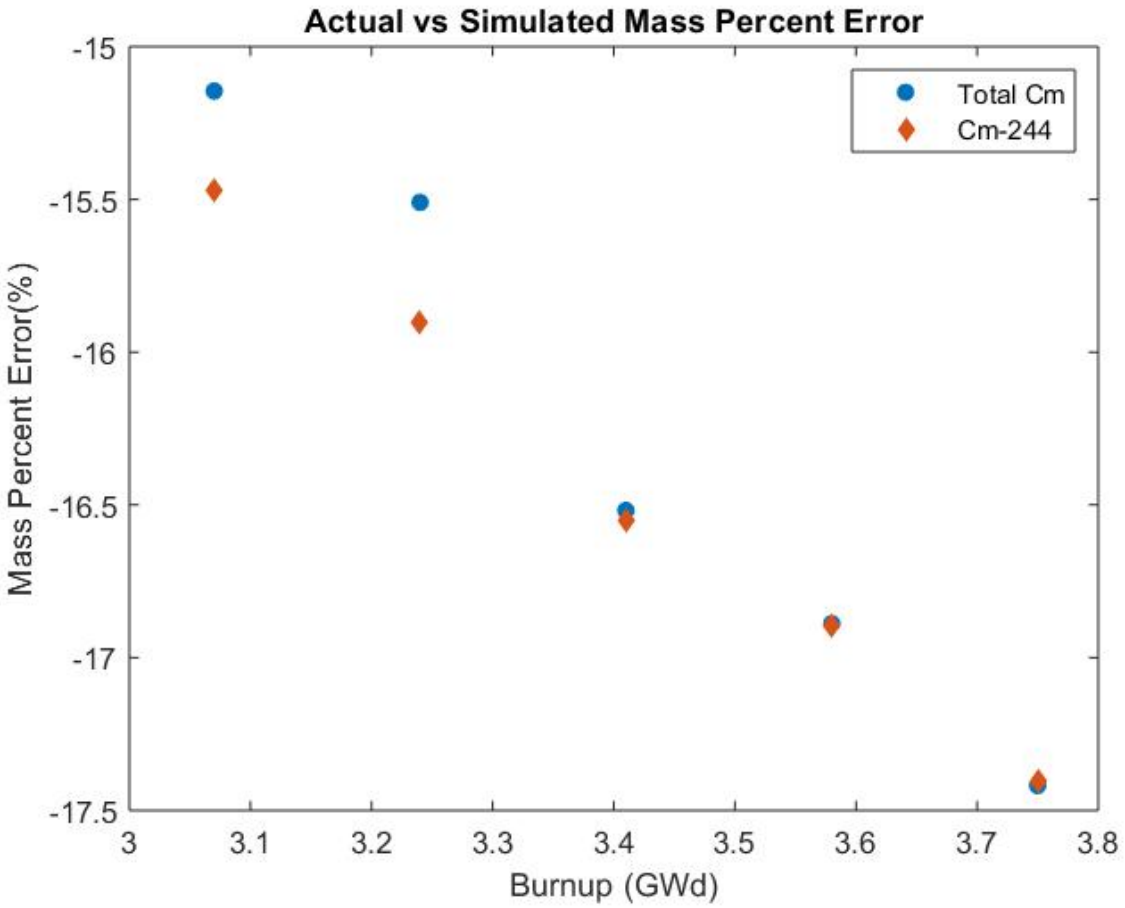


Figure B.20: Percent error for Cm-244 mass estimation for a 40 GWd mixed sample.

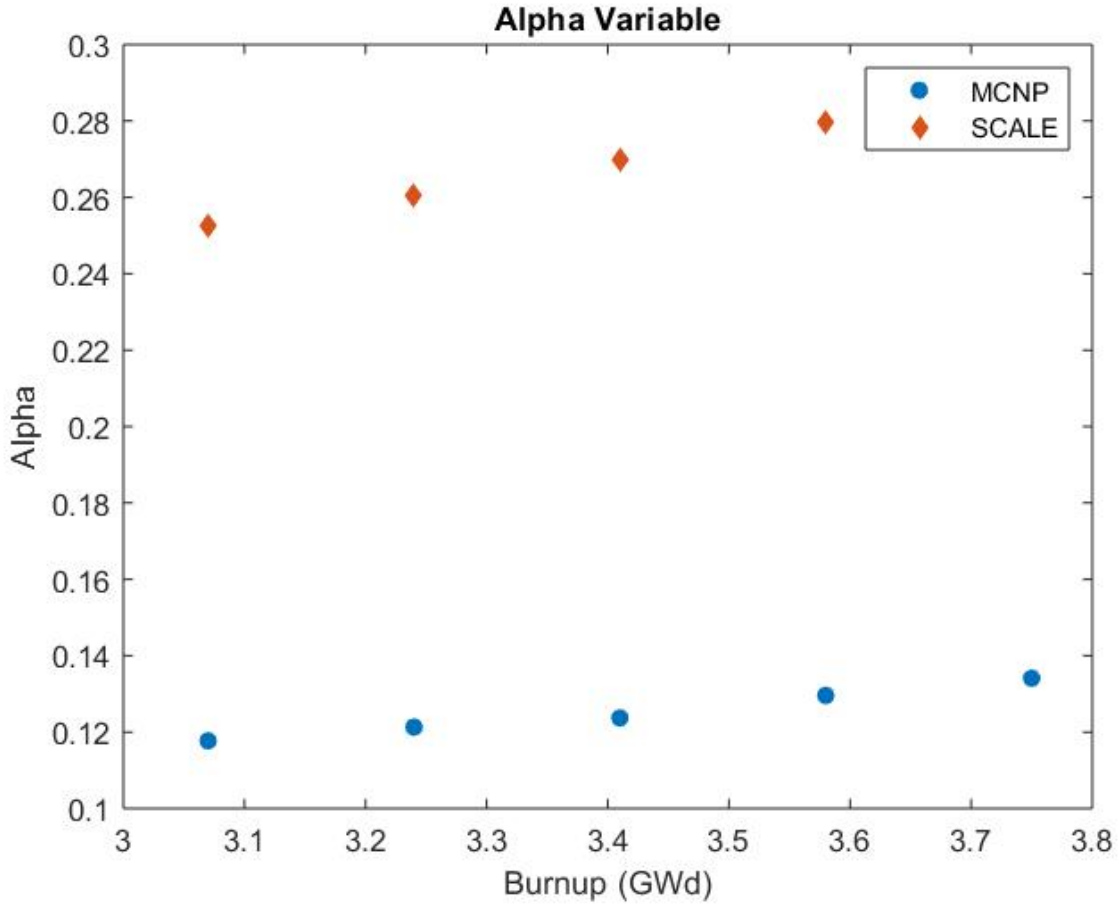


Figure B.21: Alpha variable comparison for a 40 GWd mixed sample.

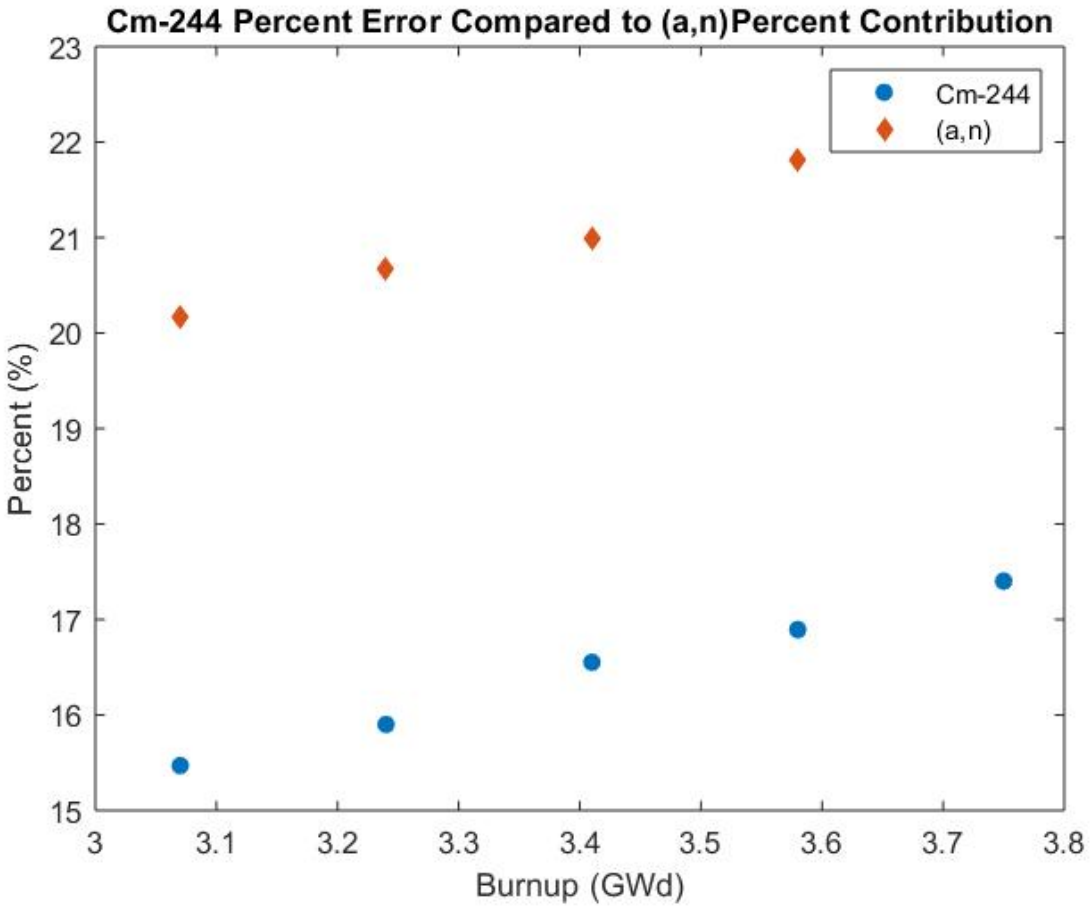


Figure B.22: Comparison for 40 GWd Cm-244 mass percent error and total (α,n) contribution to neutron yield.

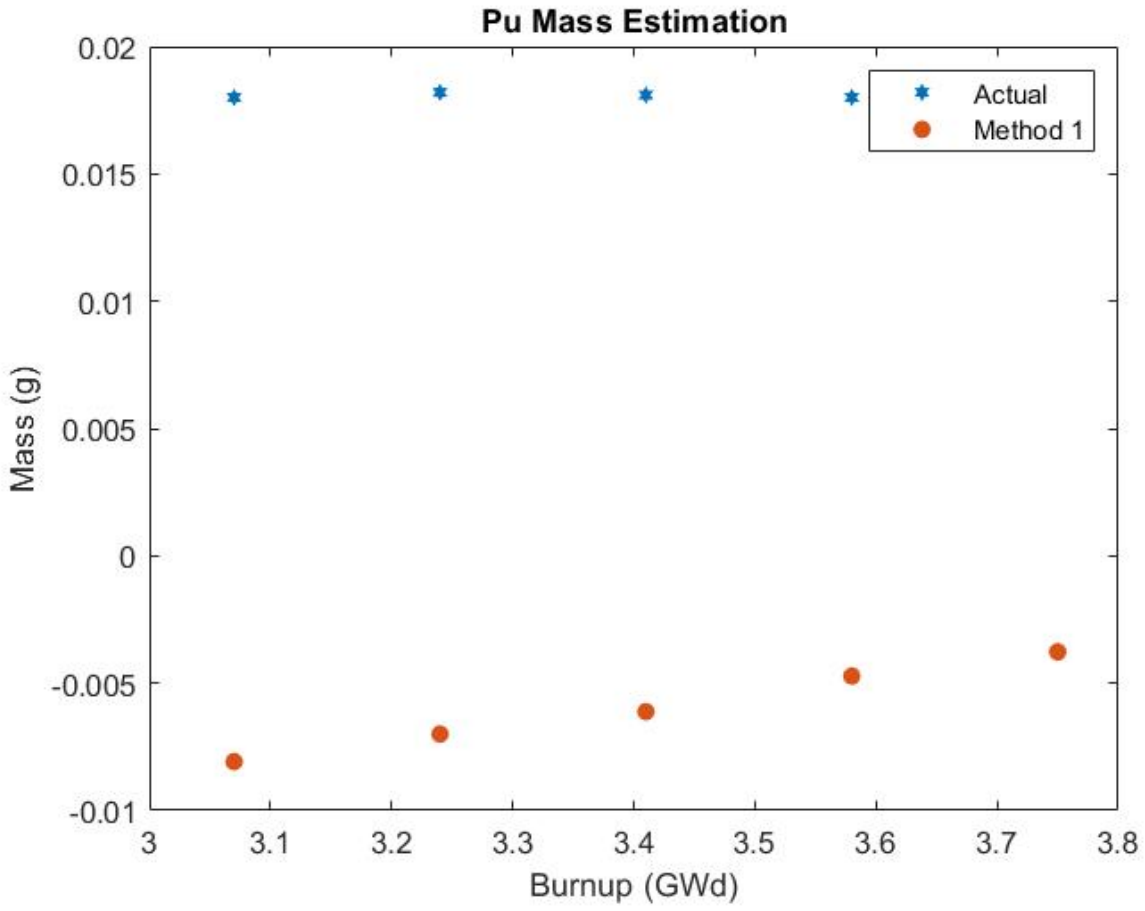


Figure B.23: Comparison between simulated mass and actual mass of plutonium for a 40 GWd mixed sample.

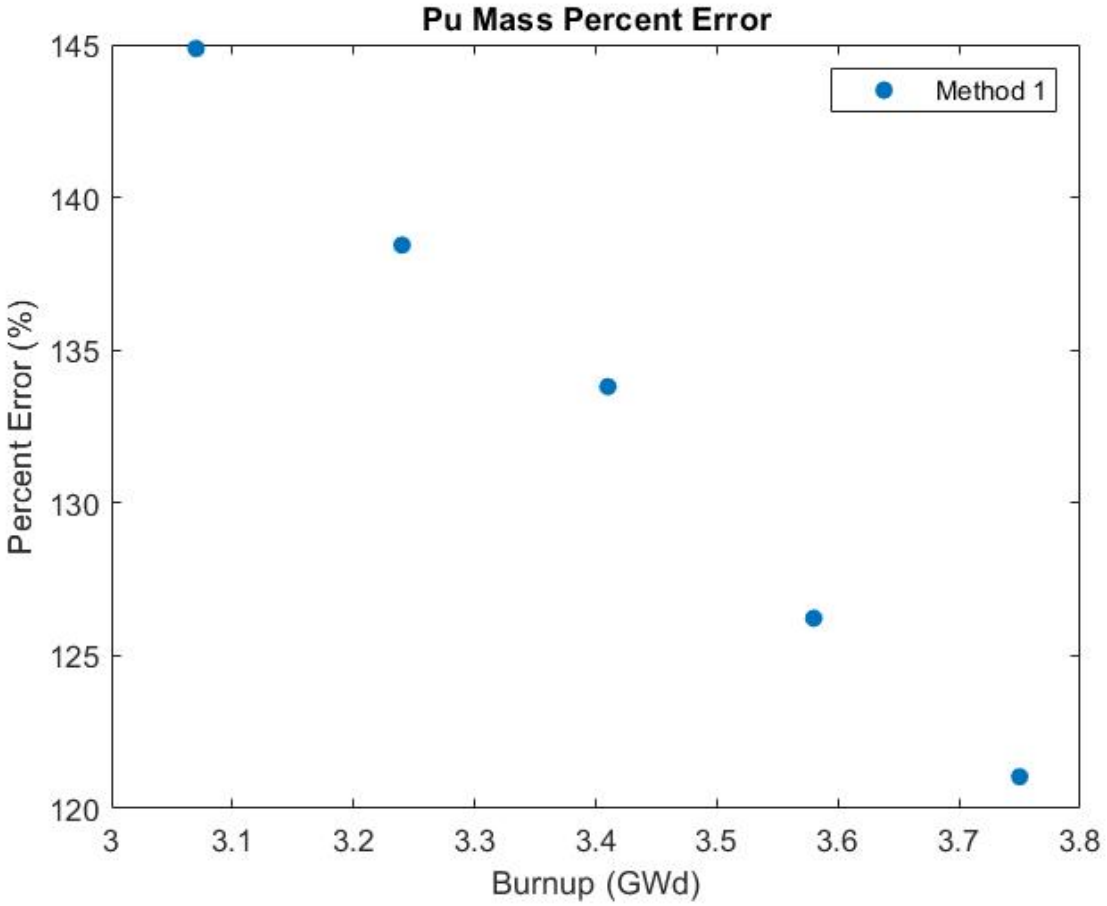


Figure B.24: Percent error for plutonium mass estimation for a 40 GWd mixed sample.

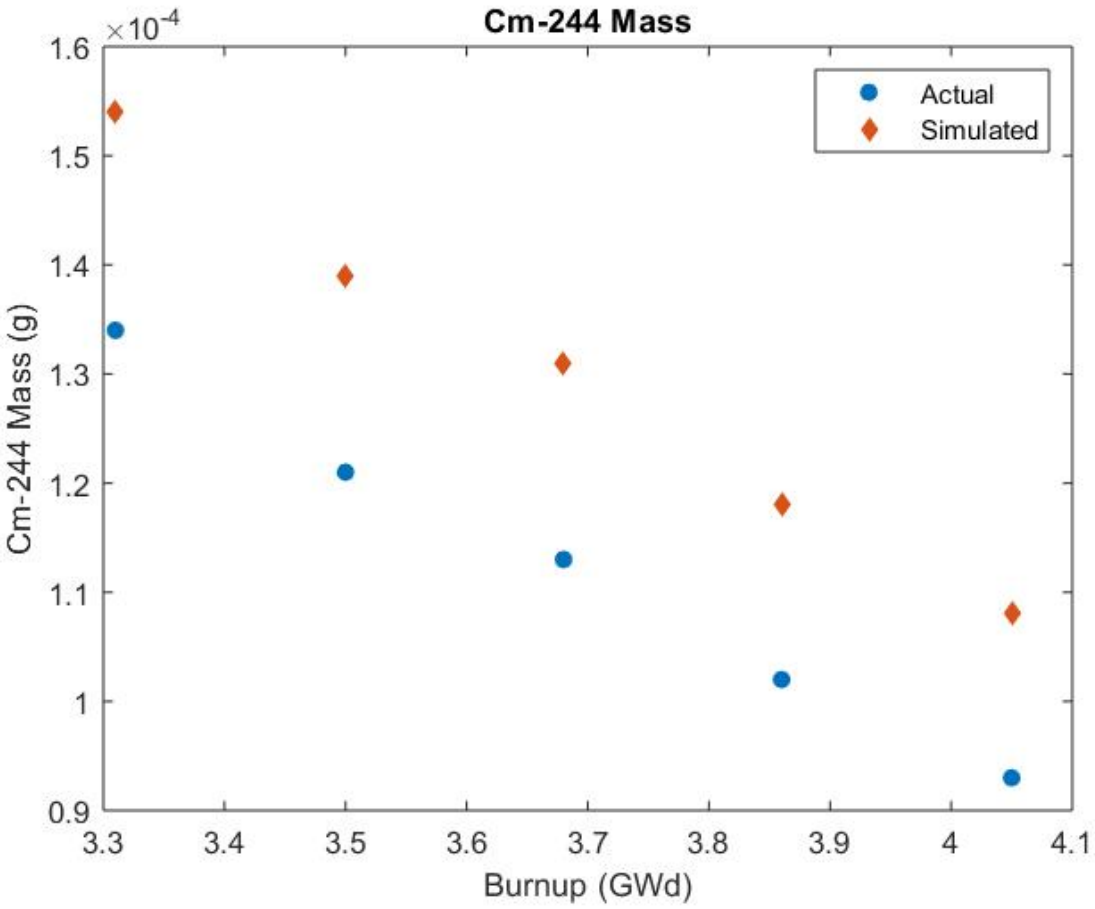


Figure B.25: Comparison between simulated mass and actual mass of Cm-244 for a 45 GWd mixed sample.

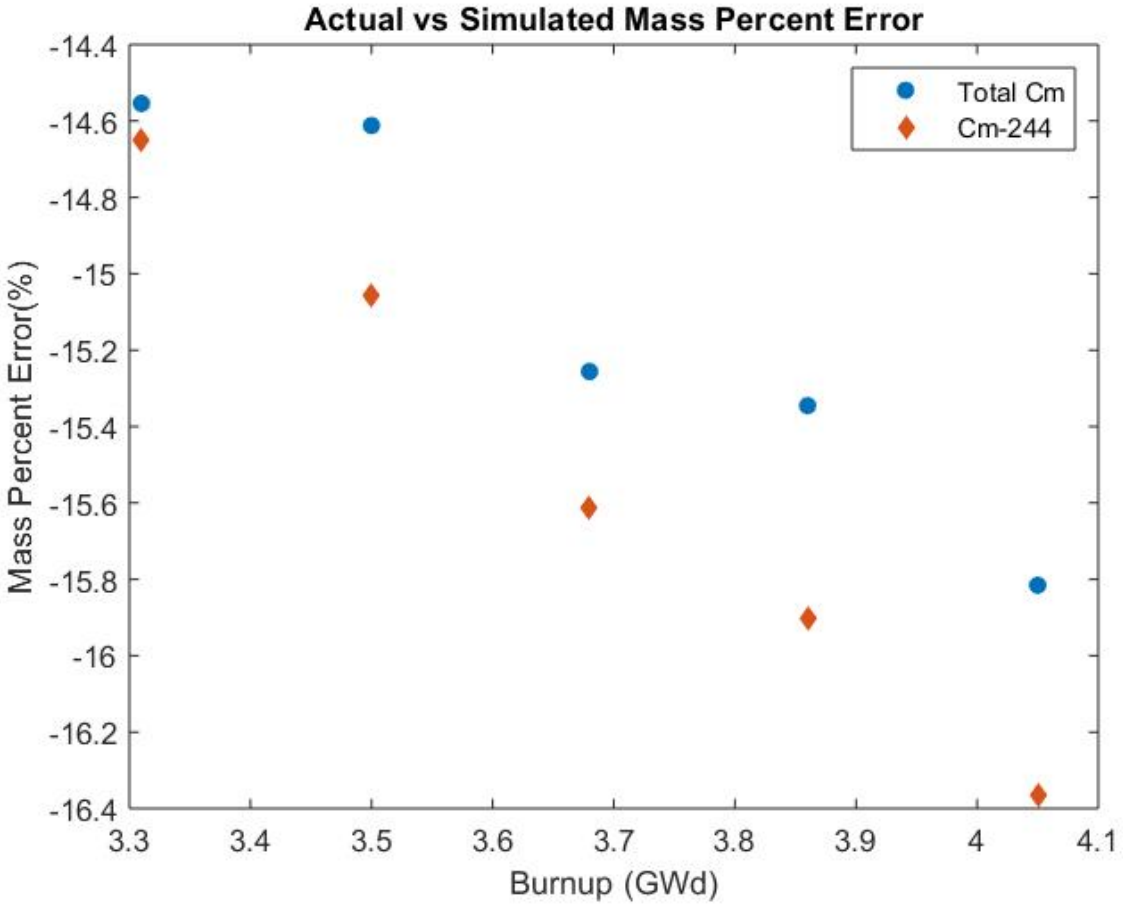


Figure B.26: Percent error for Cm-244 mass estimation for a 45 GWd mixed sample.

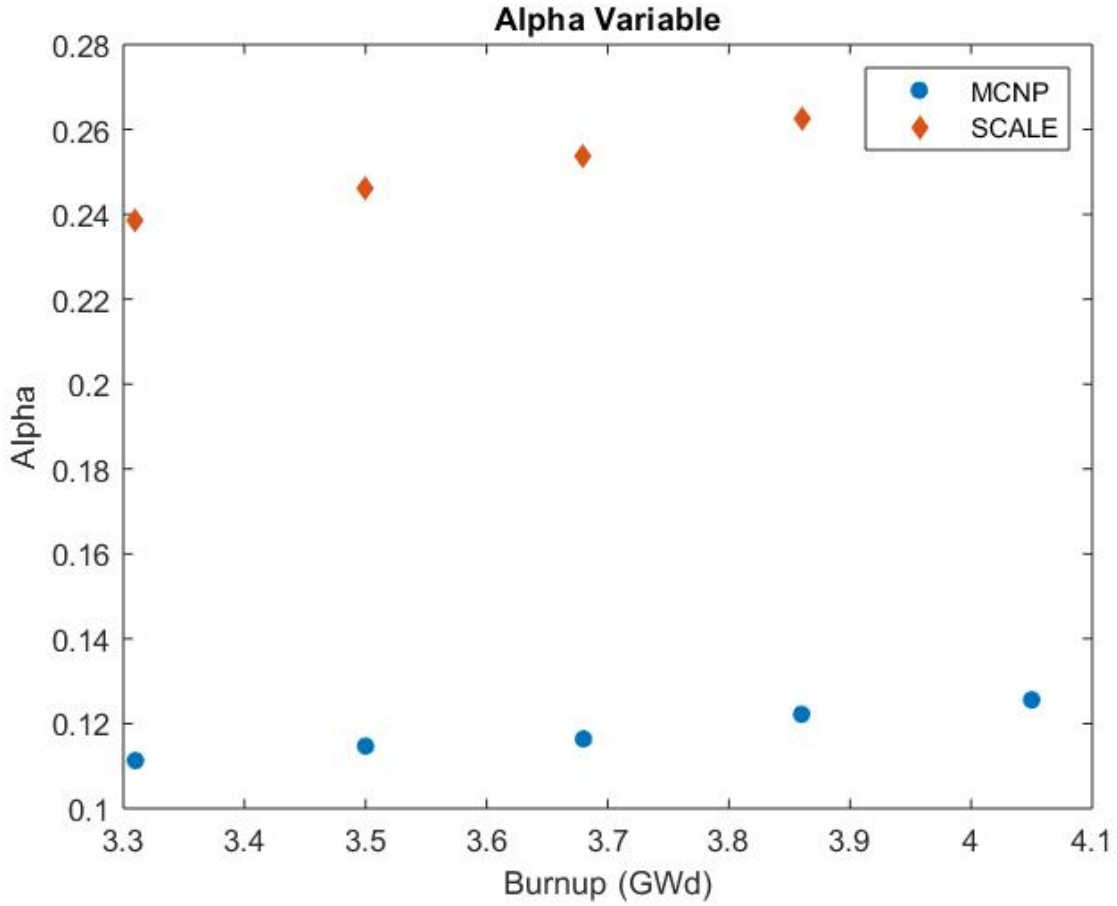


Figure B.27: Alpha variable comparison for a 45 GWd mixed sample.

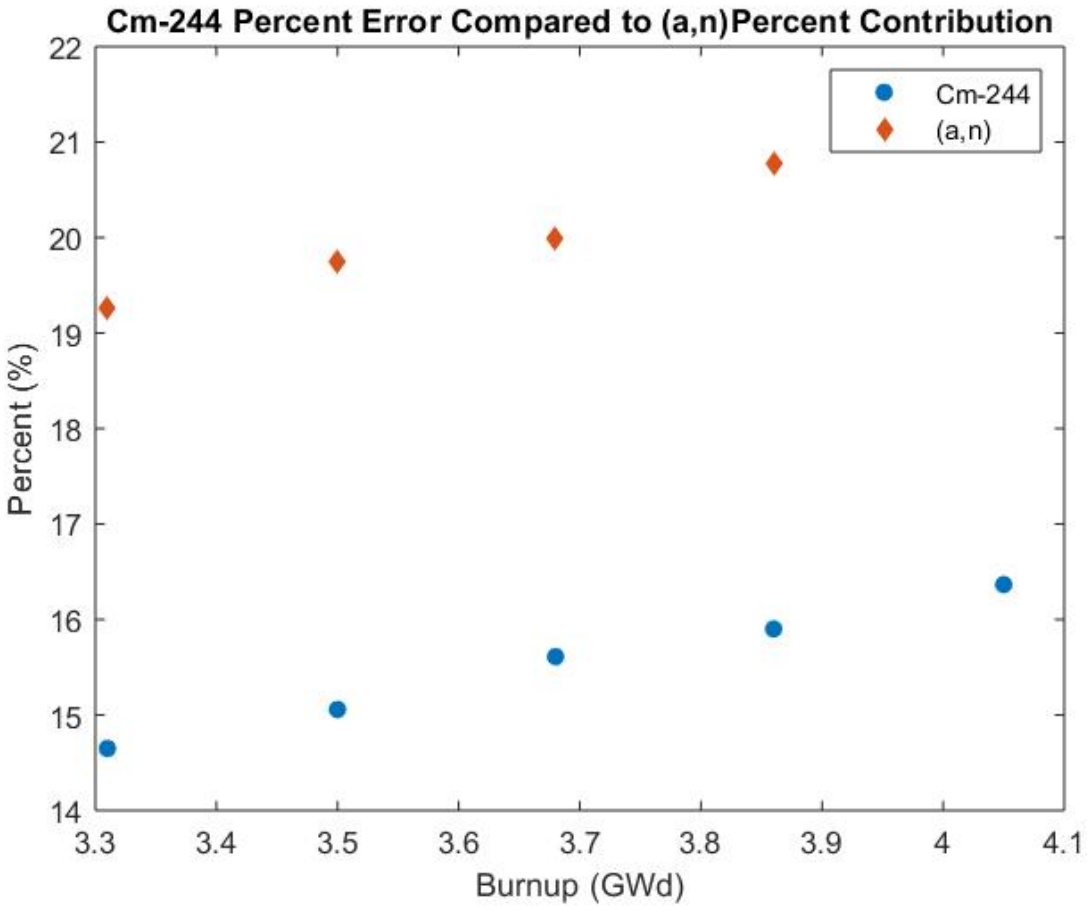


Figure B.28: Comparison for 45 GWd between Cm-244 mass percent error and total (α,n) contribution to neutron yield.

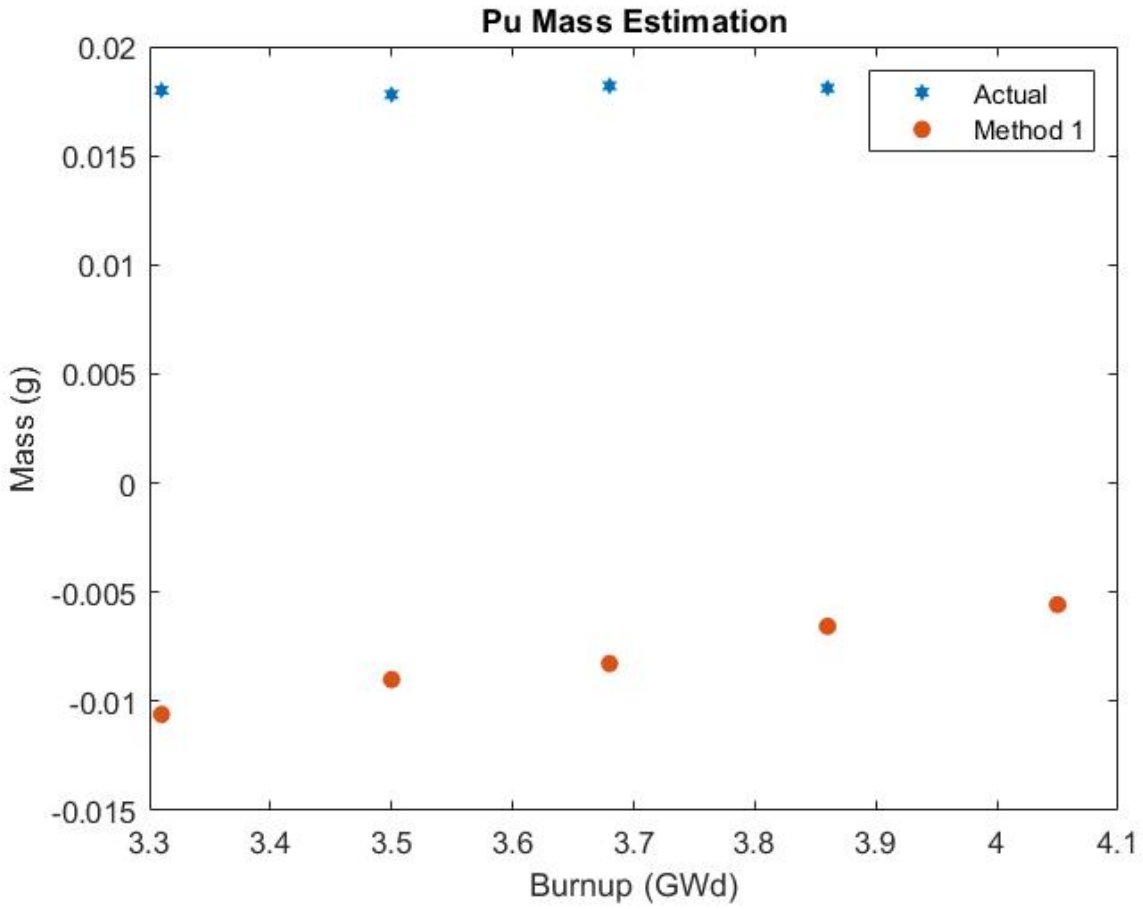


Figure B.29: Comparison between simulated mass and actual mass of plutonium for a 45 GWd mixed sample.

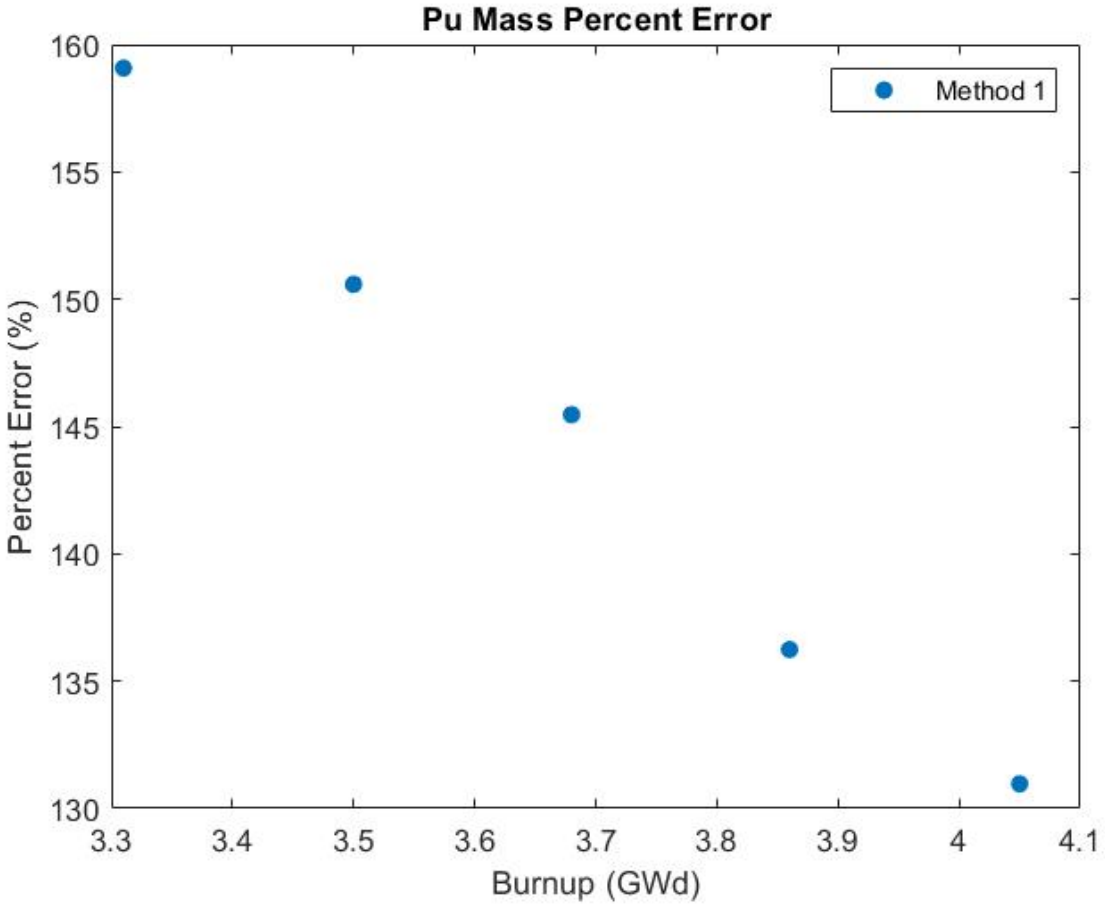


Figure B.30: Percent error for plutonium mass estimation for a 45 GWd mixed sample.

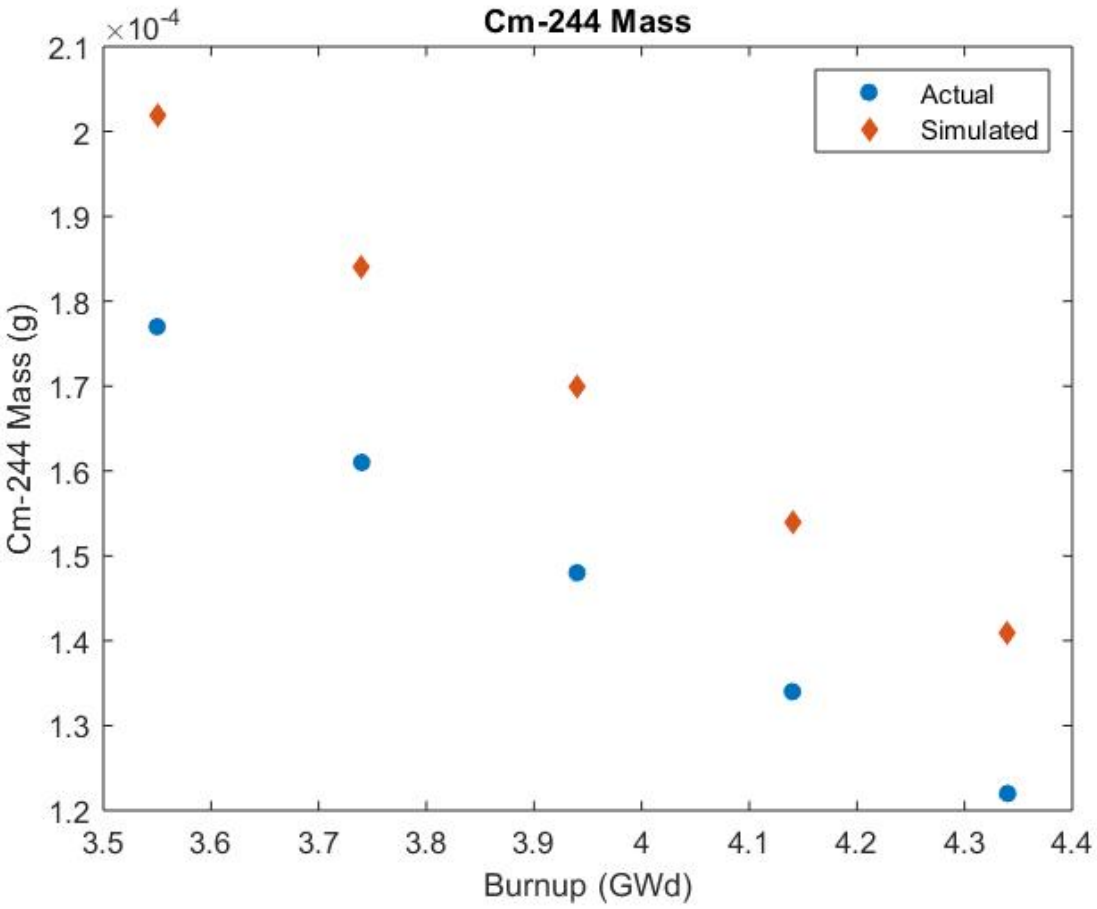


Figure B.31: Comparison between simulated mass and actual mass of Cm-244 for a 50 GWd mixed sample.

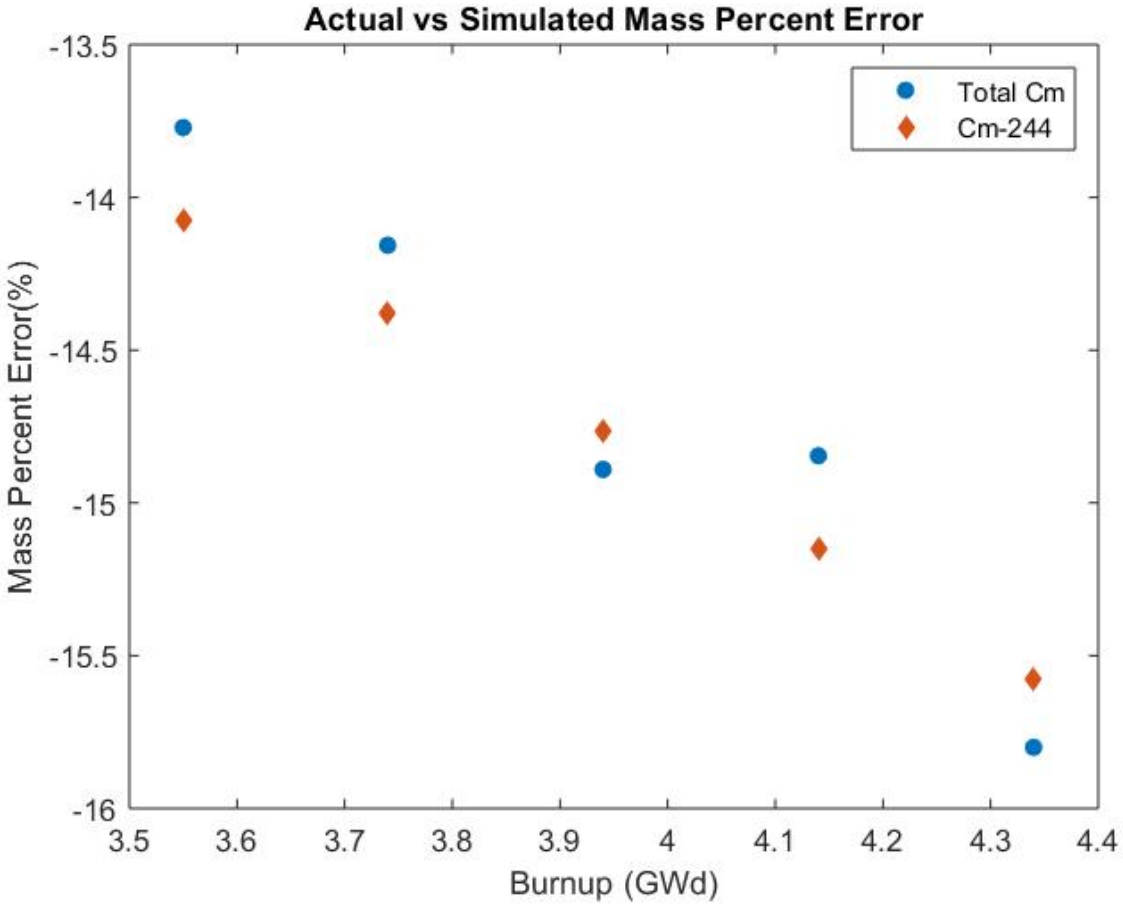


Figure B.32: Percent error for Cm-244 mass estimation for a 50 GWd mixed sample.

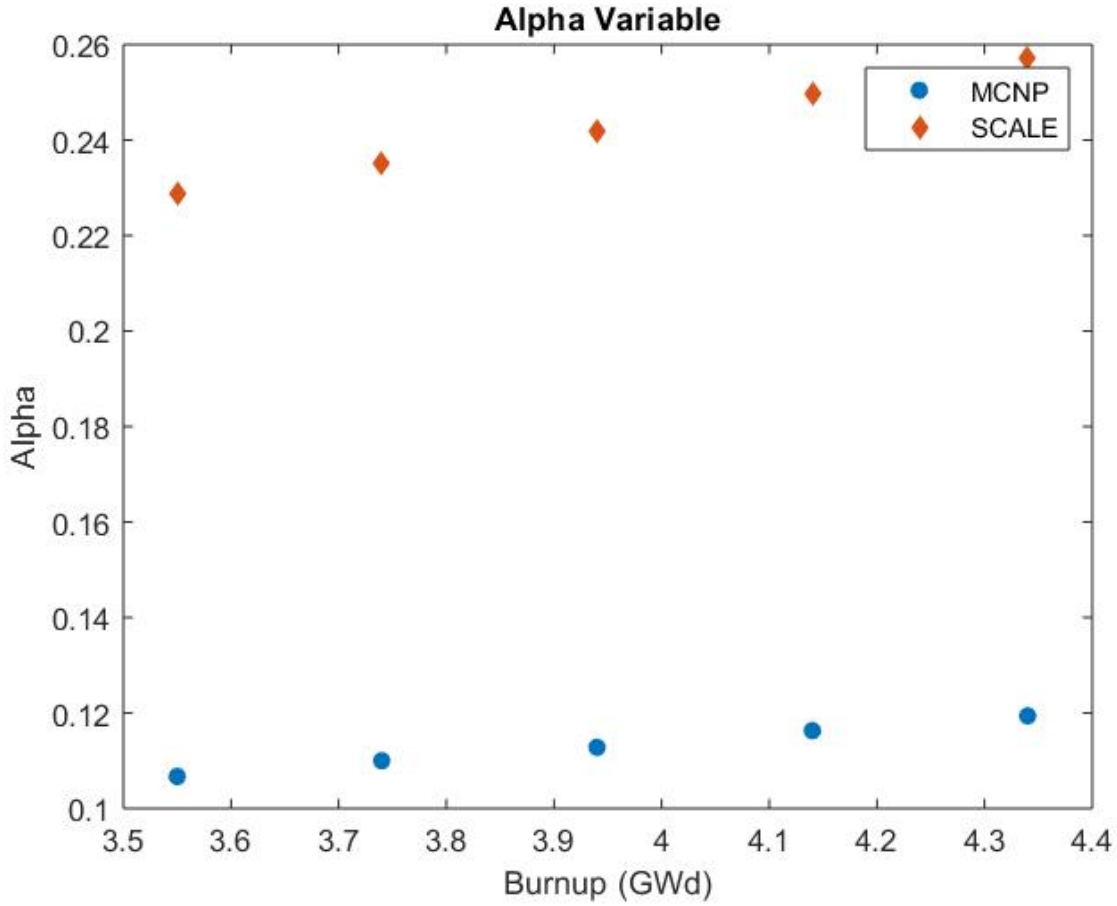


Figure B.33: Alpha variable comparison for a 50 GWd mixed sample.

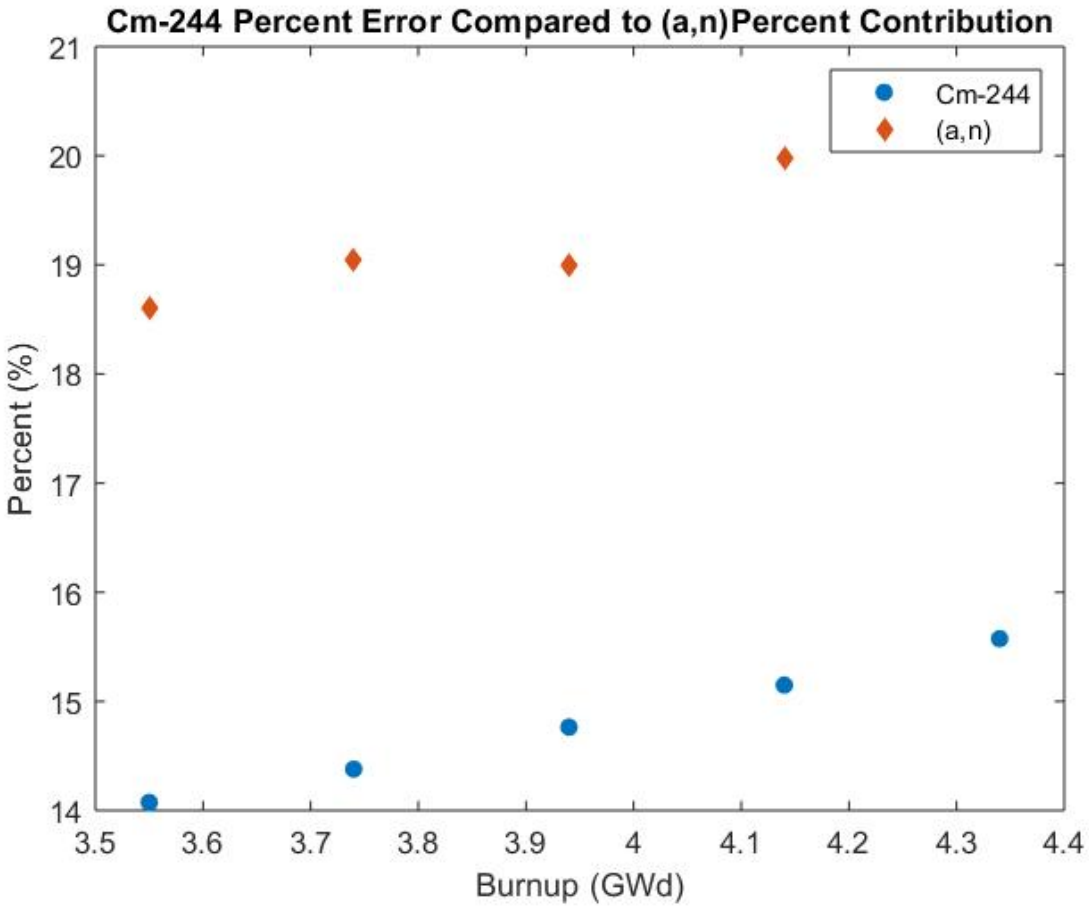


Figure B.34: Comparison for 50 GWd between Cm-244 mass percent error and total (α,n) contribution to neutron yield.

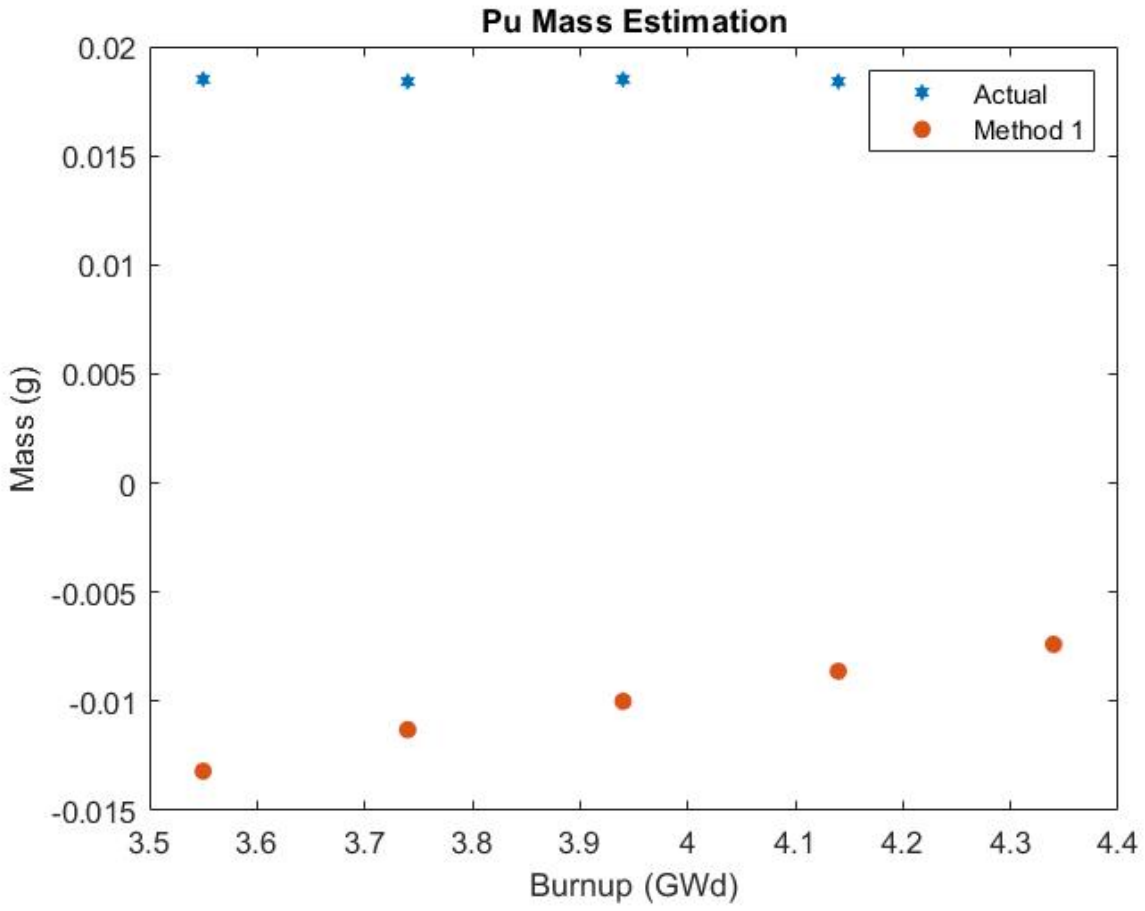


Figure B.35: Comparison between simulated mass and actual mass of plutonium for a 50 GWd mixed sample.

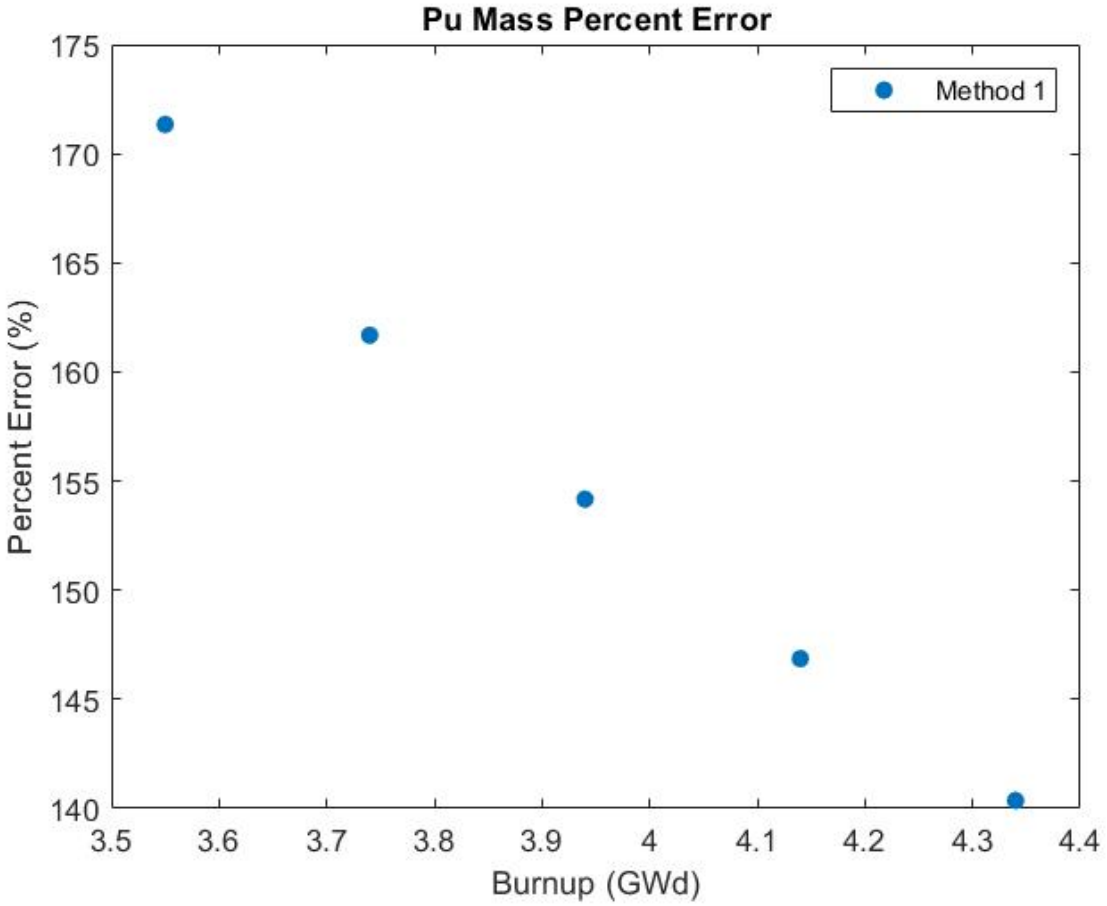


Figure B.36: Percent error for plutonium mass estimation for a 50 GWd mixed sample.

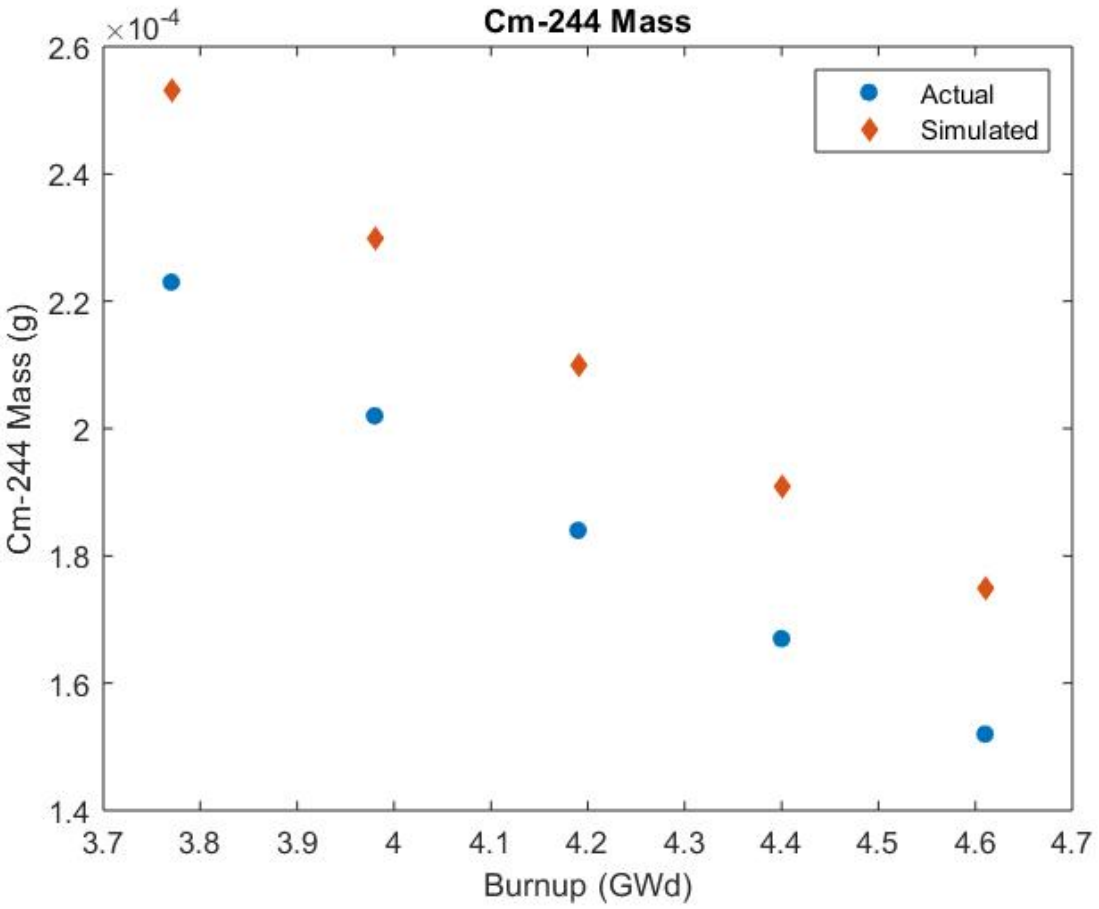


Figure B.37: Comparison between simulated mass and actual mass of Cm-244 for a 55 GWd mixed sample.

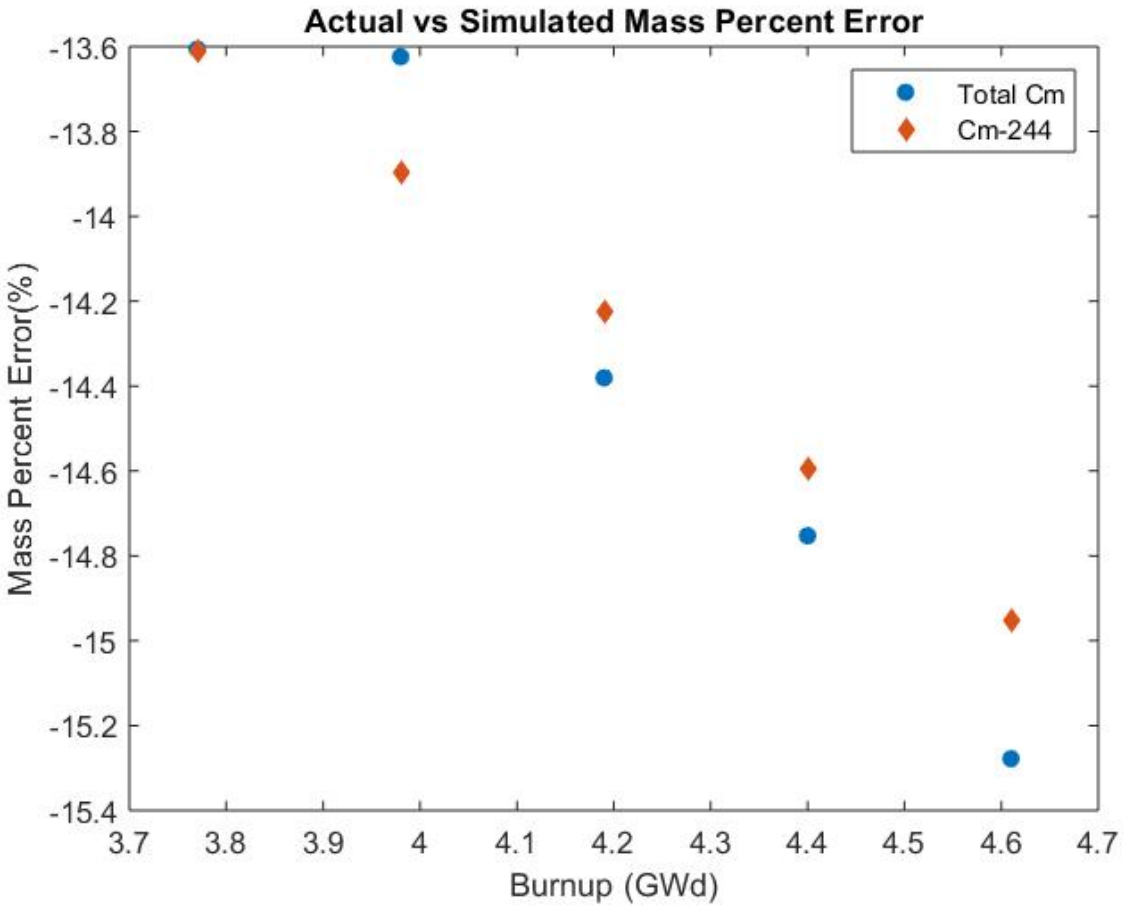


Figure B.38: Percent error for Cm-244 mass estimation for a 55 GWd mixed sample.

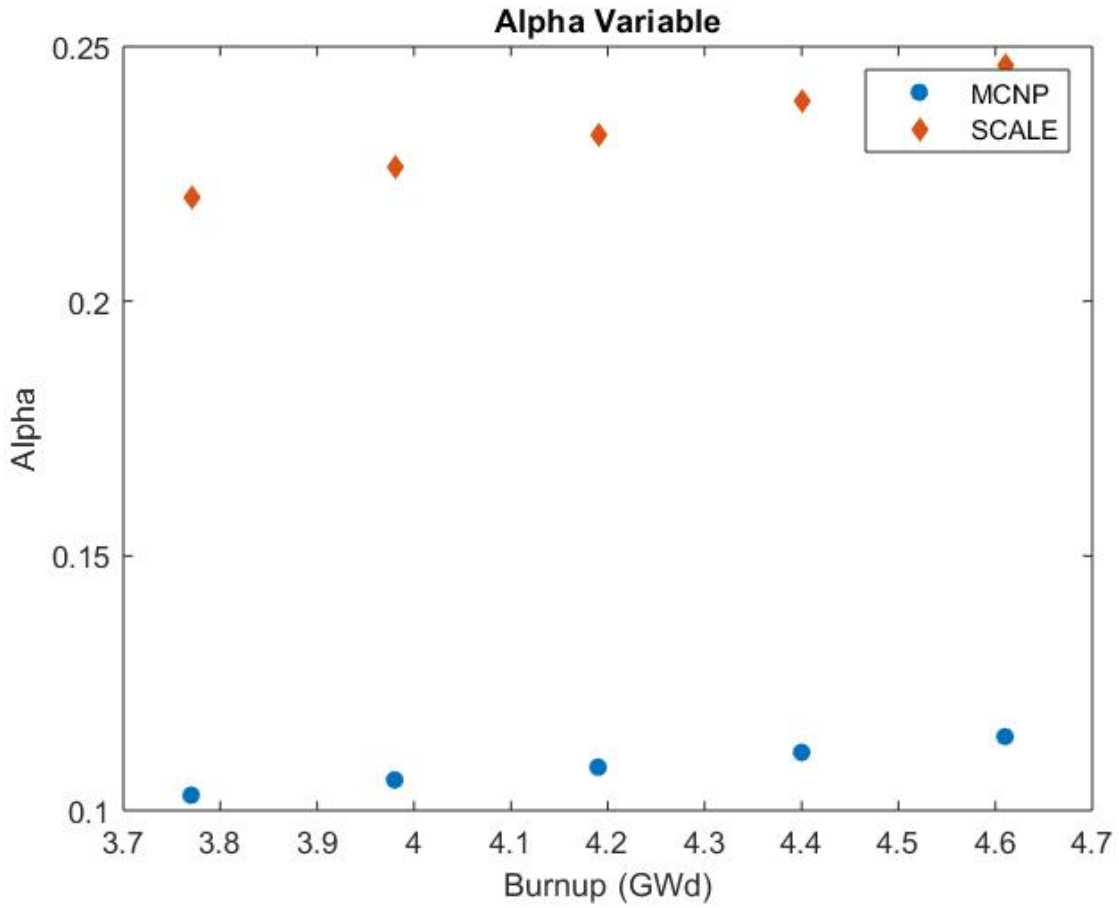


Figure B.39: Alpha variable comparison for a 55 GWd mixed sample.

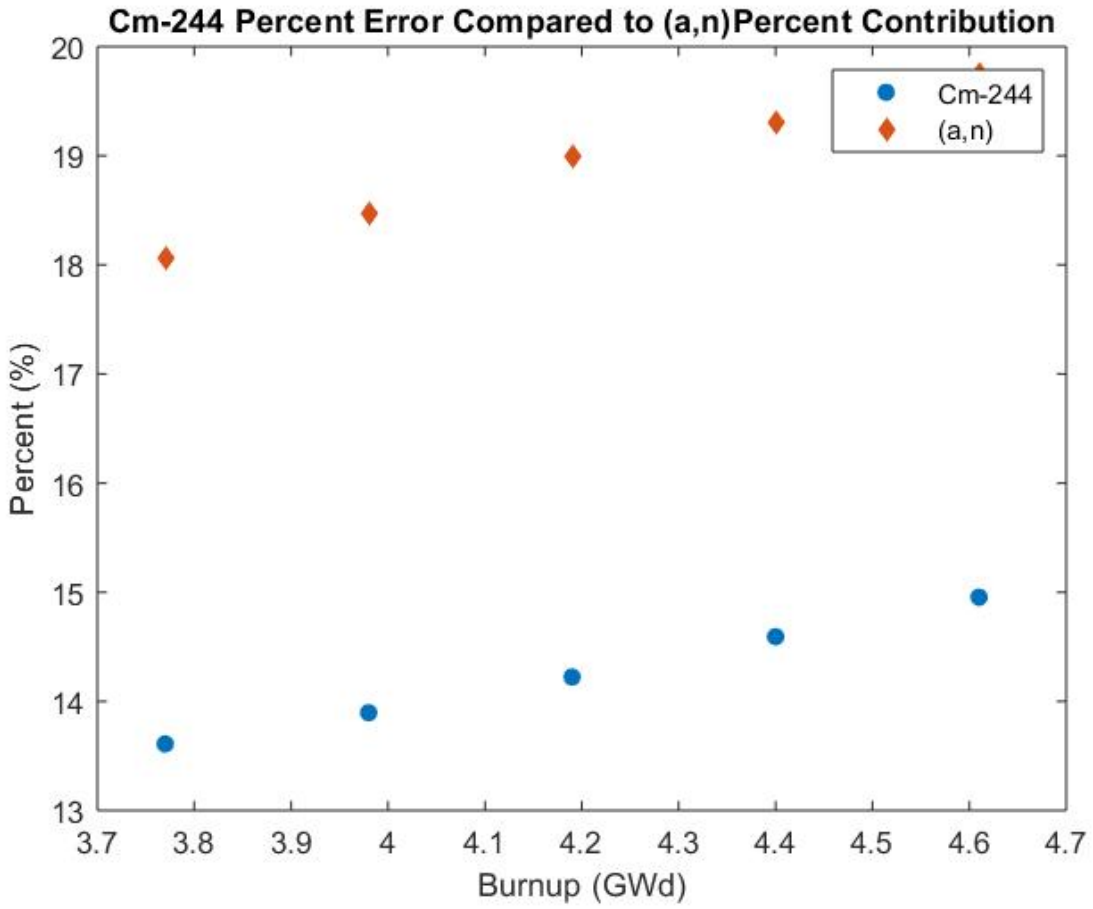


Figure B.40: Comparison for 55 GWd between Cm-244 mass percent error and total (α,n) contribution to neutron yield.

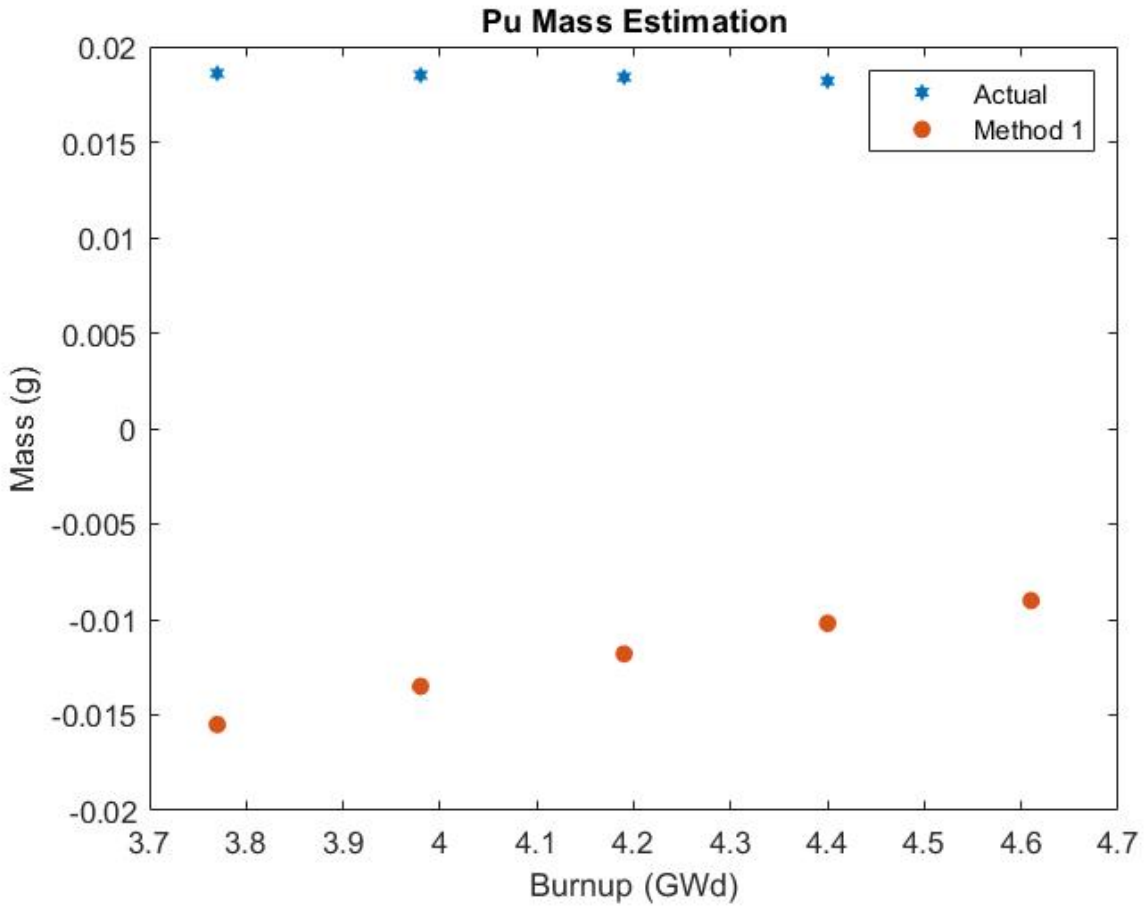


Figure B.41: Comparison between simulated mass and actual mass of plutonium for a 55 GWd mixed sample.

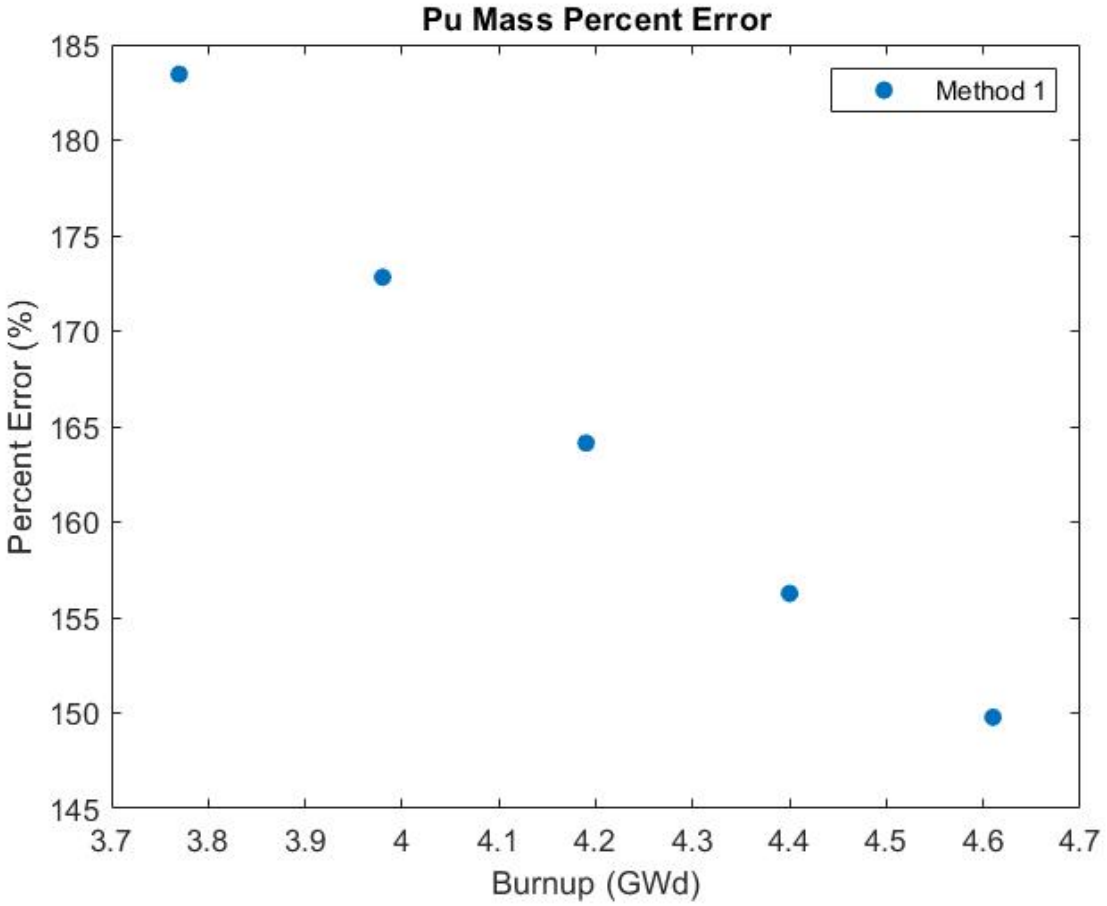


Figure B.42: Percent error for plutonium mass estimation for a 55 GWd mixed sample.

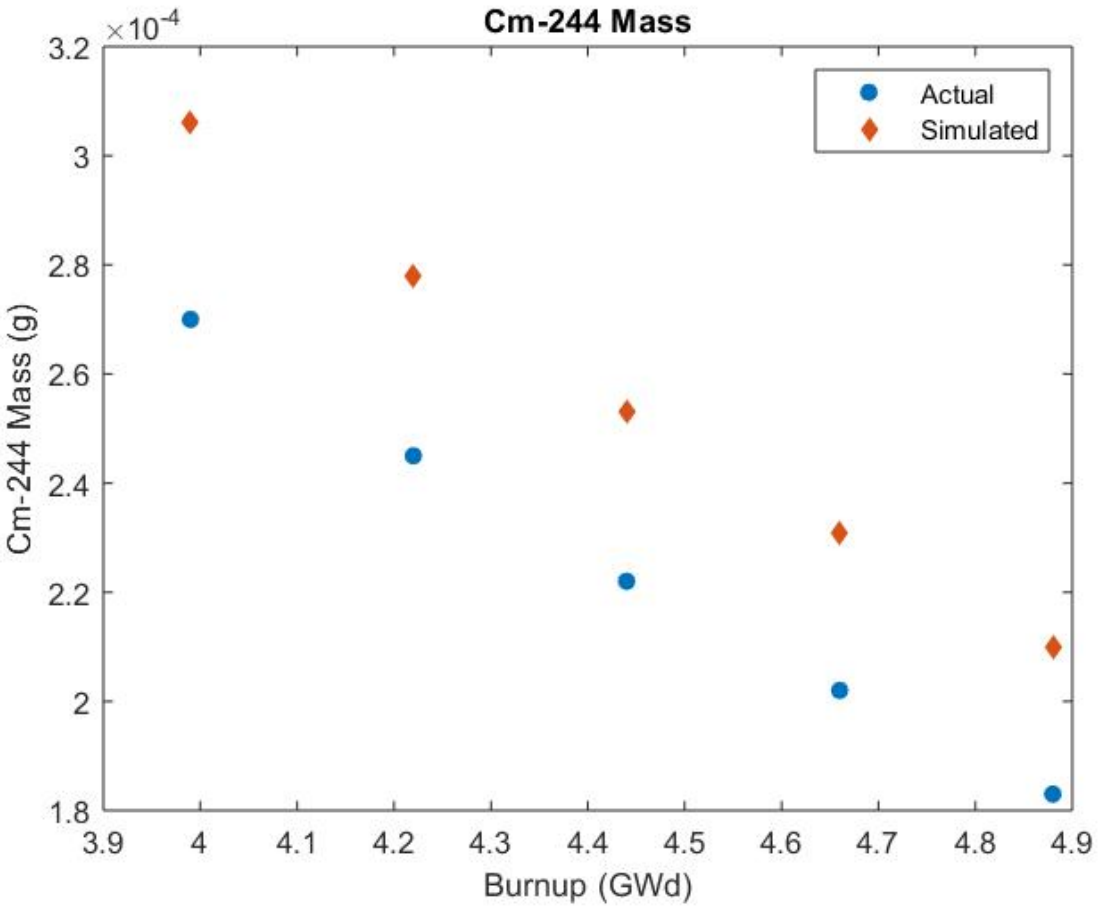


Figure B.43: Comparison between simulated mass and actual mass of Cm-244 for a 60 GWd mixed sample.

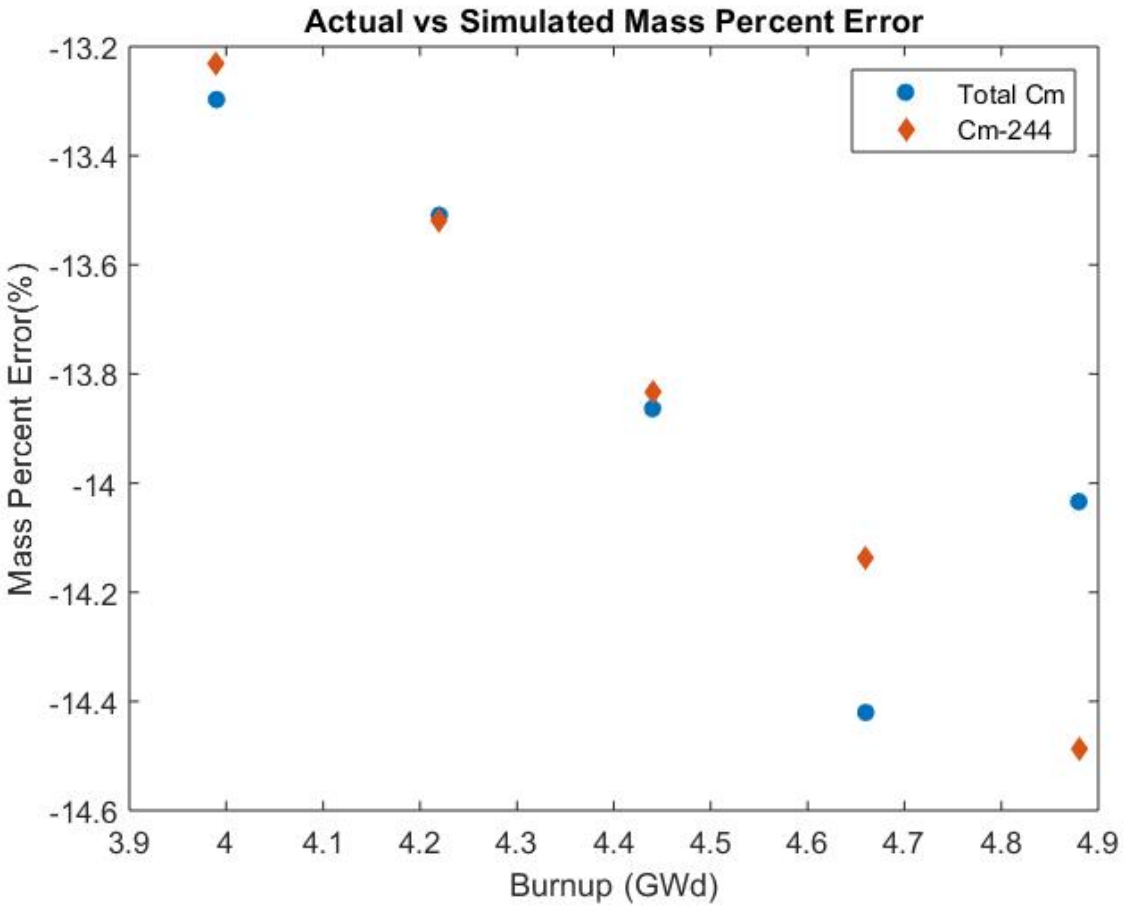


Figure B.44: Percent error for Cm-244 mass estimation for a 60 GWd mixed sample.

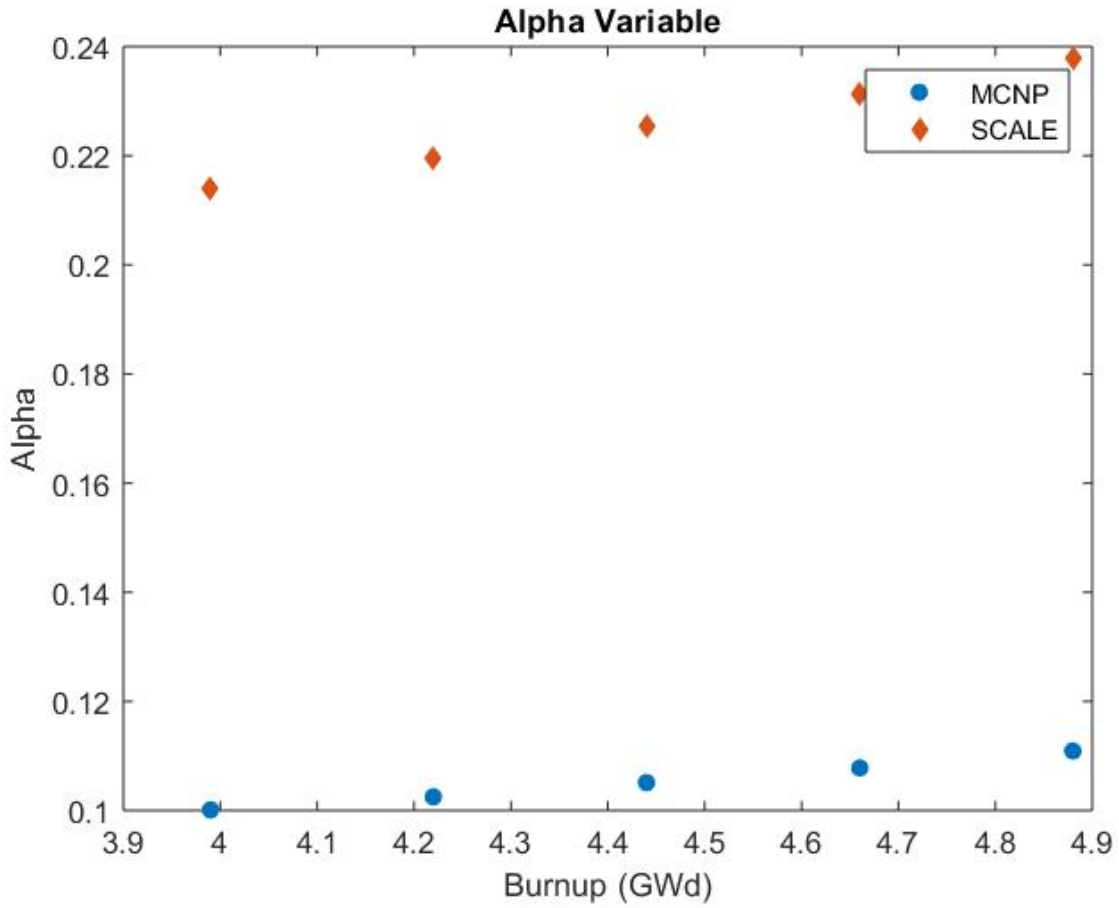


Figure B.45: Alpha variable comparison for a 60 GWd mixed sample.

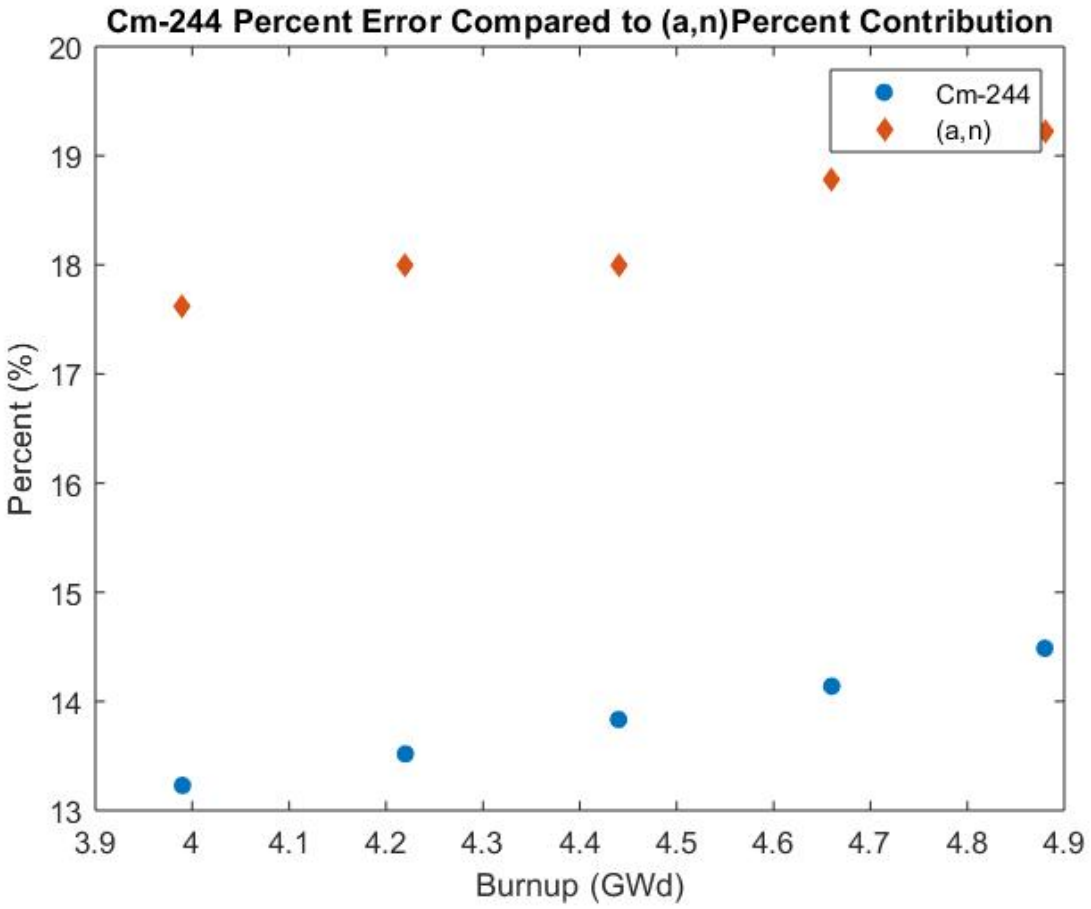


Figure B.46: Comparison for 60 GWd between Cm-244 mass percent error and total (α,n) contribution to neutron yield.

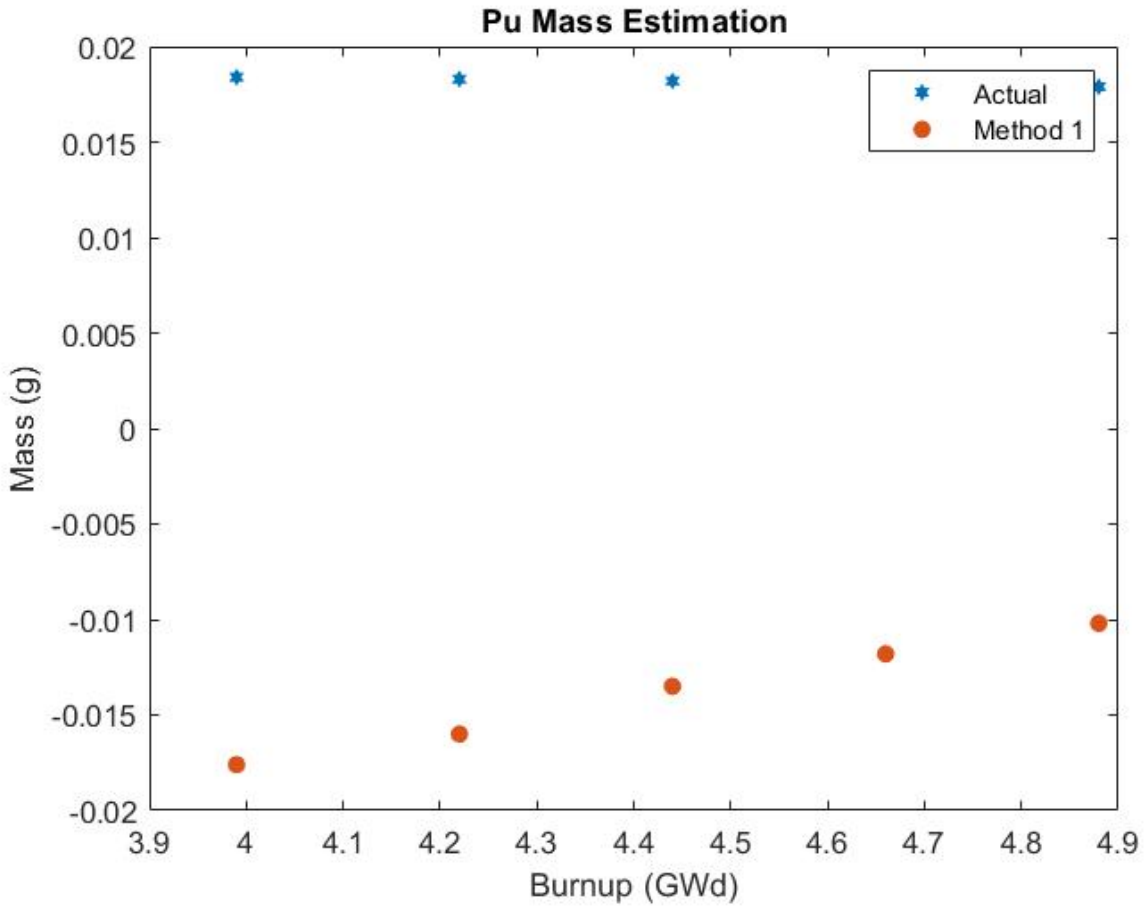


Figure B.47: Comparison between simulated mass and actual mass of plutonium for a 60 GWd mixed sample.

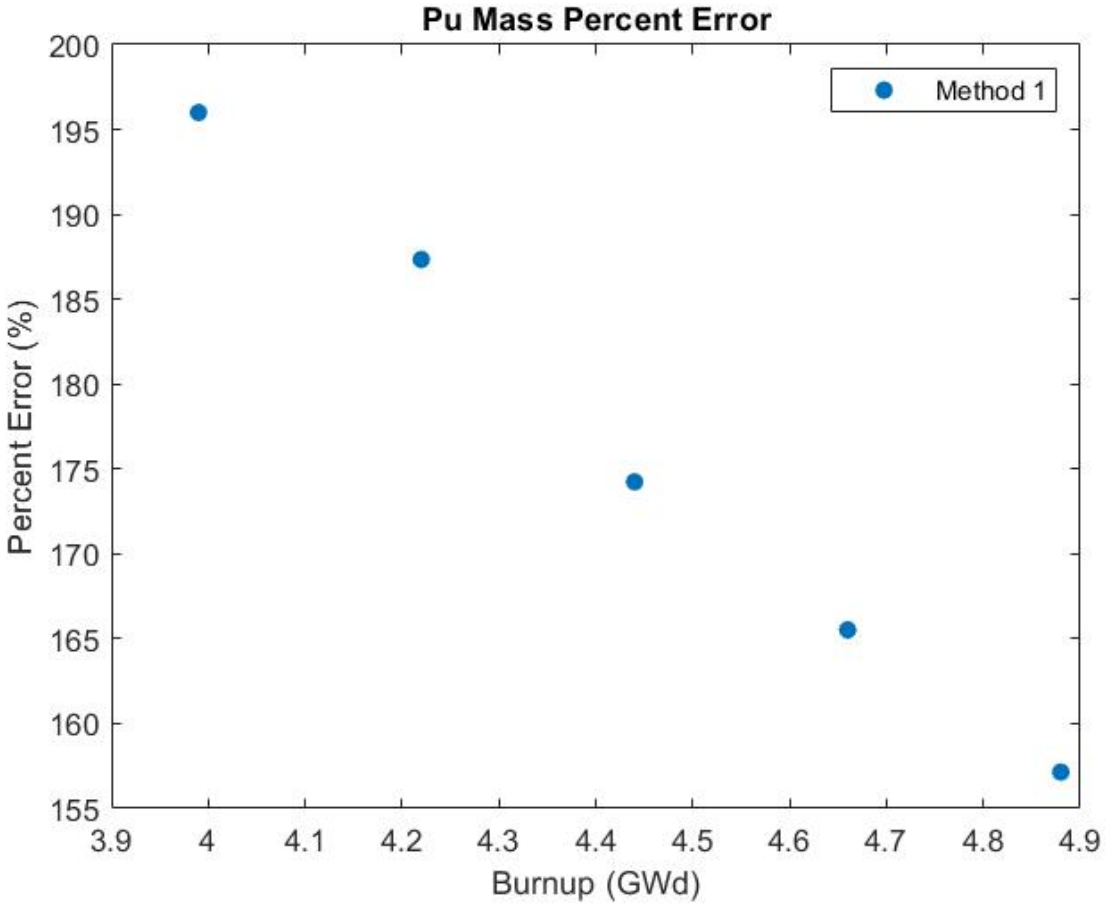


Figure B.48: Percent error for plutonium mass estimation for a 60 GWd mixed sample.

C Appendix C

Table C.1: Summary of Main Sequence Variables Used for Multiplicity Counting from a Sample Containing Cm and Eutectic Salt.

Burnup (GWd)	Enrich. (%)	FoM	$^{244}Cm_{eff}(g)$	S (cps)	D (cps)	T (cps)	SD_S	SD_D	SD_D	$\tau(\mu s)$	$\epsilon(\%)$	F_d	F_t	M
20	2.17	0.0195	2.14E-05	162.38	69.75	16.94	0.5552	0.4372	0.2379	22.006	65.43	0.6431	0.4234	1
25	2.51	0.0195	3.86E-05	293.56	125.87	30.56	0.74661	0.5918	0.3268	22.011	65.44	0.6431	0.4233	1
30	2.83	0.0195	6.00E-05	455.95	195.68	47.53	0.9301	0.7456	0.4189	22.007	65.43	0.6431	0.4234	1
35	3.13	0.0195	8.18E-05	621.93	267.04	64.85	1.0864	0.8799	0.5026	22.009	65.43	0.6431	0.4233	1
40	3.41	0.0195	1.08E-04	823.75	353.83	85.95	1.2504	1.0253	0.5968	22.008	65.43	0.6431	0.4233	1
45	3.68	0.0195	1.46E-04	1105.4	474.96	115.36	1.4486	1.2075	0.72	22.009	65.43	0.6431	0.4233	1
50	3.94	0.0194	1.88E-04	1427.6	613.55	149.02	1.6464	1.3975	0.8544	22.008	65.43	0.6431	0.4233	1
55	4.19	0.194	2.34E-04	1773	763.58	185.45	1.8366	1.5886	0.9954	22.01	65.43	0.6431	0.4233	1
60	4.44	0.0194	2.82E-04	2143.2	921.48	223.81	2.0175	1.7788	1.1409	22.009	65.42	0.6431	0.4233	1

Table C.2: Summary of 20 GWd Sequence Variables Used for Multiplicity Counting from a Sample Containing Pu, Cm, and Eutectic Salt.

Enrich. (%)	FoM	$^{244}Cm_{eff}(g)$	S (cps)	D (cps)	T (cps)	SD_S	SD_D	SD_D	$\tau(\mu s)$	$\epsilon(\%)$	F_d	F_t	M
1.96	0.0198	2.35E-05	199.87	77.43	18.71	0.5987	0.4464	0.2425	21.997	66	0.6431	0.4232	0.9982
2.06	0.0199	2.13E-05	182.90	70.29	17.0003	0.5715	0.4238	0.2298	21.978	66.05	0.6432	0.4236	0.9981
2.17	0.0199	1.93E-05	167.53	63.708	15.38	0.5454	0.4016	0.2171	21.99	66.1	0.6431	0.4233	0.9979
2.28	0.0199	1.77E-05	154.75	58.45	14.11	0.5233	0.3835	0.207	21.991	66.14	0.6431	0.4234	0.9978
2.39	0.0199	1.62E-05	142.87	53.46	12.89	0.5016	0.3653	0.1968	21.999	66.19	0.6431	0.4233	0.9976

Table C.3: Summary of 25 GWd Sequence Variables Used for Multiplicity Counting from a Sample Containing Pu, Cm, and Eutectic Salt.

Enrich. (%)	FoM	$^{244}Cm_{eff}(g)$	S (cps)	D (cps)	T (cps)	SD_S	SD_D	SD_D	$\tau(\mu s)$	$\epsilon(\%)$	F_d	F_t	M
2.26	0.0197	4.24E-05	349.25	139.52	33.806	0.798	0.6113	0.3382	21.987	65.84	0.6432	0.4234	0.9989
2.39	0.0197	3.84E-05	318.56	126.47	30.63	0.7608	0.5797	0.3195	21.989	65.88	0.6431	0.4232	0.9988
2.51	0.0197	3.50E-05	291.13	115.065	27.84	0.7265	0.5511	0.3027	21.99	65.9	0.6431	0.4232	0.9986
2.64	0.0198	3.18E-05	267.36	104.78	25.35	0.6943	0.5237	0.2868	21.996	65.94	0.6431	0.4234	0.9985
2.76	0.0198	2.90E-05	246.09	95.77	23.16	0.6652	0.4988	0.2724	21.998	65.98	0.6431	0.4232	0.9984

Table C.4: Summary of 30 GWd Sequence Variables Used for Multiplicity Counting from a Sample Containing Pu, Cm, and Eutectic Salt.

Enrich. (%)	FoM	$^{244}Cm_{eff}(g)$	S (cps)	D (cps)	T (cps)	SD_S	SD_D	SD_D	$\tau(\mu s)$	$\epsilon(\%)$	F_d	F_t	M
2.55	0.0197	6.58E-05	531.59	2116.07	52.39	0.9891	0.774	0.4366	21.986	65.74	0.6432	0.4234	0.9992
2.69	0.0197	5.97E-05	484.69	196.028	47.49	0.9433	0.7339	0.4118	22.002	65.77	0.643	0.4231	0.9991
2.83	0.0197	5.44E-05	442.75	178.701	43.28	0.9011	0.6983	0.39020222		65.78	0.643	0.423	0.999
2.97	0.0197	4.94E-05	405.44	162.38	39.36	0.8604	0.6625	0.3687	21.988	65.83	0.6431	0.4233	0.999
3.11	0.0167	4.50E-05	372.19	148.18	35.8	0.8231	0.6303	0.3494	21.999	65.85	0.643	0.4232	0.9988

Table C.5: Summary of 35 GWd Sequence Variables Used for Multiplicity Counting from a Sample Containing Pu, Cm, and Eutectic Salt.

Enrich. (%)	FoM	$^{244}Cm_{eff}(g)$	S (cps)	D (cps)	T (cps)	SD_S	SD_D	SD_D	$\tau(\mu s)$	$\epsilon(\%)$	F_d	F_t	M
2.81	0.0196	9.03E-05	720.9443	296.1841	71.8354	1.1553	0.9201	0.5287	21.996	65.68	0.6431	0.4233	0.9993
2.97	0.0196	8.17E-05	655.3902	268.2234	65.0555	1.1004	0.871	0.4974	21.999	65.7	0.6431	0.4232	0.9993
3.13	0.0196	7.43E-05	598.3399	244.0759	59.2028	1.0504	0.8271	0.4697	21.99	65.73	0.6432	0.4232	0.9993
3.28	0.0196	6.76E-05	547.0672	222.0463	53.8165	1.0031	0.7851	0.4434	22.002	65.75	0.6431	0.4231	0.9991
3.44	0.0197	6.16E-05	501.0006	202.4934	49.1165	0.9588	0.7466	0.4198	21.992	65.77	0.6432	0.4234	0.9991

Table C.6: Summary of 40 GWd Sequence Variables Used for Multiplicity Counting from a Sample Containing Pu, Cm, and Eutectic Salt.

Enrich. (%)	FoM	$^{244}Cm_{eff}(g)$	S (cps)	D (cps)	T (cps)	SD_S	SD_D	SD_D	$\tau(\mu s)$	$\epsilon(\%)$	F_d	F_t	M
3.07	0.0196	1.17E-04	922.6204	381.7834	92.6199	1.3096	1.0598	0.6203	21.997	65.64	0.64313	0.4232	0.9994
3.24	0.0196	1.08E-04	861.039	355.2229	86.1566	1.2641	1.0175	0.5922	22.002	65.66	0.643	0.4231	0.9994
3.41	0.0196	9.85E-05	784.2204	322.8544	78.3085	1.2057	0.9649	0.5577	22.001	65.67	0.6431	0.4232	0.9994
3.58	0.0196	8.94E-05	716.1376	293.3343	71.1218	1.1506	0.9145	0.5251	22.004	65.7	0.643	0.4231	0.9993
3.75	0.0196	8.15E-05	655.5397	267.66	64.9647	1.0998	0.8695	0.4966	21.989	65.72	0.6432	0.4233	0.9993

Table C.7: Summary of 45 GWd Sequence Variables Used for Multiplicity Counting from a Sample Containing Pu, Cm, and Eutectic Salt.

Enrich. (%)	FoM	$^{244}Cm_{eff}(g)$	S (cps)	D (cps)	T (cps)	SD_S	SD_D	SD_D	$\tau(\mu s)$	$\epsilon(\%)$	F_d	F_t	M
3.31	0.0196	1.55E-04	1222.1	508.5469	123.368	31.5096	1.2468	0.748	22	65.61	0.6431	0.4232	0.9995
3.5	0.0196	1.41E-04	1110.5	460.7571	111.778	81.4378	1.1782	0.7005	22	65.63	0.6431	0.4232	0.9995
3.68	0.0196	1.32E-04	1043.3	432.403	104.979	61.3931	1.1365	0.6722	21.987	65.64	0.6432	0.4233	0.9995
3.86	0.0196	1.19E-04	948.9532	391.2843	94.9823	1.3268	1.0735	0.6297	21.996	65.67	0.6431	0.4235	0.9994
4.05	0.0196	1.09E-04	871.1112	358.1448	86.9209	1.2702	1.0214	0.595	21.99	65.68	0.6432	0.4234	0.9994

Table C.8: Summary of 50 GWd Sequence Variables Used for Multiplicity Counting from a Sample Containing Pu, Cm, and Eutectic Salt.

Enrich. (%)	FoM	$^{244}Cm_{eff}(g)$	S (cps)	D (cps)	T (cps)	SD_S	SD_D	SD_D	$\tau(\mu s)$	$\epsilon(\%)$	F_d	F_t	M
3.55	0.0196	2.04E-04	1602.1	669.5069	162.576	51.7303	1.4633	0.9033	21.99	65.59	0.6432	0.4234	0.9996
3.74	0.0196	1.86E-04	1465	610.2052	148.074	71.6532	1.3851	0.8464	21.997	65.61	0.6429	0.423	0.9996
3.94	0.0196	1.72E-04	1354	562.8217	136.642	31.5884	1.3213	0.8008	21.989	65.62	0.6432	0.4234	0.9996
4.14	0.0196	1.56E-04	1233.4	511.084	124.118	1.5148	1.2493	0.7502	22	65.63	0.6429	0.4232	0.9996
4.34	0.0196	1.42E-04	1129.9	467.0493	113.386	11.4488	1.1863	0.7064	21.991	65.65	0.6432	0.4234	0.9995

Table C.9: Summary of 55 GWd Sequence Variables Used for Multiplicity Counting from a Sample Containing Pu, Cm, and Eutectic Salt.

Enrich. (%)	FoM	$^{244}Cm_{eff}(g)$	S (cps)	D (cps)	T (cps)	SD_S	SD_D	SD_D	$\tau(\mu s)$	$\epsilon(\%)$	F_d	F_t	M
3.77	0.0195	2.57E-04	2007.1	841.2424	204.198	41.9384	1.6776	1.0635	22.003	65.57	0.6431	0.4232	0.9997
3.98	0.0196	2.33E-04	1826.8	763.9836	185.509	11.8481	1.5826	0.9918	21.994	65.59	0.6432	0.4233	0.9996
4.19	0.0196	2.13E-04	1671.6	697.5143	169.341	61.7667	1.4987	0.9294	21.989	65.6	0.6432	0.4233	0.9996
4.4	0.0196	1.94E-04	1525.2	634.6414	153.988	51.6864	1.417	0.8694	22	65.61	0.6431	0.4232	0.9995
4.61	0.0196	1.77E-04	1395.8	579.2612	140.563	41.6121	1.343	0.8162	21.999	65.63	0.6431	0.4232	0.9995

Table C.10: Summary of 60 GWd Sequence Variables Used for Multiplicity Counting from a Sample Containing Pu, Cm, and Eutectic Salt.

Enrich. (%)	FoM	$^{244}Cm_{eff}(g)$	S (cps)	D (cps)	T (cps)	SD_S	SD_D	SD_D	$\tau(\mu s)$	$\epsilon(\%)$	F_d	F_t	M
3.99	0.0195	3.11E-04	2420.3	1017	246.853	42.1302	1.8853	1.2249	22.008	65.55	0.643	0.4231	0.9997
4.22	0.0195	2.83E-04	2205.1	924.644	224.427	72.0321	1.7772	1.1403	22.005	65.57	0.6431	0.4232	0.9997
4.44	0.0196	2.57E-04	2007.1	839.9053	203.972	51.9375	1.6757	1.0623	21.993	65.58	0.6432	0.4234	0.9997
4.66	0.0196	2.34E-04	1834.5	765.7309	185.829	1.8511	1.5843	0.993	22	65.59	0.6431	0.4232	0.9996
4.88	0.0196	2.12E-04	1670.7	695.5357	168.785	11.7652	1.4956	0.927	21.999	65.61	0.6431	0.4232	0.9996

Table C.11: Summary of 20 GWd Source Strength Variables Used to Calculate Plutonium Mass.

Enrichment (%)	$F_o SF(Cm)$	$F_o(\alpha, n)Cm$	$F_o(\alpha, n)Pu$	$F_o(SF)Pu$
1.96	1.03E+07	1.72E+06	2.68E+03	3.39E+02
2.06	1.03E+07	1.73E+06	2.64E+03	3.31E+02
2.17	1.03E+07	1.74E+06	2.59E+03	3.23E+02
2.28	1.03E+07	1.75E+06	2.55E+03	3.15E+03
2.39	1.03E+07	1.75E+06	2.50E+03	3.08E+02

Table C.12: Summary of 25 GWd Source Strength Variables Used to Calculate Plutonium Mass.

Enrichment (%)	$F_o SF(Cm)$	$F_o(\alpha, n)Cm$	$F_o(\alpha, n)Pu$	$F_o(SF)Pu$
2.26	1.03E+07	1.68E+06	3.43E+03	3.72E+02
2.39	1.03E+07	1.68E+06	3.37E+03	3.63E+02
2.51	1.03E+07	1.69E+06	3.32E+03	3.55E+02
2.64	1.03E+07	1.70E+06	3.26E+03	3.46E+02
2.76	1.03E+07	1.70E+06	3.21E+03	3.38E+02

Table C.13: Summary of 30 GWd Source Strength Variables Used to Calculate Plutonium Mass.

Enrichment (%)	$F_o SF(Cm)$	$F_o(\alpha, n)Cm$	$F_o(\alpha, n)Pu$	$F_o(SF)Pu$
2.55	1.02E+07	1.65E+06	4.23E+03	4.03E+02
2.69	1.02E+07	1.66E+06	4.17E+03	3.93E+02
2.83	1.02E+07	1.66E+06	4.11E+03	3.84E+02
2.97	1.02E+07	1.67E+06	4.04E+03	3.75E+02
3.11	1.02E+07	1.67E+06	3.98E+03	3.66E+02

Table C.14: Summary of 35 GWd Source Strength Variables Used to Calculate Plutonium Mass.

Enrichment (%)	$F_o SF(Cm)$	$F_o(\alpha, n)Cm$	$F_o(\alpha, n)Pu$	$F_o(SF)Pu$
2.81	1.02E+07	1.63E+06	5.07E+03	4.32E+02
2.97	1.02E+07	1.63E+06	5.01E+03	4.22E+02
3.13	1.02E+07	1.63E+06	4.94E+03	4.12E+02
3.28	1.02E+07	1.64E+06	4.87E+03	4.02E+02
3.44	1.02E+07	1.64E+06	4.79E+03	3.92E+02

Table C.15: Summary of 40 GWd Source Strength Variables Used to Calculate Plutonium Mass.

Enrichment (%)	$F_o SF(Cm)$	$F_o(\alpha, n)Cm$	$F_o(\alpha, n)Pu$	$F_o(SF)Pu$
3.07	1.02E+07	1.61E+06	5.96E+03	4.60E+02
3.24	1.02E+07	1.61E+06	5.89E+03	4.49E+02
3.41	1.02E+07	1.62E+06	5.81E+03	4.38E+02
3.58	1.01E+07	1.62E+06	5.74E+03	4.28E+02
3.75	1.01E+07	1.62E+06	5.66E+03	4.18E+02

Table C.16: Summary of 45 GWd Source Strength Variables Used to Calculate Plutonium Mass.

Enrichment (%)	$F_o SF(Cm)$	$F_o(\alpha, n)Cm$	$F_o(\alpha, n)Pu$	$F_o(SF)Pu$
3.31	1.01E+07	1.60E+06	6.87E+03	4.86E+02
3.50	1.01E+07	1.60E+06	6.80E+03	4.75E+02
3.68	1.01E+07	1.60E+06	6.73E+03	4.64E+02
3.86	1.01E+07	1.60E+06	6.64E+03	4.53E+02
4.05	1.01E+07	1.60E+06	6.56E+03	4.42E+02

Table C.17: Summary of 50 GWd Source Strength Variables Used to Calculate Plutonium Mass.

Enrichment (%)	$F_o SF(Cm)$	$F_o(\alpha, n)Cm$	$F_o(\alpha, n)Pu$	$F_o(SF)Pu$
3.55	1.01E+07	1.58E+06	7.80E+03	5.11E+02
3.74	1.01E+07	1.58E+06	7.74E+03	5.00E+02
3.94	1.01E+07	1.58E+06	7.66E+03	4.89E+02
4.14	1.01E+07	1.59E+06	7.58E+03	4.77E+02
4.34	1.01E+07	1.59E+06	7.49E+03	4.66E+02

Table C.18: Summary of 55 GWd Source Strength Variables Used to Calculate Plutonium Mass.

Enrichment (%)	$F_o SF(Cm)$	$F_o(\alpha, n)Cm$	$F_o(\alpha, n)Pu$	$F_o(SF)Pu$
3.77	1.00E+07	1.57E+06	8.76E+03	5.36E+02
3.98	1.00E+07	1.57E+06	8.70E+03	5.24E+02
4.19	1.00E+07	1.57E+06	8.63E+03	5.13E+02
4.40	1.00E+07	1.57E+06	8.54E+03	5.01E+02
4.61	1.00E+07	1.58E+06	8.45E+03	4.90E+02

Table C.19: Summary of 60 GWd Source Strength Variables Used to Calculate Plutonium Mass.

Enrichment (%)	$F_o SF(Cm)$	$F_o(\alpha, n)Cm$	$F_o(\alpha, n)Pu$	$F_o(SF)Pu$
3.99	1.00E+07	1.56E+06	9.72E+03	5.60E+02
4.22	9.99E+06	1.58E+06	9.67E+03	5.48E+02
4.44	9.99E+06	1.56E+06	9.61E+03	5.36E+02
4.66	9.98E+06	1.56E+06	9.53E+03	5.24E+02
4.88	9.98E+06	1.56E+06	9.43E+03	5.14E+02

Vita

Stephen N. Gilliam was born in Knoxville, TN to Steve and Kellie Gilliam. He is a triplet. He attended Central High School in Knoxville, TN. After graduation he spent four years at the University of Tennessee, finishing his undergraduate degree in Nuclear Engineering in May 2016. He accepted a graduate research assistantship at the University of Tennessee in the Nuclear Engineering program under his advisors Dr. Jamie Coble and Dr. Steve Skutnik. He graduates with his Doctor of Philosophy degree in Nuclear Engineering in December 2020.